Innovative approach for the application of MTT, LDH and bis-ANS: *ex vivo* modelling of the extracellular beta-amyloid precipitation

Emese Szilvia Jánosi-Mózes

PhD Thesis

Department of Psychiatry

University of Szeged, Faculty of Medicine

Supervisor: Zsolt László Datki, PhD

Doctoral School of Theoretical Medicine

Szeged

2021

Publications

Publications the Thesis is based on:

I. **Mozes E**, Hunya A, Toth A, Ayaydin F, Penke B, Datki ZL. A novel application of the fluorescent dye bis-ANS for labeling neurons in acute brain slices. Brain Res Bull. 2011;86(3-4):217-221. doi:10.1016/j.brainresbull.2011.07.004 **IF: 2.818**

II. **Mozes E**, Hunya A, Posa A, Penke B, Datki Z. A novel method for the rapid determination of beta-amyloid toxicity on acute hippocampal slices using MTT and LDH assays. Brain Res Bull. 2012;87(6):521-525. doi:10.1016/j.brainresbull.2012.02.005 **IF: 2.935**

III. Datki Z, Galik-Olah Z, **Janosi-Mozes E**, et al. Alzheimer risk factors age and female sex induce cortical Aβ aggregation by raising extracellular zinc [published online ahead of print, 2020 Jun 9]. Mol Psychiatry. 2020;10.1038/s41380-020-0800-y. doi:10.1038/s41380-020-0800-y **IF: 12.384**

The cumulative impact factor of the publications directly related to Thesis: 18.137

Publications indirectly related to the Thesis:

IV. Földi I, Datki ZL, Szabó Z, **Mózes E**, Bozsó Z, Penke B, Janáky T. Proteomic study of the toxic effect of oligomeric Aβ1-42 in situ prepared from "iso-Aβ1-42″. Neurochem Int. 2013 Jan;62(1):58-69. doi: 10.1016/j.neuint.2012.11.003. Epub 2012 Nov 12. **IF: 4.244**

V. Veszelka S, Tóth AE, Walter FR, Datki Z, **Mózes E**, Fülöp L, Bozsó Z, Hellinger E, Vastag M, Orsolits B, Környei Z, Penke B, Deli MA. Docosahexaenoic acid reduces amyloid-β induced toxicity in cells of the neurovascular unit. J Alzheimers Dis. 2013 Jan 1;36(3):487-501. doi: 10.3233/JAD-120163. **IF: 4.53**

The cumulative impact factor of the whole scientific work: 26.911

Table of Contents

Abbreviations

Aβ, Aβ1-42 → amyloid-beta 1-42

ACSF → artificial cerebrospinal fluid

AD → Alzheimer's disease

ADDLs → Aβ derived diffusible ligands

AMPA → amino-3-hydroxy-5-methyl-4-isoxazolepropionic acid

ANS → 8-Anilinonaphthalene-1-sulfonic acid

APP → amyloid precursor protein

bis-ANS → 4,4'-Dianilino-1,1'-Binaphthyl-5,5'-Disulfonic Acid, fluorescent probe

CA1, CA2, CA3 → Cornu Ammonis region of the hippocampus

CNS → central nervous system

DG → dentate gyrus (of the Hippocampus)

DiI → 1,1'-dioctadecyl-3,3,3'3'-tetramethylindocarbocyanine perchlorate, carbocyanin fluorescent dye

DiO → 3-octadecyl-2-[3-(3-octadecyl-2(3H)-benzoxazolylidene)-1-propenyl]-, perchlorate

DMSO → dimethyl sulfoxide

EDTA, CaEDTA → ethylenediaminetetraacetic acid and its Ca^{2+}-saturated version

ExViS → *ex vivo* system

FBS → fetal bovine serum

fEPSP → field excitatory postsynaptic potentials

GluR1, GluR2, GluR3 → Glutamate receptor 1, 2, 3

h-Aβ → human amyloid-beta

HBS → HEPES-buffered saline

HEPES → 4-(2-hydroxyethyl)-1-piperazineethanesulfonic acid

Hil → hilus (of the Hippocampus)

Kd → equilibrium dissociation constant

LDH → lactate dehydrogenase

LTP → long-term potentiation

MAP2 → microtubule-associated protein 2

MEA → multi-electrode array

MTT → 4,5-dimethylthiazol-2-yl)-2,5-diphenyltetrazolium bromide

NADPH → Nicotinamide adenine dinucleotide phosphate

NFI → normalized fluorescence intensity

NMDA → N-Methyl-D-aspartic acid or N-Methyl-D-aspartate

OD → optical density

OGD → oxygen-glucose deprivation

OHSC → Organotypic hippocampal slice culture

PI → propidium iodide

r-Aβ → rat amyloid-beta (AβΔ2His)

sAPPα → soluble amyloid precursor protein (cleaved by alpha-secretase)

SH-SY5Y → human neuroblastoma cell line

Sub → subiculum (of the Hippocampus)

TBS → theta-burst stimulation

TPEN → N,N,N′,N′-tetrakis(2-pyridinylmethyl)-1,2-ethanediamine

UC → untreated control

ZnT3 → zinc transporter 3

1. Introduction

1.1. Hippocampal slices for modelling events in Alzheimer's disease

Alzheimer's disease (AD) results in progressive loss of tissue throughout the brain, in particular the hippocampus (Bonner-Jackson et al. 2015) which plays central role in the progression of the disease. Hippocampal atrophy is considered to be the most predictive structural brain biomarker of AD (Jack et al., 2000). With its high density of glutamate receptors, in particular N-methyl-D-aspartate (NMDA) receptors, the hippocampus is known to play fundamental role in some forms of learning and memory. Glutamatergic synapses can demonstrate significant plasticity and are also characterized by their ability to express long-term potentiation (LTP) (Cotman et al., 1988; Collingridge and Singer, 1990), a cellular and molecular remodelling that is widely accepted to be an underlying mechanism for learning and memory (Butterfield and Pocernich, 2003). The activation of postsynaptic NMDA receptors triggers signal cascades that are crucial for inducing LTP and neuronal plasticity.

Over the course of AD, up to 80% of neurons in the hippocampus die, consequently the progressive symptoms of the disease manifest themselves as cognitive disturbances, disorientation and inability to form new, episodic memories, specifically those regarding time and location.

Recent improvements in brain slice technology have made *ex vivo* models increasingly useful for investigating the pathophysiology of neurodegenerative diseases in a tissue context. In the meantime, while preserving the tissue architecture and synaptic circuitry, the technology also has its advantages compared to *in vivo* models, excluding lengthy animal surgery to model neuropathology of brain injury or laborious monitoring of multiple physiological parameters. Brain slices have been proven to be useful in basic research and in the drug discovery process in recent years: a number of pharmacological and genetic interventions affecting the brain neurochemistry *in vivo* have been reproduced in brain slices (Cho et al., 2004; Ray et al., 2000). Hippocampal slices have been validated to be a capable experimental model for investigating the structural and functional features of synapses at the molecular, cellular, and circuit levels. The most widely used hippocampal slice preparations are the acute hippocampal slices and the organotypic hippocampal slice cultures (OHSC).

OHSCs allow the tracking of processes that take up a larger time frame (several weeks or months), but the neuronal injury and disruption of afferent and efferent connections that occur during the preparation induce neurite remodelling and reorganization of synapses among the remaining neurons (Lo et al., 1994).

The advantages of acute slices relative to slice cultures are that they involve less work to prepare and maintain, and except for the absence of afferent input, the slice is minimally altered relative to the *in vivo* patterns at the time of harvest. Hippocampal slice preparations preserve the cytoarchitecture and synaptic circuits of the intact hippocampus (Grabiec & Hohmann et al., 2017). Most commonly, acute hippocampal slice preparations are collected from the adult rodent brain and to be used for experimentation on the same day as they are prepared. They are readily accessible for electrophysiological studies and optical imaging. That said, a more in-depth study on the effects of acute hippocampal slice preparation has revealed several molecular changes, such as the loss of Glutamate receptor 1 (GluR1) and GluR3, but not of GluR2 proteins, caused by slicing (Taubenfeld et al., 2002). The results of the study suggests alterations in synaptic response, however it was also found that apoptosis did not occur 6 hours post-slicing and the inner layers of the tissue, if maintained under the proper conditions, remain reasonably intact for several hours.

The key of successful and physiologically relevant measurements performed on acute hippocampal slices is to maintain the tissue viability as long as possible within conditions mimicking the *in vivo* physiological conditions. Our laboratory developed a set up, named *ExVis* (*Ex Vivo* System), described in detail within the following chapters, that serves as a cost-effective and convenient tool to maintain acute brain tissue viability during several-hours lasting treatments.

1.2. Aβ toxicity on acute hippocampal slices

β-amyloid peptide (Aβ1-42) is one of the main protein components of senile plaques associated with AD. Although these plaques may have harmful properties, soluble oligomeric forms of Aβ have been shown to be particurarly neurotoxic (reviewed by Lee et al., 2007 and Reiss et al., 2018).

Aβ is a small peptide of 39-43 amino acids and its formation results from the metabolism of human amyloid precursor protein (APP). Aβ isoforms bear subtle differences depending on

the number of C-terminal amino acids and Aβ1−42 isoform plays a pivotal role in the pathogenesis of AD. The neuroxicity of Aβ peptide stems in its biochemical properties that make it prone to aggregate into insoluble oligomers and protofibrils. APP is a transmembrane metalloprotein, which possesses copper and zinc binding sites in its N-terminal domain and in the Aβ domain (Bush et al., 1993). The enzymatic processes responsible for APP-Aβ cleavage are now fairly well understood. APP is cleaved sequentially by two membrane-bound endoproteases, β- and γ-secretase, both targets for AD treatment to disfavor amyloid generation, however the potential adverse events of these desease modifying treatments may mask their therapeutic potential (reviewed by Maia and Sousa 2019 and Zhu et al., 2018) Non-amyloidogenic processing of APP is performed by α-secretase. The clevage site of the enzyme lies within the Aβ sequence, thus preventing aggregation-prone peptide formation and resulting in soluble APP (sAPPα) release. Genetic studies of early-onset cases of familial AD indicate that APP mutations and Aβ metabolism are associated with AD.

Aβ oligomers can be generated both extracellularly and intracellularly and can be toxic to neurons and neuronal connections in numerous ways. Hence, another potential therapeutic target are Aβ toxic oligomers and Aβ aggregation process. Measuring the toxic effect of different Aβ aggregation species as well as the neuroprotective effect of novel drug candidates requires a reliable and relevant assay. Along with electrophysiology measurements on *ex vivo* brain slices, MTT (3-(4,5-Dimethylthiazol-2-yl)-2,5-diphenyltetrazolium bromide, a yellow tetrazole) assay has been the most commonly used method for measuring the impact of Aβ toxicity on cell viability in neuronal cell cultures. The MTT assay is a colorimetric assay for measuring cell metabolic activity allowing to quantitatively compare cell viability in different treatment groups. Its mechanism of action relies on the ability of nicotinamide adenine dinucleotide phosphate (NADPH)-dependent mithocondrial oxidoreductase enzymes to reduce the dye to its purple, water insoluble formazan crystals (Fig.3.) (Lu et al., 2012; Stockert et al., 2012).

Various cell types, such as SH-SY5Y neuroblastoma cells (Datki et al., 2003), primary rat neuronal cells (Rönicke et al., 2008), murine embryonic stem cells and haematopoietic progenitor cells in culture (Nair et al., 2010), as well as primary hippocampal cell culture (Ho et al., 2015) have been exposed to Aβ 1-42 and 1-40 oligomers and then cell viability changes were quantified with MTT assay.

Although the MTT assay (performed on cell lines or primary cell cultures) proved to be suitable for measurements of Aβ toxicity, these *in vitro* methods have their limitations. Beside being unable to replicate many aspects of the *in vivo* context, we found that SH-SY5Y cells can be insensitive against Aβ peptides. Application of primary neuronal cultures is suitable in experiments with several days time-frame; however, it is complicated and expensive to prepare them and most importantly, the disruption of connections that occur during the preparation of hippocampal slices induce axonal and dendritic remodelling and reorganization of synapses among the remaining neurons. The most physiologically relevant MTT assay would use brain tissue slices where neuronal connections and glial environment remain at least partly intact.

MTT assay has already been used on acute hippocampal slices for measuring the toxic effect of Cd^{2+} (Rigon et al., 2008) and H_2O_2 (de Almaida et al., 2008). The neurotoxic effects of mercurials were also measured quantitatively with MTT assay in cerebral cortex slices (Moretto et al., 2005). Hippocampus consists of very different cell types (neuronal, glial and endothelial cells); however, all of these cells are sensitive against Aβ toxicity (Laskay et al., 1997; Jancso et al., 1998). To our knowledge, brain slice MTT assay has never been used till the publication of our study (Mozes et al., 2012) for measuring Aβ toxicity.

Our goal was to develop a rapid and reliable assay for Aβ toxicity measurement within the tissue context of the hippocampus.

1.2.1. The importance of oxigen-glucose dperivation in hippocampal slice models of the ageing brain

We enriched our model with an additional relevant event of the ageing brain: in addition to Aβ1-42 treatment acute slices underwent a mild oxygen-glucose deprivation (OGD) as well. Cerebral hypoperfusion is an early event in AD and increases the risk to develop the disease (Koike et al., 2011). OGD induced neuron-specific cell death in OHSC (Cho et al., 2004) and it has also been associated with amyloid accumulation (Horsburgh et al., 2011). A number of studies executed in hippocampal slice systems have explored the impairing effects of ischemic-like conditions on synapses and mitochondrial function. OGD caused the loss of transmembrane Na, K, and Ca gradients in CA1 (cornu ammonis) neurons (Taylor et al., 1999) and was associated with a significant increase in cytosolic Ca^{2+} in both young and aged

synapses and shown to be irreversible in the latter (Tonkikh et al., 2009). Ischemic events may directly contribute in brain capillary endothelial cells to the enhancement of the amyloidogenic metabolism, leading to intracellular deposition of Aβ, ultimately contributing to the impairment of Aβ clearance from brain and AD related blood brain barrier dysfunctions (Bulbarelli et al., 2012). Hence, application of a short and mild OGD to the medium of hippocampal slices can simulate the early events seen in AD.

The response to OGD of different brain slice systems – acutely prepared and cultured – has already been studied using MTT as well as Lactate dehydrogenase (LDH) assay (Tagliari et al., 2006; Chechetti et al., 2007; Zhou et al., 2007; Zhou et al., 2009). This latter assay is commonly used to measure the cytotoxic effect of OGD. Its concept is based on the behaviour of LDH, a cytoplasmic enzyme, expressed in almost all tissue types which is rapidly released into the medium upon the damage of the plasma membrane.

Measuring Aβ toxicity on OGD acute hippocampal slices could be a relevant model and an easy *ex vivo* quantitative method to screen protective agents.

1.3. *Ex vivo* fluorescent imaging of neuronal structures: a novel application of bis-ANS

We can gain deeper understanding about the investigated neurodegenerative phenomenons in the brain and hippocampus by correlating cellular level physiological analyses with static images obtained within the larger context of the tissue. Fluorescent imaging of the live tissue is used for the comparative visualization of different cellular, intracellular parameters as well as dynamic tissue-level processes such as microglia motility (Basilico et al., 2019), dendritic spine density changes (Zuo et al., 2005), hippocampal Zn^{2+} distribution (Santhakumar et al., 2018) or Zn^{2+}-induced Aβ aggregation (Datki et al., 2020).

In vitro studies on Aβ oligomerization and on acute hippocampal slices executed in our laboratory lead us to the discovery and further exploration of the neuron labelling properties of the oligomer-specific fluorescent dye, 4,4-bis-1-anilinonaphtalene-8-sulfonate (bis-ANS) (Mozes et al., 2011)

Due to their sensitivity and versatility, extrinsic, non-covalent fluorescent dyes such as 8-Anilinonaphthalene-1-sulfonic acid (ANS), bis-ANS, Nile Red and Thioflavin T find

widespread application in various fields of protein analysis such as characterizing folding intermediates or to detect aggregation and fibrillation (Reviewed by Hawe et al., 2008).

The oligomer-specific bis-ANS first described by Rosen and Weber in 1969, is a dimeric analogue of ANS. The fluorescence properties of this dye strongly depend on their interaction with proteins (Stryer 1965) and are sensitive to the environment of the dyes with respect to polarity, viscosity and temperature (Rosen and Weber 1969). Hydrophobic and electrostatic interactions have been suggested as possible mechanisms of bis-ANS binding to proteins (Gupta et al., 2003; Horowitz et al., 1984). Bis-ANS exhibits a chaperone-like activity, effectively suppressing protein aggregation and preventing a certain degree of heat-inactivation of enzymes (Fu et al., 2005). Horowitz et al.(1984) has shown that bis-ANS binds to tubulin, inhibiting the formation of microtubules and tubulin-binding properties were further examined and shown that the dye differs from other well-known microtubule inhibitors in its specificity of action. It has been shown that specifically inhibits C-termini mediated assembly such as microtubule-associated protein 2 (MAP2), tau and poly(L-lysine) but not taxol, dimethyl sulfoxide (DMSO) or glutamate (Mazumdar et. al, 1992). Their experiments demonstrate the presence of more than one site for the binding of bis-ANS to tubulin, and additional binding sites may appear as a function of time and temperature. Tubulin apparently has two types of bis-ANS binding sites: a primary site responsible for the inhibition of microtubule assembly with an equilibrium dissociation constant (kd) of 2 mM and six secondary sites with a kd of 19 mM (Prasad et al., 1986).

The use of fluorescent neuron labelling methods has become increasingly important in research on the nervous system and its related pathological processes. The oxazine alkaloid Darrow Red, first described by Powers et al. (1960) is one of Nissl staining dyes. Darrow Red was successfully combined with silver impregnation to visualize the neurofibrillary changes characteristic of AD (Braak et al., 1988). Compared to Nissl type stains, a more sensitive and definitive marker of neurodegeneration, Fluoro Jade, was first reported by Schmued et al. (1997). Fluoro Jade is an anionic fluorochrome capable of selectively staining degenerating neurons in *ex vivo* central nervous system (CNS) tissue, however, the detailed mechanism behind its selectivity remains to be elaborated. Other fluorescent techniques such as axonal tract tracing, immunofluorescence and Nissl counterstaining can be combined with Fluoro Jade.

Fluorescent lipophilic carbocyanine dyes, DiI (1,1'-dioctadecyl-3,3,3'3'-tetramethylindocarbocyanine perchlorate) and DiO (3-octadecyl-2-[3-(3-octadecyl-2(3H)-benzoxazolylidene)-1-propenyl]-, perchlorate), have an extensive history of use in cell biology, but their wide use as neuronal tracer has been introduced and grown recently. Their fluorescence is exhibited upon insertion of their lipophilic hydrocarbon chains into the lipid membrane. Honig and Hume (1989) reported that these dyes were applied in neurons placed in culture, and they initially labelled the processes (anterograde and retrograde tracing) as well as the cell bodies of cultured neurons, and that they apparently were not toxic. Lateral diffusion in the membrane was the major mechanism for the translocation of these molecules, rather than fast axonal transport (Honig et al., 1989). Godement et al. (1987) reported that these dyes can be used to label axonal and dendrite projections in fixed tissues, as well. DiI is suitable to illuminate the details of individual neuronal cytoarchitecture, including neurite arborization and dendritic spines. It was successfully used in acute hippocampal slices for the rapid comparison of dendritic spines with confocal microscopy (Trivino-Paredes et al., 2019) and for the characterization of dural afferent neurons (Nakamura and Jang 2018).

Our study presents a novel application of the bis-ANS for the detection of mechanically damaged neurons on the surface of acute hippocampal slices and its properties – somewhat similar to that of Fluoro Jade – are visaulized in the context of the already extensively explored propidium iodide (PI) and DiI tracers.

1.4. Acute hippocampal slice technique to model the role of Zn^{2+}-induced Aβ toxic oligomerization on cell viability, learning and memory

Zinc plays crucial role in synaptic plasticity, learning, and memory (Ueno et al., 2002; Ceccom et al., 2015) and numerous studies have suggested that the disruption of zinc homeostasis, – both depletion and excess – is linked with various neurodegenerative diseases including AD.

Zinc ion released from neurons interacts with Aβ, and is enriched in senile plaques in the brain of AD patients (Lovell et al., 1998). In APP transgenic mice the synaptic zinc distribution correlates to amyloid burden within the cortical layers (Stoltenberg et al., 2007). Aβ is rapidly precipitated by Zn^{2+} at neutral pH (Bush et al., 1994) and is reversible with chelators, such as ethylenediaminetetraacetic acid (EDTA) and clioquinol (Cherny et al.,

2001; Lee et al., 2004; Adlard et al., 2008). Aβ deposits in *post mortem* human brain can also be dissolved with agents that release the Zn^{2+} ions trapped inside the plaques (Cherny et al., 1999; Cherny et al., 2001). These findings have lead to the development of drug candidates that target Aβ-metal complexes and have reported efficacy in preclinical AD models and phase 2 clinical trials (Lee et al., 2004) although none have reached further pivotal testing. The factors that induce the aggregation and accumulation of Aβ in the ageing brain remain elusive, but a number of growing evidence indicates that neuronal Zn^{2+} release could play an important role (Bush et al., 1994; Lovell et al., 1998; Stoltenberg et al., 2007; Cherny et al., 2001).

However, it is likely that Zn^{2+} acts as a "double-edged sword": studies suggest its contribution to AD via the oligomerization effect, but also as a protective agent against the neurotoxicity of Aβ (Cuajungco et al., 2000). Reportedly, its toxic aggregation effect is concentration dependent (Lovell et al., 1999, Yoshiike et al., 2001).

Extracellular zinc is relatively low in the brain, but high levels of zinc are present in the hippocampus, the amygdala, and the cortex, where Zn^{2+} is concentrated in synaptic vesicles of specific excitatory glutamatergic neurons via the specific zinc transporter ZnT3 (Frederickson and Bush 2001) and is secreted from these vesicles into synaptic cleft along with glutamate during neuronal excitation. Remarkably, ZnT3 knock-out transgenic mice do not develop amyloid plaques in the brain (Lee et al. 2002), indicating that synaptic zinc may have a causative role in toxic amyloid oligomer formation and pathology of AD (Deibel et al. 1996; Adlard and Bush 2006).

Secreted Zn^{2+} binds to NMDA receptors, amino-3-hydroxy-5-methyl-4-isoxazolepropionic acid (AMPA) receptors and glycine receptors and it also regulates their dynamics (Paoletti et al., 2009). Hippocampal Zn^{2+} is essential for the induction of LTP (Lu et al., 2000; Takeda et al., 2013), a form of synaptic strengthening that has become a paradigm for the mechanisms of learning and memory formation.

In our recently published study (Datki et al., 2020) we showed that after inducing massive Zn^{2+} release on acute hippocampal slices, Aβ1-42 could be rapidly aggregated into bis-ANS reactive species (where bis-ANS was used as an oligomer-specific fluorescent probe). Consequently, LTP and hippocampal viability is attenuated.

2. Aims

In preclinical AD research and other neurodegenerative studies it is crucial to choose the adequate model, taking into account not just the capabilities and properties of the chosen system but as well its cost and the time needed to get the results. The living acute brain slice preparation has been developed and extensively used as a powerful experimental model for investigating the structural and functional characteristics of synaptic connectivity of neuronal circuits in the brain. Due to its three-dimensional and intact structure under the cutting surface and the conserved cell variability provides a more relevant model than monolayer cell cultures and protective or toxic agents can be rapidly tested and selected for further *in vivo* studies. *Ex vivo* brain slices also provide a suitable tool to test hypothesis of pathological mechanisms.

Therefore, during the course of my PhD work, in tight-knit teamwork, I set and completed the following goals:

1. Developing and tailoring novel approaches for the application of MTT and LDH assays on acute hippocampal slices modelling the ageing brain in order to measure the effects of Aβ1-42 aggregation and potential protective agents.

2. Exploring a novel application possibility of bis-ANS fluorophore to label neurite cross-sections and engage in detailed fluorescent imaging of neuronal structures in *ex vivo* hippocampus.

3. *Ex vivo* modelling of Zn^{2+}-induced Aβ aggregation and measuring its effect on viability and synaptic function.

3. Materials and methods

3.1. Materials

3.1.1. Fluorescent dyes

Cell-impermeant forms of bis-ANS (cat. no. 49058), PI (cat. no. P4170), DiI (cat. no. 42364) were obtained from Sigma-Aldrich, Hungary.

RhodZin-3 (cat. No. R-36350) was purchased from Molecular Probes, Invitrogen, Hungary

3.1.2. Anaesthetics, assays, devices and general reagents

Chloral hydrate (cat. no. 23100), N,N,N′,N′-tetrakis(2-pyridinylmethyl)-1,2-ethanediamine (TPEN; cat. No. P4413), CaEDTA (ethylenediaminetetraacetic acid saturated with Ca^{2+}; cat. No. ED2SC), MTT (cat. No. M5655), 96-well plates (Costar, cat. No. CLS3695), and general reagents were from Sigma-Aldrich, Hungary.

96-well plate specific NOVOstar OPTIMA plate reader was obtained from BMG Labtech, Budapest, Hungary.

Multi Channel System for electrophysiologycal recordings was obtained from MCS GmbH, Reutlingen, Germany and 3D-MEA chip from Ayanda Biosystems, S.A., CH-1015 Lausanne, Switzerland.

3.1.3. Animal models

Ten-weeks old male Wistar rats were obtained from Domaszék Kísérleti Állatház. The animal protocols applied in this study have been approved by the National Institutes of Health and by the University of Szeged; permission numbers: I-02442/001/2006.

3.1.4. *In vitro* cell culture

SH-SY5Y neuroblastoma cells were obtained from Sigma–Aldrich, Hungary.

3.1.5. Synthetic Aβ1-42 and [Ala$_{13,14}$]Aβ1-42 (Aβ$_{\Delta 2His}$)

Aβ 1-42 was synthesized in our laboratory (Bozso et al., 2010). Stock solution of oligomeric Aβ 1-42 (stock solution: 0,4 mM) was freshly prepared in distilled water (pH ≥5.0) and stored for maximum 10 minutes.

The Aβ peptides were prepared from their iso-Aβ precursors, where Gly$_{25}$ is linked through ester bond to the side chain of Ser$_{26}$. This modification allows increasing the initial solubility of the peptide. Via an intramolecular *O→N* acyl-shift iso-Aβ is rapidly ($t_{1/2}$ = 2.6 minutes) and completely converted into Aβ at pH 7.4

Peptides were cleaved by incubating the resin for 2.5 hours in a trifluoroacetic acid/phenol/ dithiotreithol/ tri-isopropylsilane/ water (1:1:1:1:36) mixture. Crude iso-Aβ was precipitated with diethyl ether, dissolved in a mixture of acetic acid and water, lyophilized and purified by HPLC on a Phenomenex Jupiter C4 column (10 µm, 300 Å, 250×21.294 mm). For [Ala$_{13,14}$]iso-Aβ (the precursor to Aβ$_{\Delta 2His}$), synthesis was performed as above, with histidine residues at positions 13 and 14 replaced with Ala.

3.1.6. Artificial cerebrospinal fluid

NaCl (cat. No. S9888), KCl (cat. No. P3911), $CaCl_2$ (cat. No. C8106), $MgCl_2$ (cat. No. M0250), HEPES (cat. No. H4034), $NaHCO_3$ (cat. No. 401676), D-Glucose (cat. No. G7528), MTT (cat. No. M5655) and 96-well plates (Costar, cat. No. CLS3695) were obtained from Sigma-Aldrich, Hungary.

The following 4-(2-hydroxyethyl)-1-piperazineethanesulfonic acid (HEPES) containing artificial cerebrospinal fluid (ACSF) solutions were used in the experiments (concentrations are given in mM):

H-ACSF/1: NaCl 122; KCl 3; $CaCl_2$ 0.3; $MgCl_2$ 3.7; $NaHCO_3$ 25; HEPES 5; D-glucose 10; pH=7.4.

H-ACSF/2: NaCl 132; KCl 3; $CaCl_2$ 2; $MgCl_2$ 2,; $NaHCO_3$ 25; HEPES 5; pH=7.4.

H-ACSF/3: NaCl 120; KCl 3; $CaCl_2$ 2; $MgCl_2$ 2; $NaHCO_3$ 25; HEPES 5; D-glucose 12; pH=7.4 (with normal calcium, magnesium and glucose levels).

3.1.7. Mini chamber system

The mini-chamber system (Fig. 1) was designed and set up in our institute (Datki *et al.*, 2007).

3.2. Methods

3.2.1. Preparation of the acute hippocampal and other brain tissue slices

In our experiments we applied a modified version of the method reported by Datki et al. (2007) to prepare the acute hippocampus, but also cerebellar, neocortical and thalamical brain slices were the specific experiment required the comparison with the hippocampal tissue.

Following narcosis with chloral hydrate (0.4 g/kg) 10 ± 1 -week-old male Wistar rats were decapitated. The heads without scalp-skin were placed in ice cold distilled water for 1 min. The brains were quickly removed and immersed in minimal Ca^{2+}-containing ACSF (preparation solution) with elevated Mg^{2+} at 4 ◦C (Lipton et al., 1995). The composition of the preparation solution was the following (in mM): NaCl 127; KCl 2; $MgCl_2$ 3.5; $CaCl_2$ 0.5; $NaHCO_3$ 25; D-glucose 10; pH = 7.4.

The 0.4 mm thick brain tissue slices were prepared from hippocampus, cerebellum and neocortex using McIlwain tissue chopper (Campden Instruments, Loughborough, UK) at 4 ºC. The surface area of the slices was determined with a preparation microscope (type Nikon SMZ800 with a 12 megapixel camera) directly after preparation. The well area (15 mm^2) was used for area calibration. The slices (area ≈9 mm^2) were rapidly transferred into a mini-chamber (*ExVis*, Fig. 1) for further treatment or into Petri dishes for labelling.

3.2.2. Fluorescent labelling of acute hippocampus slices

From the tissue chopper's plate, brain slices were rapidly transferred into Petri dishes for labelling. After rewashing, hippocampus slices were transferred to a cover slip mounted glass slide. In every case we controlled the distance between two glasses with an adhesive-paper (thickness 0.4 mm). As a result, all anatomically undamaged hippocampus slices from the median part (± 2 mm from middle) of the hippocampus were suitable for the experiments.

The labelling solution was composed of the following (in mM): NaCl 129; HEPES 20; $NaHCO_3$ 10; sucrose 10 (pH = 7.4), supplemented with 10 M bis-ANS; 3 μM PI or 50 μM DiI (with 1% DMSO in solution).

Bis-ANS and PI were applied simultaneously for 10 minutes, while in bis-ANS/DiI co-staining experiments the two dyes were applied consecutively. First, treatment with DiI for 15 min and after washing with the labelling solution described above, Bis-ANS was applied for 10 min.

3.2.3. Neuroblastoma *in vitro* cell culturing and fluorescent labelling

SH-SY5Y cell culturing was performed based on a slightly modified protocol described by Datki et al.(2003) The cells were plated for 24 h at 37 ◦C in Petri dishes (Sigma) at a density of 3×10^4 cells per well to 5% confluency.

CO_2 in a humidified atmosphere with Dulbecco's modified Eagle's medium (MEM): F-12 (1:1) with phenol red (Sigma, cat.no.: 51445C). l-Glutamine (4 mM; Gibco, Europe, cat. no.: 25030081), penicillin (200 units/mL; Gibco, cat. no.: 15140122), streptomycin (200 g/mL; Gibco, cat.no: 15140122), MEM non-essential amino acid solution (100× liquid mg/L; Gibco, cat. no.: 11140050) and 10% fetal bovine serum (FBS; Gibco, cat.no.: 10500064) were added to the medium. After mechanically damaging the cells by cutting a straight line on the Petri dish surface with a blade they were incubated in the presence of bis-ANS (10 μM) and PI (3 μM) for 10 min.

3.2.4. Fluorescence microscopy

Measurements were performed at room temperature (24 ºC). Images of figures 7, 8, 9 and 10 were taken with a 24-bit digital Colour-View II FW camera (with CCD arrays of 2080 × 1544 pixels) interlocked with the imaging system of an OLYMPUS IX71 inverted research fluorescence microscope. Image acquisition and analysis were performed by analySIS 3.2 software (OLYMPUS, Budapest, Hungary). To detect the fluorescence of the dyes we used the following wavelengths (ex./em.): 380/535 nm (bis-ANS), 530/620 nm (PI) and 550/620 nm (DiI).

3.2.5. Aβ1-42 treatment of hippocampal slices

After the preparation of the slices in ice cold H-ACSF/1 solution photos of them were made for measuring the slice area. Slices (with an area of approximately 9 mm^2) were quickly transferred into a mini-chamber (Fig. 1.; maximum 5 slices in 1 mL H-ACSF/1) for conditioning (30 min) in the carboxygenated (95/5% : O_2/CO_2) preparation solution at room temperature (24 ºC).

After 30 minutes hippocampus slices were transferred from the mini-chamber into the plastic Petri dish and was left to rest at room temperature in glucose- and carboxygen-free H-ACSF/2 (3 mL/Petri dish) for one hour. (The Petri dish was continuously being stirred at 370 rpm by a modified BIOSAN TS-100 thermo shaker). After one hour oxygen-glucose deprivation the supernatant (H-ACSF/2) in the Petri dish was changed to H-ACSF/3 solution (3 mL/Petri dish). The slices were quickly transferred into the mini-chambers (maximum 5 slices in 1 mL) for treating them with freshly prepared oligomeric Aβ1-42 peptide adding 50 µL stock solution of the peptide into 950 µL H-ACSF/3 in each chamber (final concentration of Aβ1-42: 20 µM). Foaming was inhibited by a floating plastic ball (diameter: 5 mm) applied in the mini tube chambers. Classic apoptotic factors (e.g. NaN_3, H_2O_2, KCN and Thapsigargin) were used as controls in these experiments.

3.2.6. MTT and LDH measurements

After treating the slices with 20 µM Aβ1-42 for 4 hours, the supernatant (to be used in LDH assay) was changed to H-ASCF/3 (0.9 mL/chamber) and 0.1 mL MTT stock solution (5 mg/ mL H-ACSF/3) was added (MTT final concentration: 0.5 mg/mL). The chamber was left to rest for 15 min without carboxygenation. To stop further reduction of MTT, the medium (H-ACSF/3) was removed. Then pure DMSO (100 µL/slice/well) was added for dissolving formazane from the slices. (30 min in a 96-well plate). Then 70 µL DMSO solution from each slice (well) was transferred into another 96-well plate. The optical density (OD) of the dissolved formazane was measured at 550 and 620 nm. The following formula was used for synchronizing the data: $(OD_{550} - OD_{620})$/area of slice (mm^2) = 100% in control (Aβ1-42 untreated slices).

For LDH measurements the above mentioned supernatants (H-ACSF/3) of the 4 hours Aβ1-42 treament of slices were used. Supernatants were centrifuged at 500 x *g* for 10 min and the

LDH activity was measured with a standard LDH kit (Sigma, TOX7-1KT). The results were calculated with the following formula: (OD_{450} – OD_{620})/mean area of slices (mm^2) = 100% in control (Aβ1-42 untreated chamber).

3.2.7. *Ex vivo* fluorescent detection of the vesicular Zn^{2+} release and Zn^{2+}-induced Aβ oligomerization

The kinetics of the change in the fluorescence intensity was measured with a 96-well plate specific NOVOstar OPTIMA plate reader (BMG Labtech, Budapest, Hungary) using fiberglass (Ø 3 mm, 20 flashes/well/cycle) optics that allowed the detection of the total area of the slice in a well (Datki et al. 2007).

After resting for 30 minutes in the mini-chamber system (described in Chapter 4.1) at room temperature in Ca^{2+}-free, carbogenated ACSF solution, the slices (maximum 10) were washed for 30 sec in 2 mL preheated (36 ºC) HEPES buffered saline (HBS, composition in mM: NaCl 125; KCl 2; $CaCl_2$ 2; $MgCl_2$ 2; HEPES 25; d-glucose 12; at pH=7.4. and 36 ºC). Next, brain slices were transferred from the mini-chamber into the plate wells (bottom area: 15 mm^2) using pipettes (type 20-200 µL) that were cut-off at their tip. Slices were transferred together with their media: 120 µL HBS per well. HBS solution was removed very carefully from the slices with a pipette and was replaced with

a) RhodZin3, a Zn^{2+}-specific fluorescent dye diluted in HBS solution (10µM, 40 µL per well) in order to monitor endogenous Zn^{2+} release; or

b) Bis-ANS, as Aβ oligomer specific fluorophore in 10 µM concentration to monitor Aβ-Zn^{2+} aggregation. Consequently, in the Aβ-Zn^{2+} precipitation measurements the Bis-ANS-HBS solution was supplemented with synthetic human or rat Aβ peptide (50 µM). Before each assay the stock solution of Aβ peptide (0.5 mM) was freshly prepared in distilled water (pH=5).

Each well accommodated one immobilized slice in central position. Immobilization was achieved by a round plastic web with 40 µm pore diameter, with no autofluorescence and handled with ceramic forceps. This process ideally took up a maximum of 2 minutes per 10 slices. The plates and the HBS solution were preheated at 35-36 ºC before slices were put into them. The temperature inside the plate-reader was also 36 ºC. The distance between the plastic web (which is placed on the slice) and the top of the well was consistently 9 mm (we

checked the distance at each measurement with the help of a plastic tube, which was marked at 8.9 mm).

For KCl treatment (final concentration 50 mM) we took advantage of the built-in liquid micro-pipettor (minimal pipetting capacity is 1 µL) in the plate reader with an injection speed of 420 µL/sec. Fluorescence intensity tracking begun 1 minute before the treatment of slices with KCl. *Ex vivo* Zn^{2+} release and precipitation with Aβ fluorescent tracking required high slice viability (in HBS solution) only for the period of the KCl-induced massive depolarization and intensive vesicular Zn^{2+} release (maximum 3 mins), since after the Zn^{2+} was released into the extracellular space, the detected reactions (Zn-dye or Aβ-dye complexes) were rather chemical than physiological. The normalized fluorescence intensity (NFI) in the Zn^{2+} release and Zn-Aβ precipitation measurements were calculated via the following formula: $[(F_{max}-F_0)/F_0]$/area of slice (mm^2), where F_0 is the initial fluorescence intensity of the dyes in the measurements before treatments. F_{max} is the maximum amplitude of the fluorescence intensity caused by Zn^{2-+}-release. Maximum 10 wells (one slice per well) can be scanned in one cycle (RhodZin3 λ ex. 550 and em. 580 nm; Bis-ANS: λ ex. 350 nm, em. 540 nm).

One cycle took 10 sec (the scanning of each well in a cycle lasted for 1s with 20 flashes). We detected the Zn^{2+} specificity, concerning vesicular Zn^{2+} release, by adding CaEDTA. To survey Zn^{2+} specificity, only CaEDTA could be used in Zn-Aβ precipitation measurements. The heading of excitation and emission light in the fiberglass optics was retrograde. We used the well-bottom-detection form in our measurements.

3.2.8. Multi-electrode array (MEA) electrophysiology

One acute hippocampal slice was placed in a 3D-MEA chip with 60 tip-shaped and 60-µm-high electrodes spaced by 100 µm (Ayanda Biosystems, S.A., CH-1015 Lausanne, Switzerland). The surrounding solution was removed, and the slice was immobilized by a grid. The slice was continuously perfused with carbogenated ACSF (1.5 mL/min at 34 °C) during the whole recording session. Prior to an experiment, slices were washed twice with ACSF, and then incubated (± CaEDTA 0.1 mM to reverse the Zn^{2+}-induced Aβ aggregates) for a further 1 h in the incubation chamber, to ensure that that the preparation was not affected by

residual K^+ or peptide remaining in the media. The slices were then stabilized for 30 min on the MEA chip.

Data were recorded with a Multi Channel System (MCS GmbH, Reutlingen, Germany). The Schaffer-collateral was stimulated by injecting a biphasic current waveform (100 + 100 μs) through one selected electrode at 0.033 Hz. We took care to choose the stimulating electrode in the same region from one slice to the other. The peak-to-peak amplitudes of field excitatory postsynaptic potentials (fEPSPs) at the proximal stratum radiatum of CA1 were analysed. Following a 30 min incubation period, slices were continuously stimulated with medium-strength stimuli. When stable evoked fEPSPs were detected (for at least 20 min), the stimulus threshold was determined, and a stimulus strength–evoked response curve (i.e. input–output, I–O curve) was recorded by gradually increasing stimulus intensity until the maximal stimulus strength was reached. The I–O curve for each slice did not show any significant differences between the treatment groups (not shown), indicating normal basal synaptic function. The stimulus intensity was continuously increased from 0 to 120 μA with 10 μA steps. Stronger stimulation led to large Faradic effects on the electrodes causing artifacts data sets were recorded for each stimulation intensity. The intensity of the test stimulus was set to be 30% of the threshold and maximum stimulus strength interval. After recording a 10 min stable control sequence, LTP was induced by applying theta-burst stimulation (TBS; trains of 15×100 Hz bursts, 5 pulses per burst with a 200 ms interburst interval), at the maximum stimulation intensity, then fEPSPs were recorded for 60 min.

3.2.9. Statistical analysis

Data are presented as means ± standard error of mean (S.E.M). Student-*t* test and ANOVA, *post hoc* test Bonferroni was used for statistical evaluation using Microsoft Excel and SPSS 10.0 for Windows software. The differences were compared with the control measurements of each conditions. The values were considered statistically significant at the level $p \leq 0.001$ and $p \leq 0.05$, unless otherwise stated in figure legends.

4. Results

4.1. Experiments on acute hippocampal slice viablity and Aβ toxicity

4.1.1. Solving the acute brain tissue survival at several hours lasting treatments with *ExVis* proprietary system

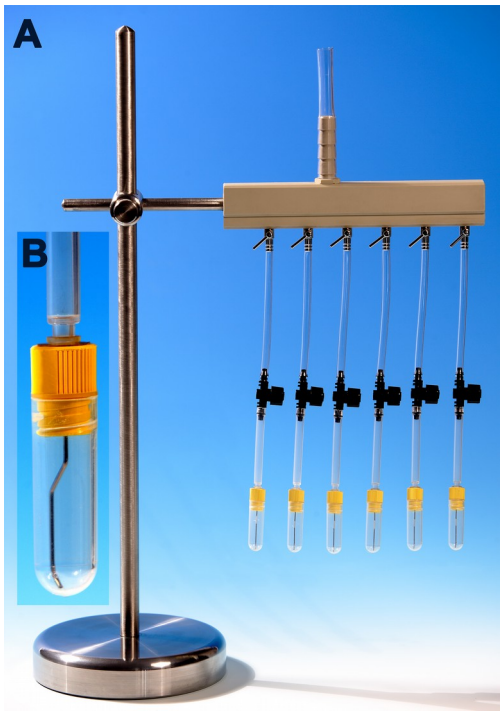

Figure 1

***Ex vivo* mini-chamber system**

The device was developed in our laboratory to serve as a cost-effective tool to maintain acute brain tissue slice viability.

The treatment and toxicity measurements on acute, *ex vivo* hippocampal slices – described in the following chapters – require approx. 4-6 hours of tissue survival. To keep the acute features of the hippocampus tissue, we placed the slices (Fig. 22) into a specific system, designed in our laboratory (*ExViS*, Fig. 1) a simple mini-tubing chamber, suitable for 4-10 rat hippocampal slices, filled with ACSF and a constant carbogen flow (95/5%: O_2/CO_2). Slices can survive several hours under these conditions.

A rounded bottom chamber with a 1 mL working volume is the crucial part of the proprietary system developed and set up in our laboratory. The treatment and/or the carbogenation of the tissue slices take place in room temperature in this semi-hermetically closed chamber by a threaded plug with a rubber sealing. By loosening this plug, the pressure of the carbogene gas – a mixture of 5% carbon dioxide and 95% oxygen gas – can be decreased; therefore, it is suitable as a precision control. A needle (Ø=0.6mm) vertically goes through the plug connected to a rigid plastic tube outside the chamber, upon which there is a regulation valve for the gas current. This valve enables precision control by regulating the flow of carbogen in very small extents. The position of the needle is functionally crucial: it has to pass along the chamber's wall and at the right angle has to move on towards the center of the chamber's bottom. Only this way can vital bubbling be evoked, that keeps the slices moving continuously. The optimal bubbling intensity is approximately 10 bubbles per second. The

number of slices that can be incubated is dependent on the working volume and treatment – or incubation time. The more slices get into the chamber, the shorter the time they can be stored in their vital form in the same volume. Up to 10 slices can be treated or incubated safely at the same time and in the same chamber for 30 min. The longest incubation or treatment time was 3 slice/180 min/1 mL standard ACSF. (Fig.4). However, in our subsequently developed method (Mozes et al. 2012) described in Chapter 4.1.3, where acute hippocampal slices had been used to determine Aβ toxicity with MTT and LDH assays, the treatment and viability was maintained for 4 hours (5 slices/1 mL).

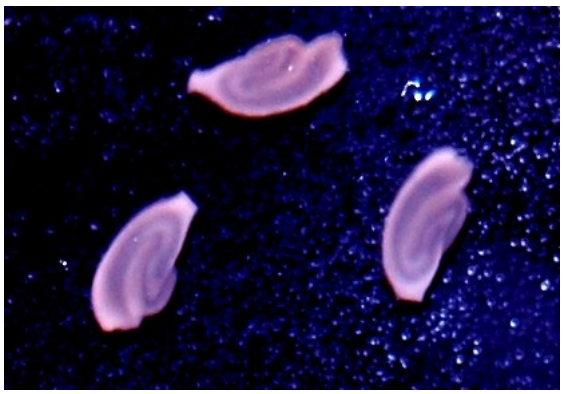

Figure 2

Acute hippocampal slices derived from rat brain

4.1.2. Validation of the *ExVis* system

4.1.2.1 Testing hippocampal slice viability with MTT assay

We determined the viability of the acute hippocampal slices using MTT assay. This method is based on the ability of a mitochondrial dehydrogenase enzyme in viable cells to cleave the tetrazolium rings of the pale yellow MTT while forming purple, water insoluble formazane crystals (Mosmann, 1983; Fig. 3). We used the assay to explore, whether changes in the viability of the slices could be observed during the incubation/treatment time.

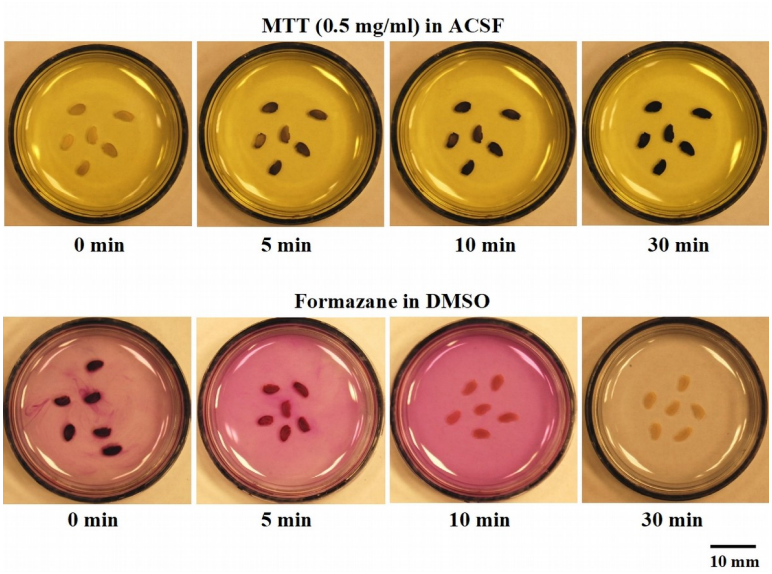

Figure 3

MTT colorimetric viability assay on rat acute hippocampal slices

The photos display *ex vivo* hippocampal slices treated with MTT for 30 minutes. Media was replaced with DMSO to dissolve the purple formazan product of the mitochondrial succinate dehydrogenase reaction in the mithochindria. Optical density (OD) of the resulting purple media is then measured to determine slice viability. OD is directly proportional with the viability.

The OD of the dissolved formazane from the hippocampal slices, which were of various sizes, is directly proportional with their areas. In 3-month-old rats, the ratio between the percentage of OD and the area of the slices displays only small differences (Table 1).

Nr. of wells with a slice	1	2	3	4	5
($OD_{550} - OD_{620}$)	1.52	1.38	1.22	1.11	0.92
Area of slice (mm^2)	11.1	10.2	9.5	8.5	7.3
($OD_{550} - OD_{620}$)/area of slice (mm^2)	0.137	0.135	0.128	0.13	0.126
	Means ± SEM: 0.131 ± 0.0021 (n=5) ➔ 100% (control)				

Table 1.

The optical density (OD) of hippocampal slices of different sizes is proportional to their areas

After 30 and 180 minutes resting or treating in carbogenated standard ACSF solution (36 ºC) we found no significant difference in the mitochondrial reduction capacity of the acute slices,

while the viability of the non-carbogenated hippocampal slices (under 180 min) decreased significantly (Fig.4.)

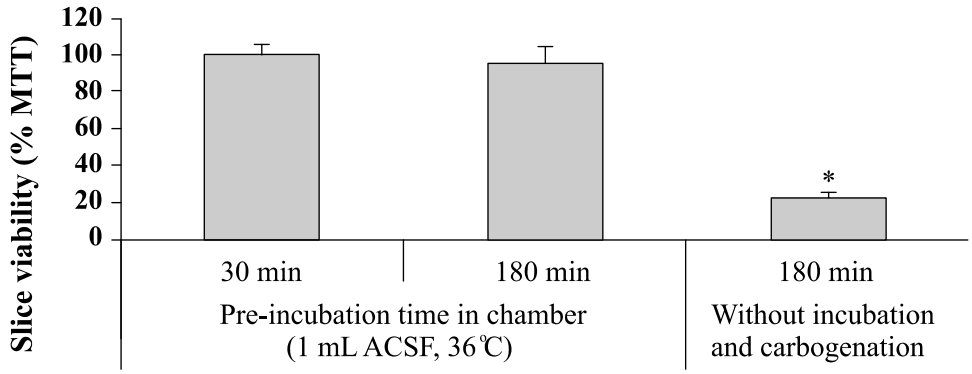

Figure 4

Acute hippocampal slice viability decline measured with MTT assay

Viability is directly proportional with OD and its loss is given in percentage of the values obtained in slices incubated in carbogenated environment in *ExVis* mini-chamber system. Slice area 9 ± 0.8 mm^2. n=20 slices (from 4 rats/case); ANOVA, Bonferroni *post hoc*, p≤0.01. [OD (550-620 nm)]/slice area (mm^2) was 100% in control. Difference was not significant from the data of 30 min pre-incubated slices.

4.1.2.2 TBS-induced LTP in rat hippocampal slices

The aim of this experiment was to determine whether any alterations in the tissue viability and synaptic transmission between neurons occur during the incubation/treatment time. TBS-induced LTP – a canonical method for studying memory circuitry – was detected for 60 minutes. Field EPSPs were recorded from the distal and proximal part of the stratum radiatum in hippocampal CA1. The increase of fEPSP amplitude was persistent in both regions: 60 min after TBS the peak-to-peak amplitude was 341 ± 29 % (n=8 recordings, 3 slices) and 140 ± 8% (n=12 recordings, 3 slices) at the proximal and distal str. radiatum, respectively (data not shown).

4.1.3. Measuring Aβ1-42 toxicity on OGD hippocampal slices with MTT and LDH assay

Based on the previous findings – *ExVis System* development and its validation – we developed a novel method to quantitatively measure Aβ toxicity on *ex vivo*, OGD acute hippocampal slice model, to serve as a screening method for testing protective agents against Aβ toxicity (Mozes et al., 2012). The workflow of the developed protocol is outlined in the following steps:

1) After removing from the brain and preparation, hippocampal slices were left to rest for 30 min in carbogenated H-ACSF/1 at 24 ºC for conditioning.

2) Next, mild OGD was applied for 1 h in H-ACSF/2 solution in Petri dish.

3) Treatment of the slices in the mini-chamber with oligomeric Aβ1-42 peptide for 4 h in H-ACSF/3 solution.

4) Slice viability was measured with MTT and LDH assays.

The concomitant use of the two assays in the acute, OGD hippocampal model provided coherent results on the toxic effect of Aβ1-42. Both MTT and LDH colorimetric assays are adequate for quantifying tissue viability by measuring optical density. In MTT assay the level of the OD is directly proportional with viability, while in LDH is inversely proportional.

The results of both MTT and LDH assays show that one-hour resting under mild glucose-oxygen deprivation reduces brain tissue viability (Fig.5 A, B).

A 4 h treatment of slices with oligomeric Aβ1-42 alone also decreased cell viability (Fig.5 C, D) compared to Aβ untreated control.

Simultaneous treatment of slices with OGD and oligomeric Aβ1-42 induced the most intensive decrease in hippocampal slice viability (Fig.5 E, F).

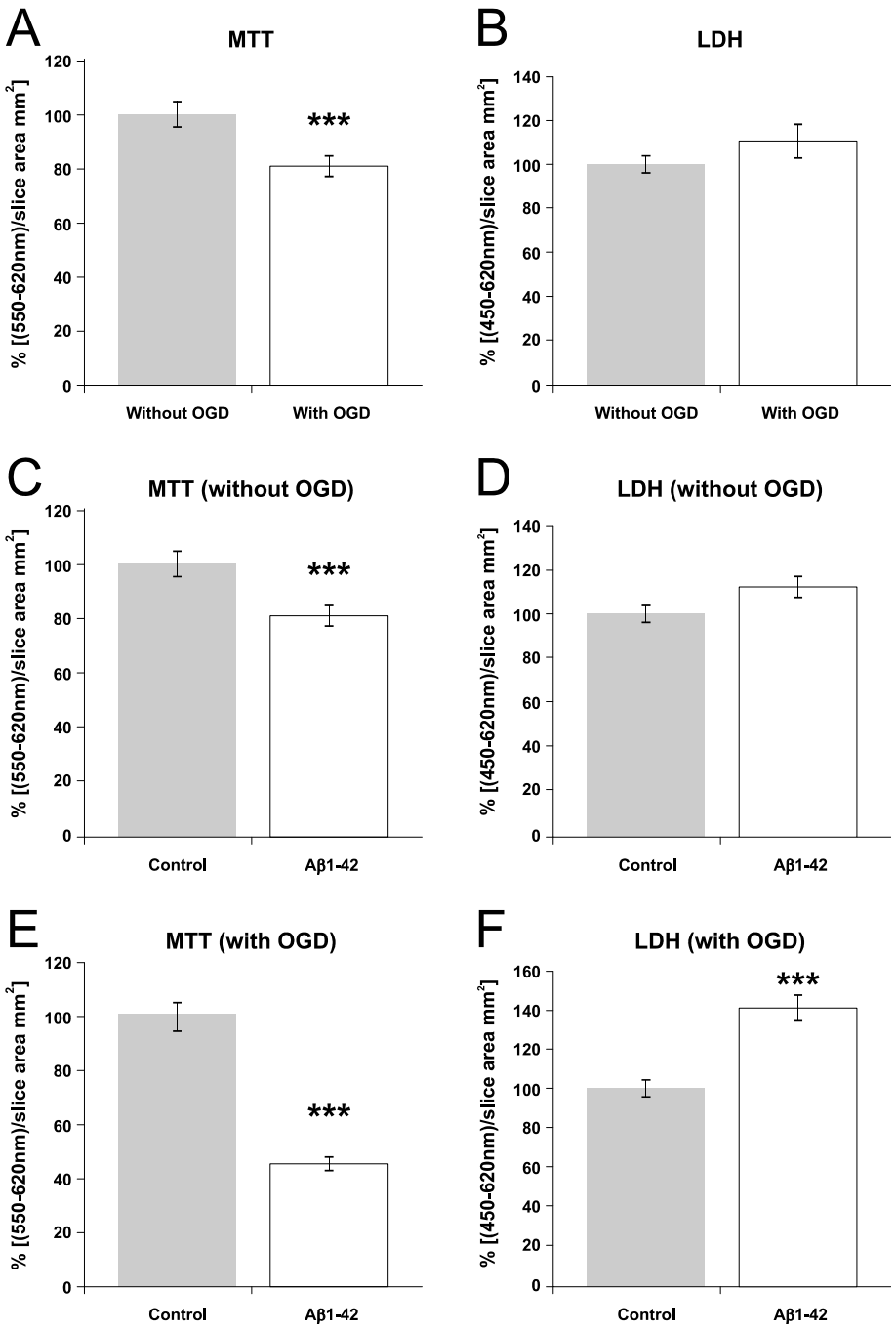

Figure 5

Measuring the acute hippocampal slice viability with MTT and LDH assays in different conditions

The effects of OGD and Aβ1-42 treatment on slice viability were tested.

Student's t-test. n = 40 slices *** p≤0.001

The synergistic effect of OGD with different toxic agents on hippocampal slices was also measured (Fig.6 A, B.) The toxic agents used (H_2O_2, NaN_3, KCN, Thapsigargin) caused significant decrease in cell viability in both assays. These results proved that the mild OGD-pretreated slice preparates are suitable for measurements of standard cell toxic agents.

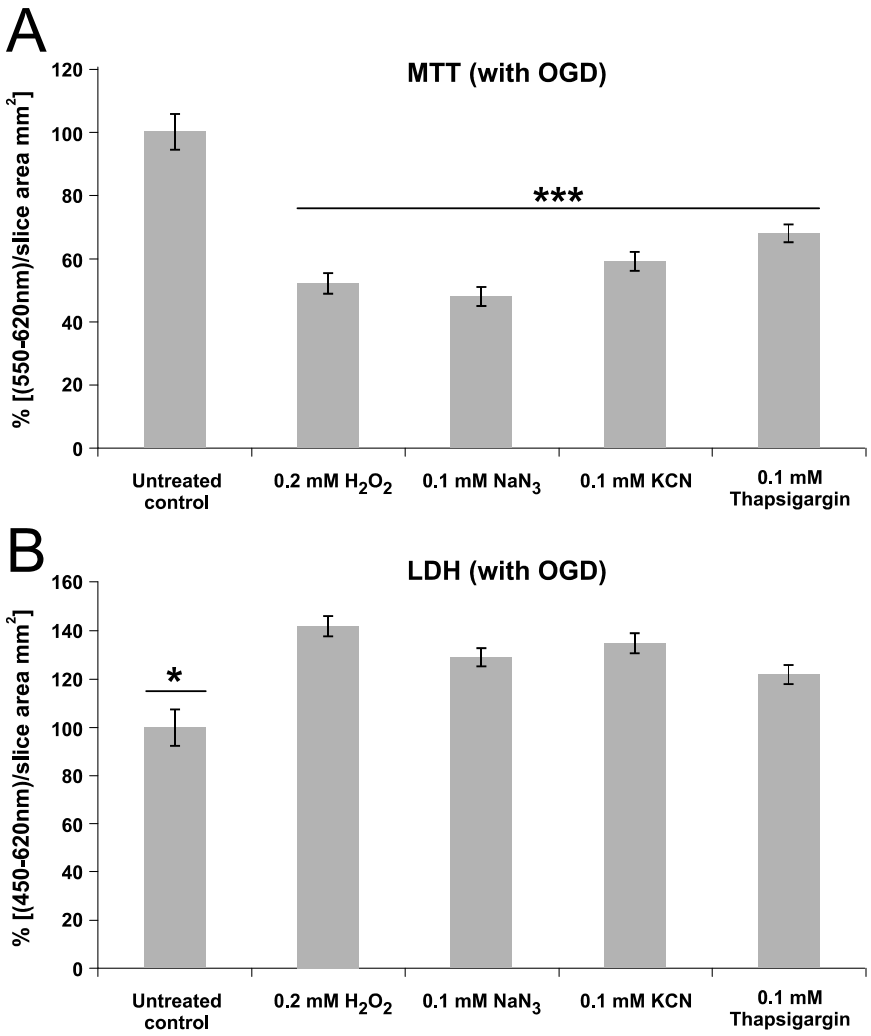

Figure 6

Treatment of acute brain slices with different toxic agents after OGD.

Slice viability is given in the OD percentage of untreated control (UC). Viability is significantly reduced by standard toxic agents. In MTT assay OD is directly proportional, while in LDH assay is inversely proportional with viability. Anova, Bonferroni *post hoc;* n = 40 slices; A: ***p≤0.001 *vs* control, B: *p≤0.05 *vs* treatment.

4.2. A novel application of the fluorescent dye, bis-ANS, labelling neurons in acute brain tissue

In our experiments described later in the following chapters we used the non-covalent extrinsic fluorophore bis-ANS to explore the relationship between zinc and Aβ1-42, as disruption in the sensitive metal balance in the brain can ultimately lead to self-perpetuating pathogenesis of AD. However, as a result of an accidental event we observed that the dye is suitable to label the tissues of acute hippocampal slices along with neuronal structures in dentate gyrus (DG), CA 1–3 regions, hilus (Hil) and subiculum (Sub) (Fig. 7A–C).

In the following paragraphs, I will briefly describe the findings we made about the neuron labelling properties of bis-ANS, that has first been shown in our laboratory (Mozes et al. 2011).

4.2.1. Bis-ANS only labels live tissue

As we studied the labelling properties of bis-ANS on rat acute brain slices, we found that formaldehyde-fixed tissue samples (before staining, Fig. 7G; after staining, Fig. 7H) emitted non-specific homogenous fluorescence in contrast to the acute, live slices derived from the hippocampus (Fig. 7A–C) neocortex (Fig. 7D) and cerebellum (Fig. 7E). In non-fixed viable tissues the neurons exhibited heterogeneous and higher fluorescence intensities compared to fixed tissues, especially in the hippocampal Sub (Fig. 7A), in CA2 region (Fig. 7B), Hil (Fig. 7C) and in cerebellar Purkinje cells (Fig. 7E).

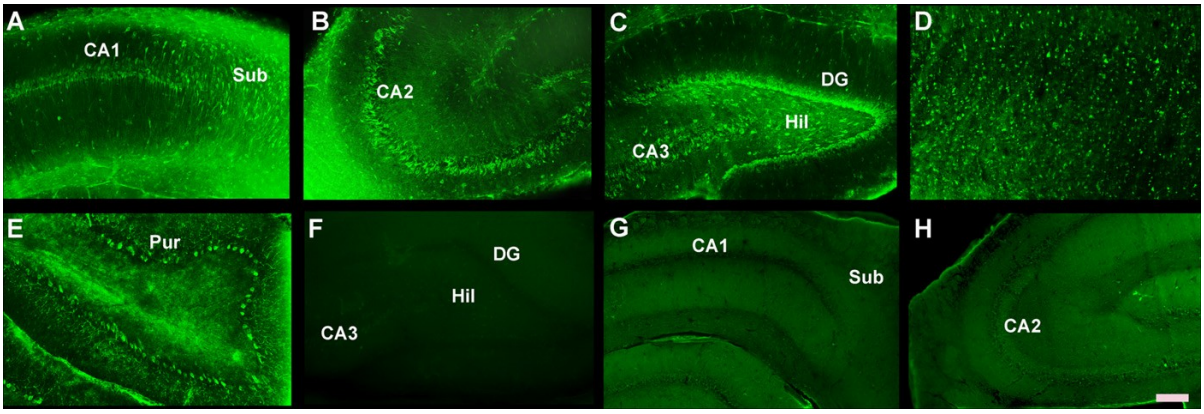

Figure 7

Labelling neurons in acute brain slices with bis-ANS

We used hippocampal (A–C, F–H), neocortical (D) and cerebellar (E) slices for these fluorescent investigations.

Samples labeled in $NaHCO_3$-free (only HEPES-buffered) solution (F) exhibited no fluorescence during 10 min. Samples fixed (before staining, G; after staining, H) in 4% formaldehyde showed the same non-specific (homogenous) bis-ANS signal emitted from the tissue structure in contrast to the viable (A–E; heterogenous labelling) slices. CA: cornu ammonis; Sub: subiculum; Hil: hilus; DG: dentate gyrus; Pur: Purkinje cells. Images were taken with a 20x objective. Scale bar: 200 µm.

In the $NaHCO_3$-free (only HEPES-buffered) solution no specific bis-ANS signals could be detected after 10 min of staining (Fig. 7F), therefore, it appears that the fluorescence emission of bis-ANS is $NaHCO_3$-dependent, although the mechanism is unknown.

4.2.2. Co-localization of labelled neuronal structures with neuronal nuclei

In addition to bis-ANS, we stained the neuronal nuclei with PI, a DNA-specific dye that can only enter the cells through damaged cell membranes. Confocal images were taken of the acute hippocampal slices, where the cells were identified by their PI-stained nuclei (Fig. 8). In all regions of the hippocampus (Fig. 8A–C), bis-ANS and PI could be co-localized and the cross-sectional view of neurites (mainly dendrites) was identified (Fig. 8C).

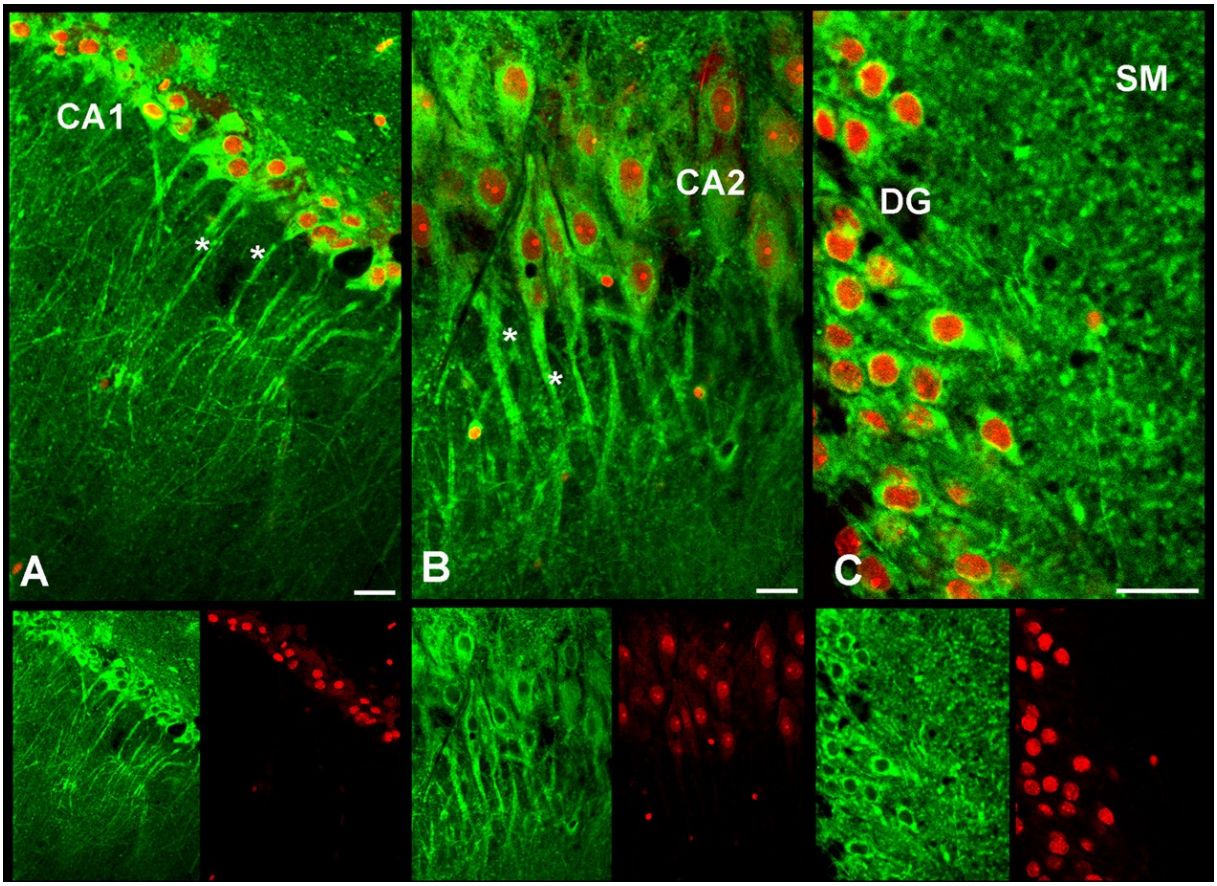

Figure 8

Co-localization of bis-ANS (in neuronal somata and neurites) and PI (in the nuclei) fluorescence in acute hippocampal slices

The cells can be identified by the presence of PI-stained nuclei. This image is a composite of confocal images taken using a 40× objective. We identified cells and their neurites (highlighted with asterisks on A and B) in different regions of hippocampus: in CA1 (A), CA2 (B) and dentate gyrus (C). We also identified the cross sectional view of dendrites and axons (C). CA: cornus ammonis; DG: dentate gyrus; SM: stratum moleculare. Scale bar: 20 µm.

4.2.3. Bis-ANS only labels cells with damaged membrane

Next, we demonstrated that bis-ANS only labels damaged cells. For this study we used non-differentiated SH-SY5Y human neuroblastoma monolayer cell culture (Fig. 9). An incision was made by the dint of a blade on the cells settled in the Petri-dish (Fig. 9A), then, the monolayer culture was labelled with bis-ANS (Fig. 9C) and PI (Fig. 9D). After 10 min we analyzed the samples using fluorescence microscopy and co-localizing the images (Fig. 9B). We noticed that exclusively cells that were situated by the incision absorbed the dyes. It is important to note that neurons in the acute hippocampal slices were damaged only on the surface of the cutting area, but the whole structure remained anatomically intact.

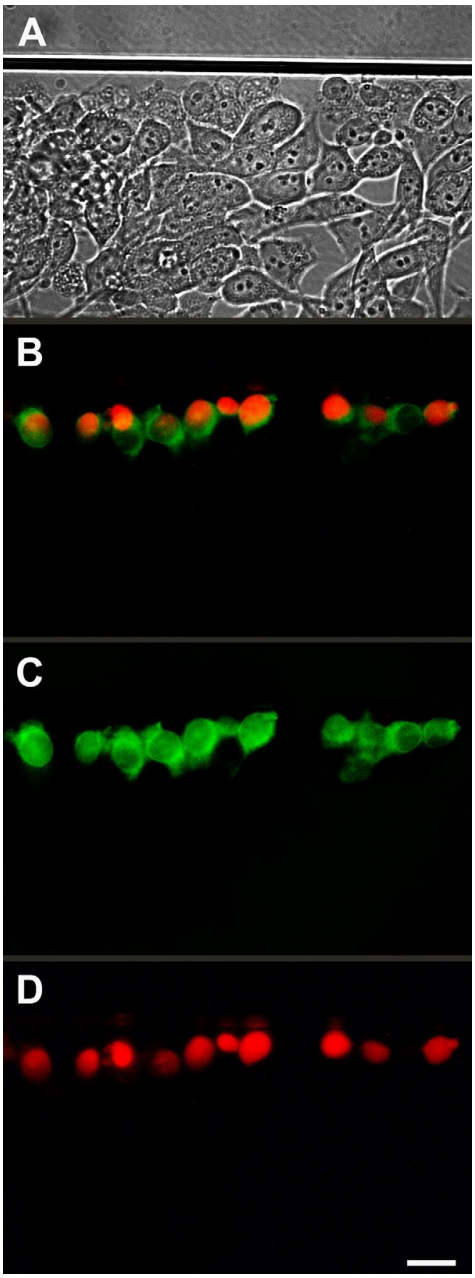

Figure 9

Using bis-ANS and PI to label neuroblastoma cells incised by a blade. By a dint of a blade an incision was made on viable, monolayers of non-differentiated SH-SY5Y human neuroblastoma cells (A), then the monolayers were labeled with bis-ANS, staining the cell bodies in green (C) and propidium iodide (PI), staining the nuclei in red (D). The samples were analyzed by fluorescent microscopy and the obtained pictures were merged (B). Scale bare: 20 µm.

4.2.4. Region-specific co-localization for detailed structural imaging of the hipppocampus

The well-known lipophilic fluorescent membrane stain DiI is specific to mechanically intact live neurons and we applied it on acute hippocampal slices to explore how the labelled structures are positioned to structures emitting specific fluorescent signals from bis-ANS. We observed region-specific (but not cell-specific) co-localization with bis-ANS-labelled neuronal structures. The co-localization patterns found in granule cells of DG (Fig. 10B) or in CA1 (Fig. 10A) regions under higher magnification (450×; Fig. 10C) demonstrated that the staining properties of bis-ANS and DiI were different in the neuronal structures (e.g. neurites and cell bodies). Bis-ANS is specific for damaged cell

bodies and neurites and allows the imaging of neurite cross sections, while DiI labels the horizontal neurites intact from the tissue chopper's blade.

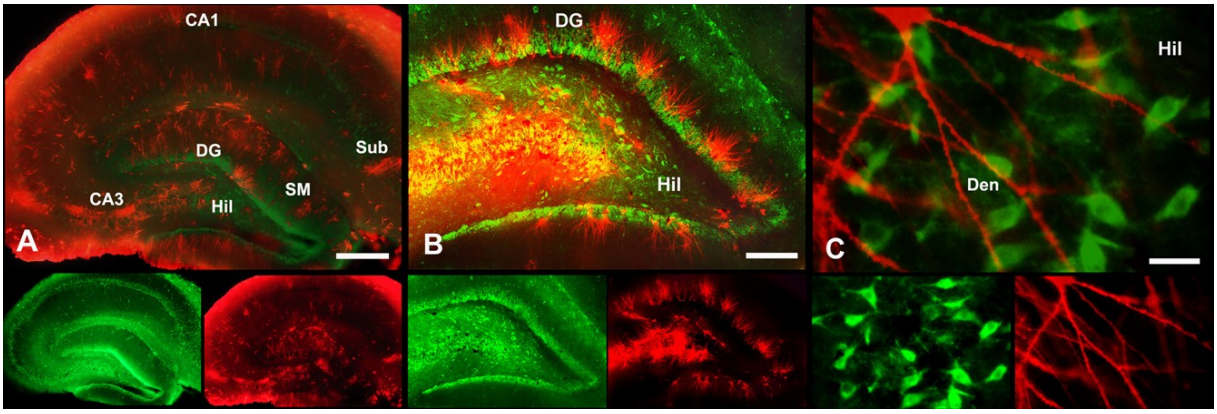

Figure 10

Region-specific co-localization of bis-ANS, labelling mechanically damaged neurons (green) and DiI labelling intact viable neurons (red) in acute hippocampal slices

We detected co-localization in granule cells of DG (B) or in CA1 (A) regions. In higher magnification (450×, C) we can see that the staining properties of bis-ANS and DiI are differently related to the cell bodies and neurites. Bis-ANS fluorescent signal is specific to damaged cell bodies and neurites and allows the imaging of neurite cross sections, while DiI labels the horizontal intact neurites. CA: cornus ammonis; DG: dentate gyrus; Hil: hilus; SM: stratum moleculare; Sub: subiculum, Den: dendrites. Scale bar: 0.5 mm on A, 200 µm on B and 20 µm on C.

4.3. Effects of Zn^{2+}-induced Aβ toxic aggregation on cell viability and synaptic function

Using the methods developed in our laboratory and described in the previous chapters, in our next experiments we aimed at gaining deeper insights into the concurring effect of zinc ions released in glutamergic synapses and extracellular, human Aβ1-42 on the viability and function of the hippocampus.

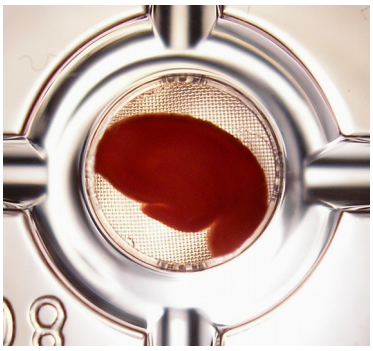

Figure 11

Immobilized acute hippocampal slice in a 96-well plate, ready for measuring Zn^{2+}-release in the fluorescent plate reader.

4.3.1. K^+-induced Zn^{2+} release in different *ex vivo* brain tissue slices

KCl (50 mM) treatment causes massive depolarization in neurons and induces Zn^{2+} release into the media. The intensity of Zn^{2+} release in tissue slices originating from different brain areas was measured using a Zn^{2+}-specific fluorescent dye, RhodZin-3. Slices were placed and

immobilized one-by-one in the wells of a 96-well plate as shown in Figure 11 and their emitted fluorescent signal was measured simultaneusly but separately in a micro-plate reader with optical fiberglass technology. The characteristic fluorescence kinetics of the thalamical, neocortical and hippocampal slices significantly differed from each other (Fig.12) and the greatest fluorescence intensity was produced by the hippocampal slices. This finding is consistent with current literature (Frederickson et al., 2005). The cortical slices emitted meaningful signal, but at smaller magnitude compared to hippocampal slices. Thalamic samples did not show detectable Zn^{2+} release, as it was expected based on the findings of previous studies (Frederickson and Moncrieff, 1994).

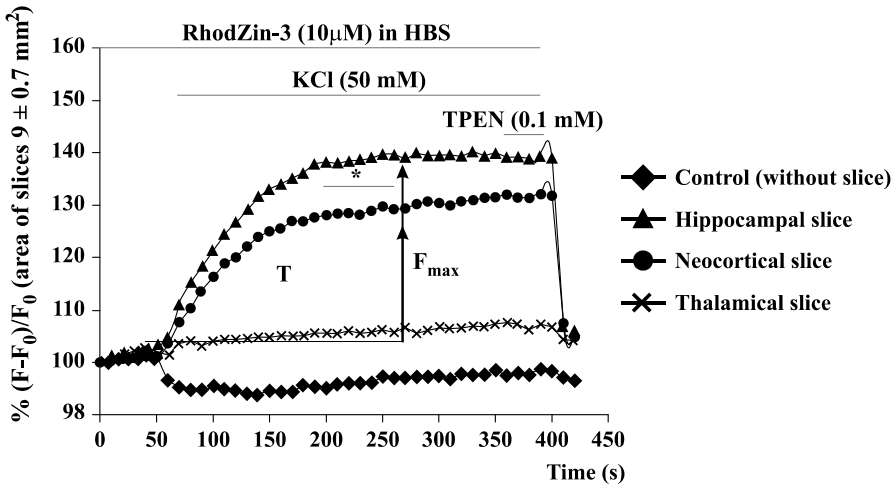

Figure 12

Comparing the intensity of Zn^{2+}-release in *ex vivo* slices obtained from different brain areas

F_0 is the value of the initial fluorescent intensity, immediately before KCl treatment; F_{max} is the maximum fluorescent intensity of the Zn^{2+}-specific dye RhodZin3. T is the saturation time of F. To confirm the Zn^{2+} specificity of the signal we used Zn^{2+}-specific chelator, TPEN. Slice area 9 ± 0.7 mm^2; n = 10 slices (from 2 rats/case) *p≤0.01, difference is significant from the thalamical slice signal.

4.3.2. Zn^{2+}-induced Aβ aggregartion *in vitro*

Before applying Aβ1-42 to hippocampal slices, we first characterized its response to Zn^{2+} in cell-free system (Fig.13). Aggregation was monitored with bis-ANS, the fluorophore originally designed to detect peptide aggregation into pre-fibrillar, low-order oligomers (LeVine 2002). We found that Zn^{2+} (50 μM) triggered significant aggregation of human Aβ1-42 (50 μM) within seconds, which then was rapidly reversed by adding the Zn^{2+}-selective chelator, CaEDTA (0.5 mM) into the media. In the absence of Zn^{2+}, human Aβ1-42 aggregated

relatively slowly and incompletely and was not influenced by KCl (50 mM), the compound used in our next experiments to stimulate Zn^{2+} release in acute brain slices from rat.

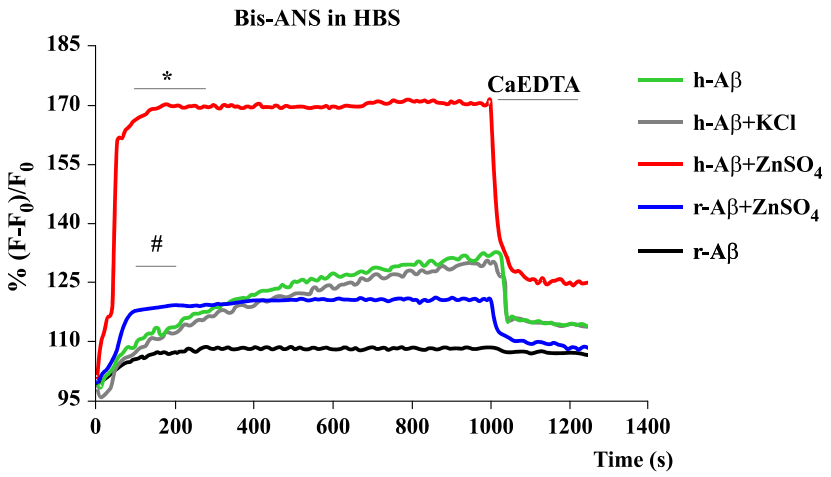

Figure 13

Tracing Aβ1-42 aggregation *in vitro* induced by Zn^{2+} with bis-ANS oligomer-specific fluorescent dye

The graph presents the kinetics of Bis-ANS fluorescence related to Aβ forms (rat or human) and the effect of zinc addition. Bis-ANS can bind the oligomeric form of the Aβ. After Zn^{2+}-treatment the fluorescence of the dye increases rapidly in HBS solution supplemented with human Aβ. Oligomerization was detected in cell-free, *in vitro* environment. The effect of KCl was also experimented (grey) in order to exclude it from later measurements on *ex vivo* hippocampal slices, where Zn^{2+}-release was induced by K^+ via massive depolarization. The fluorescent signal of the KCl treated normal Aβ shows similar kinetics to Aβ alone. r-Aβ is the amyloid-beta Δ2His mutant produced in rats, shows no significant aggregation upon the addition of zinc (blue), while human Aβ1-42 (h-Aβ) is aggregating by itself (green) and significant oligomerization is observed upon zinc addition (red) which then is rescued by the zinc-specific chelator, CaEDTA.

ANOVA *post hoc* test Bonferroni, n = 30 wells, $p \leq 0.01$; # difference is significant between h-Aβ and r-Aβ aggregation; *difference is significant from all the other data in the graph.

The results of aggregation detection (where aggregation is directly proportional with the emitted fluorescence intensity) also show that rat Aβ does not aggregate and even with the addition of Zn^{2+}, forms less oligomers than Zn^{2+}-free human Aβ.

Therefore, in our next experiments we added synthetic human Aβ1-42 to the explant media of acute rat hippocampal slices and used a synthetic mutant of Aβ1-42 as control with histidine-to-alanine substitutions at residues 13 and 14 that attenuate interactions with Zn^{2+} (AβΔ2His).

4.3.3. K^+-induced Zn^{2+} release affects Aβ aggregation on *ex vivo* acute hippocampal slices

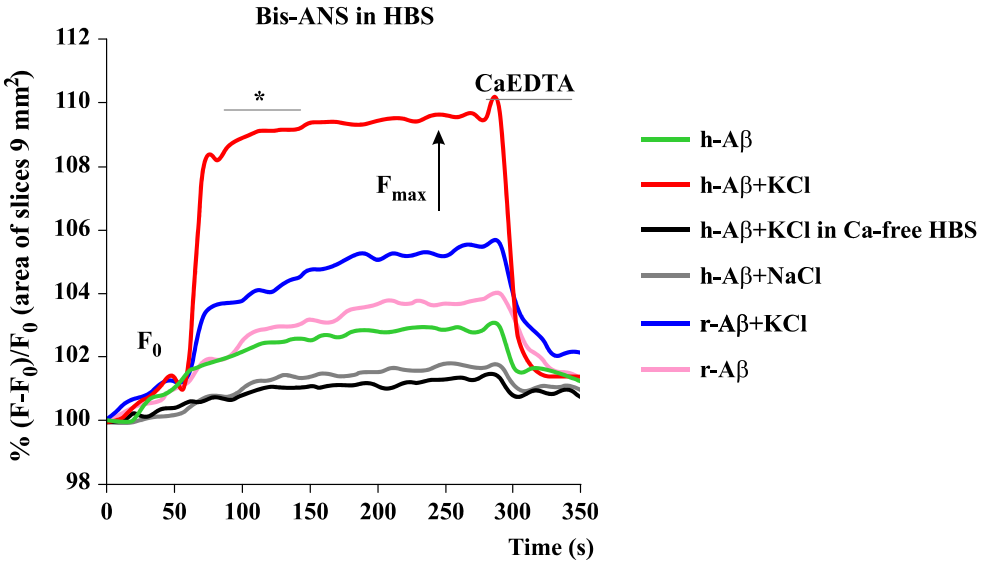

Figure 14

Tracing Aβ1-42 aggregation induced by Zn^{2+}-release in *ex vivo* hippocampal slices using bis-ANS oligomer-specific fluorescent dye

The graph presents the kinetics of Bis-ANS fluorescence and other factors such as metal ions or Aβ forms. The release of endogenic Zn^{2+} from hippocampal slices induced by KCl treatment caused a rapid increase in the fluorescent signal of Bis-ANS oligomer-spceific fluorescent dye in HBS solution supplemented with human Aβ. The KCl induced osmotic stress was controlled with NaCl treatment, but in this case drastic increase in fluorescence was not detected. The KCl treatment has no effect on the Bis-ANS signal in Ca^{2+}-free HBS solution (Ca^{2+}-free environment inhibit the vesicular Zn^{2+} release). The modified Aβ (Δ2His, shown as: r-Aβ) cannot precipitate the KCl induced free vesicular Zn^{2+}. ANOVA *post hoc* test Bonferroni, n = 25 slices (from 4 rats per case), p≤0.01; * difference is significant from all the other data in the graph.

We tested whether the endogenous Zn^{2+} released from rat hippocampal slices could induce oligomerization of exogenous synthetic human Aβ1-42 (Fig. 14). Slices from male rats were incubated with either human or rat synthetic Aβ1-42 (50 μM). After 60 seconds high K^+ or Na^+(an osmotic stress control) was introduced to the media. At 300 seconds the Zn^{2+}-selective chelator CaEDTA (0.1 mM) was introduced. Ca^{2+}-free HBS was used to determine if the Aβ aggregation was associated with synaptic vesicular release. Data are mean ΔF_{max} ± SEM, n=25 slices per condition, normalized for the surface area of each slice.

We showed that human Aβ1-42 could be rapidly aggregated into bis-ANS reactive species by endogenous hippocampal Zn^{2+} when the slices were stimulated with K^+. Aggregation could not be explained by the direct effects of K^+ on the peptide, as shown in Figure 13, where no Aβ oligomers were detected in KCl-containing media.

Rapid Aβ1-42 aggregation from the slices was inhibited when Ca^{2+} was deleted from the high K^+ buffer, consistent with the fact that the aggregating factor is being released upon synaptic activation. Aggregation could be reversed by the Zn^{2+}-selective chelator, CaEDTA, and no aggregation was observed with high K^+ treatment of slices in the presence of AβΔ2His (r-Aβ), consistent with the aggregating factor being Zn^{2+} released by the hippocampus upon depolarization.

4.3.4. *Ex vivo* Zn^{2+} and Aβ treatment of acute hippocampal slices

4.3.4.1 Toxic effect of Zn^{2+} and Aβ treatment

To determine whether the toxicity of Aβ1-42 could be induced by Zn^{2+}, we performed MTT viability assay on hippocampal slices treated with Aβ and Zn^{2+} (both 15 μM) (Fig. 15.). The slices had not been exposed to high K^+. MTT assay results indicated that, after the 3-hour treatment neither Zn^{2+} nor Aβ alone inhibited viability, but when added together, Aβ1-42 and Zn^{2+} effect was markedly toxic ($p<0.001$). There was no loss of viability following a 3-hour control incubation.

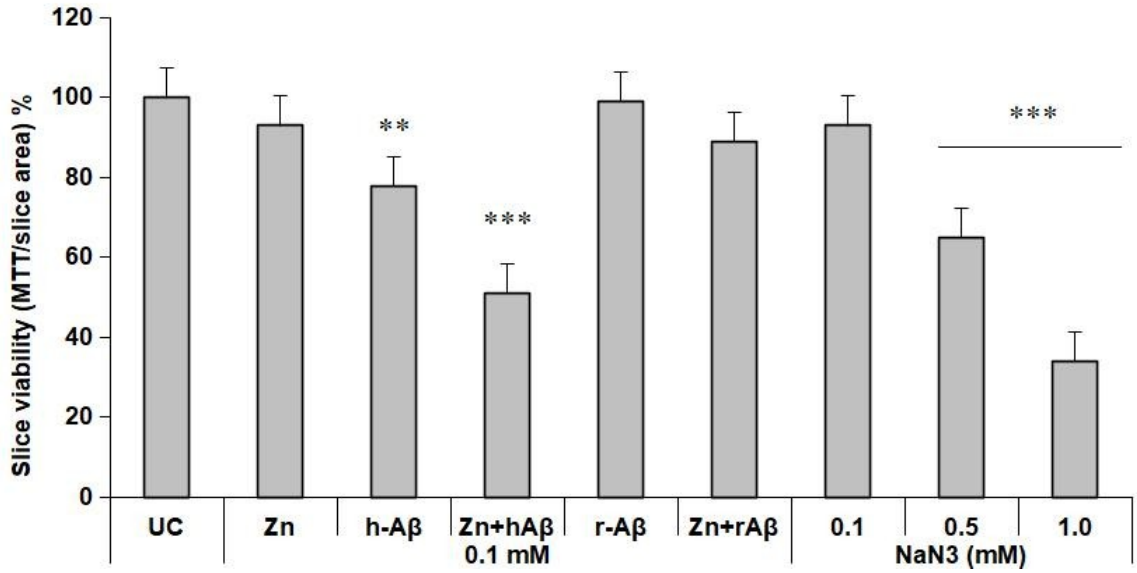

Figure 15

Viability of acute hippocampal slices treated with zinc ($ZnSO_4$) and Aβ1-42 for 5 h

Zn^{2+} and Aβ co-treatment cause significant decrease in hippocampal slice viability similar to NaN_3 treatment used as a negative control for toxicity. (NaN_3 is an inhibitor of terminal oxidation in mitochondria and exhibits dose dependent toxicity on hippocampal slices.) Viability was determined using MTT assay. The graph presents the optical density (in percentage of UC) of the solubilized MTT in the media. ANOVA *post hoc* test Bonferroni, n = 30 slices (from 4 rats per case). ** p≤0.01; ***p≤0.001.

4.3.4.2 LTP impairment after co-treatment with Zn^{2+} and Aβ

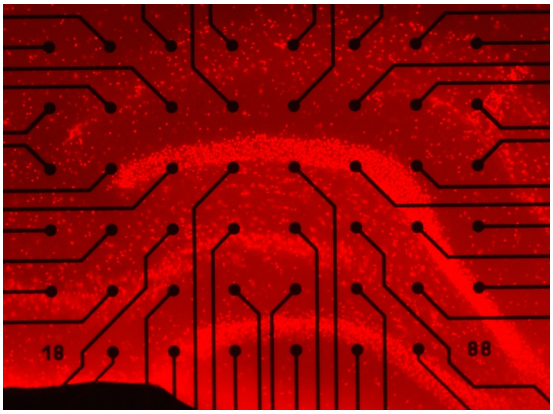

Figure 16

MEA-setup on hippocampal slice to measure synaptic activity

To record the input/output curves, the slices were placed on a micro electrode array (MEA) chip with 200 µm interelectrode distance (Fig. 16) and we studied LTP induced by TBS. We tested whether Zn^{2+}-induced Aβ aggregation affects the synaptic function of the hippocampus and we found a significant inhibitory effect of Zn^{2+}-Aβ simultaneous treatment on the synaptic transmission and connections in rat acute hippocampal slices (Fig. 17). The stimulus intensity was increased from 0 to 120 µA with 10 µA steps. (Fig. 17A) Stronger stimulation led to large Faradic effects on the electrodes causing artifacts. The steepest rise was recorded in the control slices (a total of 13 electrodes from 5 slices). Zn^{2+} treated slices displayed significantly smaller responses in the range of 50 – 90 µA stimulation (a total of 15 electrodes

from 5 slices). Aβ treated slices showed an even smaller excitation. The evoked responses were significantly smaller from 20 µA to 120 µA stimulation intensity (a total of 7 electrodes from 3 slices). Unexpectedly, the slices which were treated with both Zn^{2+} and Aβ showed no evoked responses at any stimulation strength. Only the thermal noise (base line) could be recorded after stimulation (5 slices). After recording a 10-minute stable control sequence, LTP was induced by TBS (trains of 15×100 Hz bursts, 5 pulses per burst with a 200 ms interburst interval), at the maximum stimulation intensity fEPSPs were recorded from the distal and proximal part of the *stratum radiatum* in hippocampal CA1 for 60 min (Fig. 17 B). We weren't able to induce LTP on slices treated with both Zn^{2+} and human Aβ.

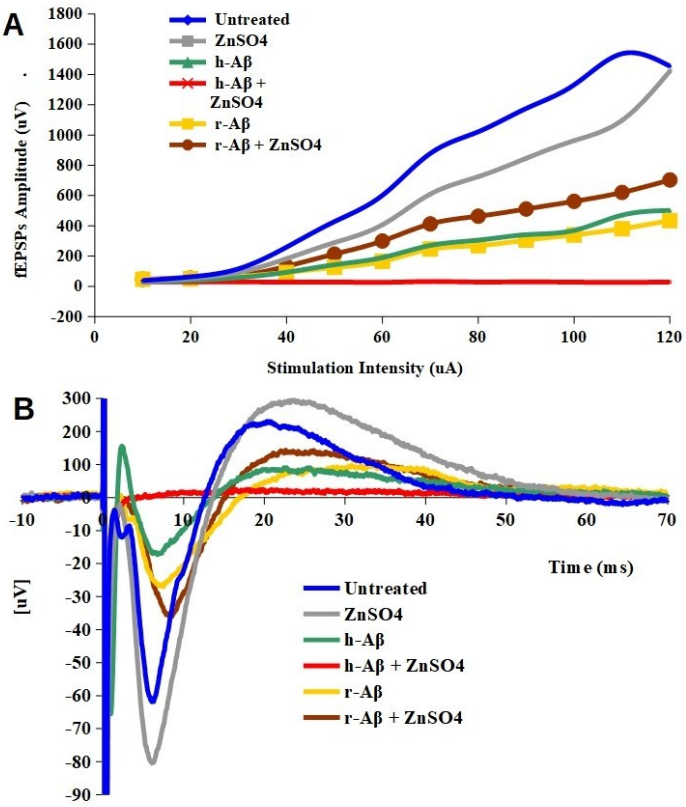

Figure 17

Effects of Zn^{2+}-Aβ complexes on acute hippocampal slice electrophysiology

A: Input/output curves of slices with different treatments. Mean amplitude ±SEM of field potentials are displayed as a function of stimulus intensity. Slices were stimulated in the Schaffer-collateral, and recordings were made in the stratum pyramidale and stratum radiatum of the CA1 region. Mean of 6 electrodes/slice and 3 slices for each protocol. ANOVA *post hoc* test Bonferroni, $p \leq 0.05$.

B: Representative fEPSPs recorded at 90 µV stimulation intensity. Treated slices have smaller peak-to-peak fEPSP amplitudes than control slices. Note the absence of evoked fEPSP in the Aβ + $ZnSO_4$ slice.

5. Discussion

5.1. Method and device development for *ex vivo* AD pathology models

Acute hippocampal slices are widely used in preclinical studies and basic research as a capable experimental model for investigating synaptic structures and functionality at the molecular, cellular, and circuit levels. We developed three novel methods based on the use of acute hippocampal slices and successfully involved these applications into our experiments aimed at exploring and modelling the effects of Aβ aggregation into toxic oligomers – a hallmark in AD – on viability and synaptic functionality of hippocampal tissue.

5.1.1. *Ex vivo* mini-chamber system preserves acute brain slice viability

Ex vivo methods, such as the use of acute tissue slices, provide more relevant models than *in vitro* cell lines and their preparation and maintenance involve less work than using organotypic cultures. Nevertheless, the lifetime of their object is relatively short. To leverage some of the most common obstacle factors of the different models, such as relevance, lifetime and cost, we developed a simple slice-incubating system for maintaining the viability of acute tissue slices.

With the development of *ExViS* (*Ex Vivo* System; Universal Mini-Chamber Tube System for Acute Tissue Slices), our goal was to be able to study the pathomechanism of various neural disorders and testing drug candidates in a flawless, effective and economic manner. The device is cost-effective to manufacture and its great advantage compared to other products on the market used for similar tasks is that it is able to keep tissue sections alive in a small media volume for a relative long time (3-4 hour). The decreased working volume (max. 1 mL) is particularly useful when very expensive agents are used for treatment. Other available products typically use higher solution-volumes (50-2000 mL). Additionally, a so called floating incubation is applied, where the slices are less exposed to the distorting effect of gravity, therefore, tissue deformation and flattening do not take place compared to other two-dimensional systems (Jensen & Harris 1989, Leiva et al. 2000).

We have validated the suitability of our mini-chamber system by testing acute hippocampal slice viability based on the mitochondrial dehydrogenase activity (MTT assay) and the synaptic transmission health by studying TBS induced LTP.

Results of MTT viability test demonstrated, that acute hippocampal slice viability can be safely maintained for 180 min in carbogenated (95/5% : O_2/CO_2) ACSF in the *ExViS* mini-chamber system and in our later experiments designed to measure Aβ toxicity, the system has proven to maintain viability up to 6 h (4 slices/1 mL)

LTP studies have shown a significant difference in potentiation rate between the distal and proximal part of *stratum radiatum*, the latter being the larger. This layer-specific difference in the rate of LTP was demonstrated earlier (Kopanitsa et al. 2006), being the character of a "healthy", well-preserved hippocampal slice. Our validation tests clearly showed that the slices incubated in our system are viable, have normal presynaptic function and synaptic activity.

5.1.2. Quantitative determination of Aβ toxicity on OGD acute hippocampal slice model with MTT and LDH assays

Precisely measuring the toxic effect of Aβ1-42 peptides and oligomers and the protective effect of novel drug candidates against them in relevant preclinical model environment poses a sensitive task in AD research. We aimed to develop an *ex vivo* model based on rat brain-derived acute hippocampal slices, being more relevant for AD studies then *in vitro* cell cultures, due to the three dimensional structure of the brain tissue, the cell variability and the almost intact cell connections. Thanks to the previously described *ExViS* system, we were able to design 3-4 h lasting treatments on acute brain slices. To quantify the viability of slices and the effects of different treatments on them, we tailored the MTT assay – widely used in cell lines and primary cell cultures – to suit our *ex vivo* model.

Application of MTT and LDH assays to quantify brain slice viability proved to be an easy *ex vivo* method for studying Aβ1-42 toxicity in brain tissue (Mozes et al., 2012). Applying an additional OGD pretreatment with Aβ1-42 on hippocampus slices aimed to provide a more relevant *ex vivo* model of the ageing brain. The concomitant use of MTT and LDH assays gave reliable results on the toxic effect of Aβ1-42 in OGD acute brain slice model. LDH assay was previously reported to being successfully used to quantify effects of OGD (Tagliari et al., 2005). Both cholorimetric assays are capable of quantifying tissue viability by measuring OD, that is directly proportional with viability in MTT and inversely proportional in LDH assay. The mechanistic explanation behind is that while MTT measures mithocondrial

dehydrogenase activity, LDH released to the supernatant medium suggests an increase of tissue and membrane damage.

We found that exposing the hippocampal slices to concurrent OGD and Aβ1-42 treatment induced a greater decrease in viability than their separate effects (Fig.5 E,F). The method was also successfully validated with classic toxic agents (Fig.6).

5.1.3. Detailed fluorescent imaging of the acute hippocampal slices' neurite structures

During our studies aimed to explore the effect of Zn^{2+}- induced Aβ aggregation, we discovered the ability of bis-ANS fluorescent dye, originally used to track low-order oligomers, to label neuronal structures in acute brain tissue. Therefore, we further explored the neuron-labelling properties of the fluorophore and during our studies we found that it only labels mechanically damaged cell membrane in live tissue and it is suitable to label neurite cross-sections on the cutting surface of hippocampal slices. The dye lost this ability if the labelling solution was $NaHCO_3$-free, however the mechanism behind is unknown. Labelled structures could be co-localized with the fluorescent signal of the DNA-specific PI on the cell level and with intact membrane specific DiI emission on the slice region-level, allowing to obtain detailed imaging of *ex vivo* brain tissue structures. Hence, beside its oligomer-specificity, bis-ANS is suitable and easy to use for visualizing the neuronal structures – and to count neurite cross-sections with image analysis methods – on the surface of *ex vivo* brain slices.

5.2. Effect of Zn^{2+}-induced Aβ aggregation on hippocampal slice viability and function: an *ex vivo* amyloid neuropathology model

A multitude of genetic and biochemical evidence implicates Aβ or its precursor in the pathogenesis of AD. However, a decade of clinical trials targeting cortical amyloid pathology failed to demonstrate clinical benefit despite moderating fibrillar amyloid burden (reviewed by Nikseresht et al., 2019). One standpoint of possible explantion lies in the hypothesis that neurodegenerative toxicity might be triggered by a minor oligomeric species not yet engaged in extensive intervention testing, as Aβ aggregates in the brain are highly polymorphic (Gong et al., 2003).

Metal ion dis-homeostasis is an existing concept in the AD research. Abnormally elevated load of Zn^{2+}, Cu^{2+}, Fe^{3+} ions were found in senile plaques of *postmortem* human AD brains (Lovell et al., 1998)

Our developed *ex vivo* modelling had been successfully used to explore the effects of Aβ aggregation into bis-ANS reactive species by Zn^{2+} released from glutamatergic neurons, ultimately leading to our recently published study that reported age and female sex to be a major risk factor in this particular amyloid neuropathology in AD (Datki et al. 2020). In this study we found that while there was no difference in the volume of Zn^{2+} released upon K^+ stimulus and massive depolarization between young male and female rats, in acute hippocampal slices derived from old females Zn^{2+} elevation was significantly higher than in their younger counterparts and old males. In this study we proposed a model that as a consequence of energy failure with ageing, cells do not re-uptake efficiently the released Zn^{2+} during neurotransmission, leading to increased average extracellular Zn^{2+} promoting Aβ aggregation.

We showed that Aβ1-42 could be rapidly aggregated into bis-ANS reactive species (low-order oligomers) both *in vitro,* in cell-free environment (Fig 13.) and by endogenous hippocampal Zn^{2+} (Fig. 14). The metal ions, including Zn^{2+} and Cu^{2+}, were identified to interact with histidine residues at N-terminal of Aβ (Minicozzi et al., 2008, Nair et al., 2010), explaining why no aggregation was observed with high K^+ treatment of slices in the presence of AβΔ2His (r-Aβ). The rat sequence of Aβ has substitutions of key residues that mediate Zn^{2+} coordination and is not readily precipitated by Zn^{2+} (Bush et al. 1994). Consistent with the literature, we found that the reaction produces toxic Aβ oligomers that form much faster than by spontaneous aggregation (Ferrao-Gonzales et al., 2005). Consequently, LTP and hippocampal viability/mitochondrial activity is inhibited (Fig. 15, 17). This is consistent with a recent report (Lee et al. 2018), but seemingly contradicts previous findings where Zn^{2+} inhibited the Aβ toxicity in cell culture (Cuajungco et al., 2000). An important difference of these experiments is that they were performed over a longer – 48 hours – time-frame, enough for Zn^{2+} and Aβ to form amyloid fibrils (Lee at al. 2018; Bush et al., 1994) which lose toxicity (Ferrao-Gonzales et al., 2005, Hung et al., 2008).

The mechanism of bis-ANS positive Zn^{2+} -Aβ oligomer toxicity remains uncertain. Soluble Aβ oligomers – also known as Aβ derived diffusible ligands (ADDLs) – have previously been

found to be toxic (Gong et al., 2003; Kayed et al. 2003), are formed by an alternative mechanism and are distinct from bis-ANS reactive Zn^{2+}-Aβ oligomers (Lee et al., 2018). LTP inhibition that was reported by our laboratory (Datki et al., 2020) could be caused by toxicity from the bis-ANS positive oligomers induced by Zn^{2+}. The high local flux of Zn^{2+} might attract Aβ into the glutamatergic synapses and then traps Zn^{2+}, preventing it from facilitating LTP (Lu et al., 2000). Soluble Aβ oligomers have indeed been reported to cause Zn^{2+}-dependent synaptotoxicity in hippocampal slices when they attach to the NMDA receptor. (Desphande et al., 2009). Acute hippocampal slice treatment with Aβ- Zn^{2+} aggregates (Zn^{2+} was added externally, not by K^{+} induction) has unexpectedly resulted in zero evoked response at any stimulation strength in our electrophysiological measurements (Fig.17).

We propose an *ex vivo* model for extracellular Aβ aggregation into toxic oligomers that are triggered by endogenous Zn^{2+} release and as a consequence of energy failure with ageing, the tissue does not efficiently reuptake Zn^{2+} released during neurotransmission. This mechanism leads to increased average extracellular Zn^{2+} promoting Aβ aggregation (Fig.18). It has been shown that Aβ can be released by synaptic activity (Cirrito et al., 2003). Both the Aβ and the Zn^{2+} are trapped into aggregates that initially form close to the synapse and contribute to synaptic dysfunction (Tamano et al., 2019) and aggregates are decomposed after zinc-specific chelator is added to the slices. The reuptake mechanisms employed to reassimilate Zn^{2+} released in synapses remain to be clarified. Twenty-four zinc transporter proteins are known to date to be specialized to traffic Zn^{2+} into or out of the cytoplasm (e.g. ZnT3 into glutamatergic synaptic vesicles) or out of the cell (Reviewed by Kambe et al., 2019). There are also known to exist additional ports of uptake into the cell such as the Divalent Metal Transporter 1, AMPA/kainate and NMDA receptors (Frederickson et al., 2005; Sensi et al., 2009; Xu et al., 2019). Presenilin expression also promotes cellular uptake of Zn^{2+} (Greenough et al., 2011). The NMDA receptor can mediate some Zn^{2+} uptake (Colvin et al., 2000), but is not known to be a significant route for Zn^{2+} entry. However, Zn^{2+} binds to and inhibits the activity of the NMDA receptor (Westbrook and Mayer 1987; Mayer et al., 1989; Jalali-Yazdi et al., 2018) and so we hypothesize that the Zn^{2+} intake might reflect internalization through recycling of the NMDA receptor (Ferreira et al., 2017). The NMDA receptor can mediate some Zn^{2+} uptake, but is not known to be a significant route for Zn^{2+} entry. This could be consistent with the report of Zn^{2+} promoting attachment of Aβ to the

NMDA receptor (Desphande et al., 2009). Nonetheless, the Zn^{2+} uptake mechanism that might attract Aβ attachment remains to be confirmed.

It is important to note that our hippocampal slice model of Zn^{2+}-induced Aβ aggregation should be translated with caution. Aβ peptide concentrations were deliberately applied in supra-physiological concentrations to permit its detection with bis-ANS in dynamic peptide oligomerization studies. Hence, the peptide acted as an indicator of the extracellular Zn^{2+} released by the tissue. The aggregation of Aβ1-42 could therefore occur at much lower peptide concentrations *in vivo*, in response to the same Zn^{2+} dynamics and consequently this may mean that Zn^{2+}- Aβ toxic intearction might be less aggressive in the living brain than in our experimental system.

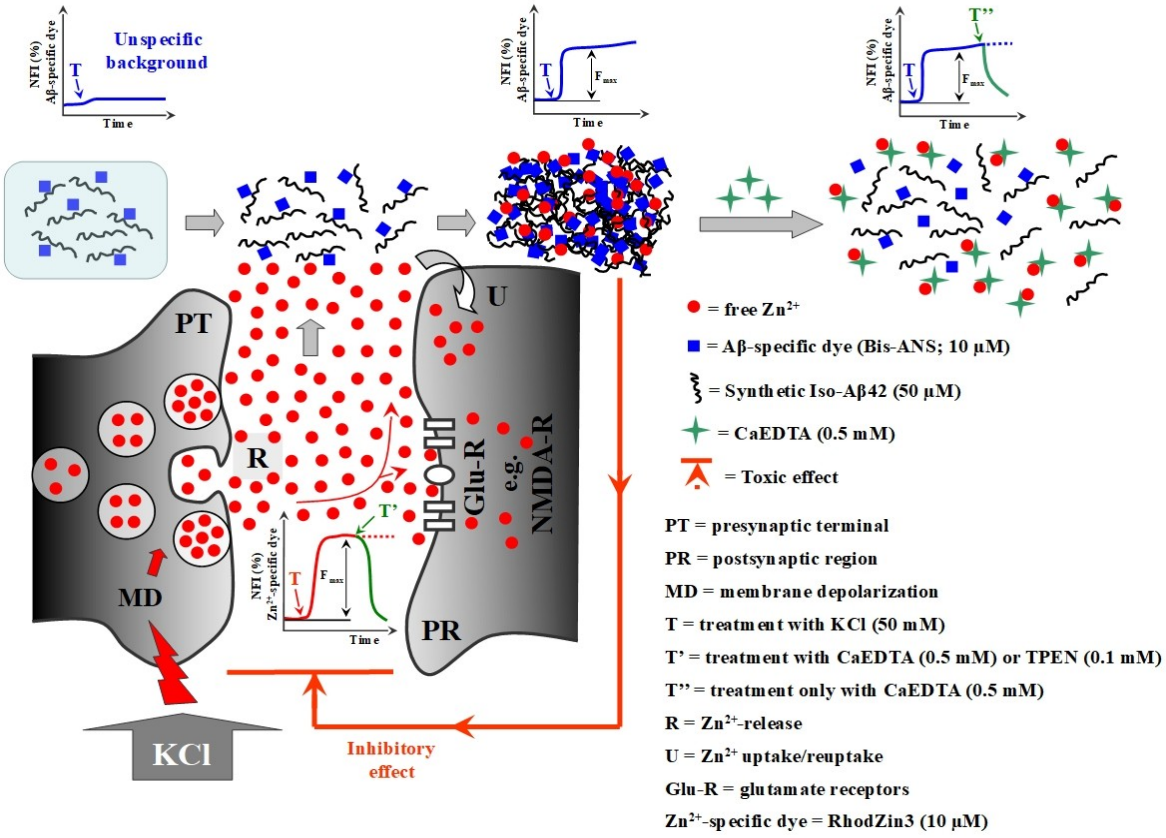

Figure 18

Schematic representation of Aβ aggregation induced by zinc release in the synaptic cleft and its effect on hippocampal synaptic functionality

Zn^{2+} is released during synaptic activity and within healthy conditions is rapidly taken up by energy dependent mechanisms. Energy failure during ageing impairs the reuptake mechanism of the extracellular Zn^{2+}. Accumulated Zn^{2+} in the synaptic cleft will react with Aβ released in the vicinity and will trigger its aggregation into toxic oligomers. Zn^{2+}- Aβ complexes are trapped in the synaptic cleft and impair its function.

5.3. Perspectives

Neuroscientific investigations, including AD pathology require feasible and relevant models with fair throughput screening capabilities. There are in general four primary approaches employed when a disease is being modelled: *in vivo*, *in vitro*, *in silico* and *ex vivo*. Although *in vivo* animal models were the first to provide critical insights into AD pathology, they require tedious and costly experimentations involving multiple factors to consider and monitor and few results have been translated into clinical therapy. Two dimensional, *in vitro* neuronal culture models are still predominant in preclinical screening, but fail to reliably imitate complex cell-to-cell interactions in the tissue context (Benam, et al., 2015). Recently *in silico* methods are also emerging and mathematical models are able to analyse big data produced in high-throughput screening techniques and provide a system-level view of AD pathological events. However, since these models are based on information that already exists, results highly depend on information accuracy and completeness. They are rather a useful addition to "real-world" experimentation to gain understanding from a wider, systemic perspective about the obtained results and suggest new potential avenues to explore.

By overcoming some shortfalls of *in vivo* and *in vitro* models, *ex vivo*, acute brain slice technology has been proven to be suitable for studies aiming at exploring molecular events as direct responses to a specific stimulus or treatment affecting viability and function in three dimensional tissue context. The methodology based on acute hippocampal slices developed in our laboratory to measure Aβ1-42 oligomer toxicity provides relevant and cost-effective model for screening protective agents and test hypothesis in preclinical studies in relatively short time frame. It allows iterative testing, tissue-level toxicology as well as detailed and easy imaging.

6. Conclusion

To overcome the shortcomings of the *in vitro* and *in vivo* methods, we developed a cost effective and simple apparatus for maintaining the viability of acute tissue slices, named: *ExViS* (*Ex Vivo* System; Universal Mini-Chamber Tube System for Acute Tissue Slices). The system allowed us to further develop methods that use acute (*ex vivo*) hippocampal slices to model AD-related patomechanisms. Over the course of my PhD studies we have developed the following techniques and *ex vivo* models based on the features of acute hippocampal slices:

1. Rapid, reliable and quantitative determination of Aβ1-42 toxicity in ageing (OGD) acute hippocampal slice model using MTT and LDH assays.

2. Quantitative determination of zinc-induced Aβ1-42 oligomerization toxicity in acute hippocampal slice model using MTT assay.

3. Fluorescent imaging of neurite cross-sections and detailed imaging of neurite structures in acute hippocampal slices via a novel application of bis-ANS and its co-staining variations.

4. Modelling the effect of Zn^{2+} released in glutamergic synaptic cleft in the hippocampus on Aβ1-42 aggregation and its consequences on cell viability and synaptic functionality, learning and memory (LTP).

The acute hippocampus slice-based models can serve as a feasible tool to gain deeper understanding on how pathological events in AD, in particular Aβ oligomerization, influence hippocampal functionality and therefore paving the way to develop and test related hypothesis but also to screen potential protective agents or validate results seen *in vivo* or predicted *in silico*.

7. Acknowledgement

I would like to thank the following people, without whom I would not have been able to complete this research, and without whom I would not have made it through my PhD degree.

My Supervisor and friend Dr. Zsolt Datki, whose expertise and knowledge of the subject matter steered me through this research. He supported me both professionally and as a human in challenging times and created a new opportunity for me to reuptake the thread of a research we had started a while ago.

I am especially grateful to Prof. Dr. Botond Penke, who offered many opportunities to evolve professionally and was a role model of dedicated scientist for me.

To Dr. Ákos Hunya, who introduced me into the main skills and techniques necessary to become a useful member of our lab team.

To Dr. Lívia Fülöp and Dr. Zsolt Bozsó for their expert support in biochemistry and to Dr. Viktor Szegedi for his expertise and for making the electrophysiological studies possible.

To Dr. Zita Galik-Oláh for offering her time and patience to thoroughly review this dissertation.

To Mónika Országné Mihók and Mária Batki who are the most amazing laboratory technicians I've ever met, for their patience and expert support, that made all procedures flawless, as well as for their friendship and all the fun moments we've had together.

As the mother of a wonderful but demanding toddler, I wouldn't been able to find uninterrupted time to write this thesis and to pass my exam, without the dedication of my husband (who has also helped me with editing the figures of this thesis) and my family who created a peaceful environment and supported and encouraged me along the way.

8. References

- Adlard PA, Bush AI. Metals and Alzheimer's disease. *J Alzheimers Dis*. 2006;10(2-3):145-163. doi:10.3233/jad-2006-102-303
- Adlard PA, Cherny RA, Finkelstein DI, Gautier E, Robb E, Cortes M, Volitakis I, Liu X, Smith JP, Perez K, Laughton K, Li QX, Charman SA, Nicolazzo JA, Wilkins S, Deleva K, Lynch T, Kok G, Ritchie CW, Tanzi RE, Cappai R, Masters CL, Barnham KJ, Bush AI. Rapid restoration of cognition in Alzheimer's transgenic mice with 8-hydroxy quinoline analogs is associated with decreased interstitial Abeta. Neuron. 2008 Jul 10;59(1):43-55. doi:10.1016/j.neuron.2008.06.018
- Basilico B, Pagani F, Grimaldi A, Cortese B, Di Angelantonio S, Weinhard L, Gross C, Limatola C, Maggi L, Ragozzino D. Microglia shape presynaptic properties at developing glutamatergic synapses. Glia. 2019 Jan;67(1):53-67. doi: 10.1002/glia.23508. Epub 2018 Nov 11.
- Benam KH, Dauth S, Hassell B, Herland A, Jain A, Jang KJ, Karalis K, Kim HJ, MacQueen L, Mahmoodian R, Musah S, Torisawa YS, van der Meer AD, Villenave R, Yadid M, Parker KK, Ingber DE. Engineered in vitro disease models. Annu Rev Pathol. 2015;10:195-262. doi: 10.1146/annurev-pathol-012414-040418.
- Bonner-Jackson A, Mahmoud S, Miller J, Banks SJ. Verbal and non-verbal memory and hippocampal volumes in a memory clinic population. Alzheimers Res Ther. 2015 Oct 15;7(1):61. doi: 10.1186/s13195-015-0147-9.
- Bozso Z, Penke B, Simon D, Laczkó I, Juhász G, Szegedi V, Kasza A, Soós K, Hetényi A, Wéber E, Tóháti H, Csete M, Zarándi M, Fülöp L. Controlled in situ preparation of A beta(1-42) oligomers from the isopeptide "iso-A beta(1-42)", physicochemical and biological characterization. Peptides. 2010 Feb;31(2):248-56. doi: 10.1016/j.peptides.2009.12.001. Epub 2009 Dec 6.
- Braak H, Braak E, Ohm T, Bohl J. Silver impregnation of Alzheimer's neurofibrillary changes counterstained for basophilic material and lipofuscin pigment. *Stain Technol*. 1988;63(4):197-200. doi:10.3109/10520298809107184
- Bulbarelli A, Lonati E, Brambilla A, Orlando A, Cazzaniga E, Piazza F, Ferrarese C, Masserini M, Sancini G. Aβ42 production in brain capillary endothelial cells after oxygen and glucose deprivation. Mol Cell Neurosci. 2012 Apr;49(4):415-22. doi: 10.1016/j.mcn.2012.01.007. Epub 2012 Feb 3.
- Bush AI, Multhaup G, Moir RD, Williamson TG, Small DH, Rumble B, Pollwein P, Beyreuther K, Masters CL. A novel zinc(II) binding site modulates the function of the beta A4 amyloid protein precursor of Alzheimer's disease. J Biol Chem. 1993 Aug 5;268(22):16109-12. PMID: 8344894
- Bush AI, Pettingell WH, Multhaup G, d Paradis M, Vonsattel JP, Gusella JF, Beyreuther K, Masters CL, Tanzi RE. Rapid induction of Alzheimer A beta amyloid formation by zinc. Science. 1994 Sep 2;265(5177):1464-7. doi: 10.1126/science.8073293.
- Butterfield DA, Pocernich CB. The glutamatergic system and Alzheimer's disease: therapeutic implications. CNS Drugs. 2003;17(9):641-52. doi: 10.2165/00023210-200317090-00004.

- Ceccom J, Bouhsira E, Halley H, Daumas S, Lassalle JM. Differential needs of zinc in the CA3 area of dorsal hippocampus for the consolidation of contextual fear and spatial memories. *Learn Mem*. 2013;20(7):348-351. Published 2013 Jun 14. doi:10.1101/lm.029017.112
- Cechetti F, Rhod A, Simão F, Santin K, Salbego C, Netto CA, Siqueira IR. Effect of treadmill exercise on cell damage in rat hippocampal slices submitted to oxygen and glucose deprivation. Brain Res. 2007 Jul 9;1157:121-5. doi: 10.1016/j.brainres.2007.04.045. Epub 2007 Apr 24.
- Cherny RA, Atwood CS, Xilinas ME, Gray DN, Jones WD, McLean CA, Barnham KJ, Volitakis I, Fraser FW, Kim Y, Huang X, Goldstein LE, Moir RD, Lim JT, Beyreuther K, Zheng H, Tanzi RE, Masters CL, Bush AI. Treatment with a copper-zinc chelator markedly and rapidly inhibits beta-amyloid accumulation in Alzheimer's disease transgenic mice. Neuron. 2001 Jun;30(3):665-76. doi: 10.1016/s0896-6273(01)00317-8.
- Cho S, Liu D, Fairman D, Li P, Jenkins L, McGonigle P, Wood A. Spatiotemporal evidence of apoptosis-mediated ischemic injury in organotypic hippocampal slice cultures. Neurochem Int. 2004 Jul;45(1):117-27. doi: 10.1016/j.neuint.2003.11.012.
- Cirrito JR, May PC, O'Dell MA, Taylor JW, Parsadanian M, Cramer JW, Audia JE, Nissen JS, Bales KR, Paul SM, DeMattos RB, Holtzman DM. In vivo assessment of brain interstitial fluid with microdialysis reveals plaque-associated changes in amyloid-beta metabolism and half-life. J Neurosci. 2003 Oct 1;23(26):8844-53. doi: 10.1523/JNEUROSCI.23-26-08844.2003.
- Collingridge GL, Singer W. Excitatory amino acid receptors and synaptic plasticity. Trends Pharmacol Sci. 1990 Jul;11(7):290-6. doi: 10.1016/0165-6147(90)90011-v.
- Colvin RA, Davis N, Nipper RW, Carter PA. Zinc transport in the brain: routes of zinc influx and efflux in neurons. J Nutr. 2000 May;130(5S Suppl):1484S-7S. doi: 10.1093/jn/130.5.1484S.
- Cotman CW, Monaghan DT, Ganong AH. Excitatory amino acid neurotransmission: NMDA receptors and Hebb-type synaptic plasticity. Annu Rev Neurosci. 1988;11:61-80. doi: 10.1146/annurev.ne.11.030188.000425.
- Cuajungco MP, Goldstein LE, Nunomura A, Smith MA, Lim JT, Atwood CS, Huang X, Farrag YW, Perry G, Bush AI. Evidence that the beta-amyloid plaques of Alzheimer's disease represent the redox-silencing and entombment of abeta by zinc. J Biol Chem. 2000 Jun 30;275(26):19439-42. doi: 10.1074/jbc.C000165200.
- Datki Z, Juhász A, Gálfi M, Soós K, Papp R, Zádori D, Penke B. Method for measuring neurotoxicity of aggregating polypeptides with the MTT assay on differentiated neuroblastoma cells. Brain Res Bull. 2003 Dec 30;62(3):223-9. doi: 10.1016/j.brainresbull.2003.09.011.
- Datki Z, Galik-Olah Z, Janosi-Mozes E, Szegedi V, Kalman J, Hunya ÁG, Fulop L, Tamano H, Takeda A, Adlard PA, Bush AI. Alzheimer risk factors age and female sex induce cortical Aβ aggregation by raising extracellular zinc. Mol Psychiatry. 2020 Nov;25(11):2728-2741. doi: 10.1038/s41380-020-0800-y. Epub 2020 Jun 9.
- Datki ZL, Hunya A, Penke B. A novel and simple fluorescence method for the measurement of presynaptic vesicular zinc release in acute hippocampal slices with a

fluorescence plate reader. Brain Res Bull 2007; 74(1-3): 183-187. doi: 10.1016/j.brainresbull.2007.06.001. Epub 2007 Jun 25.

- de Almeida LM, Leite MC, Thomazi AP, Battu C, Nardin P, Tortorelli LS, Zanotto C, Posser T, Wofchuk ST, Leal RB, Gonçalves CA, Gottfried C. Resveratrol protects against oxidative injury induced by H2O2 in acute hippocampal slice preparations from Wistar rats. Arch Biochem Biophys. 2008 Dec 1;480(1):27-32. doi: 10.1016/j.abb.2008.09.006. Epub 2008 Sep 22.
- Deibel MA, Ehmann WD, Markesbery WR. Copper, iron, and zinc imbalances in severely degenerated brain regions in Alzheimer's disease: possible relation to oxidative stress. *J Neurol Sci*. 1996;143(1-2):137-142. doi:10.1016/s0022-510x(96)00203-1
- Deshpande A, Kawai H, Metherate R, Glabe CG, Busciglio J. A role for synaptic zinc in activity-dependent Abeta oligomer formation and accumulation at excitatory synapses. Journal of Neuroscience 2009; 29(13): 4004-4015. doi: 10.1523/JNEUROSCI.5980-08.2009.
- Dyrks T, Dyrks E, Masters CL, Beyreuther K. Amyloidogenicity of rodent and human beta A4 sequences. *FEBS Lett*. 1993;324(2):231-236. doi:10.1016/0014-5793(93)81399-k
- Ferrão-Gonzales AD, Robbs BK, Moreau VH, Ferreira A, Juliano L, Valente AP, Almeida FC, Silva JL, Foguel D. Controlling {beta}-amyloid oligomerization by the use of naphthalene sulfonates: trapping low molecular weight oligomeric species. J Biol Chem. 2005 Oct 14;280(41):34747-54. doi: 10.1074/jbc.M501651200. Epub 2005 Jul 22.
- Ferreira JS, Papouin T, Ladépêche L, Yao A, Langlais VC, Bouchet D, Dulong J, Mothet JP, Sacchi S, Pollegioni L, Paoletti P, Oliet SHR, Groc L. Co-agonists differentially tune GluN2B-NMDA receptor trafficking at hippocampal synapses. Elife. 2017 Jun 9;6:e25492. doi: 10.7554/eLife.25492.
- Frederickson CJ, Bush AI. Synaptically released zinc: physiological functions and pathological effects. *Biometals*. 2001;14(3-4):353-366. doi:10.1023/a:1012934207456
- Frederickson CJ, Koh JY, Bush AI. The neurobiology of zinc in health and disease. Nat Rev Neurosci. 2005 Jun;6(6):449-62. doi: 10.1038/nrn1671.
- Frederickson CJ, Moncrieff DW. Zinc-containing neurons. Biol Signals. 1994 May-Jun;3(3):127-39. doi: 10.1159/000109536.
- Fu X, Zhang X, Chang Z. 4,4'-Dianilino-1,1'-binaphthyl-5,5'-sulfonate, a novel molecule having chaperone-like activity. *Biochem Biophys Res Commun*. 2005;329(3):1087-1093. doi:10.1016/j.bbrc.2005.01.164
- Fukuyama R, Mizuno T, Mori S, Nakajima K, Fushiki S, Yanagisawa K. Age-dependent change in the levels of Abeta40 and Abeta42 in cerebrospinal fluid from control subjects, and a decrease in the ratio of Abeta42 to Abeta40 level in cerebrospinal fluid from Alzheimer's disease patients. *Eur Neurol*. 2000;43(3):155-160. doi:10.1159/000008156
- Godement P, Vanselow J, Thanos S, Bonhoeffer F. A study in developing visual systems with a new method of staining neurones and their processes in fixed tissue. *Development*. 1987;101(4):697-713. PMID: 2460302
- Gong Y, Chang L, Viola KL, Lacor PN, Lambert MP, Finch CE, Krafft GA, Klein WL. Alzheimer's disease-affected brain: presence of oligomeric A beta ligands (ADDLs)

suggests a molecular basis for reversible memory loss. Proc Natl Acad Sci U S A. 2003 Sep 2;100(18):10417-22. doi: 10.1073/pnas.1834302100. Epub 2003 Aug 18.

- Grabiec U, Hohmann T, Hammer N, Dehghani F. Organotypic Hippocampal Slice Cultures As a Model to Study Neuroprotection and Invasiveness of Tumor Cells. J Vis Exp. 2017 Aug 27;(126):55359. doi: 10.3791/55359.
- Greenough MA, Volitakis I, Li QX, Laughton K, Evin G, Ho M, Dalziel AH, Camakaris J, Bush AI. Presenilins promote the cellular uptake of copper and zinc and maintain copper chaperone of SOD1-dependent copper/zinc superoxide dismutase activity. J Biol Chem. 2011 Mar 18;286(11):9776-86. doi: 10.1074/jbc.M110.163964. Epub 2011 Jan 14.
- Gupta S, Chakraborty S, Poddar A, Sarkar N, Das KP, Bhattacharyya B. BisANS binding to tubulin: isothermal titration calorimetry and the site-specific proteolysis reveal the GTP-induced structural stability of tubulin. *Proteins*. 2003;50(2):283-289. doi:10.1002/prot.10292
- Hawe A, Sutter M, Jiskoot W. Extrinsic fluorescent dyes as tools for protein characterization. *Pharm Res*. 2008;25(7):1487-1499. doi:10.1007/s11095-007-9516-9
- Ho SL, Poon CY, Lin C, Yan T, Kwong DW, Yung KK, Wong MS, Bian Z, Li HW. Inhibition of β-amyloid Aggregation By Albiflorin, Aloeemodin And Neohesperidin And Their Neuroprotective Effect On Primary Hippocampal Cells Against β-amyloid Induced Toxicity. Curr Alzheimer Res. 2015;12(5):424-33. doi: 10.2174/1567205012666150504144919.
- Honig MG, Hume RI. Dil and diO: versatile fluorescent dyes for neuronal labelling and pathway tracing. *Trends Neurosci*. 1989;12(9):333-341. PMID: 2480673
- Horowitz P, Prasad V, Luduena RF. Bis(1,8-anilinonaphthalenesulfonate). A novel and potent inhibitor of microtubule assembly. J Biol Chem. 1984 Dec 10;259(23):14647-50. PMID: 6548750.
- Horsburgh K, Reimer MM, Holland P, Chen G, Scullion G, Fowler JH. Axon-glial disruption: the link between vascular disease and Alzheimer's disease? Biochemical Society Transactions 39 (2011) 881-885. doi: 10.1042/bst0390881.
- Hung LW, Ciccotosto GD, Giannakis E, Tew DJ, Perez K, Masters CL, Cappai R, Wade JD, Barnham KJ. Amyloid-beta peptide (Abeta) neurotoxicity is modulated by the rate of peptide aggregation: Abeta dimers and trimers correlate with neurotoxicity. J Neurosci. 2008 Nov 12;28(46):11950-8. doi: 10.1523/JNEUROSCI.3916-08.2008.
- Jack CR Jr, Petersen RC, Xu Y, O'Brien PC, Smith GE, Ivnik RJ, Boeve BF, Tangalos EG, Kokmen E. Rates of hippocampal atrophy correlate with change in clinical status in aging and AD. Neurology. 2000 Aug 22;55(4):484-89. doi: 10.1212/wnl.55.4.484.
- Jalali-Yazdi F, Chowdhury S, Yoshioka C, Gouaux E. Mechanisms for Zinc and Proton Inhibition of the GluN1/GluN2A NMDA Receptor. Cell. 2018 Nov 29;175(6):1520-1532.e15. doi: 10.1016/j.cell.2018.10.043.
- Jancsó G, Domoki F, Sántha P, et al. Beta-amyloid (1-42) peptide impairs blood-brain barrier function after intracarotid infusion in rats. *Neurosci Lett*. 1998;253(2):139-141. doi:10.1016/s0304-3940(98)00622-3

- Jensen FE, Harris KM. Preservation of neuronal ultrastructure in hippocampal slices using rapid microwave-enhanced fixation. J Neurosci Methods. 1989 Sep;29(3):217-30. doi: 10.1016/0165-0270(89)90146-5.
- Kambe T, Suzuki E, Komori T. Zinc Transporter Proteins: A Review and a New View from Biochemistry. Zinc Signaling 2019, pp 23-56.
- Kawahara M, Negishi-Kato M, Sadakane Y. Calcium dyshomeostasis and neurotoxicity of Alzheimer's beta-amyloid protein. *Expert Rev Neurother*. 2009;9(5):681-693. doi:10.1586/ern.09.28
- Kayed R, Head E, Thompson JL, McIntire TM, Milton SC, Cotman CW, Glabe CG. Common structure of soluble amyloid oligomers implies common mechanism of pathogenesis. Science. 2003 Apr 18;300(5618):486-9. doi: 10.1126/science.1079469.
- Koike M.A., Garcia F.G., Kitazawa M., Green K.N., LaFerla F.M. Long term changes in phospho-APP and tau aggregation in the 3xTg-AD mice following cerebral ischemia. Neuroscience Letters. 495 (2011):55-59. doi: 10.1016/j.neulet.2011.03.034
- Kopanitsa MV, Afinowi NO, Grant SG. Recording long-term potentiation of synaptic transmission by three-dimensional multi-electrode arrays. BMC Neurosci. 2006 Aug 30;7:61. doi: 10.1186/1471-2202-7-61.
- Lannfelt L, Blennow K, Zetterberg H, Batsman S, Ames D, Harrison J, Masters CL, Targum S, Bush AI, Murdoch R, Wilson J, Ritchie CW; PBT2-201-EURO study group. Safety, efficacy, and biomarker findings of PBT2 in targeting Abeta as a modifying therapy for Alzheimer's disease: a phase IIa, double-blind, randomised, placebo-controlled trial. Lancet Neurol. 2008 Sep;7(9):779-86. doi: 10.1016/S1474-4422(08)70167-4. Epub 2008 Jul 30. Erratum in: Lancet Neurol. 2009 Nov;8(11):981.
- Laskay G, Zarándi M, Varga J, Jost K, Fónagy A, Torday C, Latzkovits L, Penke B. A putative tetrapeptide antagonist prevents beta-amyloid-induced long-term elevation of [Ca2+]i in rat astrocytes. Biochem Biophys Res Commun. 1997 Jun 27;235(3):479-81. doi: 10.1006/bbrc.1997.6806.
- Lee JY, Cole TB, Palmiter RD, Suh SW, Koh JY. Contribution by synaptic zinc to the gender-disparate plaque formation in human Swedish mutant APP transgenic mice. *Proc Natl Acad Sci U S A*. 2002;99(11):7705-7710. doi:10.1073/pnas.092034699
- Lee JY, Friedman JE, Angel I, Kozak A, Koh JY. The lipophilic metal chelator DP-109 reduces amyloid pathology in brains of human beta-amyloid precursor protein transgenic mice. *Neurobiol Aging*. 2004;25(10):1315-1321. doi:10.1016/j.neurobiolaging.2004.01.005
- Lee MC, Yu WC, Shih YH, Chen CY, Guo ZH, Huang SJ, Chan JCC, Chen YR. Zinc ion rapidly induces toxic, off-pathway amyloid-β oligomers distinct from amyloid-β derived diffusible ligands in Alzheimer's disease. Sci Rep. 2018 Mar 19;8(1):4772. doi: 10.1038/s41598-018-23122-x.
- Lee S, Fernandez EJ, Good TA. Role of aggregation conditions in structure, stability, and toxicity of intermediates in the Abeta fibril formation pathway. Protein Sci. 2007;16(4):723-732. doi:10.1110/ps.062514807
- Leiva J, Palestini M, Tetas M, López J. Copper sensitivity in dorsal hippocampus slices. Arch Ital Biol. 2000 Apr;138(2):175-84. PMID: 10782257.

- LeVine H. The challenge of inhibiting Abeta polymerization. Curr Med Chem. 2002 Jun;9(11):1121-33. doi: 10.2174/0929867023370167.
- Li Y, Hough CJ, Frederickson CJ, Sarvey JM. Induction of mossy fiber --> Ca3 long-term potentiation requires translocation of synaptically released Zn2+. J Neurosci. 2001 Oct 15;21(20):8015-25. doi: 10.1523/JNEUROSCI.21-20-08015.2001.
- Lipton P, Aitken PG, Dudek FE, Eskessen K, Espanol MT, Ferchmin PA, Kelly JB, Kreisman NR, Landfield PW, Larkman PM, et al. Making the best of brain slices: comparing preparative methods. J Neurosci Methods. 1995 Jun;59(1):151-6. doi: 10.1016/0165-0270(94)00205-u.
- Lo DC, McAllister AK, Katz LC. Neuronal transfection in brain slices using particle-mediated gene transfer. *Neuron*. 1994;13(6):1263-1268. doi:10.1016/0896-6273(94)90412-x
- Lovell MA, Xie C, Markesbery WR. Protection against amyloid beta peptide toxicity by zinc. Brain Res. 1999;823(1-2):88-95. doi:10.1016/s0006-8993(99)01114-2
- Lovell MA, Robertson JD, Teesdale WJ, Campbell JL, Markesbery WR. Copper, iron and zinc in Alzheimer's disease senile plaques. J Neurol Sci. 1998 Jun 11;158(1):47-52. doi: 10.1016/s0022-510x(98)00092-6.
- Lü L, Zhang L, Wai MS, Yew DT, Xu J. Exocytosis of MTT formazan could exacerbate cell injury. Toxicol In Vitro. 2012 Jun;26(4):636-44. doi: 10.1016/j.tiv.2012.02.006. Epub 2012 Feb 28.
- Lu YM, Taverna FA, Tu R, Ackerley CA, Wang YT, Roder J. Endogenous Zn(2+) is required for the induction of long-term potentiation at rat hippocampal mossy fiber-CA3 synapses. Synapse. 2000 Nov;38(2):187-97. doi: 10.1002/1098-2396(200011)38:2<187::AID-SYN10>3.0.CO;2-R.
- Maia MA, Sousa E. BACE-1 and γ-Secretase as Therapeutic Targets for Alzheimer's Disease. Pharmaceuticals (Basel). 2019;12(1):41. Published 2019 Mar 19. doi:10.3390/ph12010041
- Mayer ML, Vyklicky L Jr. The action of zinc on synaptic transmission and neuronal excitability in cultures of mouse hippocampus. J Physiol. 1989 Aug;415:351-65. doi: 10.1113/jphysiol.1989.sp017725.
- Mazumdar M, Parrack PK, Mukhopadhyay K, Bhattacharyya B. Bis-ANS as a specific inhibitor for microtubule-associated protein induced assembly of tubulin. *Biochemistry*. 1992;31(28):6470-6474. doi:10.1021/bi00143a016
- Minicozzi V, Stellato F, Comai M, Dalla Serra M, Potrich C, Meyer-Klaucke W, Morante S. Identifying the minimal copper- and zinc-binding site sequence in amyloid-beta peptides. J Biol Chem. 2008 Apr 18;283(16):10784-92. doi: 10.1074/jbc.M707109200. Epub 2008 Jan 30.
- Moretto MB, Funchal C, Santos AQ, Gottfried C, Boff B, Zeni G, Pureur RP, Souza DO, Wofchuk S, Rocha JB. Ebselen protects glutamate uptake inhibition caused by methyl mercury but does not by Hg2+. Toxicology. 2005 Oct 15;214(1-2):57-66. doi: 10.1016/j.tox.2005.05.022.

- Mosmann T. Rapid colorimetric assay for cellular growth and survival: application to proliferation and cytotoxicity assays. J Immunol Methods. 1983 Dec 16;65(1-2):55-63. doi: 10.1016/0022-1759(83)90303-4.
- Mozes E, Hunya A, Posa A, Penke B, Datki Z. A novel method for the rapid determination of beta-amyloid toxicity on acute hippocampal slices using MTT and LDH assays. Brain Res Bull. 2012 Apr 10;87(6):521-5. doi: 10.1016/j.brainresbull.2012.02.005. Epub 2012 Feb 25.
- Mozes E, Hunya A, Toth A, Ayaydin F, Penke B, Datki ZL. A novel application of the fluorescent dye bis-ANS for labeling neurons in acute brain slices. Brain Res Bull. 2011 Oct 10;86(3-4):217-21. doi: 10.1016/j.brainresbull.2011.07.004. Epub 2011 Jul 18.
- Nair NG, Perry G, Smith MA, Reddy VP. NMR studies of zinc, copper, and iron binding to histidine, the principal metal ion complexing site of amyloid-beta peptide. J Alzheimers Dis. 2010;20(1):57-66. doi: 10.3233/JAD-2010-1346.
- Nakamura M, Jang IS. Characterization of dural afferent neurons innervating cranial blood vessels within the dura in rats. *Brain Res*. 2018;1696:91-102. doi:10.1016/j.brainres.2018.06.007
- Nikseresht S, Bush AI, Ayton S. Treating Alzheimer's disease by targeting iron. Br J Pharmacol. 2019 Sep;176(18):3622-3635. doi: 10.1111/bph.14567. Epub 2019 Feb 11.
- Paoletti P, Vergnano AM, Barbour B, Casado M. Zinc at glutamatergic synapses. *Neuroscience*. 2009;158(1):126-136. doi:10.1016/j.neuroscience.2008.01.061
- Powers MM, Clark G, Darrow MA, Emmel VM. Darrow red, a new basic dye. *Stain Technol*. 1960;35:19-21. doi:10.3109/10520296009114710
- Prasad AR, Luduena RF, Horowitz PM. Bis(8-anilinonaphthalene-1-sulfonate) as a probe for tubulin decay. *Biochemistry*. 1986;25(3):739-742. doi:10.1021/bi00351a035
- Ray AM, Owen DE, Evans ML, Davis JB, Benham CD. Caspase inhibitors are functionally neuroprotective against oxygen glucose deprivation induced CA1 death in rat organotypic hippocampal slices. *Brain Res*. 2000;867(1-2):62-69. doi:10.1016/s0006-8993(00)02230-7
- Reiss AB, Arain HA, Stecker MM, Siegart NM, Kasselman LJ. Amyloid toxicity in Alzheimer's disease. *Rev Neurosci*. 2018;29(6):613-627. doi:10.1515/revneuro-2017-0063
- Rigon AP, Cordova FM, Oliveira CS, et al. Neurotoxicity of cadmium on immature hippocampus and a neuroprotective role for p38 MAPK. *Neurotoxicology*. 2008;29(4):727-734. doi:10.1016/j.neuro.2008.04.017
- Rönicke R, Klemm A, Meinhardt J, Schröder UH, Fändrich M, Reymann KG. Abeta mediated diminution of MTT reduction--an artefact of single cell culture?. *PLoS One*. 2008;3(9):e3236. Published 2008 Sep 18. 10.1371/journal.pone.0003236
- Rosen CG, Weber G. Dimer formation from 1-amino-8-naphthalenesulfonate catalyzed by bovine serum albumin. A new fluorescent molecule with exceptional binding properties. *Biochemistry*. 1969;8(10):3915-3920. doi:10.1021/bi00838a006
- Santhakumar H, Nair RV, Philips DS, et al. Real Time Imaging and Dynamics of Hippocampal Zn2+ under Epileptic Condition Using a Ratiometric Fluorescent Probe. *Sci Rep*. 2018;8(1):9069. Published 2018 Jun 13. doi:10.1038/s41598-018-27029-5

- Schmued LC, Albertson C, Slikker W Jr. Fluoro-Jade: a novel fluorochrome for the sensitive and reliable histochemical localization of neuronal degeneration. *Brain Res*. 1997;751(1):37-46. doi:10.1016/s0006-8993(96)01387-x
- Sensi SL, Paoletti P, Bush AI, Sekler I. Zinc in the physiology and pathology of the CNS. Nat Rev Neurosci 2009; 10(11): 780-791. doi: 10.1038/nrn2734.
- Stockert JC, Blázquez-Castro A, Cañete M, Horobin RW, Villanueva A. MTT assay for cell viability: Intracellular localization of the formazan product is in lipid droplets. *Acta Histochem*. 2012;114(8):785-796. doi:10.1016/j.acthis.2012.01.006
- Stoltenberg M, Bush AI, Bach G, et al. Amyloid plaques arise from zinc-enriched cortical layers in APP/PS1 transgenic mice and are paradoxically enlarged with dietary zinc deficiency. *Neuroscience*. 2007;150(2):357-369. doi:10.1016/j.neuroscience.2007.09.025
- Stryer L. The interaction of a naphthalene dye with apomyoglobin and apohemoglobin. A fluorescent probe of non-polar binding sites. *J Mol Biol*. 1965;13(2):482-495. doi:10.1016/s0022-2836(65)80111-5
- Tagliari B, Zamin LL, Salbego CG, Netto CA, Wyse AT. Hyperhomocysteinemia increases damage on brain slices exposed to in vitro model of oxygen and glucose deprivation: prevention by folic acid. *Int J Dev Neurosci*. 2006;24(4):285-291. doi:10.1016/j.ijdevneu.2006.01.002
- Takeda A, Nakamura M, Fujii H, Tamano H. Synaptic Zn(2+) homeostasis and its significance. *Metallomics*. 2013;5(5):417-423. doi:10.1039/c3mt20269k
- Tamano H, Suzuki H, Kobuchi S, Adlard PA, Bush AI, Takeda A. Difference in ability for extracellular Zn2+ influx between human and rat amyloid β1-42 and its significance. Neurotoxicology. 2019 May;72:1-5. doi: 10.1016/j.neuro.2019.01.005. Epub 2019 Jan 18. .
- Taubenfeld SM, Stevens KA, Pollonini G, Ruggiero J, Alberini CM. Profound molecular changes following hippocampal slice preparation: loss of AMPA receptor subunits and uncoupled mRNA/protein expression. J Neurochem. 2002 Jun;81(6):1348-60. doi: 10.1046/j.1471-4159.2002.00936.x.
- Taylor CP, Weber ML, Gaughan CL, Lehning EJ, LoPachin RM. Oxygen/glucose deprivation in hippocampal slices: altered intraneuronal elemental composition predicts structural and functional damage. *J Neurosci*. 1999;19(2):619-629. doi:10.1523/jneurosci.19-02-00619.1999
- Tonkikh AA, Carlen PL. Impaired presynaptic cytosolic and mitochondrial calcium dynamics in aged compared to young adult hippocampal CA1 synapses ameliorated by calcium chelation. *Neuroscience*. 2009;159(4):1300-1308. doi:10.1016/j.neuroscience.2008.12.057
- Trivino-Paredes JS, Nahirney PC, Pinar C, Grandes P, Christie BR. Acute slice preparation for electrophysiology increases spine numbers equivalently in the male and female juvenile hippocampus: a DiI labeling study. *J Neurophysiol*. 2019;122(3):958-969. doi:10.1152/jn.00332.2019
- Ueno S, Tsukamoto M, Hirano T, et al. Mossy fiber Zn^{2+} spillover modulates heterosynaptic N-methyl-D-aspartate receptor activity in hippocampal CA3 circuits. *J Cell Biol*. 2002;158(2):215-220. doi:10.1083/jcb.200204066

- Weng W, Li D, Peng C, Behnisch T. Recording Synaptic Plasticity in Acute Hippocampal Slices Maintained in a Small-volume Recycling-, Perfusion-, and Submersion-type Chamber System. J Vis Exp. 2018 Jan 1;(131):55936. doi: 10.3791/55936.
- Westbrook GL, Mayer ML. Micromolar concentrations of Zn2+ antagonize NMDA and GABA responses of hippocampal neurons. Nature. 1987 Aug 13-19;328(6131):640-3. doi: 10.1038/328640a0.
- Xu Y, Xiao G, Liu L, Lang M. Zinc transporters in Alzheimer's disease. Mol Brain 2019; 12(1):106. doi: 10.1186/s13041-019-0528-2.
- Yankner BA, Duffy LK, Kirschner DA. Neurotrophic and neurotoxic effects of amyloid beta protein: reversal by tachykinin neuropeptides. *Science*. 1990;250(4978):279-282. doi:10.1126/science.2218531
- Yoshiike Y, Tanemura K, Murayama O, et al. New insights on how metals disrupt amyloid beta-aggregation and their effects on amyloid-beta cytotoxicity. *J Biol Chem*. 2001;276(34):32293-32299. doi:10.1074/jbc.M010706200
- Zhou M, Baudry M. EUK-207, a superoxide dismutase/catalase mimetic, is neuroprotective against oxygen/glucose deprivation-induced neuronal death in cultured hippocampal slices. *Brain Res*. 2009;1247:28-37. doi:10.1016/j.brainres.2008.10.016
- Zhou M, Dominguez R, Baudry M. Superoxide dismutase/catalase mimetics but not MAP kinase inhibitors are neuroprotective against oxygen/glucose deprivation-induced neuronal death in hippocampus. *J Neurochem*. 2007;103(6):2212-2223. doi:10.1111/j.1471-4159.2007.04906.x
- Zhu K, Peters F, Filser S, Herms J. Consequences of Pharmacological BACE Inhibition on Synaptic Structure and Function. Biol Psychiatry. 2018 Oct 1;84(7):478-487. doi: 10.1016/j.biopsych.2018.04.022. Epub 2018 Jun 23.
- Zuo Y, Lin A, Chang P, Gan WB. Development of long-term dendritic spine stability in diverse regions of cerebral cortex. *Neuron*. 2005;46(2):181-189. doi:10.1016/j.neuron.2005.04.001

9. Appendix

Társszerzői lemondó nyilatkozat

Co-author certification

Alulírott Dr. Datki Zsolt László (felelős társszerző) kijelentem, hogy Jánosi-Mózes Emese (pályázó) PhD értekezésének tézispontjaiban bemutatott - közösen publikált - tudományos eredmények elérésében a pályázónak meghatározó szerepe volt, ezért ezeket a téziseket más a PhD fokozat megszerzését célzó minősítési eljárásban nem használta fel, illetve nem kívánja felhasználni.

2021.01.20.
dátum

szerző

SZEGEDI TUDOMÁNYEGYETEM Pszichiátriai Klinika 35 SZEGED

A pályázó tézispontjaiban érintett, közösen publikált közlemények:

- Mozes E, Hunya A, Toth A, Ayaydin F, Penke B, **Datki ZL**. A novel application of the fluorescent dye bis-ANS for labeling neurons in acute brain slices. Brain Res Bull. 2011;86(3-4):217-221. doi:10.1016/j.brainresbull.2011.07.004
- Mozes E, Hunya A, Posa A, Penke B, **Datki Z**. A novel method for the rapid determination of beta-amyloid toxicity on acute hippocampal slices using MTT and LDH assays. Brain Res Bull. 2012;87(6):521-525. doi:10.1016/j.brainresbull.2012.02.005
- **Datki Z**, Galik-Olah Z, Janosi-Mozes E, et al. Alzheimer risk factors age and female sex induce cortical Aβ aggregation by raising extracellular zinc [published online ahead of print, 2020 Jun 9]. Mol Psychiatry. 2020;10.1038/s41380-020-0800-y. doi:10.1038/s41380-020-0800-y

Molecular Psychiatry
https://doi.org/10.1038/s41380-020-0800-y

IMMEDIATE COMMUNICATION

Alzheimer risk factors age and female sex induce cortical Aβ aggregation by raising extracellular zinc

Zsolt Datki[1] · Zita Galik-Olah[1] · Emese Janosi-Mozes[1] · Viktor Szegedi[2] · Janos Kalman[1] · Ákos Gábor Hunya[3] · Livia Fulop[3] · Haruna Tamano[4] · Atsushi Takeda[4] · Paul A. Adlard[5] · Ashley I. Bush[5]

Received: 15 October 2019 / Revised: 16 May 2020 / Accepted: 21 May 2020

Abstract

Aging and female sex are the major risk factors for Alzheimer's disease and its associated brain amyloid-β (Aβ) neuropathology, but the mechanisms mediating these risk factors remain uncertain. Evidence indicates that Aβ aggregation by Zn^{2+} released from glutamatergic neurons contributes to amyloid neuropathology, so we tested whether aging and sex adversely influences this neurophysiology. Using acute hippocampal slices, we found that extracellular Zn^{2+}-elevation induced by high K^+ stimulation was significantly greater with older (65 weeks vs 10 weeks old) rats, and was exaggerated in females. This was driven by slower reuptake of extracellular Zn^{2+}, which could be recapitulated by mitochondrial intoxication. Zn^{2+}:Aβ aggregates were toxic to the slices, but Aβ alone was not. Accordingly, high K^+ caused synthetic human Aβ added to the slices to form soluble oligomers as detected by bis-ANS, attaching to neurons and inducing toxicity, with older slices being more vulnerable. Age-dependent energy failure impairing Zn^{2+} reuptake, and a higher maximal capacity for Zn^{2+} release by females, could contribute to age and sex being major risk factors for Alzheimer's disease.

Introduction

The major risk factors for Alzheimer's disease (AD) are age and female sex, both known to drive the hallmark β-amyloid (Aβ) neuropathology in humans and amyloid protein precursor (APP) transgenic mice [1–3]. Aβ itself is a normally secreted polypeptide and its production is not increased with normal aging or with AD. The changes that induce the aggregation of Aβ in the brain with aging are unproven, but a body of growing evidence indicates that neuronal Zn^{2+} release could play an important role [4–6]. Aβ peptide is rapidly precipitated by Zn^{2+} at neutral pH [7], and amyloid plaques are heavily enriched with Zn^{2+} in humans [8, 9] and APP transgenic mice [10, 11]. Zn^{2+}-induced Aβ aggregation is reversible with chelators, such as EDTA and clioquinol, and Aβ deposits in post-mortem human brain are dissolved with agents that release Zn^{2+} [12, 13]. Candidate drugs that target Aβ-metal complexes have been developed, and have reported efficacy in preclinical AD models and phase 2 clinical trials [12, 14–17], although none have reached pivotal testing.

The Zn^{2+}that aggregates Aβ in vivo is released by a subset of glutamatergic neurons during neurotransmission [4, 18], achieving maximal extracellular concentrations of 300 μM [19]. It is normally parceled into glutamatergic

Supplementary information The online version of this article (https://doi.org/10.1038/s41380-020-0800-y) contains supplementary material, which is available to authorized users.

✉ Zsolt Datki
datki.zsolt@med.u-szeged.hu

✉ Ashley I. Bush
ashley.bush@florey.edu.au

[1] Department of Psychiatry, University of Szeged, Szeged 6725, Hungary

[2] Department of Physiology, Anatomy and Neuroscience, University of Szeged, Szeged 6726, Hungary

[3] Department of Medical Chemistry, University of Szeged, Szeged 6726, Hungary

[4] Department of Neurophysiology, School of Pharmaceutical Sciences, University of Shizuoka, 52-1 Yada, Suruga-ku, Shizuoka 422-8526, Japan

[5] Melbourne Dementia Research Centre, Florey Institute of Neuroscience & Mental Health, and The University of Melbourne, Parkville, VIC 3052, Australia

Published online: 09 June 2020

presynaptic vesicles by the activity of ZnT3, a transmembrane protein whose expression overlaps with brain regions prone to amyloid deposition [10, 20]. ZnT3 is concentrated at dystrophic neurites in amyloid plaques [10], and genetic ablation of ZnT3 markedly inhibits amyloid pathology in APP transgenic mice [4, 18].

Since relatively high concentrations of Zn^{2+} are released by synaptic activity in amyloid-prone cortical tissue, there must be mechanisms at play to prevent this pool of Zn^{2+} from precipitating Aβ in early life. We hypothesized that these Zn^{2+} clearance mechanisms might fatigue with aging in a manner that may be exaggerated by female sex. We utilized acute hippocampal slices to model Zn^{2+} release throughout the neocortex (since ZnT3 is expressed throughout both sites), and to study changes that occur with age and sex that may explain the natural history of amyloid neuropathology. Using this system, we monitored the formation of soluble oligomeric Aβ-Zn^{2+} complexes as detected by bis-ANS, which have been described recently as being structurally distinct and more neurotoxic than non-metallated Aβ-derived diffusible ligands (ADDLs) [21], inducing greater astrogliosis when injected into mouse hippocampus [22]. Some of these findings and methods have been presented in a PhD thesis [23].

Methods

Materials

Cell impermeant forms of RhodZin-3 (cat. No. R-36350), FluoZin-3 (cat. No. F24194), and Newport Green (cat. No. N7990) were from Molecular Probes, Invitrogen, Hungary. ZnAF-2 (cat. No. 67975), TFLZn (cat. No. T3445), 4,4(′)-dianilino-1,1(′)-binaphthyl-5,5(′)-disulfonate dipotassium salt (Bis-ANS, cat. No. 49058), TPEN (cat. No. P4413), CaEDTA (cat. No. ED2SC), DNP (cat. No. D198501), pyrithione (cat. No. H3261), chloral hydrate (cat. No. 23100), MTT (cat. No. M5655), 96-well plates (Costar, cat. No. CLS3695), and general reagents were from Sigma-Aldrich, Hungary.

Synthetic Aβ1–42 and [Ala^{13,14}]Aβ1–42 (Aβ$_{\Delta 2His}$)

We prepared Aβ peptides from their iso-Aβ precursors, where Gly25 is linked to the side chain of Ser26 through an ester bond. This modification maximizes the initial solubility of the peptide. Iso-Aβ is rapidly ($t_{1/2} = 2.6$ min) and completely converted to Aβ at pH 7.4 via an intramolecular *O*→*N* acyl-shift [24].

Peptides were synthesized on a H-Ala-Wang-Chemmatrix resin using N^{α}-Fmoc protected amino acids. Peptide chain elongation was carried out using DCC/HOBt (1:1) activation and threefold molar excess of amino acids in a DCM/DMF (1:1) mixture. Coupling was monitored with qualitative ninhydrin test to detect deprotected amines. If the test was positive, the coupling step was repeated using HATU/HOAt/DIEA (1:1:2) activation. The Fmoc protecting group was removed by treating the peptide-resin with 20% piperidine/DMF twice (5 + 20 min). Ser26 was introduced into the peptide chain as Boc-Ser-OH. Acylation of the side chain of Ser26 with Fmoc-Gly-OH was done as in [25].

Peptides were cleaved by incubating the resin for 2.5 h in a trifluoroacetic acid/phenol/dithiotreithol/triisopropylsilane/water (1:1:1:1:36) mixture. Crude iso-Aβ was precipitated with diethyl ether, dissolved in a mixture of acetic acid and water, lyophilized and purified by HPLC on a Phenomenex Jupiter C4 column (10 µ, 300 Å, 250 × 21.2 mm).

For [Ala^{13,14}]iso-Aβ (the precursor to Aβ$_{\Delta 2His}$), synthesis proceeded as above, with histidine residues at positions 13 and 14 replaced with Ala.

Preparation of acute hippocampal slices

A modified version of the method reported in Datki et al. [26] was used. After anesthesia with chloral hydrate (0.4 g/kg), 10 ± 1 and 65 ± 4-week-old male and female Wistar rats were decapitated and the whole heads (without scalp-leather) were put in the ice cold ddH_2O for 1 min. The brains were quickly removed and immersed in Ca^{2+}-free artificial cerebrospinal fluid (ACSF) with elevated Mg^{2+} at 4 °C [27]. The composition of this preparation solution (in mM): NaCl 127, KCl 2, $MgCl_2$ 5, $NaHCO_3$ 25, D-glucose 10, pH = 7.4. Brain slices (thickness 400 µm) were prepared from the hippocampus with a McIlwain tissue chopper at 4 °C. The surface area of the slices was determined with a preparation microscope (type Nikon SMZ800 with a 12 megapixel camera) directly after preparation. The well area (15 mm^2) was used for area calibration. The slices (area ≈ 9 mm^2) were rapidly transferred into a mini-chamber (ExVis, Fig. S1) [28] made from Greiner freezer tubes (maximum 10 slices in 1 ml) for conditioning (30 min) in carboxygenated (95/5%: O_2/CO_2) Ca^{2+}-free ACSF preparation solution at room temperature (23 °C). Normal ACSF composition in mM: NaCl 125, KCl 2.5, $CaCl_2$ 2, $MgCl_2$ 1.3, $NaHCO_3$ 25, D-glucose 10, pH 7.4. Differential vulnerability to mechanical trauma as a confounder was excluded by measuring LDH release into the ACSF after preparation, which demonstrated no difference between slices taken from young and old rats (2.819 ± 0.029 U/mL, $n = 12$ vs 2.849 ± 0.130 U/mL, $n = 12$, $p = 0.46$). Experimental allocation of the slices or animals was not randomized and the operator was not blinded.

Measurement of the vesicular Zn^{2+} release and Aβ aggregation

Fluorescence was measured with a 96-well plate reader (NOVOstar OPTIMA, BMG Labtech, Budapest, Hungary) with a xenon lamp and fiberglass (3 mm diameter, 20 flashes/well/cycle) optics, which permitted fluorescence assay of the total area of the slice in each well [26].

After resting (30 min) in the carboxygenated Ca^{2+}-free ACSF solution at room temperature, the acute hippocampal slices (maximum 10) were washed for 30 s in 2 ml preheated (36 °C) HEPES buffered saline (HBS, composition in mM: NaCl 125, KCl 2; $CaCl_2$ 2, $MgCl_2$ 2, HEPES 25, D-glucose 12, pH 7.4). The slices were then transferred from the mini chamber to the plate wells (bottom area: 15 mm^2), where one centralized slice was immobilized within a round nonfluorescent plastic web (pore diameter: 45 µm) that was placed on the slice with ceramic forceps. The transfer process was rapid (5 slices/min). The HBS was carefully removed and substituted with HBS (40 µl per well) containing either Zn^{2+} fluorophore (10 µM), or peptide aggregation fluorophore (bis-ANS: 4,4(′)-dianilino-1,1(′)-binaphthyl-5,5(′)-disulfonate dipotassium salt, 10 µM) for 10 min. For bis-ANS peptide aggregation assays, the HBS solution was also supplemented with Aβ peptide (50 µM) taken from a stock solution of freshly prepared Aβ peptide in ddH_2O (0.5 mM, pH = 5). The plates and the HBS solution were preheated to 36 °C before slices were transferred. The temperature within the plate-reader was maintained at 36 °C. The distance between the plastic web and the top of the well was 9 mm. In the presence of bicarbonate, bis-ANS becomes a fluorophore marker for neurons in hippocampal slices, but the background fluorescence becomes negligible when the bicarbonate is not present [29]. Thus, HBS was used in hippocampal slice studies where bis-ANS was used to detect Aβ oligomers.

The acute hippocampal slices were treated with additional KCl (50 mM) to induce depolarization or additional NaCl (50 mM) as an osmotic control, which was introduced by a built-in liquid micro-pipettor (minimal pipetting capacity is 1 µl), and for the other treatments we used two built-in liquid injectors (minimal injection capacity is 2 µl). Injection speed was 420 µl/s. Measurement of fluorescence in the acute hippocampal preparations was started 1 min before the treatment with KCl/NaCl. A maximum of 10 wells (one slice per well) could be scanned in one cycle. One cycle took 10 s (1 s per well, flashes at 20 Hz). The excitation and emission wavelengths for the Zn fluorophores are detailed in Table S1. For bis-ANS $\lambda_{ex.} =$ 350 nm, $\lambda_{em.} = 540$ nm. Excitation light was projected from the bottom of the wells, and detection was from the same direction. Zn^{2+} selectivity was determined by abolishing fluorescence with the cell impermeant chelator CaEDTA [30, 31] or TPEN. We checked for the contribution of reagents to fluorescence in the presence of bis-ANS, and found that only TPEN caused a nonspecific fluorescence signal. Therefore, TPEN was not utilized in experiments involving bis-ANS.

Measurement of the extracellular Zn^{2+} uptake in acute hippocampal slices

Ten slices together in each mini-chamber were treated with dinitrophenol (DNP, 0.3 mM) or pyrithione (50 µM) for 30 min in carboxygenated Ca^{2+}-free ACSF at room temperature. The media were then changed to normal ACSF (1.15 mL, 36 °C) ± DNP or pyrithione, supplemented with 2 µM $ZnSO_4$. We then sampled (0.15 mL) the Zn^{2+}-containing ACSF media from the same chamber at 30 s and 10 min. The remaining Zn^{2+} in the samples was assayed with RhodZin-3 and ZnAF-2 fluorophores (both at 10 µM). DNP or pyrithione did not alter the background fluorescent signal of the Zn^{2+} detection reagents.

In vivo microdialysis

Male Wistar Rats (8 weeks old, $n = 9$ and 90–100 weeks old, $n = 6$) rats were anesthetized with chloral hydrate (300–350 mg/kg) and individually placed in a stereotaxic apparatus. The skull was exposed, a burr hole was drilled, and a guide tube (CMA Microdialysis, Solna, Sweden) was implanted into the hippocampus (AP –5.6 mm, ML +4.6 mm, VD +4.1 mm). The guide tube was secured with dental cement and screws. After the surgery, each rat was housed individually.

Forty-eight hours after implantation of the guide tube, a microdialysis probe (3-mm membrane CMA 12 probe, CMA Microdialysis) was inserted into the hippocampus of chloral hydrate-anesthetized rats through the guide tube. The hippocampus was preperfused at 5.0 µl/min with ACSF (127 mM NaCl, 2.5 mM KCl, 1.3 mM $CaCl_2$, 0.9 mM $MgCl_2$, 1.2 mM Na_2HPO_4, 21 mM $NaHCO_3$ and 3.4 mM D-glucose (pH 7.3)) for 60 min to stabilize under anesthesia. Then the hippocampus was perfused at 5.0 µl/min with ACSF for 60 min to determine the basal concentration of extracellular zinc. The perfusate was collected every 20 min. The perfusate samples (50 µl) were diluted with 2% nitric acid (100 µl).

Analysis of the samples in triplicate was conducted using a flameless atomic absorption spectrophotometer (Shimadzu AA6800F, Kyoto, Japan). The accuracy was checked by analysis of the samples in the presence of a standard solution of zinc.

3-(4,5-Dimethylthiazol-2-yl)-2,5-diphenyltetrazolium bromide (MTT) viability assay of hippocampal slices

Acute hippocampal slices were treated ± different Aβ forms in carboxygenated ACSF at 36 °C (Aβ or $A\beta_{\Delta 2His}$, 15 μM) for 10 min. Then the slices were treated with KCl (50 mM) or NaCl (50 mM) for 5 min. Then the slices were washed twice with ACSF, whereupon they were incubated ±CaEDTA (0.1 mM) for 3 h in carboxygenated ACSF solution (1 ml) at room temperature. Hence, the toxicity of Aβ could only be attributed to material that had precipitated (e.g., by endogenous Zn^{2+} release) and been trapped on the slices, and not been washed off. After 3 h we added 0.1 ml MTT (stock solution 5 mg/ml) to the chamber for 30 min. The reduction of MTT was stopped by transferring the slices from ACSF to ice-cold ddH_2O. We then transferred the slices to pure dimethyl sulfoxide for 30 min to dissolve the formazan precipitate, followed by absorbance assay at 550 and 620 nm. The results were normalized with the formula: $(OD_{550} - OD_{620})$/area of slice $(mm^2) = 100\%$ in control rats.

Multi-electrode array (MEA) electrophysiology

One acute hippocampal slice was placed in a 3D-MEA chip with 60 tip-shaped and 60-μm-high electrodes spaced by 100 μm (Ayanda Biosystems, S.A., CH-1015 Lausanne, Switzerland). The surrounding solution was removed, and the slice was immobilized by a grid. The slice was continuously perfused with carboxygenated ACSF (1.5 mL/min at 34 °C) during the whole recording session. Prior to an experiment, slices were washed twice with ACSF, and then incubated (±CaEDTA 0.1 mM to reverse the Zn^{2+}-induced Aβ aggregates) for a further 1 h in the incubation chamber, to ensure that that the preparation was not affected by residual K^+ or peptide remaining in the media. The slices were then stabilized for 30 min on the MEA chip.

Data were recorded with a Multi Channel System (MCS GmbH, Reutlingen, Germany). The Schaffer-collateral was stimulated by injecting a biphasic current waveform (100 + 100 μs) through one selected electrode at 0.033 Hz. Care was taken to choose the stimulating electrode in the same region from one slice to the other. The peak-to-peak amplitudes of field excitatory postsynaptic potentials (fEPSPs) at the proximal stratum radiatum of CA1 were analyzed. Following a 30 min incubation period, slices were continuously stimulated with medium-strength stimuli. When stable evoked fEPSPs were detected (for at least 20 min), the stimulus threshold was determined, and a stimulus strength–evoked response curve (i.e., input–output, *I–O* curve) was recorded by gradually increasing stimulus intensity until the maximal stimulus strength was reached. The *I–O* curve for each slice did not show any significant differences between the treatment groups (not shown), indicating normal basal synaptic function. The stimulus intensity was continuously increased from 0 to 120 μA with 10 μA steps. Stronger stimulation led to large Faradic effects on the electrodes causing artifacts. Three datasets were recorded for each stimulation intensity. The intensity of the test stimulus was set to be 30% of the threshold and maximum stimulus strength interval. After recording a 10 min stable control sequence, long-term potentiation (LTP) was induced by applying theta-burst stimulation (TBS; trains of 15 × 100 Hz bursts, 5 pulses per burst with a 200 ms interburst interval), at the maximum stimulation intensity, then fEPSPs were recorded for 60 min Normal LTP could be induced in the K^+-treated slices, demonstrating that the underlying pathways of LTP remained intact.

Statistical analysis

Analysis was performed by an operator blinded to group status. Data are reported as means ± SEM, with the *n* for technical and experimental replicated detailed in the figure legends, unless otherwise noted. Pilot experiments ascertained the estimated effect size, powered with $\alpha = 0.8$. Generally, significance levels of ANOVA results are reported (after confirming that groups are comparable for variance), with multiple testing or post-hoc corrections noted in the figure legends. Significance was set at $p < 0.05$.

Results

Activated hippocampal slices from aged and female rats release more zinc

Slices from young (10-week old) rats released Zn^{2+}upon 50 mM K^+ stimulation, in a Ca^{2+}-dependent manner (Fig. 1a), as reported previously [26]. Using this system, we found that the maximal extracellular Zn^{2+} concentrations produced by K^+ stimulation were significantly greater (+50–70%; ANOVA $p < 0.001$) in slices from old rats (65 weeks) (Fig. 1b). While there was no difference between young males and females in the amounts of Zn^{2+} released, old male hippocampi released ≈50% more Zn^{2+} than young males, and old females released ≈70% more Zn^{2+} than young males and significantly more (10–15%; $p < 0.001$) than old males (Fig. 1b). These results were confirmed using two different impermeant Zn^{2+} indicators, RhodZin3 and ZnAF2 (Fig. 1b). Post-synaptic Cu^{2+} release during neurotransmission [32] could not account for these results since Cu^{2+}suppresses RhodZin3 and ZnAF2 fluorescence (Fig. S2).

While the increased release of Zn^{2+} could be due to greater ZnT3 expression in female hippocampus [4, 33],

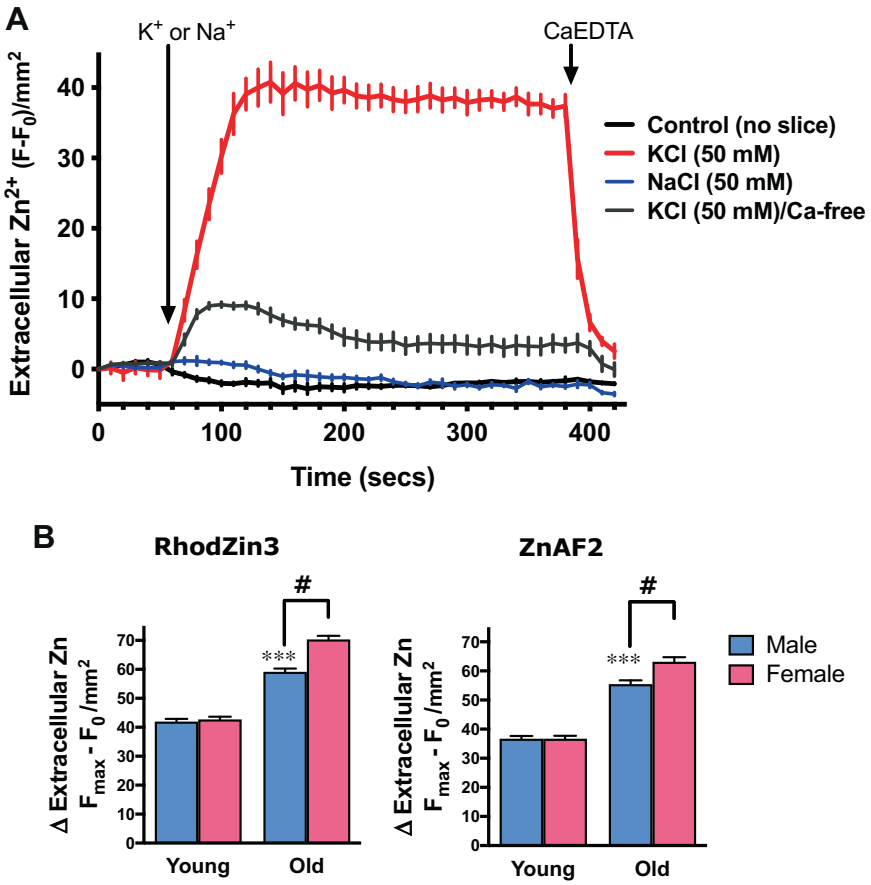

Fig. 1 Age and sex affect Zn^{2+} release from rat acute hippocampal slices. a Release of Zn^{2+} from slices taken from 10-week-old male rats, depolarized with high K^+ in HEPES buffered saline (HBS) supplemented with the cell-impermeable Zn^{2+}-indicator RhodZin3 (10 μM). Zn^{2+}-selective chelators CaEDTA (0.5 mM) or TPEN (0.1 mM, not shown) abolished the fluorescent signal. Data are means ± SEM, $n = 5$ experiments. **b** Increased depolarization-induced Zn^{2+} release from older and female slices. Data are mean ΔF_{max} (±SEM, $n = 60$) of two different impermeant Zn^{2+} fluorophores (RhodZin3 and ZnAF2, indicated) taken 120 s after depolarization with high K^+. The ΔZn^{2+} was significantly greater from old (65 weeks) rat tissue than young (10 weeks) rat tissue, and old female tissue released significantly more Zn^{2+} than old males. Slices were observed separately in a multiwell format, one slice per well, adjusted for the surface area of each individual slice. ***$p < 0.001$, compared with the mean ΔZn of young male and female slices; #$p < 0.001$, between old male and female slices, Tukey's multiple comparison test.

hippocampal ZnT3 levels fall with aging [34]. Indeed, hippocampal Timm's staining, a proxy for ZnT3-mediated vesicular Zn^{2+} [35], was not increased in old rats (Fig. S3A). Yet interstitial zinc levels measured by in vivo microdialysis confirmed that extracellular zinc levels are approximately four-fold elevated in the brains of old animals compared with young adults (Fig. S3B; $p < 0.01$). Thus, the extracellular Zn^{2+} from stimulated hippocampal explants that was increased with age and sex (Fig. 1) could have resulted from impaired reuptake of released Zn^{2+}. Sustained levels of extracellular Zn^{2+} are neurotoxic [36], therefore synaptic Zn^{2+} must rise only briefly during neurotransmission. We hypothesized that the net increase in extracellular Zn^{2+} that we observed in the hippocampal tissue was not only a product of synaptic release but also the robust, energy-dependent reuptake of Zn^{2+} previously described [37].

Indeed, using a double-labeling method, intracellular Zn^{2+} rose seconds after high K^+ stimulation of slices induced extracellular Zn^{2+} release (Fig. 2a). To confirm that the Zn^{2+} released is subject to reuptake, we stimulated the slice with high K^+ in the presence of CaEDTA (rather than adding it after stimulation), so that Zn^{2+} released was captured by the impermeable chelator. Indeed, CaEDTA abolished the rise in intracellular Zn^{2+}(Fig. 2b), consistent with the released Zn^{2+} normally being recycled. Ca-free medium, which prevents vesicular release of Zn^{2+}, also suppressed the poststimulation rise in intracellular Zn^{2+} (Fig. 2b). NMDA receptor block by either memantine ($p < 0.05$) or MK801 ($p < 0.001$) modestly but significantly increased the levels extracellular Zn^{2+} post stimulation, and concomitantly inhibited the subsequent rise in intracellular Zn^{2+} (Fig. 2b; $p < 0.01$), consistent with inhibition of some Zn^{2+} re-entry through the Ca^{2+} channel [38, 39].

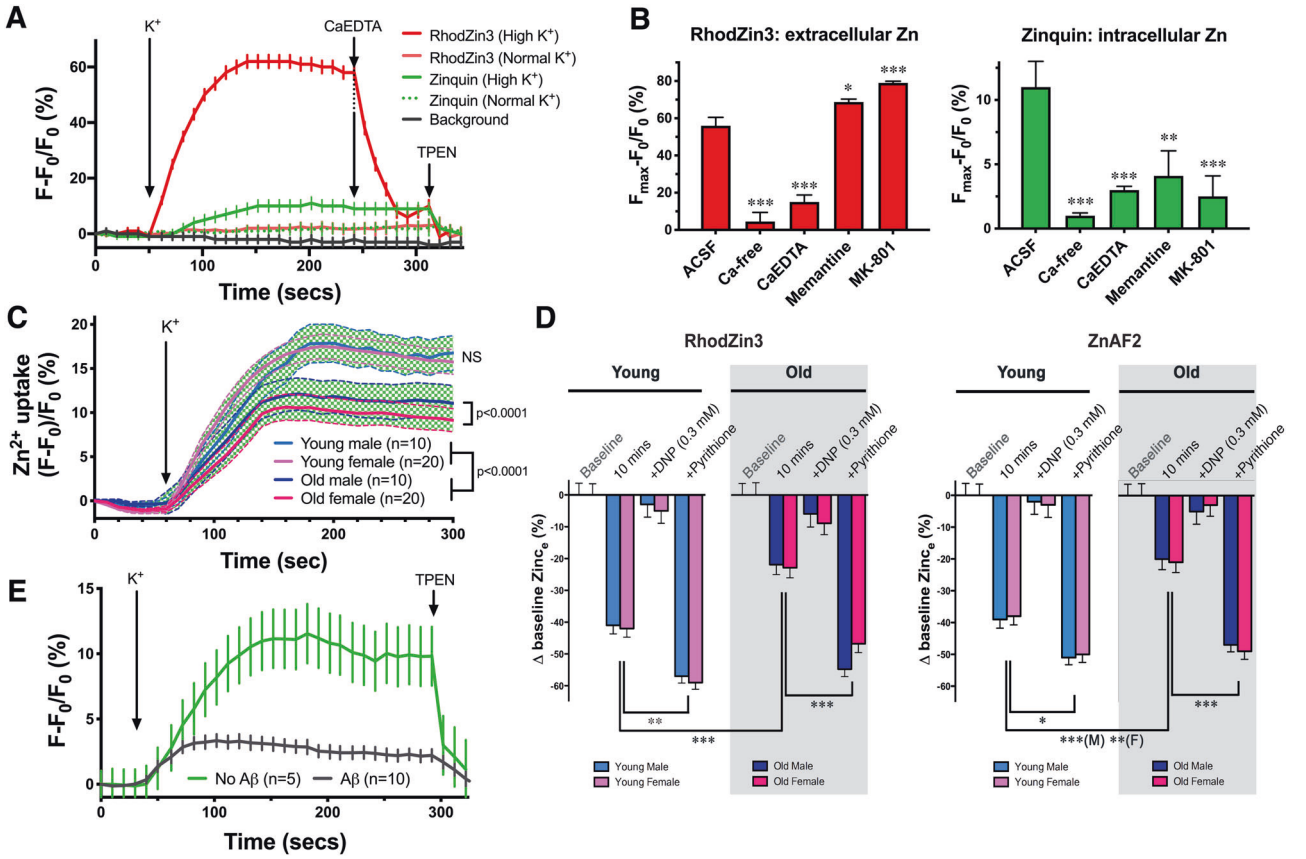

Fig. 2 Effects of age, sex and mitochondrial function on Zn^{2+} uptake in rat acute hippocampal slices. a Slices from young male rats were preloaded with zinquin, which detects free intracellular Zn^{2+}, then placed into HBS supplemented with RhodZin-3, which detects extracellular Zn^{2+}. Stimulation with high K^+ caused an immediate increase in extracellular Zn^{2+}, shortly followed by increased intracellular Zn^{2+} reflecting reuptake. As controls, application of the cell-impermeable Zn^{2+}-chelator, CaEDTA, quenched the fluorescence of extracellular but not intracellular Zn^{2+}. The cell-permeable Zn^{2+}-chelator, TPEN, quenched both signals. **b** The maximal rise in extracellular and intracellular free Zn^{2+} in slices from young compared with old rats following K^+ stimulation is shown. **c** Differential rise of intracellular Zn^{2+} monitored by zinquin in male and female, young and old rat hippocampal slices, following high K^+ stimulation. **d** Residual extracellular Zn^{2+} ($Zinc_e$) levels in ACSF bathing hippocampal slices 30 s (baseline) and 10 min after introducing 2 µM $ZnSO_4$. RhodZin3 readings were corroborated by ZnAF2. The drop in $Zinc_e$, reflecting uptake into the tissue, was significantly inhibited with slices from old (65 week) rats compared with young (10 week) rats. The mitochondrial toxin DNP abolished the drop in $Zinc_e$ (consistent with preventing tissue uptake), in contrast to pyrithione, a Zn^{2+}-ionophore, which increased uptake as expected. There were no significant differences between males and female means for any condition. **e** High concentrations (50 µM) of Aβ1–42 block the apparent uptake of $Zinc_e$ reflected by a rise in intracellular zinc fluorescence assayed by zinquin. Data are means (±SEM, $n = 5$ chambers, each containing 10 slices). *P* values are shown for One-way ANOVA with Dunnett's multiple comparison test. $*p < 0.05$, $**p < 0.01$, $***p < 0.001$. For **b**, comparisons against ACSF.

To test whether decreased reuptake could contribute to the increased extracellular Zn^{2+} we observed in stimulated old rat slices (Fig. 1b), we compared Zn^{2+} uptake following K^+ stimulation of slices from old and young rats. The rate and maximal reuptake of Zn^{2+} released from old rat slices were both significantly less than the reuptake into young rat slices, for both males and females (Fig. 2c; $p < 0.0001$). While there was no difference in Zn^{2+} uptake in young tissue from either sex, old male tissue took up significantly more released Zn^{2+} than old female tissue (Fig. 2c; $p < 0.0001$). This pattern was in concordance with the levels of extracellular Zn^{2+}released by excitement of the respective tissues (Fig. 1b), indicating that the elevated extracellular Zn^{2+} observed in older and especially older female tissue was caused, at least partly, by slower Zn^{2+} reuptake.

To confirm that slices from older rats have more limited Zn^{2+} uptake, we studied uptake when a fixed amount of Zn^{2+} was added to the incubation media of rat hippocampal slices. We observed that ≈40% of the Zn^{2+} (2 µM, a subtoxic concentration) was cleared within 10 min from the media of young slices, but significantly less Zn^{2+} (≈20%) was cleared from the media of old slices (Fig. 2d; $p < 0.001$). As a reference, the Zn^{2+} ionophore pyrithione [40] increased the drop in extracellular Zn^{2+} at 10 min (Fig. 2d; $p < 0.01$), consistent with the loss of fluorescence being caused by extracellular Zn^{2+} uptake. Treatment of the

slices with a sub-toxic concentration of the mitochondrial uncoupler 2,4-dinitrophenol (DNP) [41] (0.3 mM, Fig. S4) markedly impaired the uptake of Zn^{2+} by young slices (Fig. 2d), indicating that the brain mitochondrial impairment of aging [42] might contribute to sluggish Zn^{2+} reuptake. These results were confirmed using both extracellular zinc indicators, RhodZin3 and ZnAF2, and no difference in uptake between male and female slices was observed under these conditions (Fig. 2d). Therefore, the higher extracellular Zn^{2+} from K^+-treated older female slices that is then transferred intracellularly (Figs. 1b, 2c) probably reflects greater Zn^{2+} release, which would be consistent with previous reports of higher ZnT3 expression in female rodents [4].

We previously reported that Aβ1–42 injected into the rat hippocampus at physiological (picomolar to low nanomolar) concentrations promotes the uptake of Zn^{2+} into dentate granule cells [5, 43]. Notably, extracellular Aβ1–42 applied to the slices at higher concentrations, reflecting accumulations in AD (50 µM), markedly inhibited Zn^{2+} reuptake following high K^+ stimulation of hippocampal slices (Fig. 2e). Trapping of extracellular Zn^{2+} by Aβ aggregates could interfere with electrophysiological functions by preventing Zn^{2+} reaching post-synaptic targets, leading to consequences such as lowering the expression of NMDA receptor subunits and post-synaptic scaffolding defects [34, 44].

More zinc-induced Aβ1–42 oligomers are formed by aged and female tissue

The rat sequence of Aβ has substitutions of key residues that mediate Zn^{2+} coordination, and is not readily precipitated by Zn^{2+}, possibly explaining why endogenous Aβ aggregation does not occur in rat brain [7]. Therefore, we studied synthetic human Aβ1–42 added to the explant media to test whether its aggregation could be induced by Zn^{2+} release from the hippocampal slices. We monitored aggregation with bis-ANS, a fluorophore for peptide assembly that detects prefibrillar, low-order oligomers of Aβ [45] that exhibit increased toxicity [22, 46]. As a control, we studied a synthetic mutant of Aβ1–42 with histidine-to-alanine substitutions at residues 13 and 14 that attenuate interactions with Zn^{2+} [47] ($Aβ_{Δ2His}$).

Before applying human Aβ1–42 to hippocampal slices, we first characterized its response to Zn^{2+} in cell-free systems. We found that bis-ANS detected marked aggregation of Aβ1–42 (50 µM) induced by Zn^{2+} (50 µM) within seconds, which was rapidly reversed by addition of the impermeant Zn^{2+}-selective chelator, CaEDTA (0.5 mM, Fig. S5A,B). In the absence of Zn^{2+}, Aβ1–42 aggregated comparatively slowly and incompletely (Fig. S5A) and was not influenced by K^+ 50 mM (used next to stimulate slices).

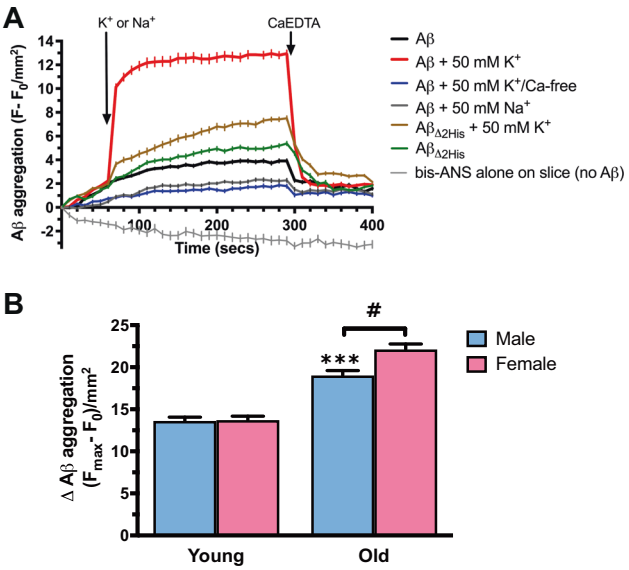

Fig. 3 Aβ aggregation on hippocampal slices assayed by bis-ANS. **a** Slices from young male rats were incubated with Aβ1–42 (50 µM) or mutant Aβ1–42 lacking Zn^{2+}-coordinating histidines ($Aβ_{Δ2His}$). After 60 secs high K^+ or Na^+ (an osmotic stress control) was introduced to the media. At 300 s the Zn^{2+}-selective chelator CaEDTA (0.1 mM) was introduced. Ca^{2+}-free HBS was used to determine if the Aβ aggregation was associated with synaptic vesicular release. Data are mean ΔF ± SEM, $n = 25$ slices per condition, normalized for the surface area of each slice. **b** Age and sex modulate Aβ aggregation monitored by bis-ANS fluorescence. The data are mean $ΔF_{max}$ of bis-ANS fluorescence induced by high K^+ treatment of hippocampal slices. As with $ΔZn^{2+}$ changes (Fig. 1c), ΔAβ aggregation was significantly greater on old (65 weeks) rat tissue than young (10 weeks) rat tissue, and old female tissue induced significantly more ΔAβ aggregation than old males. $^{***}p < 0.001$, $^{\#}p < 0.002$, ANOVA with post hoc *t*-tests, $n = 30$ slices per condition.

$Aβ_{Δ2His}$ aggregation by 50 µM Zn^{2+} was markedly attenuated, as expected (Fig. S5A).

We then tested whether the endogenous Zn^{2+} released from rat hippocampal slices could induce oligomerization of exogenous synthetic human Aβ1–42. Bis-ANS detected that Aβ1–42 aggregation was rapidly induced when the slices were stimulated with 50 mM K^+ (Fig. 3a). This could not be explained by the direct effects of K^+ on the peptide (Fig. S5A). Rapid Aβ1–42 aggregation from the slices was inhibited when Ca^{2+} was deleted from the high K^+ buffer (Fig. 3a), consistent with the aggregating factor being released upon synaptic activation. Aggregation could be reversed by the zinc-selective chelator, CaEDTA, and no aggregation was observed with high K^+ treatment of slices in the presence of $Aβ_{Δ2His}$ (Fig. 3a), consistent with the aggregating factor being Zn^{2+} released by the hippocampus upon depolarization. Could Cu^{2+} that is released post-synaptically during neurotransmission [32] account for these changes? While Cu^{2+} can bind Aβ, it does not aggregate Aβ at physiological pH [48], and the fluorescence from the bis-ANS indicator in the presence of synthetic

Aβ1–42 was not increased by Cu^{2+} at concentrations (50 µM) that would be beyond maximal in the system (Fig. S5C).

Hippocampal slices from older (65 weeks old) rats treated with high K^+ induced significantly more aggregation of Aβ1–42 than slices from younger (10 weeks old) rats (Fig. 3b; $p < 0.001$), and slices from older female rats induced significantly more aggregation than slices from older male rats (Fig. 3b; $p < 0.05$). These observations are consistent with more Aβ aggregation being induced by the increased extracellular Zn^{2+} levels from older and female slices that we observed under these conditions (Fig. 1b).

Fluorescent microscopy determined the sites of Aβ attachment detected by bis-ANS on the Aβ-treated slices. Slices from young rats treated with Aβ1–42 (50 µM) and high K^+, as in Fig. 3, were washed with ACSF to remove unbound Aβ, yet showed strong labeling of cells that had the morphology of neurons but not glia in the granule cell layer, CA3 pyramidal cell layer, as well as hilar pyramidal neurons and the mossy fibers (Fig. 4a–e). The sites of Aβ attachment are consistent with the sites of high extracellular Zn^{2+} flux in the tissue. To determine whether this fluorescence was due to Aβ1–42 adhering to the surface, we studied the effects of carbonate pH 12 washing of the slices after being treated with Aβ1–42 and high K^+. This technique for stripping surface-bound polypeptides removed much of, but did not abolish, the bis-ANS signal (Fig. 4f, g). The signal we detected was not non-specific since the fluorescence of bis-ANS treated tissue, without added Aβ, was negligible under these conditions (Fig. 5a).

Using bis-ANS fluorescence microscopy we examined the reversibility of Aβ oligomer attachment by washing ±CaEDTA after the slices had been exposed for 10 min to endogenous or exogenous Zn^{2+} to induce oligomerization. Treatment with Aβ alone induced only slight bis-ANS fluorescence (Fig. 5b). However, both depolarization of Aβ-treated slices with K^+, or aggregation of the Aβ with added Zn^{2+}, caused markedly increased bis-ANS fluorescence of the same hippocampal structures observed in Fig. 4a (Fig. 5c, e). Aβ-treated slices treated with K^+ or Zn^{2+} and then washed with CaEDTA exhibited far less bis-ANS fluorescence (Fig. 5d, f) than slices washed with ACSF alone. This is consistent with CaEDTA reversing the aggregation of Aβ induced by K^+ on slices (Fig. 2a).

Nuclear sparing was observed (Fig. 4b–e), indicating that some of the peptide may have entered the neurons. However, since much of the signal was reversed by CaEDTA or carbonate treatment, it is likely that most of the Aβ aggregated on the neuronal surface. The possibility of some intraneuronal uptake of peptide aggregates could not be excluded. Slices that were first fixed with ethanol or formaldehyde and then treated, as above, with Aβ ± K^+ or Zn^{2+} did not label with bis-ANS (data not shown). Thus

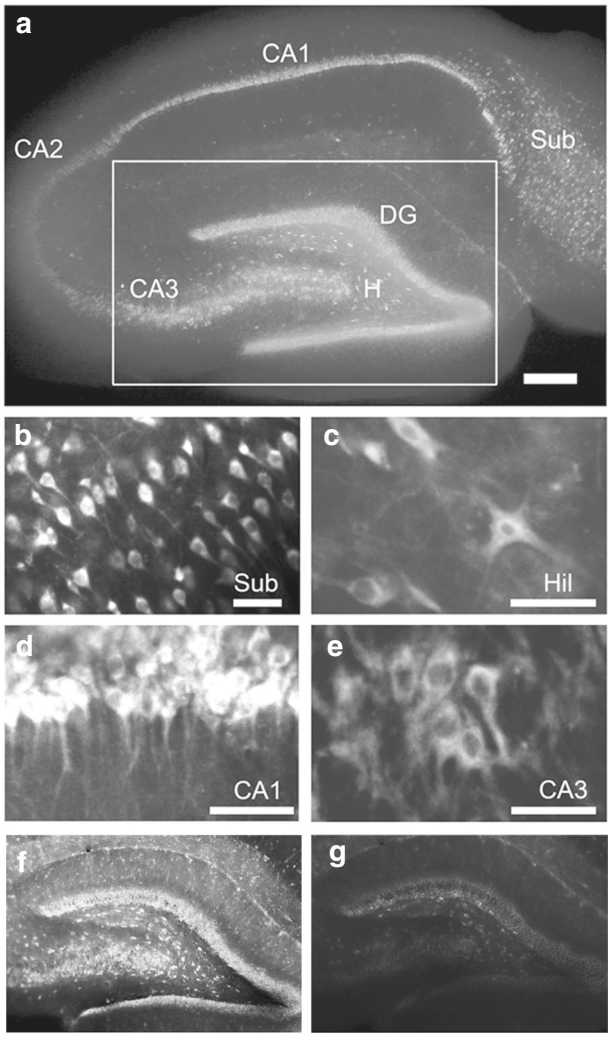

Fig. 4 Bis-ANS fluorescence of adherent Aβ1–42 predominantly on neuronal dendrites and soma of acute hippocampal slices. Acute hippocampal slices from 10-week old male rats were treated with freshly prepared Aβ1–42 (50 µM) for 10 min in HBS, then ±50 mM KCl for 5 min, washed again with HBS, labeled with bis-ANS (10 µM in HBS, 10 min), washed again, and analyzed by fluorescent microscopy. **a** Image of bis-ANS labeling of a complete slice. The box indicates the field of interest for **b–e** and Fig. 5. Scale bar = 300 µ. **b–e** Enlargements of subiculum, hilus, CA1 and CA3 pyramidal cell layer showing that bis-ANS detects neurons but not glia. Scale bar = 50 µ. Effect of carbonate wash on bis-ANS labeling. The slices were prepared as for **a**, but after washing off the unbound bis-ANS, the slices were washed with either **f** ACSF or **g** 110 mM NaCl, 50 mM Na_2CO_3, pH = 12, for 5 min, and then washed twice with ACSF before microscopy. pH 12 treatment removed much of the surface-bound Aβ detected by bis-ANS. Parallel slice-free control experiments on Aβ solutions showed that the bis-ANS fluorescence is not perturbed by bringing the mixture to pH 12 and back to pH 7.4 (not shown). Data are representative of $n = 10$ replicates.

Aβ:Zn^{2+} complexes can be detected by bis-ANS only on living neurons, obviating the possibility of examining fixed human or APP transgenic mouse post-mortem tissue for bis-ANS fluorescence.

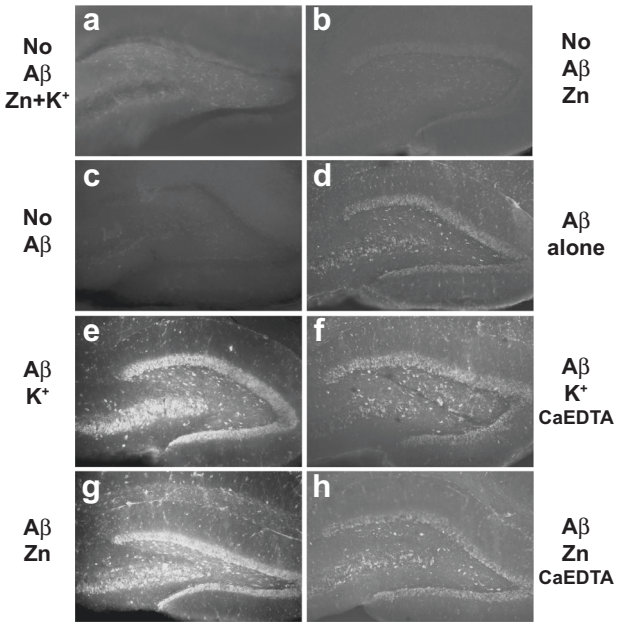

Fig. 5 Bis-ANS fluorescence within acute hippocampal slices treated with Aβ1–42. The slices in **a–c** were treated with bis-ANS in buffer conditions as indicated without Aβ1–42. The remaining slices were treated with Aβ1–42 and prepared as for Fig. 3 (±50 mM K^+ or 50 μM Zn^{2+} treatment, as indicated) but after washing off the unbound bis-ANS, the slices were washed with either **d**, **e**, **g** HBS, or **f**, **h** CaEDTA (0.5 mM in HBS), for 5 min, and then washed twice with HBS before microscopy. Data are representative of $n = 10$ replicates.

The pattern of Aβ attachment detected by bis-ANS does not fully match the sites of greatest likelihood of Zn^{2+} release during neurotransmission. For example, the dentate granule cells are a prominent site for Aβ attachment despite being a site where Zn^{2+} release is not anticipated. Despite not being a major projection target for zincergic terminals, the granule cells of the dentate gyrus must have a very active zinc uptake mechanism, since they are the origin of the mossy fiber pathway, which is dense with vesicular Zn^{2+} that is ultimately released remotely e.g., CA3. Indeed, one of the earliest reports of Zn^{2+} release described highly avid granule cell uptake of zinc [37]. In agreement, we reported in vivo zinc uptake into the granule cells that is exaggerated by the presence of pM-nM concentrations of exogenously applied Aβ [5, 43], while our current findings show that it could be blocked by higher (μM) concentrations (Fig. 2e) that might emulate the effects of amyloid pathology. So, we hypothesize that the distribution of exogenous Aβ attaching to K^+-stimulated slices could reflect sites of zinc uptake, rather than sites of zinc release. Notably, the rise in intracellular zinc occurring upon high K^+ stimulation was blocked by NMDA receptor blockade (Fig. 2b). Aβ has been described to adhere to the NMDA receptor in a zinc-dependent manner [49], and NMDA receptors are found throughout the fields [50] where we observed Aβ attachment. In physiological systems, it has been reported zinc can act in a paracrine manner to be taken up at a distance from where it is released [51, 52]. Consistent with this extrasynaptic diffusion of zinc contributing to amyloid deposition in vivo, zinc-enriched amyloid plaques form prominently at sites in the hippocampus remote from mossy fiber projections [53].

Zinc-induced Aβ1–42 oligomers induce more impairment of aged hippocampus

We tested whether Zn^{2+}-induced Aβ aggregation affects the function and viability of the hippocampus. Using multi-electrode array (MEA) observations of slices from 10-week old male rats, we studied long-term potentiation (LTP) induced by TBS, a canonical method for studying memory circuitry. Acute slices were treated with Aβ1–42 (15 μM in ACSF) for 10 min, followed by high K^+ (50 mM in ACSF) for 5 min to induce Zn^{2+} release and Aβ aggregation.

Hippocampal slices treated with Aβ1–42 (15 μM) + high K^+ exhibited markedly impaired LTP compared with slices treated with high K^+ alone (Fig. 6a). CaEDTA, applied to slices after Aβ/high K^+ treatment, rescued this LTP suppression (Fig. 6a), consistent with the reversal of Zn^{2+}-induced Aβ aggregates (Figs. 3a, 4, 5, S5A). CaEDTA alone, applied after high K^+ treatment, slightly inhibited LTP (Fig. 6a), which could reflect Zn^{2+} flux needed for optimal LTP [54, 55].

We tested for the toxicity of Zn^{2+}-induced Aβ1–42 aggregates by adding Aβ ± Zn^{2+} (both 15 μM) to acute hippocampal slices that had not been exposed to high K^+. MTT assay of the slices indicated that, after 3-h treatment, Zn^{2+} or Aβ alone did not inhibit viability, but when added together Aβ1–42 + Zn^{2+} was toxic (Fig. 6b; $p < 0.001$). There was no loss of viability following a 1 h incubation. To determine whether the toxicity of Aβ could be induced by endogenous Zn^{2+}, we performed MTT viability assays on hippocampal slices that were treated as in the LTP studies (Fig. 6a) with Aβ1–42 (15 μM) for 10 min followed by adding high K^+ (or high Na^+, 50 mM, to control for changed osmolarity) for 5 min, then washed twice, and incubated ±CaEDTA (0.1 mM) for 3 h in carboxygenated ACSF. Indeed, Aβ-induced toxicity only occurred with high K^+, where the slices release Zn^{2+} (Fig. 6c; $p < 0.001$). The toxicity was abolished by CaEDTA added after the high K^+ treatment (Fig. 6c), consistent with the disaggregation of Zn^{2+}-induced Aβ aggregates (Figs. 3a, 4, 5, S5A). $Aβ_{Δ2His}$ was not toxic with high K^+ (Fig. 6c), consistent with its inability to form Zn^{2+}-induced aggregates (Figs. 3a and S5A). The responses of old (65 weeks old) and young (10 weeks old) male hippocampi were compared. The viability of the older tissue was significantly more impaired after high K^+ exposure (Fig. 6c; $p < 0.05$), consistent with the higher extracellular Zn^{2+} levels achieved by older

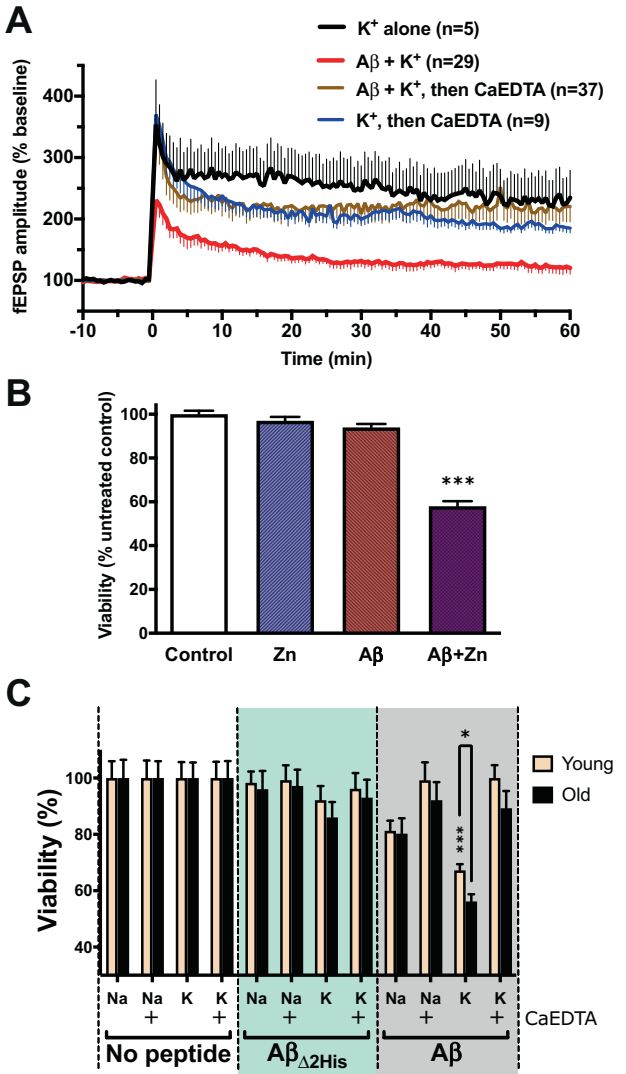

Fig. 6 Effects of Zn^{2+}-Aβ complexes on acute hippocampal slice electrophysiology and viability. Data are means ± SEM. **a** Aβ suppression of LTP on depolarized tissue is rescued by Zn^{2+}-chelation. Slices (10 weeks old male) were treated with Aβ1–42 (15 μM, 10 min), followed by depolarization with KCl (50 mM, 5 min), washed twice, and then incubated ±CaEDTA (0.1 mM) for 1 h. Slices then underwent TBS (at time 0). LTP was impaired by Aβ + K^+, which was rescued by CaEDTA. fEPSP slope analysis and representative fEPSPs are in Fig. S6. **b** Zn^{2+}-Aβ complexes inhibit slice viability. Slices (10 weeks old male) were treated ±Aβ1–42, Zn^{2+} or both (each 15 μM) for 3 h, and then assayed for mitochondrial MTT reductase activity. ***$p <$ 0.001, ANOVA post hoc Bonferroni, $n = 10$ slices. **c** Hippocampal depolarization induces Aβ toxicity that is rescued by Zn^{2+}-chelation. Male slices ($n = 10$) were treated with Aβ or $Aβ_{Δ2His}$ (15 μM) for 10 min, followed by KCl (50 mM) or NaCl (50 mM) for 5 min The slices were then washed twice and incubated for 3 h ±CaEDTA (0.1 mM). Mitochondrial MTT reductase activity was then assayed. ***$p <$ 0.001, ANOVA post hoc Bonferroni; Aβ inhibited viability only with depolarized tissue (*$p < 0.05$, tissue from 65 weeks old rats was more affected, $n = 30$ slices for this comparison), which was rescued by Zn^{2+}-chelation.

hippocampi upon high K^+ exposure (Fig. 1b), leading to greater Aβ aggregation (Fig. 3b).

Discussion

A host of genetic, biochemical and other evidence implicates Aβ or its precursor in the pathogenesis of AD. Yet, a large succession of phase 3 clinical trials targeting cortical amyloid pathology have failed to demonstrate clinical benefit despite lowering the burden of fibrillar amyloid (reviewed [56]). One school of thought to explain this is that because Aβ aggregates in the brain are highly polymorphic [21], neurodegenerative toxicity might be mediated by a minor oligomeric species that has not yet been successfully engaged by the various broad spectrum interventions tested in phase 3 so far. Our current findings propose one such Aβ oligomer that forms under conditions that are exaggerated by age and female sex, conforming to the natural neuropathology of AD.

We showed that Aβ1–42 could be rapidly aggregated into bis-ANS reactive species by endogenous hippocampal Zn^{2+} (Fig. 3a), and that LTP and hippocampal viability is inhibited as a consequence (Fig. 6). This is consistent with a recent report [22], but at variance with previous findings that Zn^{2+} inhibited the toxicity of Aβ in cell culture [57]. It is likely that the soluble oligomeric species detected by bis-ANS is relatively short-lived, formed in minutes and toxic within hours, as we have observed. After days, the bis-ANS positive Zn^{2+}-induced soluble Aβ oligomers organize into fibrils [22], which lose toxicity. This may explain why the burden of amyloid neuropathology in AD, while markedly enriched with Zn^{2+} [8, 9, 18, 58, 59], corresponds poorly to cognitive loss [60].

The mechanism of toxicity of bis-ANS positive Zn^{2+}-Aβ oligomers remains uncertain. Soluble Aβ oligomers have been described to be toxic [21, 61], although these are formed by an alternative assembly mechanism and are not readily detected by bis-ANS fluorescence [22]. The mechanism of LTP inhibition that we observed (Fig. 6a) could be due to toxicity from the bis-ANS positive oligomers induced by Zn^{2+} (Fig. 6b, c), or it is possible that Aβ is attracted into glutamatergic synapses by the high local flux of Zn^{2+} and then traps Zn^{2+}, preventing it from facilitating LTP [54, 55]. Indeed, soluble Aβ oligomers have been reported to attach to the NMDA receptor in hippocampal slices, causing Zn^{2+}-dependent synaptotoxicity [49].

There are caveats with the translatability of the slice system that we have studied. Notably, the Aβ peptide concentrations were deliberately supraphysiological to permit bis-ANS detection, which was used for dynamic studies of peptide oligomerization that would have been cumbersome by immunoassays. This way the peptide acted as an indicator of the extracellular Zn^{2+} being released by the tissue. By implication, the aggregation of Aβ could occur at much lower peptide concentrations in response to the same Zn^{2+} dynamics, but this remains to be confirmed. Similarly,

the toxicity of Aβ that was promoted by Zn^{2+} involved supraphysiological peptide concentrations, and we could not evince this effect at lower peptide concentrations under the conditions and time-intervals we studied. Again, this may mean that toxicity promoted by Zn^{2+} at the lower Aβ concentrations of the living brain might be less aggressive than in our experimental system. Nonetheless, as previously observed [49], Aβ-Zn^{2+} complexes at lower concentrations may irritate the synapse and lie upstream in the chain of events that leads to neurodegeneration in AD. Even so, bis-ANS may be detecting only a small fraction of the total added peptide [22]. The hippocampus is not greatly affected by amyloid plaque pathology in AD but its function may be impaired by forms of soluble oligomeric Aβ such as the Aβ-Zn^{2+} complexes studied here, as well as forms such as ADDLs that are not detected by bis-ANS [22]. The respective contribution of these soluble Aβ species to neurodegeneration in AD is uncertain, but recent data indicate that the Aβ-Zn^{2+} oligomers detected by bis-ANS are more cytotoxic than ADDLs [22]. Despite the caveats, our findings indicate that age and sex are the major risks for Aβ accumulation in the natural history of AD potentially because of their impacts on extracellular Zn^{2+} regulation in the brain.

We propose a model that, as a consequence of energy failure with aging, the tissue does not efficiently reassimilate Zn^{2+} released during neurotransmission (Fig. 2), which leads to increased average extracellular Zn^{2+} promoting Aβ aggregation (Fig. 7). Aβ is also released by synaptic activity [62]. Both the Aβ and the Zn^{2+} are trapped into aggregates that initially form close to the synapse and contribute to synaptic dysfunction [6]. Failure of Zn^{2+} to enter the cytoplasm suppresses the expression of ZnT3, which may, in turn play an indirect role in the uptake of extracellular Zn^{2+} [63] (Fig. 7). The reuptake mechanisms employed to reassimilate synaptically-released Zn^{2+} remain to be elaborated. There are 24 zinc transporter proteins specialized to traffic Zn^{2+} into or out of the cytoplasm and into specific compartments (e.g., ZnT3 into glutamatergic synaptic vesicles) or out of the cell [64]. Additional ports of uptake into the cell include the Divalent Metal Transporter 1, AMPA/kainate and NMDA receptors [38, 39, 65], and presenilin expression promotes cellular uptake [66]. Our data confirm [67] that the NMDA receptor can mediate some Zn^{2+} uptake (Fig. 2b), but the NMDA receptor is not known to be a significant route for Zn^{2+} entry. However, Zn^{2+} binds to and inhibits the activity of the NMDA receptor [68–70], and so we hypothesize that the Zn^{2+} intake that was blocked by memantine and MK-801 (Fig. 2b) might reflect internalization through recycling of the NMDA receptor [71]. This could be consistent with the report of Zn^{2+} promoting attachment of Aβ to the NMDA receptor [49]. Nonetheless, the Zn^{2+} uptake mechanism that might attract Aβ attachment remains to be confirmed, and how female sex in old age (Fig. 2c) or mitochondrial uncoupling (Fig. 2d) act to impair this requires further study.

In one possible model, we conjecture that extracellular exchangeable Zn^{2+} levels increase with age in female rodent hippocampi because, as has been reported, estrogen loss induces an increase in ZnT3 protein levels in mice [72] (Fig. 7). Although we did not measure ZnT3 directly, an elevation relative to males might explain why hippocampal tissue from old female rats releases more Zn^{2+} upon synaptic activation, so inducing increased Aβ aggregation (Figs. 1b, 3b). Indeed, ZnT3 genetic ablation attenuates brain amyloid deposition in both sexes of APP transgenic mouse, but abolishes the differential amyloid increase in the females [4].

The importance of ZnT3 to cognitive resilience has recently been underscored by unbiased large-scale proteomic analysis of post-mortem brain from two tissue banks, which identified hub proteins associated with antecedent cognitive preservation in late life. In that study, higher levels of ZnT3 were associated with slower cognitive decline even when adjusted for AD pathology [73]. Consistent with ZnT3 influencing cortical function independent of its role in amyloid pathology, ZnT3 knockout mice (lacking amyloid neuropathology) express memory impairment in later life [34] that is corrected by the Zn^{2+}-ionophoric effects of clioquinol [74]. Indeed, lower cortical ZnT3 levels observed in Lewy Body and Parkinson's Disease dementia tissue [33] are associated with more severe neuropsychiatric symptomatology [75, 76]. Thus, the decrease in cortical ZnT3 expression observed in AD tissue [34, 77] might itself contribute to cognitive dysfunction in AD outside of its effects on amyloid oligomerization. Therefore, we hypothesize that amyloid accumulation could be a pathological marker for functional ZnT3 fatigue in species that express the human sequence. In this model, amyloid plaques are absent in aged rodents because their Aβ sequence contains substitutions, similar to the inert Δ2His Aβ variant we studied (Figs. 3a, 6c), which abolish Zn^{2+}-induced oligomerization [7].

More work will be needed to elaborate the mechanism by which ZnT3 expression influences extracellular Zn^{2+} reuptake and its presumed trafficking through the cytoplasm towards synaptic vesicles. Our current findings show that the interplay of aging and sex on this machinery may reveal insights into the influence of these risk factors on amyloid pathology in AD. Our model of slow Zn^{2+} reuptake at the synapse (Fig. 7) also supports facilitation of Zn^{2+} reuptake as the potential therapeutic mechanism of ionophores like PBT2, which rapidly reversed cognitive loss not only in AD mouse models [15, 78], but also corrected cognitive deficits in normal aged mice without amyloid pathology [79].

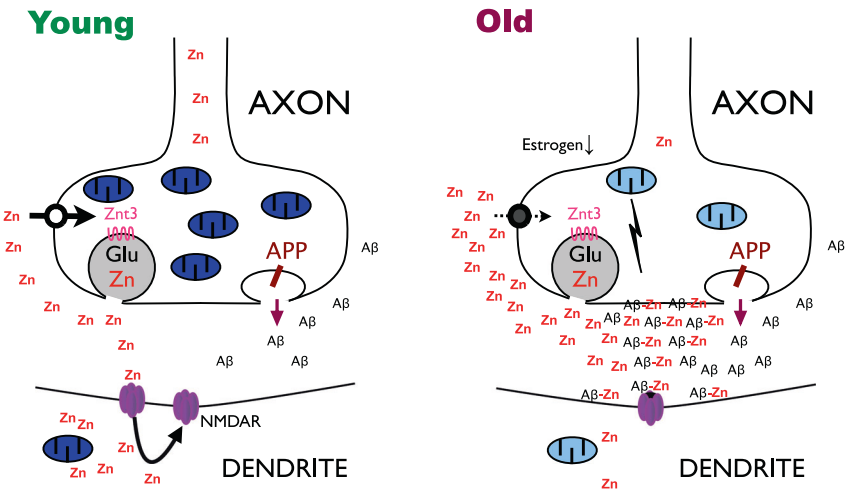

Fig. 7 Model for synaptic Zn^{2+} release in the pathogenesis of AD. Zn^{2+} is released upon synaptic activity and is normally rapidly taken up by energy-dependent mechanisms. With age, mitochondrial energy is decreased, leading to more sluggish reuptake of extracellular Zn^{2+}. This allows Zn^{2+} to react with Aβ, which is also released upon neurotransmission. The illustration shows a notional synapse, but the Zn^{2+} may migrate to other hippocampal vicinities and form Aβ-Zn^{2+} complexes that adhere to targets (e.g., NMDA receptor) at a distance from where the Zn^{2+} is released. Each unit of Aβ may trap three equivalents of Zn^{2+} with abnormally increased affinity caused by precipitation, which creates a perturbed equilibrium [82]. This will prevent Zn^{2+} reuptake, which can lead to metabolic impairments.

Notably, PBT2 induced cognitive benefit within 12 weeks in a phase 2 clinical trial in AD patients [16, 80], although it had marginal benefits on amyloid accumulation [81]. This class of therapeutic approach could yet warrant further investigation.

Author contributions ZD and AIB designed the experimental approach, analyzed and interpreted the data, generated the figures, funded the studies, and wrote the manuscript. ZD performed the major experiments, with experimental contributions from the other authors. All authors edited the manuscript.

Funding This project was funded by grants from The National Health and Medical Research Council (GNT1103703, GNT1101533). The Florey Institute of Neuroscience and Mental Health acknowledges the strong support from the Victorian Government and in particular the funding from the Operational Infrastructure Support Grant.

Compliance with ethical standards

Conflict of interest AIB is a shareholder in Alterity Ltd, Cogstate Ltd, Brighton Biotech LLC, Grunbiotics Pty Ltd, Eucalyptus Pty Ltd, and Mesoblast Ltd. He is a paid consultant for, and has a profit share interest in Collaborative Medicinal Development Pty Ltd.

Ethical approval All applicable international, national, and/or institutional guidelines for the care and use of animals were followed. All procedures performed in studies involving animals were in accordance with the ethical standards of the institution or practice at which the studies were conducted (The University of Szeged; approval number: I-02442/001/2006).

Publisher's note Springer Nature remains neutral with regard to jurisdictional claims in published maps and institutional affiliations.

References

1. Davies L, Wolska B, Hilbich C, Multhaup G, Martins R, Simms G, et al. A4 amyloid protein deposition and the diagnosis of Alzheimer's disease: prevalence in aged brains determined by immunocytochemistry compared with conventional neuropathologic techniques. Neurology. 1988;38:1688–93.
2. Callahan MJ, Lipinski WJ, Bian F, Durham RA, Pack A, Walker LC. Augmented senile plaque load in aged female beta-amyloid precursor protein-transgenic mice. Am J Pathol. 2001;158:1173–7.
3. Corder EH, Ghebremedhin E, Taylor MG, Thal DR, Ohm TG, Braak H. The biphasic relationship between regional brain senile plaque and neurofibrillary tangle distributions: modification by age, sex, and APOE polymorphism. Ann NY Acad Sci. 2004;1019:24–8.
4. Lee J-Y, Cole TB, Palmiter RD, Suh SW, Koh J-Y. Contribution by synaptic zinc to the gender-disparate plaque formation in human Swedish mutant APP transgenic mice. Proc Natl Acad Sci USA. 2002;99:7705–10.
5. Takeda A, Tamano H, Tempaku M, Sasaki M, Uematsu C, Sato S, et al. Extracellular Zn(2+) is essential for amyloid beta1-42-induced cognitive decline in the normal brain and its rescue. J Neurosci. 2017;37:7253–62.
6. Tamano H, Suzuki H, Kobuchi S, Adlard PA, Bush AI, Takeda A. Difference in ability for extracellular Zn(2+) influx between human and rat amyloid beta1-42 and its significance. Neurotoxicology. 2019;72:1–5.
7. Bush AI, Pettingell WH, Multhaup G, Paradis MD, Vonsattel JP, Gusella JF, et al. Rapid induction of Alzheimer Aß amyloid formation by zinc. Science. 1994;265:1464–7.
8. Lovell MA, Robertson JD, Teesdale WJ, Campbell JL, Markesbery WR. Copper, iron and zinc in Alzheimer's disease senile plaques. J Neurol Sci. 1998;158:47–52.
9. Suh SW, Jensen KB, Jensen MS, Silva DS, Kesslak PJ, Danscher G, et al. Histochemically-reactive zinc in amyloid plaques, angiopathy, and degenerating neurons of Alzheimer's diseased brains. Brain Res. 2000;852:274–8.

10. Stoltenberg M, Bush AI, Bach G, Smidt K, Larsen A, Rungby J, et al. Amyloid plaques arise from zinc-enriched cortical layers in APP/PS1 transgenic mice and are paradoxically enlarged with dietary zinc deficiency. Neuroscience. 2007;150:357–69.
11. Lee J-Y, Mook-Jung I, Koh J-Y. Histochemically reactive zinc in plaques of the Swedish mutant beta-amyloid precursor protein transgenic mice. J Neurosci. 1999;19:RC10. 1-5.
12. Cherny RA, Atwood CS, Xilinas ME, Gray DN, Jones WD, McLean CA, et al. Treatment with a copper-zinc chelator markedly and rapidly inhibits ß-amyloid accumulation in Alzheimer's disease transgenic mice. Neuron. 2001;30:665–76.
13. Cherny RA, Legg JT, McLean CA, Fairlie D, Huang X, Atwood CS, et al. Aqueous dissolution of Alzheimer's disease Aß amyloid deposits by biometal depletion. J Biol Chem. 1999;274:23223–8.
14. Lee JY, Friedman JE, Angel I, Kozak A, Koh JY. The lipophilic metal chelator DP-109 reduces amyloid pathology in brains of human beta-amyloid precursor protein transgenic mice. Neurobiol Aging. 2004;25:1315–21.
15. Adlard PA, Cherny RA, Finkelstein DI, Gautier E, Robb E, Cortes M, et al. Rapid restoration of cognition in Alzheimer's transgenic mice with 8-hydroxy quinoline analogs is associated with decreased interstitial Abeta. Neuron. 2008;59:43–55.
16. Lannfelt L, Blennow K, Zetterberg H, Batsman S, Ames D, Harrison J, et al. Safety, efficacy, and biomarker findings of PBT2 in targeting Abeta as a modifying therapy for Alzheimer's disease: a phase IIa, double-blind, randomised, placebo-controlled trial. Lancet Neurol. 2008;7:779–86.
17. Ritchie CW, Bush AI, Mackinnon A, Macfarlane S, Mastwyk M, MacGregor L, et al. Metal-protein attenuation with iodochlorhydroxyquin (clioquinol) targeting Aß amyloid deposition and toxicity in Alzheimer's disease: a pilot phase 2 clinical trial. Arch Neurol. 2003;60:1685–91.
18. Friedlich AL, Lee JY, van Groen T, Cherny RA, Volitakis I, Cole TB, et al. Neuronal zinc exchange with the blood vessel wall promotes cerebral amyloid angiopathy in an animal model of Alzheimer's disease. J Neurosci. 2004;24:3453–9.
19. Frederickson CJ, Giblin LJ 3rd, Balaji RV, Masalha R, Frederickson CJ, Zeng Y, et al. Synaptic release of zinc from brain slices: factors governing release, imaging, and accurate calculation of concentration. J Neurosci Methods. 2006;154:19–29.
20. Palmiter RD, Findley SD. Cloning and functional characterization of a mammalian zinc transporter that confers resistance to zinc. Embo J. 1995;14:639–49.
21. Gong Y, Chang L, Viola KL, Lacor PN, Lambert MP, Finch CE, et al. Alzheimer's disease-affected brain: presence of oligomeric A beta ligands (ADDLs) suggests a molecular basis for reversible memory loss. Proc Natl Acad Sci USA. 2003;100:10417–22.
22. Lee M-C, Yu W-C, Shih Y-H, Chen C-Y, Guo Z-H, Huang S-J, et al. Zinc ion rapidly induces toxic, off-pathway amyloid-β oligomers distinct from amyloid-β derived diffusible ligands in Alzheimer's disease. Sci Rep. 2018;8:4772.
23. Hunya AG. Physiological factors could enhance amyloid-beta toxicity. PhD thesis, Szeged, Hungary: University of Szeged; 2013.
24. Sohma Y, Hayashi Y, Kimura M, Chiyomori Y, Taniguchi A, Sasaki M, et al. The 'O-acyl isopeptide method' for the synthesis of difficult sequence-containing peptides: application to the synthesis of Alzheimer's disease-related amyloid beta peptide (Abeta) 1–42. J Pept Sci. 2005;11:441–51.
25. Coin I, Dolling R, Krause E, Bienert M, Beyermann M, Sferdean CD, et al. Depsipeptide methodology for solid-phase peptide synthesis: circumventing side reactions and development of an automated technique via depsidipeptide units. J Org Chem. 2006;71:6171–7.
26. Datki ZL, Hunya A, Penke B. A novel and simple fluorescence method for the measurement of presynaptic vesicular zinc release in acute hippocampal slices with a fluorescence plate reader. Brain Res Bull. 2007;74:183–7.
27. Lipton P, Aitken PG, Dudek FE, Eskessen K, Espanol MT, Ferchmin PA, et al. Making the best of brain slices: comparing preparative methods. J Neurosci Methods. 1995;59:151–6.
28. Mozes E, Hunya A, Posa A, Penke B, Datki Z. A novel method for the rapid determination of beta-amyloid toxicity on acute hippocampal slices using MTT and LDH assays. Brain Res Bull. 2012;87:521–5.
29. Mozes E, Hunya A, Toth A, Ayaydin F, Penke B, Datki ZL. A novel application of the fluorescent dye bis-ANS for labeling neurons in acute brain slices. Brain Res Bull. 2011;86:217–21.
30. Koh J-H, Suh SW, Gwag BJ, He YY, Hsu CY, Choi DW. The role of zinc in selective neuronal death after transient global cerebral ischemia. Science. 1996;272:1013–6.
31. Calderone A, Jover T, Mashiko T, Noh KM, Tanaka H, Bennett MV, et al. Late calcium EDTA rescues hippocampal CA1 neurons from global ischemia-induced death. J Neurosci. 2004;24:9903–13.
32. Schlief ML, Craig AM, Gitlin JD. NMDA receptor activation mediates copper homeostasis in hippocampal neurons. J Neurosci. 2005;25:239–46.
33. Whitfield DR, Vallortigara J, Alghamdi A, Howlett D, Hortobágyi T, Johnson M, et al. Assessment of ZnT3 and PSD95 protein levels in Lewy body dementias and Alzheimer's disease: association with cognitive impairment. Neurobiol Aging. 2014;35:2836–44.
34. Adlard PA, Parncutt JM, Finkelstein DI, Bush AI. Cognitive loss in zinc transporter-3 knock-out mice: a phenocopy for the synaptic and memory deficits of Alzheimer's disease? J Neurosci. 2010;30:1631–6.
35. Lee JY, Kim JS, Byun HR, Palmiter RD, Koh JY. Dependence of the histofluorescently reactive zinc pool on zinc transporter-3 in the normal brain. Brain Res. 2011;1418:12–22.
36. Choi DW, Yokoyama M, Koh J. Zinc neurotoxicity in cortical cell culture. Neuroscience. 1988;24:67–79.
37. Howell GA, Welch MG, Frederickson CJ. Stimulation-induced uptake and release of zinc in hippocampal slices. Nature. 1984;308:736–8.
38. Frederickson CJ, Koh JY, Bush AI. The neurobiology of zinc in health and disease. Nat Rev Neurosci. 2005;6:449–62.
39. Sensi SL, Paoletti P, Bush AI, Sekler I. Zinc in the physiology and pathology of the CNS. Nat Rev Neurosci. 2009;10:780–91.
40. Colvin RA, Bush AI, Volitakis I, Fontaine CP, Thomas D, Kikuchi K, et al. Insights into Zn2+ homeostasis in neurons from experimental and modeling studies. Am J Physiol Cell Physiol. 2008;294:C726–742.
41. Mattson MP, Zhang Y, Bose S. Growth factors prevent mitochondrial dysfunction, loss of calcium homeostasis, and cell injury, but not ATP depletion in hippocampal neurons deprived of glucose. Exp Neurol. 1993;121:1–13.
42. Lejri I, Grimm A, Eckert A. Mitochondria, estrogen and female brain aging. Front Aging Neurosci. 2018;10:124.
43. Takeda A, Nakamura M, Fujii H, Uematsu C, Minamino T, Adlard PA, et al. Amyloid β-mediated Zn2+ influx into dentate granule cells transiently induces a short-term cognitive deficit. PLoS One. 2014;9:e115923.
44. Grabrucker AM, Schmeisser MJ, Udvardi PT, Arons M, Schoen M, Woodling NS, et al. Amyloid beta protein-induced zinc sequestration leads to synaptic loss via dysregulation of the ProSAP2/Shank3 scaffold. Mol Neurodegener. 2011;6:65.
45. LeVine H 3rd. 4,4(′)-dianilino-1,1(′)-binaphthyl-5,5(′)-disulfonate: report on non-beta-sheet conformers of Alzheimer's peptide beta (1-40). Arch Biochem Biophys. 2002;404:106–15.
46. Ferrao-Gonzales AD, Robbs BK, Moreau VH, Ferreira A, Juliano L, Valente AP, et al. Controlling {beta}-amyloid oligomerization

by the use of naphthalene sulfonates: trapping low molecular weight oligomeric species. J Biol Chem. 2005;280:34747–54.
47. Liu ST, Howlett G, Barrow CJ. Histidine-13 is a crucial residue in the zinc ion-induced aggregation of the Aß peptide of Alzheimer's disease. Biochemistry. 1999;38:9373–8.
48. Atwood CS, Moir RD, Huang X, Bacarra NME, Scarpa RC, Romano DM, et al. Dramatic aggregation of Alzheimer Aß by Cu (II) is induced by conditions representing physiological acidosis. J Biol Chem. 1998;273:12817–26.
49. Deshpande A, Kawai H, Metherate R, Glabe CG, Busciglio J. A role for synaptic zinc in activity-dependent Abeta oligomer formation and accumulation at excitatory synapses. J Neurosci. 2009;29:4004–15.
50. Geddes JW, Chang-Chui H, Cooper SM, Lott IT, Cotman CW. Density and distribution of NMDA receptors in the human hippocampus in Alzheimer's disease. Brain Res. 1986;399:156–61.
51. Dietz RM, Weiss JH, Shuttleworth CW. Zn2+ influx is critical for some forms of spreading depression in brain slices. J Neurosci. 2008;28:8014–24.
52. Anderson CT, Radford RJ, Zastrow ML, Zhang DY, Apfel U-P, Lippard SJ, et al. Modulation of extrasynaptic NMDA receptors by synaptic and tonic zinc. Proc Natl Acad Sci USA; 2015: 201503348.
53. Lee J-Y, Cho E, Seo J-W, Hwang JJ, Koh J-Y. Alteration of the cerebral zinc pool in a mouse model of Alzheimer disease. J Neuropathol Exp Neurol. 2012;71:211–22.
54. Lu YM, Taverna FA, Tu R, Ackerley CA, Wang YT, Roder J. Endogenous Zn(2+) is required for the induction of long-term potentiation at rat hippocampal mossy fiber-CA3 synapses. Synapse. 2000;38:187–97.
55. Li Y, Hough CJ, Frederickson CJ, Sarvey JM. Induction of mossy fiber –>Ca3 long-term potentiation requires translocation of synaptically released Zn2+. J Neurosci. 2001;21:8015–25.
56. Nikseresht S, Bush AI, Ayton S. Treating Alzheimer's disease by targeting iron. Br J Pharm. 2019;176:3622–35.
57. Cuajungco MP, Goldstein LE, Nunomura A, Smith MA, Lim JT, Atwood CS, et al. Evidence that the beta-amyloid plaques of Alzheimer's disease represent the redox-silencing and entombment of Aß by zinc. J Biol Chem. 2000;275:19439–42.
58. Stoltenberg M, Bruhn M, Sondergaard C, Doering P, West MJ, Larsen A, et al. Immersion autometallographic tracing of zinc ions in Alzheimer beta-amyloid plaques. Histochem Cell Biol. 2005;123:605–11.
59. Schmued L, Raymick J, Sarkar S. High contrast and resolution labeling of amyloid plaques in tissue sections from APP-PS1 mice and humans with alzheimer's disease with the zinc chelator HQ-O: practical and theoretical considerations. Curr Alzheimer Res. 2019;16:577–86.
60. Ayton S, Wang Y, Diouf I, Schneider JA, Brockman J, Morris MC, et al. Brain iron is associated with accelerated cognitive decline in people with Alzheimer pathology. Mol Psychiatry. 2019;45:358–67.
61. Kayed R, Head E, Thompson JL, McIntire TM, Milton SC, Cotman CW. et al.Common structure of soluble amyloid oligomers implies common mechanism of pathogenesis. Science. 2003;300:486–9.
62. Cirrito JR, May PC, O'Dell MA, Taylor JW, Parsadanian M, Cramer JW, et al. In vivo assessment of brain interstitial fluid with microdialysis reveals plaque-associated changes in amyloid-beta metabolism and half-life. J Neurosci. 2003;23:8844–53.
63. Sanford L, Carpenter MC, Palmer AE. Intracellular Zn(2+) transients modulate global gene expression in dissociated rat hippocampal neurons. Sci Rep. 2019;9:9411.
64. Kambe T, Suzuki E, Komori T. Zinc transporter proteins: a review and a new view from biochemistry. Zinc Signaling. Fukada T, Kambe T. (eds.) Springer Nature Singapore Pte Ltd., 2019.
65. Xu Y, Xiao G, Liu L, Lang M. Zinc transporters in Alzheimer's disease. Mol Brain. 2019;12:106.
66. Greenough MA, Volitakis I, Li Q-X, Laughton K, Evin G, Ho M, et al. Presenilins promote the cellular uptake of copper and zinc and maintain copper chaperone of SOD1-dependent copper/zinc superoxide dismutase activity. J Biol Chem. 2011;286:9776–86.
67. Colvin RA, Davis N, Nipper RW, Carter PA. Zinc transport in the brain: routes of zinc influx and efflux in neurons. J Nutr. 2000;130 (5S Suppl):1484S–7S.
68. Westbrook GL, Mayer ML. Micromolar concentrations of Zn2+ antagonize NMDA and GABA responses of hippocampal neurons. Nature. 1987;328:640–3.
69. Mayer ML, Vyklicky L Jr. The action of zinc on synaptic transmission and neuronal excitability in cultures of mouse hippocampus. J Physiol. 1989;415:351–65.
70. Jalali-Yazdi F, Chowdhury S, Yoshioka C, Gouaux E. Mechanisms for zinc and proton inhibition of the GluN1/GluN2A NMDA receptor. Cell. 2018;175:1520–32. e1515.
71. Ferreira JS, Papouin T, Ladepeche L, Yao A, Langlais VC, Bouchet D, et al. Co-agonists differentially tune GluN2B-NMDA receptor trafficking at hippocampal synapses. Elife. 2017;6:e25492.
72. Lee J-Y, Kim J-H, Hong SH, Lee JY, Cherny RA, Bush AI, et al. Estrogen decreases zinc transporter 3 expression and synaptic vesicle zinc levels in mouse brain. J Biol Chem. 2004;279:8602–7.
73. Wingo AP, Dammer EB, Breen MS, Logsdon BA, Duong DM, Troncosco JC, et al. Large-scale proteomic analysis of human brain identifies proteins associated with cognitive trajectory in advanced age. Nat Commun. 2019;10:1619.
74. Adlard PA, Parncutt J, Lal V, James S, Hare D, Doble P, et al. Metal chaperones prevent zinc-mediated cognitive decline. Neurobiol Dis. 2015;81:196–202.
75. Whitfield DR, Vallortigara J, Alghamdi A, Hortobágyi T, Ballard C, Thomas AJ, et al. Depression and synaptic zinc regulation in Alzheimer disease, dementia with lewy bodies, and Parkinson disease dementia. Am J Geriatr Psychiatry. 2014;23:141–8.
76. Whitfield DR, Francis PT, Ballard C, Williams G. Associations between ZnT3, tau pathology, agitation, and delusions in dementia. Int J Geriatr Psychiatry. 2018;33:1146–52.
77. Beyer N, Coulson DT, Heggarty S, Ravid R, Irvine GB, Hellemans J, et al. ZnT3 mRNA levels are reduced in Alzheimer's disease post-mortem brain. Mol Neurodegener. 2009;4:53.
78. Sedjahtera A, Gunawan L, Bray L, Hung LW, Parsons J, Okamura N, et al. Targeting metals rescues the phenotype in an animal model of tauopathy. Metallomics. 2018;10:1339–47.
79. Adlard PA, Sedjahtera A, Gunawan L, Bray L, Hare D, Lear J, et al. A novel approach to rapidly prevent age-related cognitive decline. Aging Cell. 2014;13:351–9.
80. Faux NG, Ritchie CW, Gunn A, Rembach A, Tsatsanis A, Bedo J, et al. PBT2 rapidly improves cognition in Alzheimer's disease: additional phase II analyses. J Alzheimers Dis. 2010;20:509–16.
81. Villemagne VL, Rowe CC, Barnham KJ, Cherny R, Woodward M, Bozinosvski S, et al. A randomized, exploratory molecular imaging study targeting amyloid beta with a novel 8-OH quinoline in Alzheimer's disease: the PBT2-204 IMAGINE study. Alzheimers Dement. 2017;3:622–35.
82. Atwood CS, Scarpa RC, Huang X, Moir RD, Jones WD, Fairlie DP, et al. Characterization of copper interactions with alzheimer amyloid beta peptides: identification of an attomolar-affinity copper binding site on amyloid beta1-42. J Neurochem. 2000;75:1219–33.

Brain Research Bulletin 87 (2012) 521–525

Contents lists available at SciVerse ScienceDirect

Brain Research Bulletin

journal homepage: www.elsevier.com/locate/brainresbull

Research report

A novel method for the rapid determination of beta-amyloid toxicity on acute hippocampal slices using MTT and LDH assays

Emese Mozes[a,*], Akos Hunya[a,1], Aniko Posa[b,2], Botond Penke[a,3], Zsolt Datki[a,4]

[a] Department of Medical Chemistry, University of Szeged, Szeged, Hungary
[b] Department of Anatomy, Physiology and Neuroscience, University of Szeged, Hungary

ARTICLE INFO

Article history:
Received 9 November 2011
Received in revised form 6 February 2012
Accepted 7 February 2012
Available online 25 February 2012

Keywords:
Amyloid-beta
Hippocampus
Brain slice
MTT
LDH

ABSTRACT

It is difficult task to measure precisely the toxic effect of beta-amyloid (Aβ 1–42) peptides and also the protective effect of novel drug candidates against Aβ-peptides. The widely used MTT-assay in cell lines or primary cell cultures could be insensitive against Aβ-peptides.

We describe here an easy and relevant method for testing Aβ 1–42 toxicity on acute hippocampal slices derived from rat. Brain slice viability in different conditions was measured using MTT and LDH assays. The concomitant use of these two assays can give detailed and relevant results on the toxic effect of Aβ 1–42 in oxygen–glucose deprived (OGD) acute brain slice model. Both assays are capable of quantifying tissue viability by measuring optical density (OD). We found that simultaneous application of OGD and Aβ 1–42 treatment induced a more intensive decrease in hippocampal slice viability than their separate effects.

The use of MTT and LDH assay for quantifying brain slice viability proved to be an easy *ex vivo* method for investigating Aβ toxicity. Testing brain slices is more relevant in Alzheimer's Disease research than using *in vitro* cell cultures, due to maintenance of the three dimensional cellular network, the cell variability and intact cell connections.

1. Introduction

Beta-amyloid (Aβ) toxicity may be crucial in Alzheimer's disease (AD) pathology [6]. Measuring the toxic effect of different Aβ aggregation species as well as the neuroprotective effect of novel drug candidates requires a reliable and relevant assay. Till now (beside other methods, e.g. electrophysiology) MTT (3-(4,5-dimethylthiazol-2-yl)-2,5-diphenyltetrazolium bromide, a yellow tetrazole) assay has been the most commonly used method for measuring Aβ toxicity.

MTT assay has been used in studying the toxicity of β-amyloid peptides on various cell types such as SH-SY5Y neuroblastoma cells [3] and primary rat neuronal cells [17,15]. Murine embryonic stem cells and hematopoietic progenitor cells in culture have also been exposed to Aβ 1–42 oligomers [14] and then cell viability changes were measured with MTT test.

Although the MTT assay (performed on cell lines or primary cell cultures) proved to be suitable for measurements of Aβ toxicity, these *in vitro* methods have some disadvantages. We found that SH-SY5Y cells can be insensitive against Aβ peptides. The use of primary neuronal cultures is complicated, expensive and often not physiologically relevant. The most physiological MTT assay would use brain tissue slices where neuronal connections and glial environment remain at least partly intact.

MTT assay has already been used for toxicity measurement of Cd^{2+} [16] and H_2O_2 [5] on acute hippocampal slices. The neurotoxic effects of mercurials were also measured quantitatively with MTT assay in cerebral cortex slices [13]. Brain slice MTT assay has never been used till now for measuring Aβ toxicity to our knowledge.

Our goal was to develop a rapid and reliable assay for Aβ toxicity measurement using brain slices. We chose rat hippocampal slices to develop the Aβ toxicity assay. We need to mention that acute hippocampal slices contain very different cell types (neuronal, glial and endothelial cells), however, all of these cells are sensitive against Aβ toxicity [11,9].

The hippocampus plays a central role in the progression of AD, and hippocampal atrophy is considered to be the most predictive

Abbreviations: ACSF, artificial cerebrospinal fluid; AD, Alzheimer's disease; Aβ, amyloid-beta; HEPES, 4-(2-hydroxyethyl)-1-piperazineethanesulfonic acid; LDH, Lactate dehydrogenase; MTT, 3-(4,5-dimethylthiazol-2-yl)-2,5-diphenyltetrazolium bromide; OD, optical density; OGD, oxygen–glucose deprivation.

* Corresponding author. Tel.: +36 62 546853; fax: +36 62 546 826.
E-mail addresses: mese859@gmail.com (E. Mozes), hunya@dnt.u-szeged.hu (A. Hunya), paniko@bio.u-szeged.hu (A. Posa), pbotond@mdche.szote.u-szeged.hu (B. Penke), datkiz@yahoo.com (Z. Datki).
[1] Tel.: +36 62 546853.
[2] Tel.: +36 20 2698721.
[3] Tel.: +36 62 545135.
[4] Tel.: +36 62 546788.

0361-9230/$ – see front matter © 2012 Elsevier Inc. All rights reserved.
doi:10.1016/j.brainresbull.2012.02.005

structural brain biomarker for AD [8]. It is easy to prepare rat hippocampal slices for toxicity studies [16]. Cerebral hypoperfusion (an early event in AD) increases the risk of AD [10] and has also been shown to be associated with amyloid accumulation [7]. Thus application of a short and mild oxygen–glucose deprivation (OGD) to the medium of hippocampal slices may simulate the early events seen in AD. Mielke et al. [12] and Cechetti et al. [2] already studied the response of different brain slice systems (acutely prepared and cultured) to OGD by MTT as well as LDH assay. Ischemic-like conditions significantly decreased synaptic and mitochondrial activity within acutely prepared slices. Measuring Aβ toxicity on acute hippocampal slices could be a relevant model and an easy *ex vivo* method for quantitive analysis of tissue viability. LDH assay can be also used to quantify effects of OGD [18]. LDH released to the supernatant medium suggests an increase of tissue and membrane damage.

We describe here an easy and relevant method for testing Aβ 1–42 toxicity on acute rat hippocampal slices, using the MTT and LDH assay. The concomitant application of OGD pretreatment followed by Aβ treatment of hippocampal slices provides a relevant *ex vivo* model of the aging brain.

2. Materials and methods

2.1. Materials

Aβ 1–42 was synthesized in our laboratory [1]. Stock solution of oligomeric Aβ 1–42 (stock solution: 0.4 mM) was freshly prepared in distilled water (pH ≥ 5.0) and stored for maximum 10 min.

NaCl (cat. No. S9888), KCl (cat. No. P3911), $CaCl_2$ (cat. No. C8106), $MgCl_2$ (cat. No. M0250), HEPES (cat. No. H4034), $NaHCO_3$ (cat. No. 401676), D-glucose (cat. No. G7528), MTT (cat. No. M5655) and 96-well plates (Costar, cat. No. CLS3695) were obtained from Sigma–Aldrich, Hungary. The mini-chamber system (Fig. 1.) was obtained from our institute [4]. The animal protocols applied in this study were approved by the National Institute of Health, and by the University of Szeged; permission number: I-02442/001/2006.

The following HEPES-containing ACSF solutions were used in the experiments (concentrations are given in mM):

H-ACSF/1: NaCl 122, KCl 3, $CaCl_2$ 0.3, $MgCl_2$ 3.7, $NaHCO_3$ 25, HEPES 5, D-glucose 10, pH 7.4.
H-ACSF/2: NaCl 132, KCl 3, $CaCl_2$ 2, $MgCl_2$ 2, $NaHCO_3$ 25, HEPES 5, pH 7.4.
H-ACSF/3: NaCl 120, KCl 3, $CaCl_2$ 2, $MgCl_2$ 2, $NaHCO_3$ 25, HEPES 5, D-glucose 12, pH 7.4 (with normal calcium, magnesium and glucose levels).

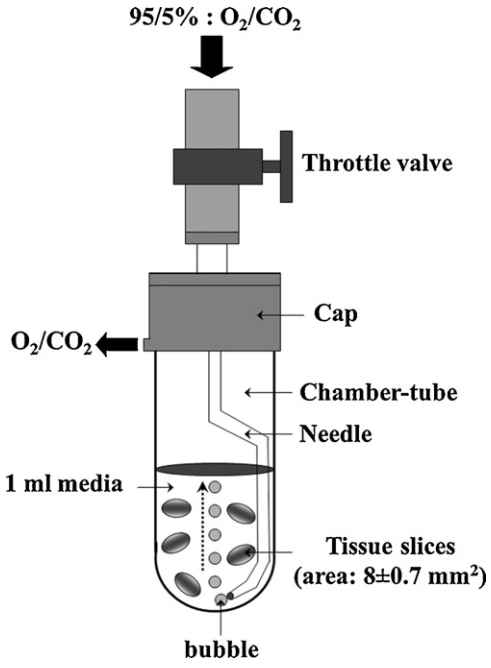

Fig. 1. Schematic structure of *ExViS* mini tube chamber.

2.2. Preparation and treatment of acute hippocampal slices

A slightly modified version of the method reported by Datki et al. [4] was used in our slice viability experiments. After anesthesia with chloral hydrate (0.4 g/kg), 10 ± 1-week-old male Wistar rats were decapitated and the whole heads (without scalp-leather) were put in ice cold distilled water for 1 min. The brains were quickly removed and immersed in H-ACSF/1 preparation solution containing HEPES with very low Ca^{2+} and with elevated Mg^{2+} at 4 °C [4]. Brain slices (thickness: 400 μm) were prepared from the hippocampus with a McIlwain tissue chopper at 4 °C.

2.3. Treatment of hippocampal slices

Freshly prepared slices in ice cold H-ACSF/1 solution were photographed to measure the slice area. Slices (with an area of approximately 9 mm^2) were quickly transferred into a mini-chamber (Fig. 1; maximum 5 slices in 1 ml H-ACSF/1) for conditioning (30 min) in the carboxygenated (95/5%: O_2/CO_2) preparation solution at room temperature (24 °C).

After 30 min hippocampal slices were transferred from the mini-chamber into a plastic Petri dish and was left to rest at room temperature in glucose- and carboxygen-free H-ACSF/2 (3 ml/Petri dish) for 1 h. "Carboxygen-free" means that the tissue slices in H-ACSF/2 take up the oxygen and the carbon-dioxide only from the atmosphere, since they are removed from the mini-chamber system presented in Fig. 1. (The Petri dish was continuously being stirred at 370 rpm by a modified BIOSAN TS-100 thermo shaker). After 1 h oxygen–glucose deprivation the supernatant (H-ACSF/2) in the Petri dish was changed to H-ACSF/3 solution (3 ml/Petri dish). The slices were quickly transferred into the mini-chambers (maximum 5 slices in 1 ml) and treated with freshly prepared oligomeric Aβ 1–42 peptide by adding 50 μl stock solution of the peptide into 950 μl H-ACSF/3 in each chamber (final concentration of Aβ 1–42: 20 μM). Foaming was inhibited by a floating plastic ball (diameter: 5 mm) applied in the mini tube chambers. Classic apoptotic factors (e.g. NaN_3, H_2O_2, KCN and Thapsigargin) were used as controls in these experiments.

2.4. MTT and LDH measurements

After treating the slices with 20 μM Aβ 1–42 for 4 h, supernatant (to be used in LDH assay) was removed and replaced by fresh H-ASCF/3 (0.9 ml/chamber) to which 0.1 ml MTT stock solution (5 mg/ml H-ACSF/3) was added (MTT final concentration: 0.5 mg/ml). The chamber was left to rest for 15 min without carboxygenation. To stop further reduction of MTT, the medium (H-ACSF/3) was removed. The slices were transferred into 96-well plate, then pure DMSO (100 μl/slice/well) was added for dissolving formazane from the slices. (30 min in a 96-well plate). Then 70 μl DMSO solution from each slice (well) was transferred into another 96-well plate. The optical density (OD) of the dissolved formazane was measured at 550 and 620 nm. The following formula was used for standardizing the data: (OD_{550}–OD_{620})/area of slice (mm^2) = 100% in control (Aβ 1–42 untreated slices).

For LDH measurements the above-mentioned supernatants (H-ACSF/3) from the 4 h Aβ 1–42 treatment of slices were used. Supernatants were centrifuged at 500 × *g* for 10 min and the LDH activity was measured with a standard LDH kit (Sigma, TOX7-1KT). The results were calculated with the following formula: (OD_{450}–OD_{620})/mean area of slices (mm^2) = 100% in control (Aβ 1–42 untreated chamber).

2.5. Statistical analysis

Data are presented as means ± standard error of mean (S.E.M). Student's-*t* test and ANOVA, Bonferroni was used for statistical evaluation using Microsoft Excel and SPSS 10.0 for Windows software. The data (from $n = 40$ slices) were compared with the control measurements of each condition. Differences were considered statistically significant at $p \leq 0.001$ or $p \leq 0.05$.

3. Results and discussion

We solved the problem of survival of hippocampal slices (4–10 slices) in carboxygenated ACSF by using a simple mini-tubing-chamber (*ExViS*, Fig. 1.). Slices can survive several hours under these conditions.

The scheme of steps of our novel and rapid method for measuring toxicity of Aβ peptides is summarized in Fig. 2. This figure illustrates the most important steps of the novel method:

(1) Resting the slices for 30 min in carboxygenated H-ACSF/1 at 24 °C for conditioning.

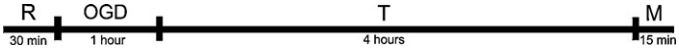

Fig. 2. Schematic illustration of steps of the novel slice viability method.

(2) Mild oxygen–glucose deprivation of the slices (1 h) in H-ACSF/2 solution in Petri dish.
(3) Treatment of the slices in the mini-chamber with oligomeric Aβ 1–42 peptide for 4 h in H-ACSF/3 solution.
(4) Measuring slice viability with MTT and LDH assay.

The concomitant use of these two assays gives a relevant result for the toxic effect of Aβ 1–42. Both MTT and LDH colorimetric assays are adequate for quantifying tissue viability by measuring optical density (OD). In MTT assay the level of the OD is directly proportional with viability, while in LDH it is inversely proportional.

Fig. 3 summarizes the results of the different assays. The results of both MTT and LDH assays show that 1-h resting under mild oxygen–glucose deprivation reduces brain tissue viability (Fig. 3A and B).

Four-hour treatment of slices with oligomeric Aβ 1–42 alone also decreased cell viability (Fig. 3C and D) compared to Aβ untreated control.

Simultaneous treatment of slices with both OGD and oligomeric Aβ 1–42 induced the most intensive decrease in hippocampal slice viability (Fig. 3E and F).

The synergistic effect of OGD with different toxic agents on hippocampal slices was measured (Fig. 4). The toxic agents used (H_2O_2, NaN_3, KCN, Thapsigargin) caused significant decrease in cell viability in both assays, however there were differences between their toxicity. In the MTT assay NaN_3, while in the LDH assay H_2O_2 had the most toxic effect. The possible explanation of the phenomenon is that the LDH assay measures the necrosis (loss of membrane

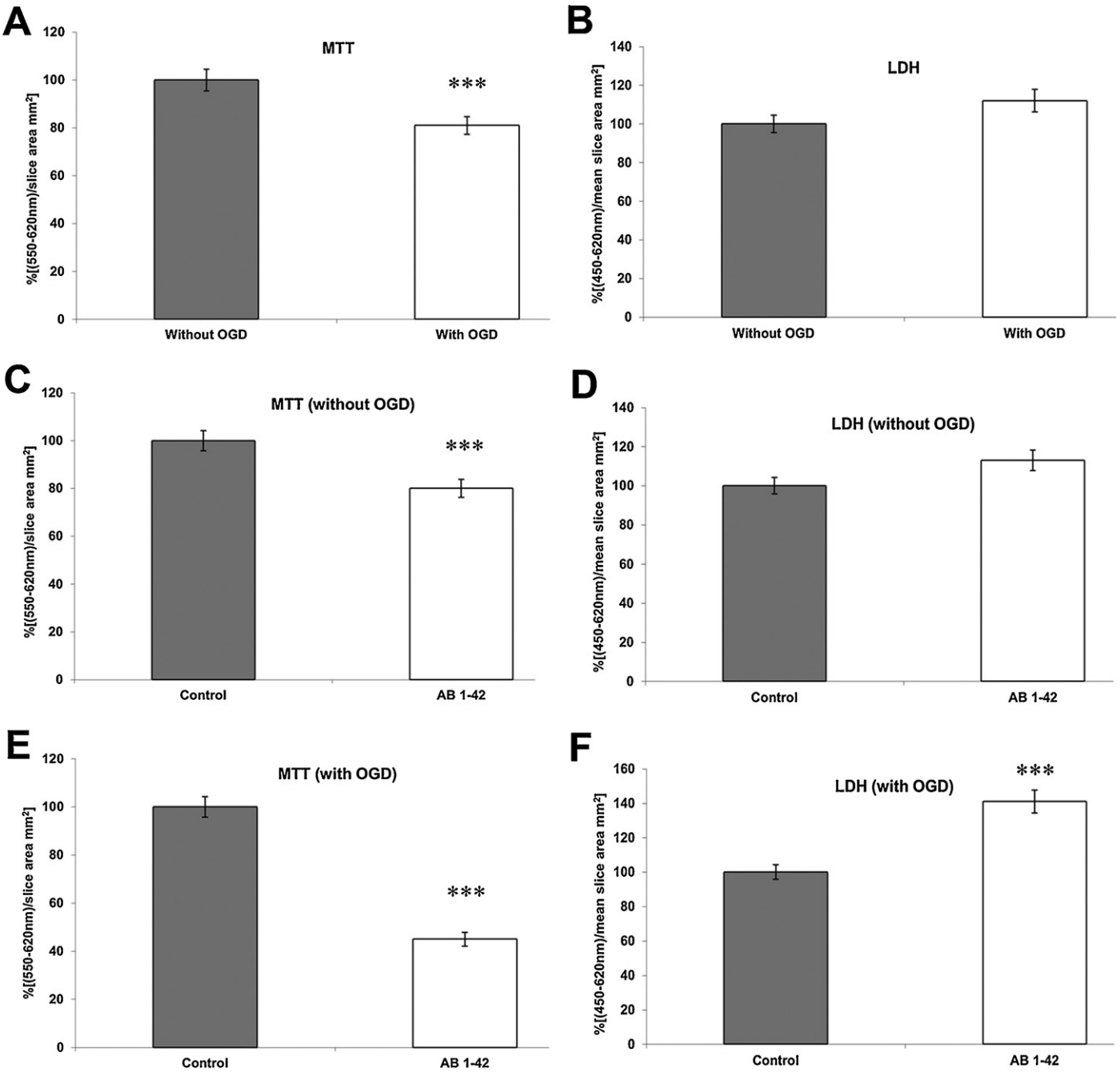

Fig. 3. Measuring the acute hippocampal slice viability with MTT and LDH assay in different conditions (OGD and Aβ treatment).

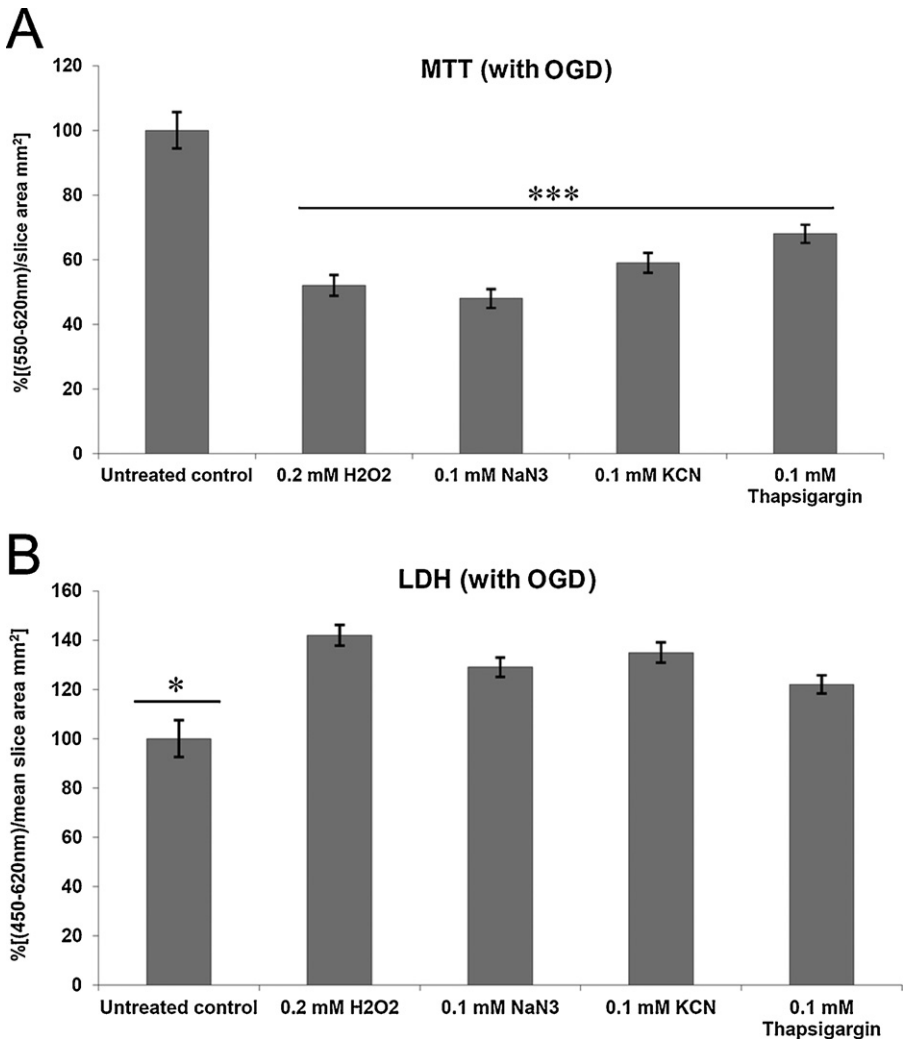

Fig. 4. Treatment of acute brain slices with different toxic agents after OGD.

integrity) while the MTT assay measures the decreased viability (mitochondrial activity) and the cell death together. The results obtained from MTT assay are influenced not only by the amount of dead cells (apoptosis and necrosis), but also by the reduction capacity of living cells. The simultaneous use of the two assays can provide a more detailed view on the toxic effects of a particular agent.

The results show that the mild OGD-pretreated slice preparations are suitable for measurements of standard cell toxic agents.

4. Conclusion

Application of MTT and LDH assay to quantify brain slice viability proved to be an easy *ex vivo* method for studying Aβ 1–42 toxicity in brain tissue. This novel method is more relevant in AD studies than using *in vitro* cell cultures, due to the three dimensional structure of the brain slice, the cell variability and the almost intact cell connections. Applying OGD pretreatment and Aβ 1–42 treatment together on hippocampus slices can provide a good *ex vivo* model of the aging brain.

This instrument can hold maximum 10 slices, but optimally 4 brain slices in small amount of solution (1 ml) and provides carboxygenated conditions (95/5%: O_2/CO_2) for the tissues.

After resting (30 min) in the (95/5%: O_2/CO_2) H-ACSF/1 solution at room temperature (24 °C), the brain slices were removed from the *ExViS* mini-chamber into the plastic Petri dish and were left in glucose- and carboxygen-free H-ACSF/2 solution for 1 h (OGD). Slices were quickly transferred back into the *ExViS* mini-chamber for a 4 h treatment with Aβ 1–42 peptide. After treatment, viability was measured with MTT and LDH assay. R = resting, OGD = oxygen–glucose deprivation, T = treating with 20 μM Aβ 1–42, M = measuring slice viability with MTT and LDH assay.

In each case the mean of optical densities is given as percentages relative to the control. Effect of OGD on hippocampal slice viability was measured with MTT (A) and LDH (B) assay. Both assays show that OGD treatment reduces brain tissue viability (in LDH assay OD is inversely proportional with viability).

Effect of Aβ 1–42 on hippocampal slice viability measured with MTT (C) and LDH (D) assay shows reduction of the brain tissue viability.

OGD and Aβ 1–42 together have a synergistic negative effect on hippocampal slice viability measured with MTT (E) and LDH (F) assay. In both assays the decrease of viability was significant.

For MTT assay we measured the OD of formazane dissolved in DMSO with the formula (OD_{550}–OD_{620})/area of slice (mm^2). The supernatant of brain slices was also measured with LDH kit and the results were calculated with the following formula:

(OD_{450}–OD_{620})/mean area of slices (mm^2). Statistical analysis was made with Student's *t*-test. $n = 40$ (slices); $^{***}p < 0.001$.

After 1 h of pretreatment in glucose- and carboxygenated-free H-ACSF/2 solution, hippocampal slices of rat were treated with different toxic agents. The toxic effect and slice viability were quantified with MTT (A) and LDH (B) assay. "With OGD" stands for the 1 h long pretreatment in glucose- and carboxygenated-free H-ACSF/2 solution. The media were changed to H-ACSF/3 solution for the treatment with toxic agents, but also in the control. Both colorimetric assays show that every treatment was toxic. In MTT assay the 0.1 mM NaN_3, in LDH assay the 0.2 mM H_2O_2 had the most toxic effect on hippocampal slices.

The MTT assay was measured by detecting the OD of formazane dissolved in DMSO with the formula (OD_{550}–OD_{620})/area of slice (mm^2). The supernatant of brain slices was also measured with an LDH kit, and the results were calculated with the following formula: (OD_{450}–OD_{620})/mean area of slices (mm^2). Statistical analysis was made with *ANOVA*, *Bonferroni* $n = 40$ (slices); $^{***}p < 0.001$ *vs.* control (A), $^{*}p < 0.05$ *vs.* treatments (B).

Conflict of interest statement

The authors declare no potential conflict of interest.

Acknowledgements

This work was supported by the grants TAMOP 4.2.2-08/1-2008-0002 and TAMOP 4.2.1B-09/1/konv-2010-0005. The research leading to these results has received funding from the European Community 7th Framework Programme (FP7/2007-2013) under grant agreement No. 201159.

References

[1] Z. Bozso, B. Penke, D. Simon, I. Laczkó, G. Juhász, V. Szegedi, A. Kasza, K. Soós, A. Hetényi, E. Wéber, H. Tóháti, M. Csete, M. Zarándi, L. Fülöp, Controlled in situ preparation of A beta(1–42) oligomers from the isopeptide iso-A beta(1–42), physicochemical and biological characterization, Peptides 31 (2010) 248–256.
[2] F. Cechetti, A. Rhod, F. Simao, K. Santin, C. Salbego, A. Netto, I.R. Siqueira, Effect of treadmill exercise on cell damage in rat hippocampal slices submitted to oxygen and glucose deprivation, Brain Research 1157 (2007) 121–125.
[3] Z. Datki, A. Juhász, M. Gálfi, K. Soós, R. Papp, D. Zádori, B. Penke, Method for measuring neurotoxicity of aggregating polypeptides with the MTT assay on differentiated neuroblastoma cells, Brain Research Bulletin 62 (2003) 223–229.
[4] Z.L. Datki, A. Hunya, B. Penke, A novel and simple fluorescence method for the measurement of presynaptic vesicular zinc release in acute hippocampal slices with a fluorescence plate reader, Brain Research Bulletin 74 (2007) 183–187.
[5] L.M. de Almeida, M.C. Leite, A.P. Thomazi, C. Battu, P. Nardin, L.S. Tortorelli, C. Zanotto, T. Posser, S.T. Wofchuk, R.B. Leal, C.A. Gonçalves, C. Gottfried, Resveratrol protects against oxidative injury induced by H_2O_2 in acute hippocampal slice preparations from Wistar rats, Archives of Biochemistry and Biophysics 480 (2008) 27–32.
[6] J. Hardy, D. Allsop, Amyloid deposition as the central event in the aetiology of Alzheimer's disease, Trends in Pharmacologycal Sciences 12 (1991) 383–388.
[7] K. Horsburgh, M.M. Reimer, P. Holland, G. Chen, G. Scullion, J.H. Fowler, Axon-glial disruption: the link between vascular disease and Alzheimer's disease, Biochemical Society Transactions 39 (2011) 881–885.
[8] C.R Jack Jr., R.C. Petersen, Y. Xu, et al., Rates of hippocampal atrophy correlate with change in clinical status in aging and AD, Neurology 55 (2000) 484–489.
[9] G. Jancsó, F. Domoki, P. Sántha, J. Varga, J. Fischer, K. Orosz, B. Penke, A. Becskei, M. Dux, L. Tóth, Beta-amyloid (1–42) peptide impairs blood–brain barrier function after intracarotid infusion in rats, Neuroscience Letters 253 (1998) 139–141.
[10] M.A. Koike, F.G. Garcia, M. Kitazawa, K.N. Green, F.M. LaFerla, Long term changes in phospho-APP and tau aggregation in the 3xTg-AD mice following cerebral ischemia, Neuroscience Letters 495 (2011) 55–59.
[11] G. Laskay, M. Zarándi, J. Varga, K. Jost, A. Fónagy, C. Torday, L. Latzkovits, B. Penke, A putative tetrapeptide antagonist prevents beta-amyloid-induced long-term elevation of $[Ca^{2+}]_i$ in rat astrocytes, Biochemical and Biophysical Research Communications 235 (1997) 479–481.
[12] J.G. Mielke, T. Comas, T. Ahuja, E. Preston, G.A. Mealing, Synaptic activity and triphenyltetrazolium chloride metabolism are correlated after oxygen–glucose deprivation in acute, but not cultured, hippocampal slices, Brain Research 1176 (2007) 113–123.
[13] M.B. Moretto, C. Funchal, A.Q. Santos, C. Gottfried, B. Boff, G. Zeni, R.P. Pureur, D.O. Souza, S. Wofchuk, J.B. Rocha, Ebselen protects glutamate uptake inhibition caused by methyl mercury but does not by Hg^{2+}, Toxicology 214 (2005) 57–66.
[14] T. Neri, M. Bucciantini, V. Rosti, S. Raimondi, A. Relini, M. Massa, M. Zuccotti, S. Donadei, M. Stefani, C.A. Redi, G. Merlini, M. Stoppini, S. Garagna, V. Bellotti, Embryonic stem and haematopoietic progenitor cells resist to Aβ oligomer toxicity and maintain the differentiation potency in culture, Amyloid 17 (2010) 137–145.
[15] J. Reifert, D. Hartung-Cranston, S.C. Feinstein, Amyloid beta-mediated cell death of cultured hippocampal neurons reveals extensive Tau fragmentation without increased full-length tau phosphorylation, The Journal of Biological Chemistry 286 (2011) 20797–20811.
[16] A.P. Rigon, F.M. Cordova, C.S. Oliveira, T. Posser, A.P. Costa, I.G. Silva, D.A. Santos, F.M. Rossi, J.B. Rocha, R.B. Leal, Neurotoxicity of cadmium on immature hippocampus and a neuroprotective role for p38 MAPK, Neurotoxicology 29 (2008) 727–734.
[17] R. Rönicke, A. Klemm, J. Meinhardt, U.H. Schröder, M. Fändrich, K.G. Reymann, Abeta mediated diminution of MTT reduction – an artefact of single cell culture? PLoS One 9 (2008) e3236.
[18] B. Tagliari, L.L. Zamin, C.G. Salbego, C.A. Netto, A.T. Wyse, Hyperhomocysteinemia increases damage on brain slices exposed to in vitro model of oxygen and glucose deprivation: prevention by folic acid, International Journal of Developmental Neuroscience 24 (2006) 285–291.

Brain Research Bulletin 86 (2011) 217–221

Contents lists available at ScienceDirect

Brain Research Bulletin

journal homepage: www.elsevier.com/locate/brainresbull

Research report

A novel application of the fluorescent dye bis-ANS for labeling neurons in acute brain slices

Emese Mozes[a,*], Akos Hunya[a,1], Aniko Toth[a,1], Ferhan Ayaydin[b,2], Botond Penke[a,3], Zsolt L. Datki[a,4]

[a] Department of Medical Chemistry, University of Szeged, H-6720 Szeged, Szikra utca 2, Hungary
[b] Cellular Imaging Laboratory, Biological Research Centre, Szeged, Hungary

ARTICLE INFO

Article history:
Received 27 April 2011
Received in revised form 24 June 2011
Accepted 7 July 2011
Available online 18 July 2011

Keywords:
Bis-ANS
Fluorescence
Neuron
Hippocampus
SH-SY5Y
Acute slice

ABSTRACT

The cell-impermeant oligomer-(e.g. beta-amyloid-, or tubulin-) specific fluorescent dye, bis-ANS (4,4′-bis-1-anilinonaphtalene-8-sulfonate), was successfully used for labeling mechanically damaged but still viable neuron bodies, neurites and neurite cross sections in acute brain slices.

Acute hippocampal brain slices of rats were co-stained with bis-ANS and the cell-impermeant, DNA-specific dye propidium iodide (PI) and were then analyzed using fluorescence and confocal microscopes. Both the neuron bodies and the neurites were found to exhibit increased fluorescence intensities, suggesting that using this method they can be detected more easily. In addition, bis-ANS showed good region – but not cell specific co-localization with the neuron-specific fluorescent dye DiI (1,1′-Dioctadecyl-3,3,3′,3′-tetramethylindocarbocyanine perchlorate). These two dyes label different neuronal structures: DiI binds specifically to intact cell membranes while bis-ANS can enter cells with compromised cell membranes and then stain the microtubules in the cytoplasm. For a quick (10 min) staining of acute brain slices with bis-ANS both HEPES and $NaHCO_3$ were needed in order to achieve high signal intensity.

Labeling with bis-ANS fluorescent dye is an easy method for imaging the neuronal structures on the surface of acute brain slices.

1. Introduction

Recently, there has been a renewed interest in the use of extrinsic fluorescent dyes such as ANS, bis-ANS, Nile Red and Thioflavin T because of their versatility, sensitivity and suitability for high-throughput screening. These non-covalent, extrinsic fluorescent dyes find widespread application in various fields of protein analysis, e.g. to characterize folding intermediates, to measure surface hydrophobicity, and to detect aggregation or fibrillation [9].

The oligomer-specific bis-ANS (4,4′-bis-1-anilinonaphtalene-8-sulfonate), first described by Rosen and Weber in 1969, is a dimeric analogue of ANS. The fluorescence properties of this dye strongly depend on their interaction with proteins, which results in changes in the polarity and viscosity of the environment [17]. The fluorescence is sensitive to the environment of the dyes with respect to polarity, viscosity and temperature [15]. Hydrophobic and electrostatic interactions have been suggested as possible mechanisms for binding of bis-ANS to proteins [2,8,11,12].

Bis-ANS exhibits a chaperone-like activity, effectively suppressing protein aggregation and preventing a certain degree of heat-inactivation of enzymes [5]. Horowitz et al. have recently shown that bis-ANS binds to tubulin, inhibiting the formation of microtubules [2,11]. Their experiments demonstrate the presence of more than one site for the binding of bis-ANS to tubulin, and additional binding sites may appear as a function of time and temperature. Tubulin apparently has two types of bis-ANS binding sites: a primary site responsible for the inhibition of microtubule assembly with a kd of 2 mM and six secondary sites with a kd of 19 mM [14]. Chakraborty et al. [2] reported that the binding of bis-ANS to tubulin occurs instantaneously, specifically at one high affinity site when 1 mM guanosine 5′-triphosphate (GTP) is present in the reaction medium. However, in the absence of GTP, binding of bis-ANS increases with time and occurs at multiple sites, but substantial portions of the secondary structure along with the colchicine-binding activity of tubulin are lost upon bis-ANS binding [2,8].

The use of fluorescent neuron labeling methods has become increasingly important in research on the nervous system and its

Abbreviations: DG, dentate gyrus; CA, cornus ammonis; Hil, hilus; PI, propidium iodide; SM, stratum moleculare; Sub, subiculum.

* Corresponding author. Tel.: +36 62 546 853/854; fax: +36 62 546 826.
E-mail addresses: mese859@gmail.com (E. Mozes), hunya@dnt.u-szeged.hu (A. Hunya), animoni@gmail.com (A. Toth), ferhan@brc.hu (F. Ayaydin), pbotond@mdche.szote.u-szeged.hu (B. Penke), datkiz@yahoo.com (Z.L. Datki).
[1] Tel.: +36 62 546853.
[2] Tel.: +36 62 599600.
[3] Tel.: +36 62 545135.
[4] Tel.: +36 62 546788.

0361-9230/$ – see front matter © 2011 Elsevier Inc. All rights reserved.
doi:10.1016/j.brainresbull.2011.07.004

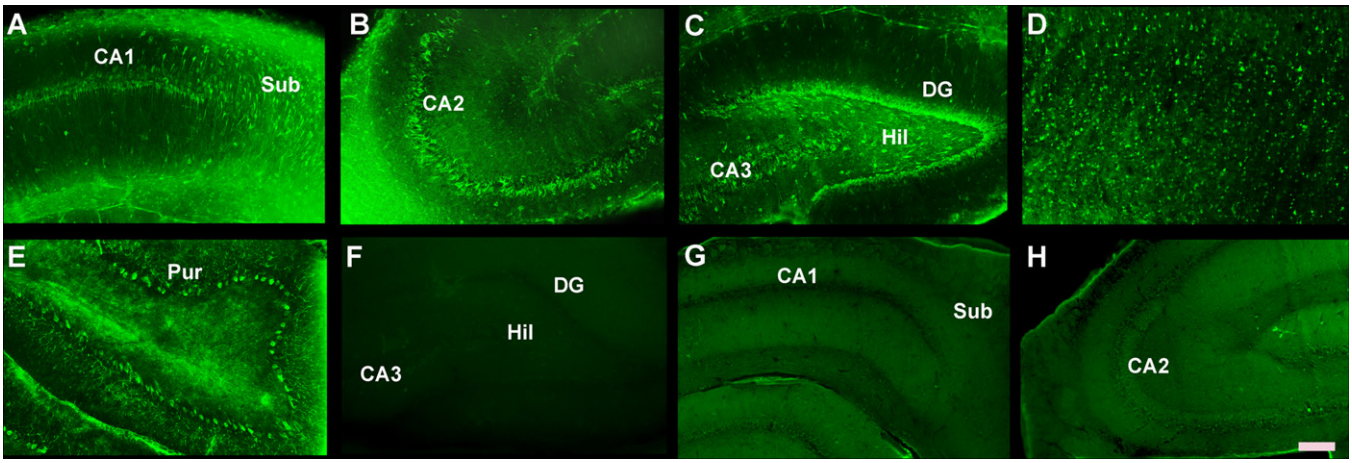

Fig. 1. Using the fluorescent dye bis-ANS to label neurons in acute brain slices. Samples labeled in $NaHCO_3$-free (only HEPES-buffered) solution (F) exhibited no fluorescence during 10 min. Samples fixed (before staining, G; after staining, H) in 4% formaldehyde showed the same non-specific (homogenous) bis-ANS signal emitted from the tissue structure in contrast to the viable (A–E; heterogenous labeling) slices. We used hippocampal (A–C, F–H), neocortical (D) and cerebellar (E) slices for these fluorescent investigations. CA: cornus ammonis; Sub: subiculum; Hil: hilus; DG: dentate gyrus; Pur: Purkinje cells. Scale bar: 200 μm.

related pathological processes. The oxazine alkaloid Darrow Red, first described by Powers et al. [13] is one of Nissl staining dyes. Darrow Red was successfully combined with silver impregnation to visualize the neurofibrillary changes characteristic of Alzheimer's disease [1]. Compared to Nissl type stains, a more sensitive and definitive marker of neuronal degradation, Fluoro Jade, was first reported by Schmued et al. [16]. Fluoro-Jade is an anionic fluorochrome capable of selectively staining degenerating neurons in brain slices. This dye can be combined with other fluorescent techniques including immunofluorescence, fluorescent axonal tracing, and fluorescent Nissl counterstaining [16]. Fluorescent lipophilic carbocyanine dyes, Dil and DiO, have an extensive history of use in cell biology, but their use as neuronal tracer has been introduced recently. Honig and Hume [10] reported that these dyes

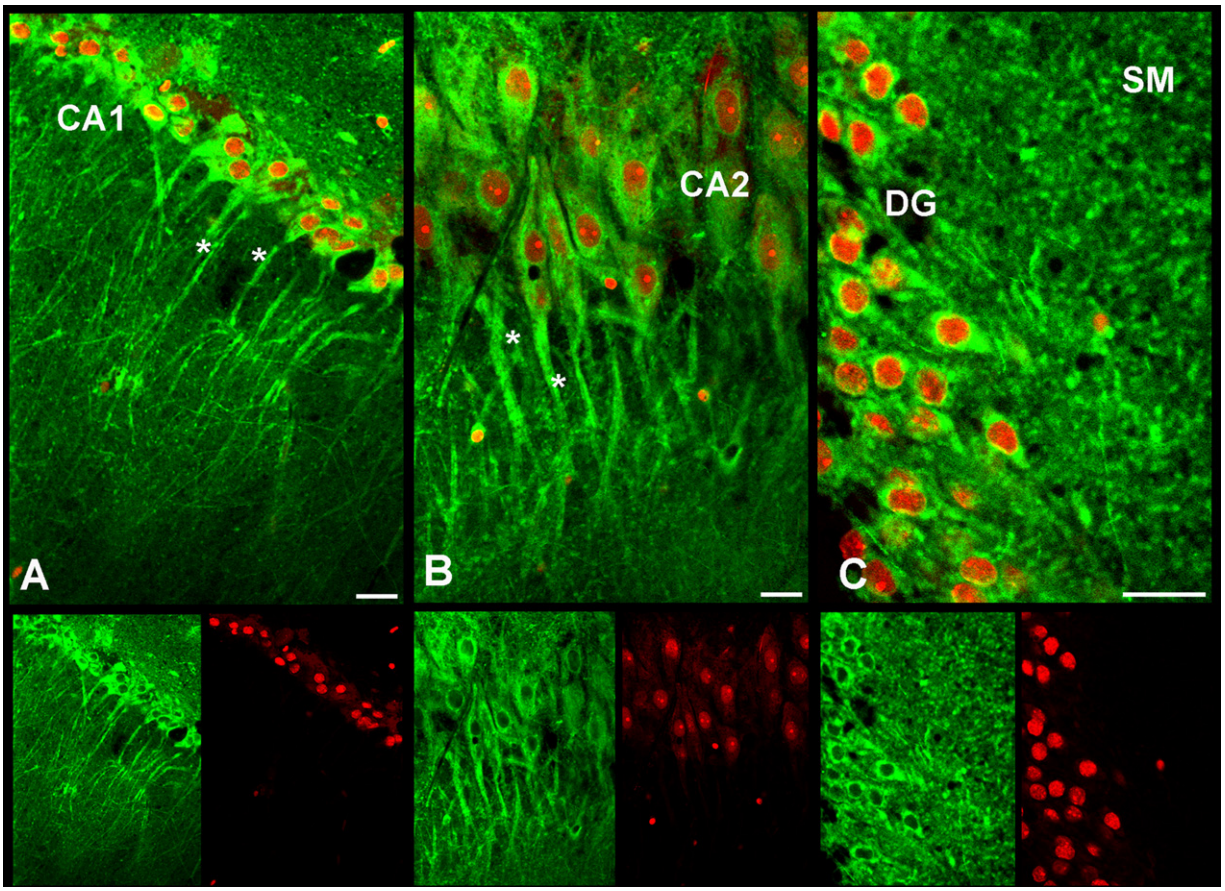

Fig. 2. Co-localization of bis-ANS (in neuronal somata and neurites) and PI (in the nuclei) fluorescence on acute hippocampal slices. The cells can be identified by the presence of PI-stained nuclei. This image is a composite of confocal images taken using a 40× objective. We identified cells and their neurites (highlighted with asterisks on A and B) in different regions of hippocampus: in CA1 (A), CA2 (B) and dentate gyrus (C). We also identified the cross sectional view of dendrites and axons (C). CA: cornus ammonis; DG: dentate gyrus; SM: stratum moleculare. Scale bar: 20 μm.

were applied in neurons placed in culture, and they initially labeled the processes (anterograde and retrograde tracing) as well as the cell bodies of cultured neurons, and that they were seemingly non-toxic. Lateral diffusion in the membrane was the major mechanism for the translocation of these molecules, rather than fast axonal transport [10]. Godement et al. [7] reported that these dyes can be used to label axonal and dendrite projections in fixed tissues, as well. Our recent work presents a novel application of the bis-ANS for the detection of mechanically damaged neurons. Our results suggest that bis-ANS could be used for neuronal staining in the surface of acute brain slices, owing to the tubulin-binding properties of this dye.

2. Materials and methods

2.1. Materials

Cell-impermeant forms of bis-ANS (4,4′-Dianilino-1,1′-binaphthyl-5,5′-disulfonic acid dipotassium salt, cat. no. D4162), propidium iodide (cat. no. P4170), DiI (1,1′-Dioctadecyl-3,3,3′,3′-tetramethylindocarbocyanine perchlorate, cat. no. 42364), chloral hydrate (cat. no. 23100), and general reagents were obtained from Sigma–Aldrich, Hungary. The animal protocols applied in this study had been approved by the National Institutes of Health and by the University of Szeged; permission/licence numbers: I-02442/001/2006.

2.2. Neuroblastoma cell culturing

SH-SY5Y cells were obtained from Sigma–Aldrich (Hungary) and were used with a method slightly modified from Datki et al. [3]. The cells were plated for 24 h at 37 °C in Petri dishes (Sigma) at a density of 3×10^4 cells per well to confluency with 5% CO_2 in a humidified atmosphere with Dulbecco's modified Eagle's medium (MEM): F-12 (1:1) with phenol red (Sigma). L-Glutamine (4 mM; Gibco, Europe), penicillin (200 units/ml; Gibco), streptomycin (200 μg/ml; Gibco), MEM non-essential amino acid solution (100× liquid mg/L; Gibco) and 10% fetal bovine serum (FBS; Gibco) were added to the medium. After mechanically damaging the cells by cutting a straight line on the Petri dish surface with a blade they were incubated in the presence of bis-ANS (10 μM) and PI (3 μM) for 10 min.

2.3. Preparation of acute brain slices

A modified version of the method reported by Datki et al. [4] was used in our experiments. Following narcosis with chloral hydrate (0.4 g/kg), 3-months-old male *Wistar* rats were decapitated and the heads (without scalp-skin) were placed in ice cold distilled water for 30 s. The brains were quickly removed and immersed in minimal Ca^{2+}-containing ACSF (preparation solution) with elevated Mg^{2+} at 4 °C. The composition of the preparation solution was the following (in mM): NaCl 127, KCl 2, $MgCl_2$ 3.5, $CaCl_2$ 0.5, $NaHCO_3$ 25, D-glucose 10, pH = 7.4. Brain slices with a thickness of 400 μm were prepared from the hippocampus with a McIlwain tissue chopper (Campden Instruments, Loughborough, UK) at 4 °C and were rapidly transferred into the Petri dish for labeling.

2.4. Cell line and acute slice labeling

SH-SY5Y human neuroblastoma cells and the acute hippocampal brain slices (with an area of approximately 8 mm^2) were labeled with the fluorescent dyes (bis-ANS, PI or DiI) in a labeling solution at room temperature (24 °C). This solution was composed of the following (in mM): NaCl 129, HEPES 20, $NaHCO_3$ 10, sucrose 10 (pH = 7.4), supplemented with 10 μM bis-ANS, 3 μM propidium iodide (PI) or 50 μM DiI (with 1% DMSO in solution). Bis-ANS and PI were used simultaneously (10 min), but in bis-ANS/DiI co-labeling experiments we first added DiI for 15 min, and after washing with labeling solution, we added bis-ANS for 10 min. After labeling and re-washing we transferred the slices to a cover slip mounted glass slide. In every case we controlled the distance (0.4 mm) between two glasses with an adhesive-paper (thickness 0.4 mm). As a result, all of the anatomically undamaged hippocampal slices from the median part (±2 mm from middle) of hippocampus could be used for the experiments.

2.5. Fluorescence microscopy

Measurements were performed at room temperature (24 °C). Images (Figs. 1, 3 and 4) were taken by a 24-bit digital Colour-View II FW camera (with CCD arrays of 2080 × 1544 pixels) interlocked with the imaging system of an OLYMPUS IX71 inverted research fluorescence microscope. Image acquisition and analysis were performed by *analySIS 3.2* software (OLYMPUS, Budapest, Hungary). To detect the fluorescence of the dyes we used the following wavelengths (ex./em.): 380/535 nm (bis-ANS), 530/620 nm (PI) and 550/620 nm (DiI).

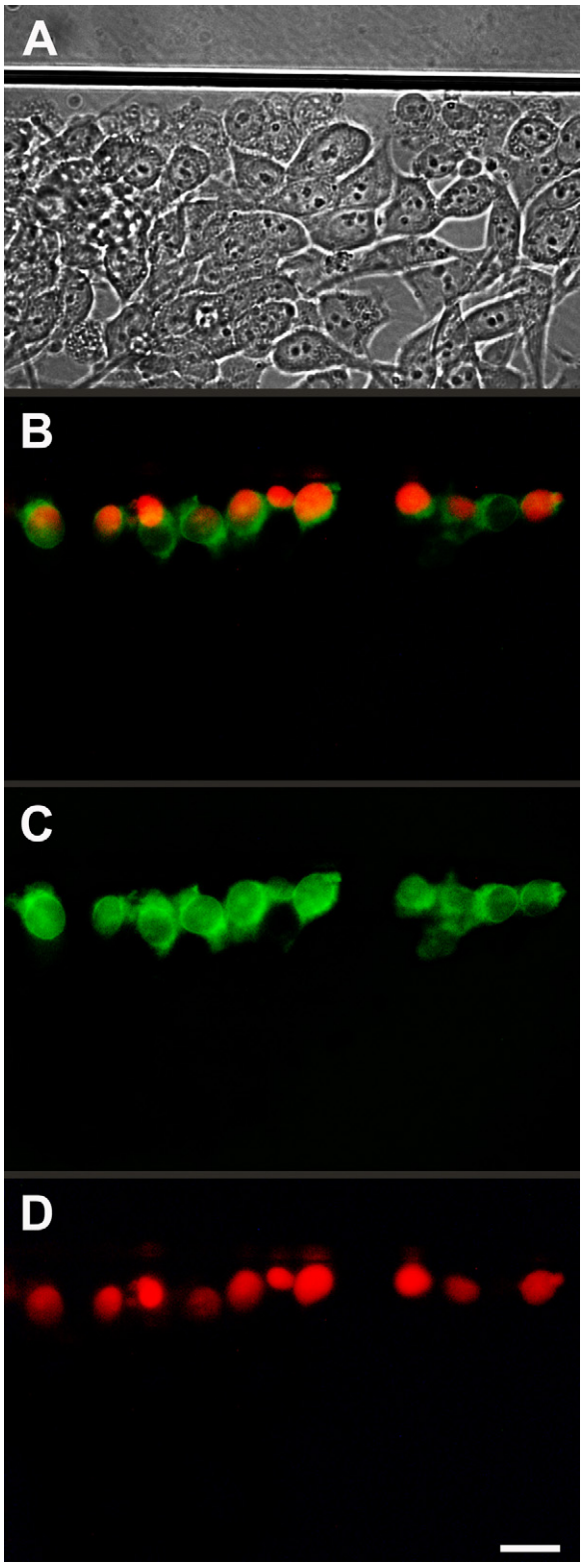

Fig. 3. Using bis-ANS and PI to label neuroblastoma cells incised by a blade. By a dint of a blade an incision was made on viable, monolayers of non-differentiated SH-SY5Y human neuroblastoma cells (A), then the monolayers were labeled with bis-ANS, staining the cell bodies in green (C) and propidium iodide (PI), staining the nuclei in red (D). The samples were analyzed by fluorescent microscopy and the obtained pictures were merged (B). Scale bar: 20 μm. (For interpretation of the references to color in this figure legend, the reader is referred to the web version of the article.)

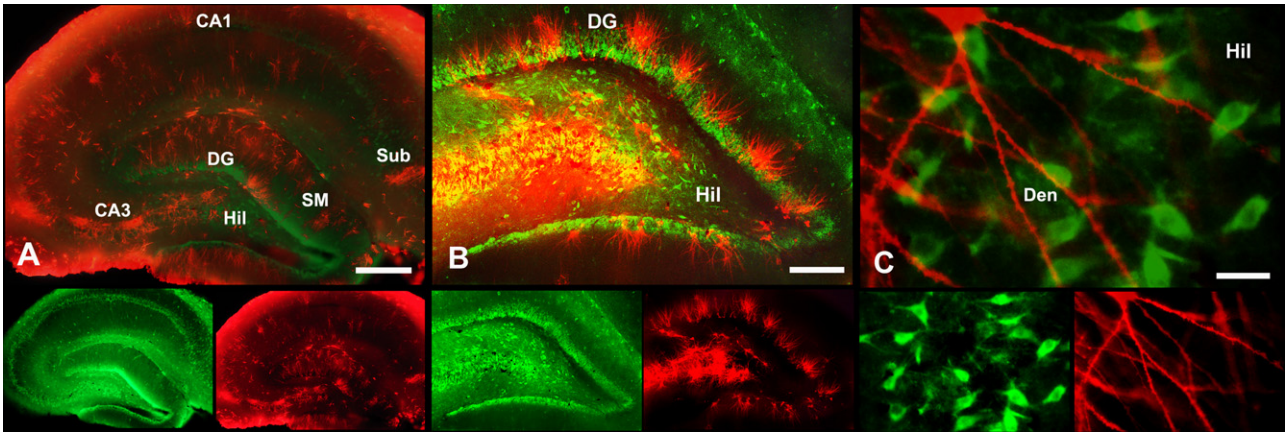

Fig. 4. Region-specific co-localization of bis-ANS (in mechanically damaged neurons, green) and DiI (in intact viable neurons, red) fluorescence in acute hippocampal brain slices. We detected co-localization in granule cells of DG (B) or in CA1 (A) regions. In higher magnification (450×, C) we can see that the staining properties of bis-ANS and DiI are differently related to the cell bodies and neurites. Bis-ANS is specific for damaged cell bodies and neurites and allows the imaging of neurite cross sections, while DiI labels the horizontal intact neurites. CA: cornus ammonis; DG: dentate gyrus; Hil: hilus; SM: stratum moleculare; Sub: subiculum, Den: dendrites. Scale bar: 0.5 mm on A, 200 μm on B and 20 μm on C. (For interpretation of the references to color in this figure legend, the reader is referred to the web version of the article.)

2.6. Confocal microscopy

Fluorescence detection (Fig. 2) was performed by using an Olympus Fluoview FV1000 confocal laser scanning microscope (Olympus Life Science Europa GmbH, Hamburg, Germany). The microscope configuration was the following: objective lens: UPLFLN 40× oil immersion objective with the numerical aperture of 1.30; scanning dimensions: 800 × 800 pixel; sampling speed: 8 μs/pixel; confocal aperture: 211 μm; zoom: 1× or 2×; line averaging: 2×; scanning mode: sequential unidirectional; excitation: 405 nm (bis-ANS) and 543 nm (PI); laser transmissivity: 1% and 10% were used for bis-ANS and PI, respectively; main dichoroic beam splitter: DM405/488/543; intermediate dichoroic beam splitter: SDM 490; bis-ANS was detected between 410 and 490 nm using spectrum separation, PI was detected between 584 and 684 nm. Using Olympus Fluoview software (version 1.7.2.2) bis-ANS and PI images were pseudo colored green and red, respectively.

3. Results and discussion

Using the non-covalent extrinsic fluorescent dye bis-ANS for staining acute hippocampal slices, we observed that the dye could label the tissues along with neuronal structures in dentate gyrus (DG), cornus ammonis (CA) 1–3 regions, hilus (Hil) and subiculum (Sub) (Fig. 1A–C). As we studied the labeling properties of bis-ANS on rat acute brain slices, we found that formaldehyde-fixed tissue samples (before staining, Fig. 1G; after staining, Fig. 1H) emitted non-specific homogenous fluorescence in contrast to the viable slices taken from the hippocampus (Fig. 1A–C) neocortex (Fig. 1D) and cerebellum (Fig. 1E). In non-fixed viable tissues the neurons exhibited heterogeneous and higher fluorescence intensities compared to fixed tissues, especially in the hippocampal Sub (Fig. 1A), in CA2 region (Fig. 1B), Hil (Fig. 1C) and in cerebellar Purkinje cells (Fig. 1E). In the $NaHCO_3$-free (only HEPES-buffered) solution no specific bis-ANS signals could be detected after 10 min of staining (Fig. 1F). We concluded that the fluorescence emission of bis-ANS is $NaHCO_3$-dependent (the mechanism is unknown).

In addition to bis-ANS, we stained the neuronal nuclei with PI, a DNA-specific dye that can only stain cells having damaged cell membranes. Then confocal images were taken of live acute hippocampal slices, where the cells were identified by their PI-stained nuclei (Fig. 2). In all regions of the hippocampus (Fig. 2A–C), bis-ANS and PI were co-localized and the cross-sectional view of neurites (mainly dendrites) was identified (Fig. 2C).

It was necessary to prove that the extrinsic fluorescent dye bis-ANS only labels damaged cells. For this assay we used non-differentiated SH-SY5Y human neuroblastoma monolayer cell culture (Fig. 3). An incision was made by a dint of a blade on the cells settled in the Petri-dish (Fig. 3A), then it was labeled with bis-ANS (Fig. 3C) and PI (Fig. 3D). After 10 min we analyzed the samples using fluorescence microscopy and co-localizing pictures (Fig. 3B). We noticed that exclusively the cells near the cut absorbed the dyes. These cells were damaged by the blade. It is important to note that neurons in the acute hippocampal slices were damaged only around the cutting area, but the whole structure remained anatomically intact.

Using the well-known fluorescent dye DiI (specific for intact viable neurons), we observed region-specific co-localization with bis-ANS in mechanically damaged neurons in acute hippocampal slices. These co-localization patterns were found in granule cells of DG (Fig. 4B) or in CA1 (Fig. 4A) regions. In a higher magnification (450×; Fig. 4C) we could see that the staining properties of bis-ANS and DiI were different in the neuronal structures (e.g. neurites and cell bodies). Bis-ANS is specific for damaged cell bodies and neurites and allows the imaging of neurite cross sections, while DiI labels the horizontal intact neurites.

4. Conclusion

Labeling with bis-ANS fluorescent dye is an easy method for imaging the neuronal structures on the surface of acute brain slices. The dye only labels damaged cells in non-fixed tissue and co-staining with different fluorescent dyes (e.g. DiI) allows detailed imaging of brain tissue structures.

Conflict of interest statement

The authors declare no potential conflict of interest.

Acknowledgements

Janos Bolyai Fellowship from the Hungarian Academy of Sciences and the Support of the European Union 7th Framework programme (HEALTH-F2-2007-201159, HEALTH-F2-2007-211696); Hungarian Scientific Research Fund (OTKA NK 73672) and the European Union 7th Framework programme (HEALTH-F2-2007-201159, HEALTH-F2-2007-211696) are acknowledged.

References

[1] H. Braak, E. Braak, T. Ohm, J. Bohl, Silver impregnation of Alzheimer's neurofibrillary changes counterstained for basophilic material and lipofuscin pigment, Stain Technology 63 (1988) 197–200.

[2] S. Chakraborty, N. Sarkar, B. Bhattacharyya, Nucleotide-dependent bisANS binding to tubulin, Biochimica et Biophysica Acta 1432 (1999) 350–355.
[3] Z. Datki, A. Juhasz, M. Galfi, K. Soos, R. Papp, D. Zadori, B. Penke, Method for measuring neurotoxicity of aggregating polypeptides with the MTT assay on differentiated neuroblastoma cells, Brain Research Bulletin 62 (2003) 223–229.
[4] Z.L. Datki, A. Hunya, B. Penke, A novel and simple fluorescence method for the measurement of presynaptic vesicular zinc release in acute hippocampal slices with a fluorescence plate reader, Brain Research Bulletin 74 (2007) 183–187.
[5] X. Fu, X. Zhang, Z. Chang, 4,4′-Dianilino-1,1′-binaphthyl-5,5′-sulfonate, a novel molecule having chaperone-like activity, Biochemical and Biophysical Research Communications 329 (2005) 1087–1093.
[7] P. Godement, J. Vanselow, S. Thanos, F. Bonhoeffer, A study in developing visual systems with a new method of staining neurones and their processes in fixed tissue, Development (Cambridge, England) 101 (1987) 697–713.
[8] S. Gupta, S. Chakraborty, A. Poddar, N. Sarkar, K.P. Das, B. Bhattacharyya, BisANS binding to tubulin: isothermal titration calorimetry and the site-specific proteolysis reveal the GTP-induced structural stability of tubulin, Proteins 50 (2003) 283–289.
[9] A. Hawe, M. Sutter, W. Jiskoot, Extrinsic fluorescent dyes as tools for protein characterization, Pharmaceutical Research 25 (2008) 1487–1499.
[10] M.G. Honig, R.I. Hume, Dil and diO: versatile fluorescent dyes for neuronal labelling and pathway tracing, Trends in Neurosciences 12 (333–335) (1989) 340–341.
[11] P. Horowitz, V. Prasad, R.F. Luduena, Bis(1,8-anilinonaphthalenesulfonate). A novel and potent inhibitor of microtubule assembly, Journal of Biological Chemistry 259 (1984) 14647–14650.
[12] D.J. Laurence, A study of the adsorption of dyes on bovine serum albumin by the method of polarization of fluorescence, Biochemical Journal 51 (1952) 168–180.
[13] M.M. Powers, G. Clark, M.A. Darrow, V.M. Emmel, Darrow red, a new basic dye, Stain Technology 35 (1960) 19–21.
[14] A.R. Prasad, R.F. Luduena, P.M. Horowitz, Bis(8-anilinonaphthalene-1-sulfonate) as a probe for tubulin decay, Biochemistry 25 (1986) 739–742.
[15] C.G. Rosen, G. Weber, Dimer formation from 1-amino-8-naphthalenesulfonate catalyzed by bovine serum albumin. A new fluorescent molecule with exceptional binding properties, Biochemistry 8 (1969) 3915–3920.
[16] L.C. Schmued, C. Albertson, W. Slikker Jr., Fluoro-Jade: a novel fluorochrome for the sensitive and reliable histochemical localization of neuronal degeneration, Brain Research 751 (1997) 37–46.
[17] L. Stryer, The interaction of a naphthalene dye with apomyoglobin and apohemoglobin. A fluorescent probe of non-polar binding sites, Journal of Molecular Biology 13 (1965) 482–495.

Neurochemistry International 62 (2013) 58–69

Contents lists available at SciVerse ScienceDirect

Neurochemistry International

journal homepage: www.elsevier.com/locate/nci

Proteome-wide study of endoplasmic reticulum stress induced by thapsigargin in N2a neuroblastoma cells

István Földi [a,*,1], Anikó M. Tóth [a,1], Zoltán Szabó [a], Emese Mózes [a], Róbert Berkecz [a], Zsolt L. Datki [a], Botond Penke [a,b], Tamás Janáky [a]

[a] Department of Medical Chemistry, University of Szeged, Dóm tér 8, Szeged H-6720, Hungary
[b] Supramolecular and Nanostructured Material Research Group of the Hungarian Academy of Sciences, Dóm tér 8, H-6720 Szeged, Hungary

ARTICLE INFO

Article history:
Received 7 September 2012
Received in revised form 19 October 2012
Accepted 2 November 2012
Available online 12 November 2012

Keywords:
Endoplasmic reticulum stress
Thapsigargin
Grp78
Two-dimensional electrophoresis
Proteomics
Neurodegenerative disorder

ABSTRACT

Disturbances in intraluminal endoplasmic reticulum (ER) Ca^{2+} concentration leads to the accumulation of unfolded proteins and perturbation of intracellular Ca^{2+} homeostasis, which has a huge impact on mitochondrial functioning under normal and stress conditions and can trigger cell death. Thapsigargin (TG) is widely used to model cellular ER stress as it is a selective and powerful inhibitor of sarcoplasmic/endoplasmic reticulum Ca^{2+} ATPases. Here we provide a representative proteome-wide picture of ER stress induced by TG in N2a neuroblastoma cells. Our proteomics study revealed numerous significant protein expression changes in TG-treated N2a cell lysates analysed by two-dimensional electrophoresis followed by mass spectrometric protein identification. The proteomic signature supports the evidence of increased bioenergetic activity of mitochondria as several mitochondrial enzymes with roles in ATP-production, tricarboxylic acid cycle and other mitochondrial metabolic processes were upregulated. In addition, the upregulation of the main ER resident proteins confirmed the onset of ER stress during TG treatment. It has become widely accepted that metabolic activity of mitochondria is induced in the early phases in ER stress, which can trigger mitochondrial collapse and subsequent cell death. Further investigations of this cellular stress response in different neuronal model systems like N2a cells could help to elucidate several neurodegenerative disorders in which ER stress is implicated.

1. Introduction

The endoplasmic reticulum (ER) is a membrane-bound organelle presented in all eukaryotic cells, where it has a role in storing, modifying and transporting newly synthesized proteins and in the regulation of intracellular Ca^{2+} homeostasis (Stutzmann and Mattson, 2011). Owing to its role as an intracellular Ca^{2+} reservoir, the ER functions as an excitable system that is capable of spreading Ca^{2+}-related signals throughout the cell (Berridge, 2002). Changes in intracellular Ca^{2+} concentration regulate the activity of numerous proteins with roles in different cellular processes (Berridge et al., 2003). Disturbances in intraluminal ER Ca^{2+} concentration lead to protein unfolding because of the Ca^{2+}-dependent nature of several ER chaperones, such as glucose-regulated protein 78 (Grp78), Grp94 and calreticulin (Ma and Hendershot, 2004). These proteins are involved in protein folding, post-translational modification, Ca^{2+} storage and release, and lipid synthesis and metabolism (Michalak et al., 2002). A recent study suggests that ER may contain transient receptor potential cation channel subfamily V member 1 inducing Ca^{2+} leak (Gallego-Sandin et al., 2009). In addition, calcium homeostasis modulator 1 is able to decrease the Ca^{2+} content of the ER, which produces ER stress leading to cell death (Gallego-Sandin et al., 2011). Accumulation of unfolded proteins triggers the unfolded protein response (UPR), which is an evolutionarily conserved cell stress response that initially aims to compensate for damage, but can trigger cell death if the ER dysfunction is severe or prolonged (Xu et al., 2005).

Abbreviations: 2-DE, two-dimensional electrophoresis; AD, Alzheimer's disease; BSA, bovine serum albumin; Calr, calreticulin; CHAPS, 3-[(3-cholamidopropyl)dimethylammonio]-1-propanesulfonate; CV, coefficient of variation; DAVID, Database for Annotation, Visualisation and Integrated Discovery; DMSO, dimethyl sulfoxide; DTE, dithioerythritol; ER, endoplasmic reticulum; ERp, ER resident protein; GO, gene ontology; Grp, glucose-regulated protein; IAA, iodoacetamide; IDH, isocitrate dehydrogenase; IP_3R, inositol trisphosphate receptor; MAM, mitochondrial associated membrane; MS, mass spectrometry; MS/MS, tandem mass spectrometry; PAGE, polyacrylamide gel-electrophoresis; PDH, pyruvate dehydrogenase; PDI, protein disulphide isomerase; RuBPs, ruthenium (II) bathophenanthroline disulfonate; SDS, sodium dodecyl sulphate; SERCA, sarcoplasmic/endoplasmic reticulum Ca^{2+} ATPase; SGoF, sequential goodness of fit; TG, thapsigargin; UPR, unfolded protein response; VDAC, voltage-dependent anion channel.

* Corresponding author. Present address: School of Biosciences, University of Birmingham, Edgbaston, Birmingham B15 2TT, UK. Tel.: +44 121 414 4392; fax: +44 121 414 5925.
E-mail addresses: i.foldi@bham.ac.uk, istvanfoldi82@gmail.com (I. Földi).
[1] These authors contributed equally to this work.

0197-0186/$ - see front matter © 2012 Elsevier Ltd. All rights reserved.
http://dx.doi.org/10.1016/j.neuint.2012.11.003

Thapsigargin (TG) is a sesquiterpene alkaloid that is a highly selective and powerful inhibitor of sarcoplasmic/endoplasmic reticulum Ca^{2+} ATPase (SERCAs) pumps. By the inhibition of SERCAs, TG prevents Ca^{2+} transport into the ER lumen and subsequently increases the Ca^{2+} level in the cytosol (Lytton et al., 1991; Sagara and Inesi, 1991). TG induced a rapid rise followed by a sustained increase in free cytosolic Ca^{2+} in the murine hypothalamic cell line, GT1-7 (Wei et al., 1998). Furthermore TG triggered ER stress-induced apoptotic cell death in primary rat cortical neurons (Chung et al., 2011).

Besides many other human diseases, ER stress and UPR are also implicated in different neurological disorders (Matus et al., 2011). Investigations of clinical samples confirm that ER stress is one of the main pathological events in Parkinson's disease, Alzheimer's disease and multiple sclerosis (Hoozemans et al., 2007; Hoozemans et al., 2009; Cunnea et al., 2011). In addition, very recent studies provide direct evidence of upregulation of UPR in motor neuron disease models suggesting that ER stress plays a major role in amyotrophic lateral sclerosis (Prell et al., 2012). Despite the accumulated knowledge, the exact mechanism of the neuronal ER stress remains obscure. However, the UPR-related signalling pathways and related metabolic processes could be a potential therapeutic target for the treatment of neurological disorders.

In this study, we used two-dimensional electrophoresis (2-DE) along with mass spectrometry (MS) to identify protein expression changes in TG-treated N2a neuroblastoma cells. We showed that several ER chaperone proteins were upregulated on TG treatment, which could confirm the activation of TG-induced ER stress. Here Grp78 expression was validated meticulously by Western blot analysis. Besides ER chaperones, majority of the upregulated proteins belonged to the mitochondrial proteome suggesting a strong crosstalk between ER stress and mitochondrial bioenergetic changes. Morphological changes of cells were also observed after TG treatment resulting in a marked reduction in the number of neurites. This correlated well with the fact that a significant portion of the downregulated proteins control cytoskeletal organisation.

2. Materials and methods

2.1. Materials

High performance liquid chromatography grade acetonitrile, formic acid, dimethyl sulfoxide (DMSO), Tris, urea, thiourea, 3-[(3-cholamidopropyl)dimethylammonio]-1-propanesulfonate (CHAPS), dithioerythritol (DTE), iodoacetamide (IAA), glycerol and TG were obtained from Sigma–Aldrich (Budapest, Hungary). Sodium dodecyl sulphate (SDS) and piperazine diacrylamide were purchased from Bio-Rad (Hercules, CA, USA). Acrylamide was procured from GE Healthcare (Little Chalfont, UK).

2.2. Cell culture, treatment and cell viability assay

A slightly modified method of Datki et al. (2003) was used for cell culturing. Mouse N2a cells (Sigma–Aldrich, Hungary) were grown for 2 days on 96-well plates reaching a density of 3×10^4 cells per well to confluency with 5% CO_2 in a humidified atmosphere with Dulbecco's modified Eagle's medium (DMEM). L-Glutamine (4 mM; Gibco, Europe), penicillin (200 units/mL; Gibco), streptomycin (200 μg/mL; Gibco), MEM non-essential amino acid solution (100 × liquid mg/L; Gibco) and 10% fetal bovine serum (FBS; Gibco) were added to the medium. The cells were treated with 1 μM TG dissolved in DMSO (stock solution 1 mM) or 0.1% DMSO as control. EZ4U assay was performed to measure the toxic effect of TG on cell viability. N2a cells grown on 96-well plates were treated with 1 μM TG or 0.1% DMSO for 24 or 48 h, and the media was changed to FBS-free media during treatments. After 24 or 48 h incubation, 10 μL of EZ4U stock solution (one kit dissolved in 2.5 mL activator solution and 2.5 mL distilled water; Biomedica, Hungary) was added to each well, containing a 90 μL FBS-free medium, and the mixture was incubated for 2 h. The optical density was measured with a 96-well plate ELISA reader at 490 nm, with the reference filter set to 620 nm. Each cell viability assay was triplicated.

2.3. Sample preparation, 2D gel-electrophoresis and image analysis

For 2-DE and Western blot analysis N2a cells were grown in 60 mm Petri-dishes and were treated with TG as described above. After 24 h of treatment cells were washed three times with phosphate-buffered saline (PBS), then collected in 1.5 mL ice cold PBS. The suspensions were centrifuged at 1000*g* for 10 min at 4 °C. The supernatants were removed and the cell pellets were stored at −80 °C until lysis. Each pellet was lysed in 100 μL 2-DE lysis buffer (7 M urea, 2 M thiourea, 4% CHAPS, 50 mM DTE) supplemented with a 1% (v/v) protease inhibitor cocktail (Sigma–Aldrich). The samples were incubated on ice for 15 min then the cells were physically disrupted by sonication for 6 cycles (10 s sonication/10 s break) on ice. The lysates were centrifuged at 14,000*g* for 30 min at 4 °C. The supernatants were then pipetted into clean Eppendorf tubes. Four samples per group were pooled to obtain a sufficient amount of protein for 2-DE (12 Petri-dishes/group). On the whole three independent gels were made and analysed per group. The protein concentrations were determined by a Non-Interfering Protein Assay Kit (Calbiochem, Gibbstown, NJ, USA). A volume of samples containing 400 μg of total protein was supplemented with a 2-DE lysis buffer to a total volume of 450 μL plus 2.5 μL Bio-Lyte 3–10 buffer (Bio-Rad, Hercules, CA, USA) and left on 24 cm, pH 3–10, NL IPG strips (Bio-Rad) for overnight rehydration. Isoelectric focusing and subsequent SDS–polyacrylamide gel-electrophoresis (SDS–PAGE) were performed as described previously (Foldi et al., 2011). After SDS–PAGE, the gels were stained with ruthenium (II) bathophenanthroline disulphonate (RuBPs) according to the protocol of Rabilloud et al. (2001). Following staining, the gels were scanned on a FLA-5100 laser scanner (Fujifilm, Tokyo, Japan) using a 473 nm laser and the 575 nm lp filter at 100 μm resolution, and the photomultiplier (PMT) was adjusted to 400 V. Digitised 2-D gel images were analysed by Progenesis Samespots software version 3.3.3420.25059 (NonLinear Dynamics, Newcastle Upon Tyne, UK). Software-based analysis focused on those spots that were 100% matched across all the gels.

2.4. Mass spectrometric analysis and protein identification

RuBPs stained gels were overstained with colloidal Coomassie blue G-250 according to the "Silver Blue" staining protocol (Candiano et al., 2004). Individual spots of interest were excised from the gel, destained, and then subjected to in-gel digestion with trypsin for 24 h at 37 °C using modified protocol of Shevchenko et al. (1996). Tryptic peptides extracted from gel pieces using 50% acetonitrile and 5% formic acid were dried under a vacuum. MS analysis was performed on a Waters NanoAcquity UPLC system coupled with a Micromass Q-TOF premier mass spectrometer (Waters, Millford, MA, USA) as described previously (Foldi et al., 2011). All the obtained data were processed and peaklists were generated by the Waters Proteinlynx Global Server, ver. 2.4 software using default settings. Each MS/MS sample was analysed using a Mascot 2.2.07 (Matrix Science, London, UK). The Mascot device was set up to search in a Swissprot 2011_05 database (528048 entries) where the selected digestion enzyme was trypsin. A database search was performed with a fragment ion mass tolerance of 0.15 Da and a

Table 1
Proteins identified and used for categorisation.

Spot#[a]	Protein name	Accesion number[b]	Gene symbol	Fold change	*t*-Test[c]	Cellular localisation[a]	Biological process[d]
Up regulated proteins							
1183	78 kDa glucose-regulated protein	P20029	Hspa5	2.2	0.0025	**ER**, Cyt, Nuc, Perinuclear region	**Protein folding** (chaperone activity), negative regulation of apoptosis
1194	78 kDa glucose-regulated protein	P20029	Hspa5	2.1	0.0091	**ER**, Cyt, Nuc, Perinuclear region	**Protein folding** (chaperone activity), negative regulation of apoptosis
366	Aconitate hydratase, mitochondrial	Q99KI0	Aco2	1.9	0.0114	**Mit**, Nuc	Energy metabolism (TCA cycle)
2021	Acyl-coenzyme A thioesterase 2, mitochondrial	Q9QYR9	Acot2	1.5	0.0018	Mit	**Metabolic process** (lipid and acyl-CoA metabolic process)
2118	Adenylate kinase 2, mitochondrial	Q9WTP6	Ak2	1.7	0.0019	Mit	**Energy metabolism**, nucleotide synthesis
2118	Coiled-coil-helix-coiled-coil-helix domain-containing protein 3, mitochondrial	Q9CRB9	Chchd3	1.7	0.0019	Mit	**Scaffold protein** (maintaining mitochondrial crista architecture and protein import, Darshi et al. (2011))
1207	Aspartate aminotransferase, mitochondrial	P05202	Got2	1.6	0.0020	**Mit**, Plasma membrane	**Metabolic process** (amino-acid metabolism), lipid transport
1638	ATP synthase subunit beta, mitochondrial	P56480	Atp5b	1.9	0.0001	**Mit**, Plasma membrane	**Energy metabolism** (ATP synthesis), proton transport
1986	Calreticulin	P14211	Calr	n.d.[e]	–	**ER**, Nuc, Cyt, Golgi	**Protein folding** (chaperone activity), regulation of gene expression and cell cycle
1237	Cathepsin B	P10605	Ctsb	2.5	0.0022	**Lys**, Mit, Cyt	**Proteolysis**, negative regulation of cell death
1309	Coproporphyrinogen-III oxidase, mitochondrial	P36552	Cpox	1.7	0.0169	Mit	**Metabolic process** (heme biosynthesis)
2001	Cytosol aminopeptidase	Q9CPY7	Lap3	1.6	0.0001	**Cyt**, Mit, Nuc, Golgi	Proteolysis
820	Dihydrolipoyl dehydrogenase, mitochondrial	O08749	Dld	1.6	0.0009	Mit	**Energy metabolism** (pyruvate dehydrogenase subunit), proteolysis
628	Dihydrolipoyllysine-residue acetyltransferase component of pyruvate dehydrogenase complex, mitochondrial	Q8BMF4	Dlat	1.5	0.0059	Mit	**Energy metabolism** (pyruvate dehydrogenase subunit)
1038	Endoplasmic reticulum resident protein 44	Q9D1Q6	Erp44	1.6	0.0041	ER	**Protein folding**, cell redox homeostasis
1593	Enoyl-CoA hydratase, mitochondrial	Q8BH95	Echs1	1.5	0.0149	Mit	**Metabolic process** (lipid metabolism)
1724	Ferritin light chain 1	P29391	Ftl1	1.7	0.0086	-	Cellular iron ion homeostasis
1718	Glucosamine 6-phosphate N-acetyltransferase	Q9JK38	Gnpnat1	1.5	0.017	**Golgi,** ER-Golgi intermediate	**Metabolic process** (glucosamine metabolism)
519	Heat shock protein 75 kDa, mitochondrial	Q9CQN1	Trap1	1.5	0.0016	Mit	**Protein folding** (chaperone activity), response to oxidative stress
1362	Heat shock protein HSP 90-beta	P11499	Hsp90ab1	1.5	0.0009	**Cyt**, Mit	**Protein folding** (chaperone activity), response to stress
2113	Heterogeneous nuclear ribonucleoprotein C1/C2	Q9Z204	Hnrnpc	1.5	0.0059	Nuc	mRNA processing
1429	Hydroxyacyl-coenzyme A dehydrogenase, mitochondrial	Q61425	Hadh	1.5	0.0066	**Mit**, Nuc, Cyt	**Metabolic process** (lipid metabolism)
1234	Isocitrate dehydrogenase [NAD] subunit alpha, mitochondrial	Q9D6R2	Idh3a	1.5	0.0035	Mit	**Energy metabolism** (TCA cycle), NADH metabolic process
2090	Lamin-B1	P14733	Lmnb1	1.5	0.0154	Nuc	**Components of nuclear lamina**, regulation of JNK cascade and cyclin-dependent protein kinase activity
1584	NFU1 iron-sulfur cluster scaffold homolog, mitochondrial	Q9QZ23	Nfu1	1.5	0.0176	**Cyt**, Mit, Nuc	Iron-sulfur assembly
1057	Ornithine aminotransferase, mitochondrial	P29758	Oat	1.5	0.0083	**Mit**, Cyt	**Metabolic process** (arginine and proline metabolism)
804	Endoplasmic reticulum resident protein 57	P27773	Pdia3	2.2	0.0028	ER	**Protein folding**, cell redox homeostasis
1576	Putative ATP-dependent Clp protease proteolytic subunit, mitochondrial	O88696	Clpp	1.6	0.0082	Mit	Proteolysis
2104	Pyruvate dehydrogenase E1 component subunit alpha, somatic form, mitochondrial	P35486	Pdha1	1.5	0.0022	Mit	**Energy metabolism** (pyruvate dehydrogenase subunit)
371	Src substrate cortactin	Q60598	Cttn	1.8	0.0029	Cyt	Cytoskeleton organisation
1700	Superoxide dismutase [Mn], mitochondrial	P09671	Sod2	1.5	0.0084	Mit	**Cell redox homeostasis**, response to oxidative stress
1453	Voltage-dependent anion-selective channel protein 1	Q60932	Vdac1	1.8	0.0041	**Mit**, Plasma membrane	**Transport** (ion transport), neuron-neuron synaptic transmission
2091	Voltage-dependent anion-selective channel protein 2	Q60930	Vdac2	1.5	0.0044	Mit	**Transport** (ion transport), regulation of intrinsic apoptotic signalling
2144	V-type proton ATPase subunit B, brain isoform	P62814	Atp6v1b2	1.5	0.01	Plasma membrane, Cyt, Golgi	ATP hydrolysis coupled proton transport
Down regulated proteins							
2083	26S proteasome non-ATPase regulatory subunit 11	Q8BG32	Psmd11	−1.6	0.0020	**Cytoplasm** (proteosome)	**Proteolysis** (regulatory subunit of 26S proteosome)
1643	28 kDa heat- and acid-stable phosphoprotein	Q3UHX2	Pdap1	−1.8	0.0110	–	Cell growth and proliferation (PDGF-associated protein)

Table 1 (*continued*)

Spot#[a]	Protein name	Accesion number[b]	Gene symbol	Fold change	*t*-Test[c]	Cellular localisation[a]	Biological process[d]
1147	Activator of 90 kDa heat shock protein ATPase homolog 1	Q8BK64	Ahsa1	−1.5	0.0191	**Cyt**, ER	**Protein folding** (co-chaperone that activates Hsp90 ATPase activity)
1102	Adenosylhomocysteinase	P50247	Ahcy	−1.5	0.0019	Cytoplasm	**Metabolic process** (amino-acid metabolism)
2174	Adenosylhomocysteinase	P50247	Ahcy	−1.7	0.0165	Cytoplasm	**Metabolic process** (amino-acid metabolism)
724	Asparagine synthetase [glutamine-hydrolyzing]	Q61024	Asns	−1.7	0.0043	Cyt	**Metabolic process** (amino-acid metabolism), response to glucose starvation, toxin and amino acid stimulus
732	Asparagine synthetase [glutamine-hydrolyzing]	Q61024	Asns	−1.5	0.0001	Cyt	**Metabolic process** (amino-acid metabolism), response to glucose starvation, toxin and amino acid stimulus
735	Asparagine synthetase [glutamine-hydrolyzing]	Q61024	Asns	−1.7	0.0064	Cyt	**Metabolic process** (amino-acid metabolism), response to glucose starvation, toxin and amino acid stimulus
745	Asparagine synthetase [glutamine-hydrolyzing]	Q61024	Asns	-1.6	0.0001	Cyt	**Metabolic process** (amino-acid metabolism), response to glucose starvation, toxin and amino acid stimulus
1996	Aspartyl-tRNA synthetase, cytoplasmic	Q922B2	Dars	−1.5	0.0002	Cytoplasm	tRNA processing
455	Cytoplasmic dynein 1 intermediate chain 2	O88487	Dync1i2	−2.7	0.0004	Cytoplasm	**Cytoskeleton organisation** (intracellular retrograde transport)
716	Dihydropyrimidinase-related protein 3	Q62188	Dpysl3	−1.8	0.0029	Cytoplasm	**Cytoskeleton organisation** (axon guidance, actin crosslink formation)
2098	Dihydropyrimidinase-related protein 3	Q62188	Dpysl3	−1.5	0.0083	Cytoplasm	**Cytoskeleton organisation** (axon guidance, actin crosslink formation)
2195	DNA damage-binding protein 1	Q3U1J4	Ddb1	−1.6	0.0053	**Nuc**, Cytoplasm	**DNA repair** (response to DNA damage stimulus), ubiquitination and subsequent proteosomal degradation of target proteins
1077	Eukaryotic translation initiation factor 3 subunit G	Q9Z1D1	Eif3 g	−1.7	0.0155	Cytoplasm, Nuc	Translation
444	Ezrin	P26040	Ezr	−1.5	0.0056	**Cytoskeleton**, cyt, plasma membrane	**Cytoskeleton organisation** (actin filament bundle assembly)
1167	Glutaredoxin-3	Q9CQM9	Glrx3	−1.5	0.0067	Cytoplasm	Cell redox homeostasis
835	Inosine-5′-monophosphate dehydrogenase	P24547	Impdh2	−1.8	0.01	Cytoplasm, Nuc	**Metabolic process** (purine metabolism)
2027	Inositol-3-phosphate synthase 1	Q9JHU9	Isyna1	−1.7	0.0148	Cytoplasm	**Metabolic process** (inositol biosynthesis)
2111	Leukotriene A-4 hydrolase	P24527	Lta4 h	−1.5	0.0170	Cytoplasm, Nuc	**Metabolic process** (leukotriene biosynthesis), proteolysis
717	Phosphoglucomutase-1	Q9D0F9	Pgm1	−1.9	0.0091	**Cyt**, Cytoskeleton	**Metabolic process** (glucose metabolism)
2030	Programmed cell death 6-interacting protein	Q9WU78	Pdcd6ip	−1.5	0.0021	**Cyt**, Cytoskeleton	**Cell growth and proliferation** (regulation of both cell proliferation and apoptosis)
1045	Proliferation-associated protein 2G4	P50580	Pa2g4	−1.5	0.0016	**Nuc**, Cytoplasm	**Cell growth and proliferation** (rRNA processing, regulation of transcription)
798	Protein RCC2	Q8BK67	Rcc2	−1.8	0.0134	**Nuc**, Cytoplasm	Cell growth and proliferation
1512	Purine nucleoside phosphorylase	P23492	Pnp	−1.6	0.0004	**Cyt**, Cytoskeleton	**Metabolic process** (purine metabolism)
452	Radixin	P26043	Rdx	−1.8	0.0049	**Cytoskeleton**, Plasma membrane	**Cytoskeleton organisation** (actin filament capping)
1146	Septin-5	Q9Z2Q6	Sept5	−1.5	0.0105	**Cytoskeleton**, Plasma membrane	**Cytoskeleton organisation** (regulation of exocytosis and cell division)
1525	tRNA (adenine-N(1)-)-methyltransferase catalytic subunit TRMT61A	Q80XC2	Trmt61a	−1.7	0.0044	Nuc	tRNA processing
2031	tRNA (cytosine-5-)-methyltransferase NSUN2	Q1HFZ0	Nsun2	−1.5	0.0016	**Nuc**, Cytoplasm	tRNA processing
91	Vinculin	Q64727	Vcl	−1.7	0.0017	**Cytoskeleton**, Plasma membrane	**Cytoskeleton organisation** (regulation of cell migration)

[a] Numbers are identical with spot numbers illustrated in Fig. 2.
[b] Swiss-Prot/TrEMBLE accession number.
[c] Significance level of Student's *t*-test calculated by Progenesis SameSpots software ($p < 0.05$ was considered statistically significant).
[d] Cell compartment (Cyt – cytosol, ER – endoplasmic reticulum, Nuc – nucleus, Mit – mitochondria) and biological process terms assigned to each protein. The most common terms are in bold and used for subsequent categorisation (Fig. 3).
[e] This spot was not detected (n.d.) on control gels.

parent ion tolerance of 50 ppm (6 ppm average mass error of validated hits, 95% below 20 ppm). An iodoacetamide derivative of cysteine was specified as a fixed modification in Mascot, while the oxidation of methionine was specified as a variable modification. No efforts were made to identify protein modifications, isoforms or alternative splicing products, the applied protocols were focused on identification of proteins. Theoretical pI and Mw values of identified proteins were calculated using the Compute pI/Mw tool at the Expasy website (http://www.expasy.org/tools/pi_tool.html). Scaffold (version Scaffold_3_05_00, Proteome Software Inc., Portland, OR) was used to validate MS/MS based identifications of peptides and proteins. Protein identifications

were accepted if they could be established at greater than 95.0% probability and contained at least four identified peptides. For multiple identifications, only the protein assumed to be present in largest amount was used for subsequent categorisation. Protein quantity was estimated by the total number of MS/MS spectra assigned to the identified protein.

2.5. Functional classification

Proteins were categorised manually according to the information found on the Uniprot (www.uniprot.org) and/or on the Gene-Ontology (GO) websites (www.geneontology.org). As most of the proteins have multiple roles and/or localisations, for manual categorisation only the most common role and localisation of each protein were used. However, the multiple cellular localisations and biological roles of each protein were summarised in Table 1. Besides the manual classification, a GO-based analysis was performed using the Database for Annotation, Visualisation and Integrated Discovery (DAVID) web-based knowledge database (Huang da et al., 2007). DAVID provides a functional annotation tool which performs a gene-GO term enrichment analysis to find the most significant GO terms associated with a given list compared to background protein set – in our case the whole mouse genome annotated in DAVID. In order to present which categories were significantly overrepresented in our list "cellular compartment"- and "biological process"-associated GO terms were analysed and the significance level was set to $p < 0.05$. A network analysis of proteins was also performed using STRING web-based interaction database (Jensen et al., 2008). After exporting the data from STRING, the network was visualised and edited using Medusa 1.5 graph visualisation tool (Hooper and Bork, 2005).

2.6. Western blot

Whole cell lysates from two independent cell passages ($n = 6$) containing 20 μg of total protein were separated by 8% SDS–PAGE (6×8 cm) and transferred onto nitrocellulose membranes (Bio-Rad). After blocking in Tris-buffered saline (TBS) containing 5% bovine serum albumin (BSA), the membrane was incubated with anti-Grp78 (Stressgen, Victoria British Columbia, Canada, 1:2000) diluted in TBS containing 0.1% Tween-20 and 5% BSA (TBST-BSA), then incubated with horseradish peroxidase (HRP)-conjugated anti-mouse IgG (Dako, Glostrup, Denmark, 1:10000) also diluted in TBST-BSA. After probing the membranes with anti-Grp78 the same membranes were stripped in buffer containing 0.2 M glycine pH 2.0, 0.1% SDS, 1% Tween-20 and re-probed with anti-beta-actin (Sigma–Aldrich, 1:1000). Then, Grp78 intensities were normalised to beta-actin band intensities.

Subcellular fractions were made by using Qproteome cell compartment kit (Qiagen, Valencia, CA, USA) according to the manufacturer's instructions. A volume of fractions containing 10 μg of total protein was loaded onto polyacrylamide gels. The subsequent western blot procedure was performed as described above. Here, the Grp78 band intensities were normalised using the total protein intensities of the same membrane visualised by Ponceau red staining (Sigma–Aldrich). Supplementary Fig. 1 presents the Ponceau red stained membranes. A volume of fractions containing 10 μg of total proteins were also separated by 15% SDS–PAGE and after the transfer the nitrocellulose membrane was incubated with anti-histone H3 (Abcam, Cambridge, UK, 1:10000) and with HRP-conjugated anti-rabbit IgG (Dako, 1:10000).

For each Western blot the immune complexes were detected with a chemo-luminescent substrate of peroxidase (Pierce, Rockford, IL, USA) according to the manufacturer's instructions by exposure to X-ray film (Sigma–Aldrich). X-ray films were digitised on a FLA-5100 laser scanner using the digitising mode at 50 μm resolution. Ponceau red stained membranes were also digitised on the same scanner with the same parameters. The digitised images were analysed by ImageJ software (Schneider et al., 2012).

2.7. Statistical analysis

In 2-DE, software-based analysis was filtered to detect different spots having a $p < 0.05$, power $\geqslant 80\%$ and fold change $\geqslant 1.5$. To control the multiple testing we used the sequential goodness of fit (SGoF) statistical test with SGoF software, where only spots having SGoF-adjusted $p < 0.05$ were accepted as significant difference (Carvajal-Rodriguez et al., 2009). For further statistical analysis the normalised spot volumes were exported from Progenesis SameSpots software to calculate the coefficient of variation (CV%), which is defined as the ratio of the standard deviations of normalised spot volumes to the means, expressed in percentage terms. The variations of each group were characterised by the median CV% and the CV% that encompassed 95% of the spots (95th percentile position). In the EZ4U and Western blot analysis, the differences between treated and control samples were determined by applying Student's *t*-test with a two-tailed distribution. Student's *t*-test was performed with or without Welch's correction depending on the equality of variances of compared groups calculated by F-test. Statistical analysis was performed on GraphPad Prism 5 software (GraphPad software, CA, USA). Here a $p < 0.05$ was considered statistically significant.

3. Results

3.1. Cell viability and morphological study

To analyse the toxic effect of TG, murine N2a neuroblastoma cells were incubated with 1 μM TG for 24 or 48 h. Cell viability assays revealed a time-dependent effect of TG toxicity: cell viability reduced significantly after 24 h of treatment (reduced to 81%), and a more striking decrease occurred after 48 h of treatment, when the viability reduced to 35% (Fig. 1A). Morphological changes could also be detected after 24 h of TG treatment resulting in a reduction of neurites. However, the degeneration of cellular body and neurites were more remarkable after 48 h of treatment (Fig. 1B).

3.2. Two-dimensional electrophoresis and mass-spectrometric identification

Murine N2a neuroblastoma cells were exposed to 1 μM TG for 24 h. After treatment the cells were harvested and the lysates were separated by 2-DE. Software-based image analysis of 2-DE gels gave 910 spots that were 100% matched across all gels. Moreover, by using the SameSpots approach in the analysis, the spots compared between the gels had identical boundaries. Spot intensity data were used to assess variation in expression, as characterised by CV%. The median CV% value was 10.7 in the control group and 10.3 in the treated group. However, 95% of the spots had a CV% below 24.9 in the control group and 22.9 in the treated group.

Software-based analysis revealed 63 (33 up- and 30 downregulated) significantly altered spots (Fig. 2). 95 proteins were identified by MS, since more than one protein could be identified from same spots or the same protein could sometimes be identified from different spots (Supplementary Table 1). For multiple identifications, only the protein identified with the largest amount was used for subsequent functional classification (Table 1). Protein quantity was estimated by the total number of MS/MS spectra assigned to the identified protein. On the whole, 58 proteins (33 up- and 25 downregulated) were categorised according to function and cellular localisation.

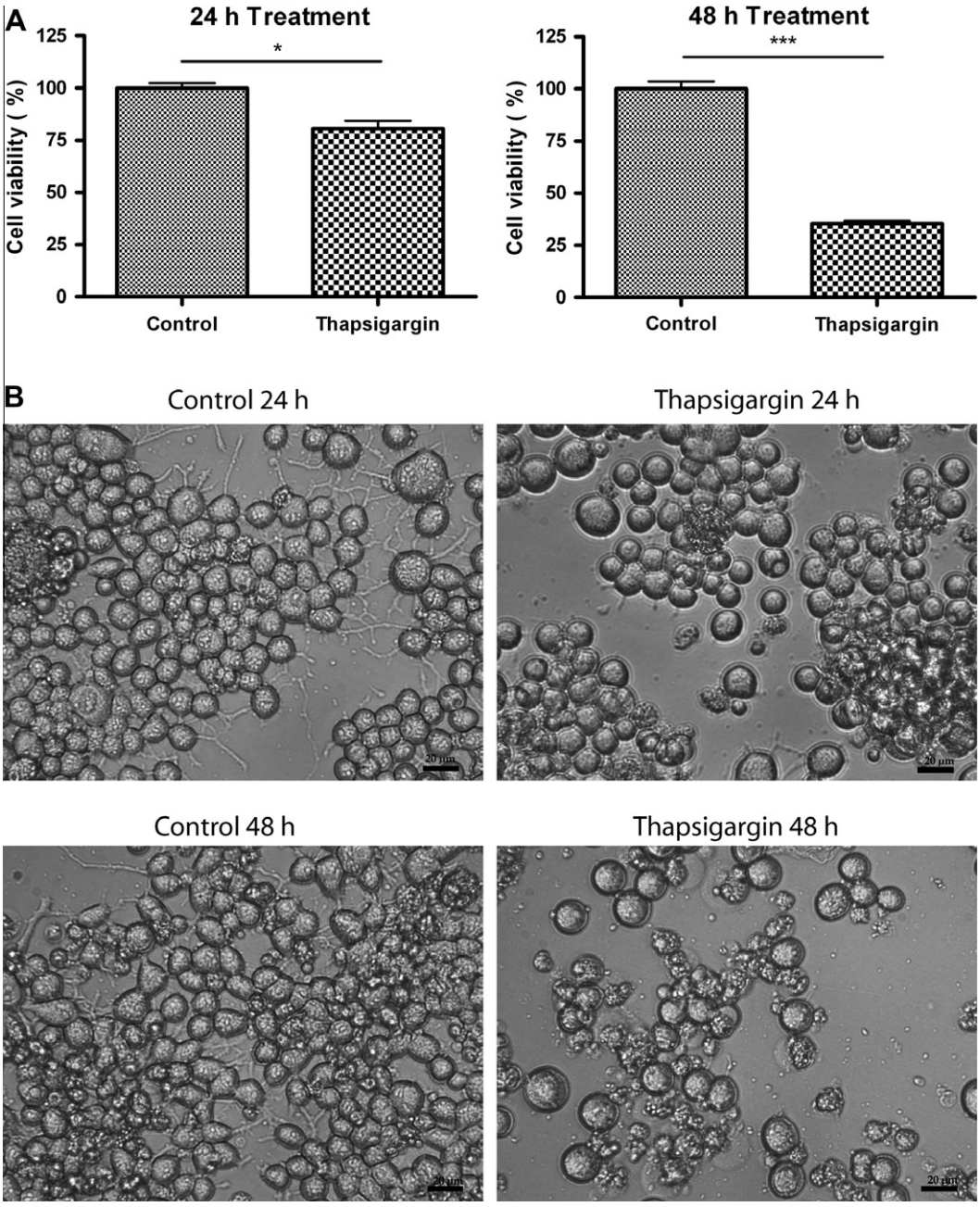

Fig. 1. Toxic effect of thapsigargin (TG) measured by EZ4U cell viability assay. Viability of N2a cell reduced significantly after 24 or 48 h of treatment with 1 μM TG (A). Major morphological changes could also be detected after TG treatment resulted in the reduction of neurites (B). Data values are presented as mean ± S.E.M. ($^{*}p < 0.05$, $^{***}p < 0.001$). Scale bar presents 20 μm.

3.3. Classification of identified proteins

The manual categorisation of the identified proteins revealed marked changes in the N2a cell proteome that reflect alterations of the main cellular functioning (Fig. 3). Taking into consideration only the most common biological functions, the majority of the upregulated proteins have roles in metabolic processes (22%), energy metabolism (21%), protein folding (18%) and proteolysis (9%). In addition, most of the upregulated proteins are localised to mitochondria (58%) reflecting relatively high number of proteins involved in energy related processes. The manual classification of the upregulated proteins was confirmed by the GO-based analysis using DAVID functional annotation tool (Supplementary Table 2). Here, the most significant "biological process"-associated GO term is the "generation of precursor metabolites and energy" (GO:0006091, $p = 4.20E-07$). Moreover, the web-based analysis also revealed other significantly enriched, metabolic process and protein folding associated GO terms. DAVID analysis also confirmed the cellular localisation of the upregulated proteins, as the most significant GO terms was the "mitochondrion" (GO:0005739, $p = 4.60E-18$). Besides the mitochondrion-associated GO terms, ER-related terms were also enriched significantly, such as "endoplasmic reticulum lumen" (GO:0005788, $p = 3.34E-04$). Four upregulated ER proteins were identified: calreticulin (Calr), ER resident protein 44 (ERp44), ERp57 and Grp78. These proteins each have a role in protein folding and their

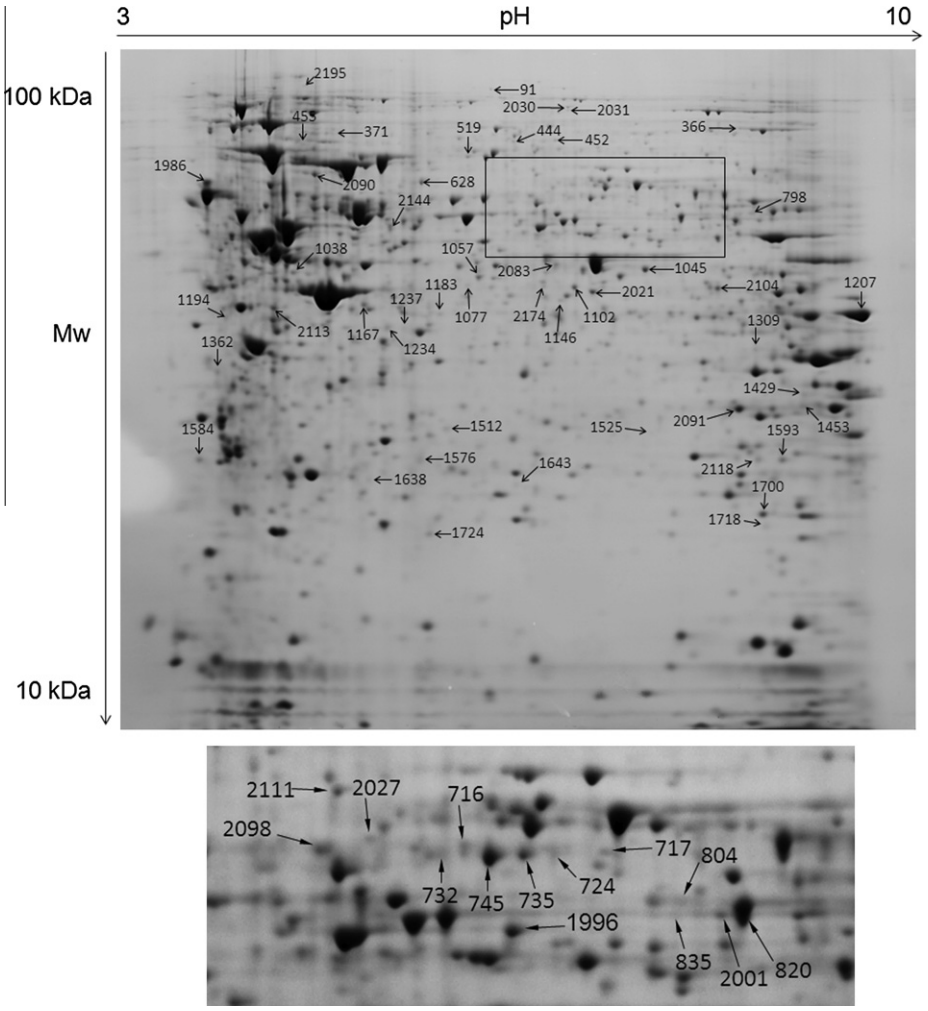

Fig. 2. Representative 2-DE image of a thapsigargin-treated N2a cell lysate. Gel area in rectangle magnified in the bottom image.

increased expression could also be related to ER stress. Amongst the identified ER resident proteins, Calr showed the most striking expression difference after TG-treatment (Supplementary Fig. 2).

The distribution and localisation of the downregulated proteins amongst functional groups differed from that of the upregulated proteins. After manual categorisation most of the downregulated proteins are related to metabolic processes (28%), cytoskeleton organisation (24%), cellular growth and proliferation (16%) and tRNA processes (12%). The vast majority of the downregulated proteins belong to the cytoplasmic (40%), cytosolic (20%), nuclear (20%) or cytoskeletal (16%) proteins. DAVID analysis of downregulated proteins revealed less, significantly enriched, "biological process"-associated GO terms, than the analysis of the upregulated proteins did. Most of these terms are related to cellular metabolic processes and RNA metabolism, which is in correlation with manual categorisation. DAVID analysis also confirmed the cellular localisation of the downregulated proteins, as the most significantly enriched terms were the "cytoplasm" (GO:0005737, $p = 6.52E-06$), "cytoskeleton" (GO:0005857, $p = 7.81E-04$) and "cytosol" (GO:0005829, $p = 7.46E-03$). However, DAVID analysis revealed only one nucleus-associated term, "nucleolus" (GO:0005730), which was not significantly enriched ($p = 6.8E-02$), therefore it was not listed in Supplementary Table 2.

In addition to the manual and GO-based categorisation, interaction analysis was performed using STRING database. Here, up- and downregulated proteins were analysed together in order to find possible interactions between proteins showing significant alterations after TG treatment. Interaction analysis revealed that most of these proteins are connected to each other (nodes = 52, edges = 240), although after increasing the confidence value of interactions to medium level (0.4, default value in STRING database) the number of interacting proteins (nodes = 27) and the number of interactions (edges = 45) were reduced dramatically (Fig. 4A and B). In order to see which cellular processes were associated with the most confident interactions, a DAVID analysis was performed using the sublist of the above mentioned 27 interacting proteins (Fig. 4C). Here, the most significantly enriched "biological process"-associated GO term was the "generation of precursor metabolites and energy" ($p = 1.72E-07$). Besides this, the vast majority of GO terms were related to different metabolic processes, such as nucleotide, amino acid and glucose metabolism, but the "protein folding" GO term was also enriched significantly ($p = 1.23E-03$).

3.4. Grp78 expression

Besides the 2-DE analysis, the upregulated expression of Grp78 was also confirmed by western blot. Here, Grp78 displayed a significant increase in protein expression after analysing whole cell protein extracts ($p = 0.046$, fold change = 2.38) (Fig. 5). Due to the multiple cellular localisations of Grp78, the expression of this protein was also investigated in different subcellular fractions. Interestingly, the expression of Grp78 was significantly elevated only in the cytosolic ($p = 0.035$, fold change = 1.29) and nuclear fractions

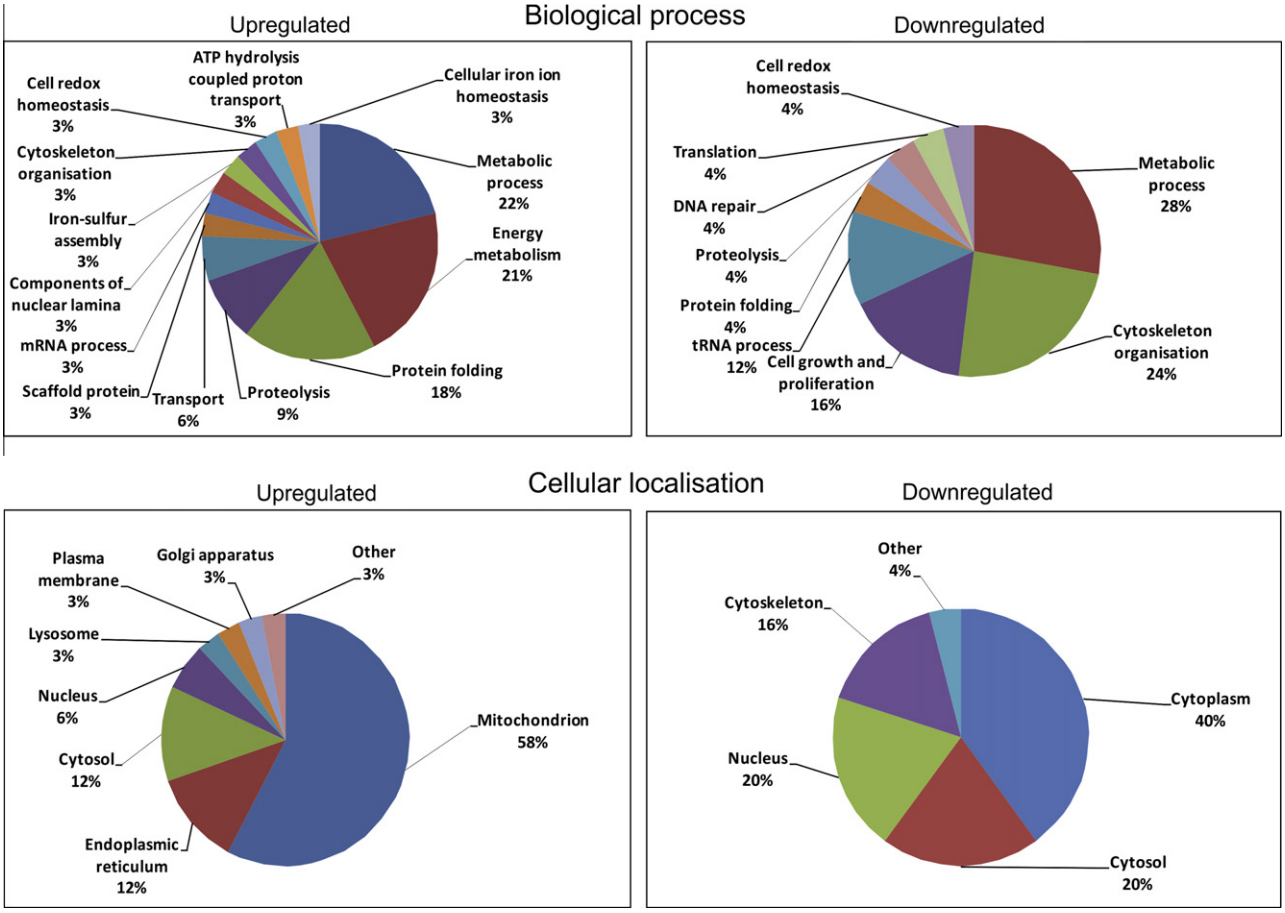

Fig. 3. Categorisation of identified proteins based on the most common functional properties and cellular localisations of each protein listed in Table 1.

($p = 0.003$, fold change = 2.51), but not in the membrane/organelle fraction ($p = 0.590$, fold change = 0.88) which contained the ER luminal proteins (Fig. 5). As the most striking induction was detected in the nuclear fraction the purity of this protein extract was verified by anti-histone H3 Western blot analysis and compared to the other subcelluar fractions (Supplementary Fig. 3). Here, histone H3 has been detected only from the nuclear fraction.

4. Discussion

ER stress and the UPR are implicated in several human diseases, such as diabetes, cardiovascular diseases and neurodegenerative diseases (Zhao and Ackerman, 2006). Further studies are therefore indispensable to characterise the signalling pathways and metabolic processes related to this cellular stress response.

Exploiting the advantages of high resolution proteomic techniques, Amodio et al. (2011) provided a proteome-wide study in TG-treated human hepatoma (Huh7) cells. In that study, several differentially expressed proteins were identified with Ca^{2+}-dependent functioning, which correlated well with perturbation of Ca^{2+} homeostasis during ER stress. Assuming a remarkable difference between hepatoma and neuronal cells, we performed a comparative 2-DE analysis using control and TG-treated murine N2a neuroblastoma cell lysates. The weak overlap between our and previously presented (Amodio et al., 2011) proteomic signatures in TG-treated cells suggests that ER stress progression could be significantly different between different tissue culture cells, such as hepatoma and neuronal cell lines. Therefore detailed analysis of ER stress-related processes in different cells types are mandatory. In our study, besides proteomic analysis cell viability assay and morphological studies were also performed. TG-induced cell death has been observed in several cell types (Rao et al., 2004; Torres et al., 2010). Our results further revealed a significant decrease in cell viability after 24 h of TG treatment and a more striking decline after only 48 h of treatment. Morphological studies also showed a more remarkable degradation of the cellular body and neurites after 48 h of treatment. A similar, delayed effect of low concentration TG (up to 3 μM) on cell viability has also been published (Park and Kim, 2011).

Comparative 2-DE results revealed numerous significant protein expression changes (33 up- and 30 downregulated spots), which reflected marked alterations in the N2a cell proteome after 24 h of TG treatment. The moderate decrease of cell viability after 24 h of treatment suggested that this period of treatment was optimal to obtain ER stress related proteomic signatures in N2a cells. To demonstrate the reproducibility and reliability of our 2-DE gels, total variations were calculated for each group and characterised by CV%. Observed variability was favourable when compared with others and our previous research papers (Molloy et al., 2003; Foldi et al., 2011).

After MS analysis of gel samples, 58 proteins (33 up- and 25 downregulated) were used for subsequent categorisation. Most of the upregulated proteins have roles in energy-related processes, protein folding and cellular stress. In addition, the vast majority of these proteins belong to the mitochondrial or ER proteome. The elevated expression of ER proteins could confirm the activation of TG-induced ER stress.

It is well known that the tight functional and structural link between ER and mitochondria is fundamental for the maintenance of

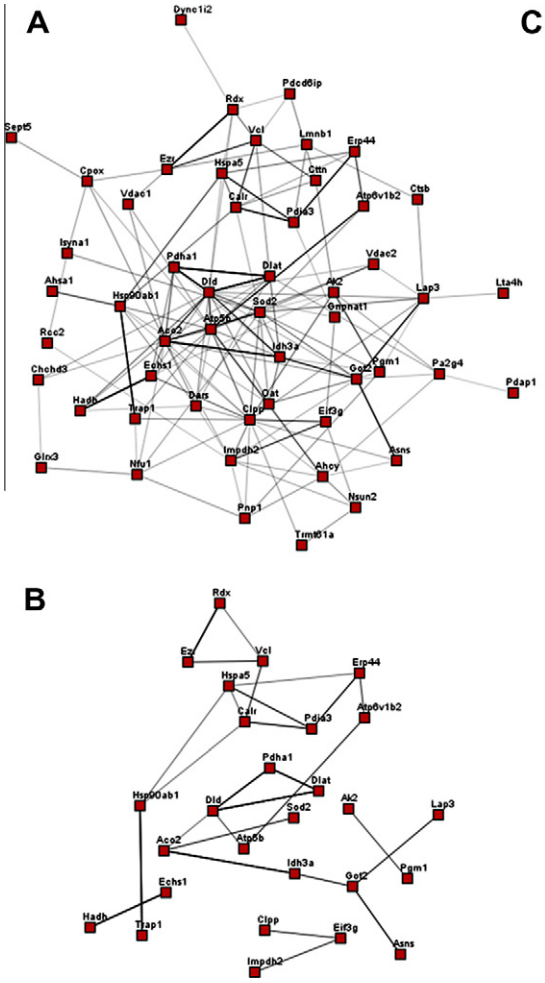

C

GO term	Count	*p*-value
GO:0006091~generation of precursor metabolites and energy	8	1.72E-07
GO:0008152~metabolic process	22	1.09E-04
GO:0045333~cellular respiration	4	1.29E-04
GO:0044238~primary metabolic process	20	4.28E-04
GO:0015980~energy derivation by oxidation of organic compounds	4	5.78E-04
GO:0019752~carboxylic acid metabolic process	6	1.06E-03
GO:0043436~oxoacid metabolic process	6	1.06E-03
GO:0006082~organic acid metabolic process	6	1.07E-03
GO:0042180~cellular ketone metabolic process	6	1.19E-03
GO:0006457~protein folding	4	1.23E-03
GO:0006084~acetyl-CoA metabolic process	3	1.23E-03
GO:0044271~nitrogen compound biosynthetic process	5	1.52E-03
GO:0006732~coenzyme metabolic process	4	1.73E-03
GO:0010149~senescence	2	3.37E-03
GO:0051186~cofactor metabolic process	4	3.43E-03
GO:0006119~oxidative phosphorylation	3	3.98E-03
GO:0055114~oxidation reduction	6	4.67E-03
GO:0045454~cell redox homeostasis	3	4.85E-03
GO:0009152~purine ribonucleotide biosynthetic process	3	1.39E-02
GO:0009260~ribonucleotide biosynthetic process	3	1.49E-02
GO:0009150~purine ribonucleotide metabolic process	3	1.70E-02
GO:0009259~ribonucleotide metabolic process	3	1.86E-02
GO:0019725~cellular homeostasis	4	1.94E-02
GO:0006164~purine nucleotide biosynthetic process	3	2.21E-02
GO:0006006~glucose metabolic process	3	2.31E-02
GO:0045429~positive regulation of nitric oxide biosynthetic process	2	2.50E-02
GO:0009067~aspartate family amino acid biosynthetic process	2	2.67E-02
GO:0009056~catabolic process	6	2.74E-02
GO:0006163~purine nucleotide metabolic process	3	2.95E-02
GO:0045428~regulation of nitric oxide biosynthetic process	2	3.16E-02
GO:0019318~hexose metabolic process	3	3.27E-02
GO:0009165~nucleotide biosynthetic process	3	3.45E-02
GO:0034404~nucleobase, nucleoside and nucleotide biosynthetic process	3	3.63E-02
GO:0034654~nucleobase, nucleoside, nucleotide and nucleic acid biosynthetic process	3	3.63E-02
GO:0009066~aspartate family amino acid metabolic process	2	3.65E-02
GO:0065008~regulation of biological quality	6	3.66E-02
GO:0006099~tricarboxylic acid cycle	2	3.81E-02
GO:0046356~acetyl-CoA catabolic process	2	3.98E-02
GO:0005996~monosaccharide metabolic process	3	4.08E-02
GO:0009060~aerobic respiration	2	4.46E-02
GO:0022904~respiratory electron transport chain	2	4.62E-02
GO:0009109~coenzyme catabolic process	2	4.79E-02

Fig. 4. STRING-based network analysis of identified proteins after thapsigargin treatment of N2a cells. The majority of deregulated proteins were connected to each other (**A**), although using more stringent confidence value of interactions (medium level, 0.4) the number of connections were reduced dramatically (**B**). GO-based functional categorisation was performed using the sublist of proteins connecting to each other with medium or higher level of confidence (**C**).

cellular homeostasis. It also controls cell metabolism and determines cell fate under stress conditions (Giorgi et al., 2009). Moreover, the two organelles physically interact through mitochondrial associated membranes (MAM), which provide direct communication between the ER and mitochondria (Vance, 1990). Mitochondrial voltage-dependent anion channel (VDAC) and ER inositol trisphosphate receptor (IP_3R) physically interact through the chaperone Grp75, an interaction that mediates metabolic flow, Ca^{2+} transfer and cell death signalling between ER and mitochondria (Szabadkai et al., 2006). On the MAM, ER folding chaperones such as calnexin and Calr and thioredoxin-related oxidoreductases such as ERp44 and ERp57 appear to modulate ER Ca^{2+} signalling (Simmen et al., 2010). Mitochondrial uptake of Ca^{2+} released by ER stimulates mitochondrial ATP production by the activation of mitochondrial ATP-synthase and several dehydrogenases such as, pyruvate dehydrogenase (PDH), isocitrate dehydrogenase (IDH) and oxoglutarate dehydrogenase (Decuypere et al., 2011; Denton, 2009; Griffiths and Rutter, 2009). Growing evidence suggests that early phases of ER stress trigger an enhanced mitochondrial metabolism that depends critically upon organelle coupling and Ca^{2+} transfer. However, if stress is prolonged, this response promotes mitochondrial collapse and subsequent cell death (Bravo et al., 2012). In our study a relatively high number of upregulated ER and mitochondrial proteins were identified, which had roles in protein folding, the regulation of the crosstalk between ER and mitochondria, and in mitochondrial energy metabolism. Our 2-DE analysis also revealed upregulated expression of mitochondrial VDACs, which are involved in the formation of MAM.

Grp78 is an abundant Ca^{2+}-dependent ER chaperone which plays an essential role in the folding of newly synthesised proteins. Its expression is markedly induced under conditions that lead to the accumulation of unfolded proteins in the ER (Gething, 1999). Beyond its role as an ER chaperone, Grp78 has multiple localisations with several atypical functions in cell viability and cellular signalling (Ni et al., 2011). Grp78 has been detected from cytosolic fraction of C6 astroglia cells (Qian et al., 2000). Moreover, TG treatment has induced Grp78 expression in cytosolic and nuclear subcellular fractions of human embryonic 293T cells (Rao et al., 2002). In our study, Grp78 also displayed a significant protein expression increase analysing whole cellular extracts after TG treatment. Besides whole cellular lysates, we also analysed the Grp78 expression in typical subcellular fractions. Interestingly, significant elevation of Grp78 expression could be detected only from cytosolic and nuclear fractions. Thus, our results also support the fact that Grp78 has multiple localisations and suggest that isoforms of Grp78 may exist and are localised specifically to different cell compartments. A novel cytosol specific isoform of Grp78 has been described that regulates the ER stress signalling (Ni et al., 2009). Besides the existence of different Grp78 isoforms, the induced level of this protein in different subcellular factions also suggests that ER stress could promote the redistribution of Grp78 into soluble and nuclear fractions (Rao et al., 2002). In our study, the

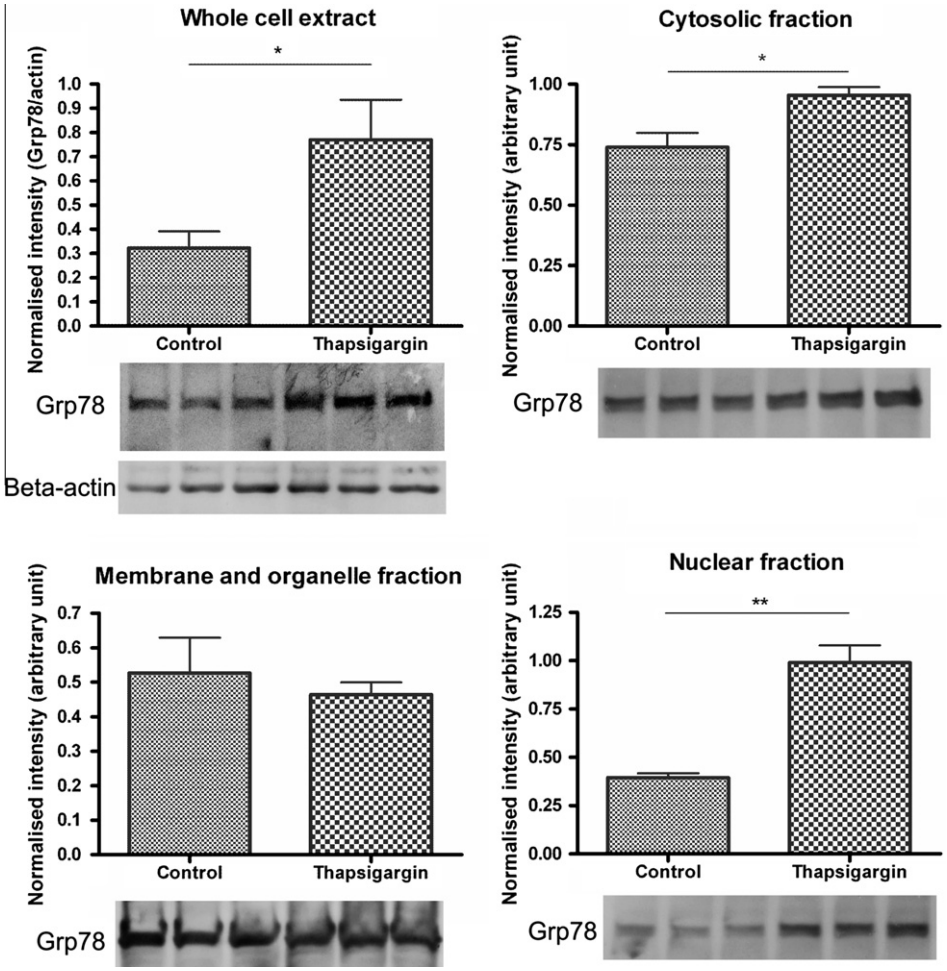

Fig. 5. Protein expression of Grp78 after thapsigargin treatment of N2a cells. Western blot analysis revealed significant upregulation of Grp78 in the whole cell lysate, cytosolic and nuclear fractions. Band intensities were normalised with beta-actin or the total protein intensities visualised by Ponceau red staining. Data values are presented as mean ± S.E.M. ($^{*}p < 0.05$, $^{**}p < 0.01$).

remarkable increase of nuclear Grp78 suggests that this protein should have specific interaction partners (protein, nucleic acid) in the nucleus and could directly regulate the gene expression during ER stress. However, further investigations are required to elucidate the nuclear function of Grp78.

After 2-DE analysis of N2a cell lysates, Calr displayed the most striking difference between control and TG-treated groups. Calr is involved in the folding of newly synthesised proteins, but also acts as an ER luminal Ca^{2+}-buffering chaperone regulating intracellular Ca^{2+} homeostasis (Michalak et al., 2009). We also identified two additional ER resident proteins that have protein disulphide-isomerase (PDI) activity (ERp44 and Erp57). PDIs primarily have a role in oxidative protein folding by catalysing the exchange of a disulphide bond with or within substrates. However, their function has been extended in recent years to include roles in other processes, such as ER-associated protein degradation and Ca^{2+} homeostasis (Appenzeller-Herzog and Ellgaard, 2008). ERp44 is involved in the control of oxidative protein folding, but can also regulate the ER intraluminal and cytosolic Ca^{2+} concentration by the modulation of IP_3R1 (Anelli et al., 2002; Higo et al., 2005). ERp57 (also known as protein disulphide-isomerase-A3) can also modulate ER Ca^{2+} signalling by the interaction with SERCA2b and Calr (Frickel et al., 2002; Li and Camacho, 2004).

Besides the proteins involved in protein folding and the regulation of the crosstalk between ER and mitochondria, we also identified upregulated proteins associated with mitochondrial energy metabolism. All of the three subunits of PDH enzyme complex (dihydrolipoyl dehydrogenase, dihydrolipoyllysine-residue acetyltransferase and pyruvate dehydrogenase) had increased protein expression. Moreover, aconitate hydratase and IDH were also induced after TG treatment. These and the PDH complex proteins are involved in the tricarboxylic acid cycle and some of them are modulated by Ca^{2+} signalling. After analysing the proteomic changes of TG-treated N2a cell lysates, a notable portion of the upregulated proteins have proteolytic enzyme activity. Amongst these proteins, cathepsin B had the most striking elevation in its protein expression (2.2-fold). Cathepsin B is a cystein protease localised in the lysosomes. Interestingly, increased cytosolic Ca^{2+} concentration can induce lysosomal cathepsin B leakage by the activation of calpain (Yamashima et al., 1998). This 'calpain–cathepsin' hypothesis suggests that there is crosstalk between apoptotic and necrotic neuronal cell death, which could have an important role in neuronal damages, such as ischaemic injuries and Alzheimer's disease (Yamashima, 2004).

Substantial portion of the downregulated proteins were associated with cytoskeleton organisation. Interestingly most of them were involved in the maintenance and dynamics of the actin-cytoskeleton. Cytoskeleton-determined neuronal morphology is a key to the transmission of signals in the nervous system (Stiess and Bradke, 2011). In our study the downregulation of several cytoskeleton-associated proteins correlated with morphological changes after TG-treatment of N2a cells. Amongst up- and downregulated

protein groups we also identified numerous enzymes that have a role in different metabolic processes, such as lipid metabolism, amino acid metabolism and nucleotide metabolism. Interestingly, the protein expression of the mitochondrial enzymes was increased uniformly, whereas, all of the identified cytosolic enzymes displayed downregulation. This further suggests that the metabolic activity of the mitochondria is stimulated during the early phases of ER stress.

5. Conclusions

Our study aimed to provide a representative proteomic signature of ER stress in N2a neuroblastoma cells. As this cell line is widely used in neurobiological investigations our findings could help to understand the ER stress-related cellular processes in neuronal cells. The presented proteomics results strongly support the evidence of increased bioenergetic activity of mitochondria in the early phases of ER stress, which finally can trigger mitochondrial collapse and subsequent cell death. Further investigation of this mechanism could provide new potential targets to elucidate cellular and molecular background of several neurodegenerative diseases in which ER stress has a crucial role.

Acknowledgements

This work was supported by the EC FP-7 201159 grant (Memoload) and "TÁMOP-4.2.1/B-09/1/KONV-2010-0005" grant supported by the EU and co-financed by the European Social Fund. The authors are also grateful to Simon Bishop (University of Birmingham) for checking this paper from a linguistic point of view. The authors declare that no conflict of interest exists.

Appendix A. Supplementary data

Supplementary data associated with this article can be found, in the online version, at http://dx.doi.org/10.1016/j.neuint.2012.11.003.

References

Amodio, G., Moltedo, O., Monteleone, F., D'Ambrosio, C., Scaloni, A., Remondelli, P., Zambrano, N., 2011. Proteomic signatures in thapsigargin-treated hepatoma cells. Chem. Res. Toxicol. 24, 1215–1222.

Anelli, T., Alessio, M., Mezghrani, A., Simmen, T., Talamo, F., Bachi, A., Sitia, R., 2002. ERp44, a novel endoplasmic reticulum folding assistant of the thioredoxin family. EMBO J. 21, 835–844.

Appenzeller-Herzog, C., Ellgaard, L., 2008. The human PDI family: versatility packed into a single fold. Biochim. Biophys. Acta 1783, 535–548.

Berridge, M.J., 2002. The endoplasmic reticulum: a multifunctional signaling organelle. Cell Calcium 32, 235–249.

Berridge, M.J., Bootman, M.D., Roderick, H.L., 2003. Calcium signalling: dynamics, homeostasis and remodelling. Nat. Rev. Mol. Cell Biol. 4, 517–529.

Bravo, R., Gutierrez, T., Paredes, F., Gatica, D., Rodriguez, A.E., Pedrozo, Z., Chiong, M., Parra, V., Quest, A.F., Rothermel, B.A., Lavandero, S., 2012. Endoplasmic reticulum: ER stress regulates mitochondrial bioenergetics. Int. J. Biochem. Cell Biol. 44, 16–20.

Candiano, G., Bruschi, M., Musante, L., Santucci, L., Ghiggeri, G.M., Carnemolla, B., Orecchia, P., Zardi, L., Righetti, P.G., 2004. Blue silver: a very sensitive colloidal Coomassie G-250 staining for proteome analysis. Electrophoresis 25, 1327–1333.

Carvajal-Rodriguez, A., de Una-Alvarez, J., Rolan-Alvarez, E., 2009. A new multitest correction (SGoF) that increases its statistical power when increasing the number of tests. BMC Bioinformatics 10, 209.

Chung, H., Chung, H.Y., Bae, C.W., Kim, C.J., Park, S., 2011. Ghrelin suppresses tunicamycin- or thapsigargin-triggered endoplasmic reticulum stress-mediated apoptosis in primary cultured rat cortical neuronal cells. Endocr. J. 58, 409–420.

Cunnea, P., Mhaille, A.N., McQuaid, S., Farrell, M., McMahon, J., FitzGerald, U., 2011. Expression profiles of endoplasmic reticulum stress-related molecules in demyelinating lesions and multiple sclerosis. Mult. Scler. 17, 808–818.

Darshi, M., Mendiola, V.L., Mackey, M.R., Murphy, A.N., Koller, A., Perkin, G.A., Ellisman, M.H., Taylor, S.S., 2011. ChChd3, an inner mitochondrial membrane protein, is essential for maintaining crista integrity and mitochondrial function. J. Biol. Chem. 286, 2918–2932.

Datki, Z., Juhasz, A., Galfi, M., Soos, K., Papp, R., Zadori, D., Penke, B., 2003. Method for measuring neurotoxicity of aggregating polypeptides with the MTT assay on differentiated neuroblastoma cells. Brain Res. Bull. 62, 223–229.

Decuypere, J.P., Monaco, G., Bultynck, G., Missiaen, L., De Smedt, H., Parys, J.B., 2011. The IP(3) receptor-mitochondria connection in apoptosis and autophagy. Biochim. Biophys. Acta 1813, 1003–1013.

Denton, R.M., 2009. Regulation of mitochondrial dehydrogenases by calcium ions. Biochim. Biophys. Acta 1787, 1309–1316.

Foldi, I., Datki, Z.L., Szabo, Z., Bozso, Z., Penke, B., Janaky, T., 2011. Proteomic study of the toxic effect of oligomeric Abeta1-42 in situ prepared from 'iso-Abeta1-42'. J. Neurochem. 117, 691–702.

Frickel, E.M., Riek, R., Jelesarov, I., Helenius, A., Wuthrich, K., Ellgaard, L., 2002. TROSY-NMR reveals interaction between ERp57 and the tip of the calreticulin P-domain. Proc. Natl. Acad. Sci. USA 99, 1954–1959.

Gallego-Sandin, S., Rodriguez-Garcia, A., Alonso, M.T., Garcia-Sancho, J., 2009. The endoplasmic reticulum of dorsal root ganglion neurons contains TRPV1 channels. J. Biol. Chem. 284, 32591–32601.

Gallego-Sandin, S., Alonso, M.T., Garcia-Sancho, J., 2011. Calcium homeostasis modulator 1 (CALHM1) reduces the calcium content of the endoplasmic reticulum (ER) and triggers ER stress. Biochem. J. 437, 469–475.

Gething, M.J., 1999. Role and regulation of the ER chaperone BiP. Semin. Cell Dev. Biol. 10, 465–472.

Giorgi, C., De Stefani, D., Bononi, A., Rizzuto, R., Pinton, P., 2009. Structural and functional link between the mitochondrial network and the endoplasmic reticulum. Int. J. Biochem. Cell Biol. 41, 1817–1827.

Griffiths, E.J., Rutter, G.A., 2009. Mitochondrial calcium as a key regulator of mitochondrial ATP production in mammalian cells. Biochim. Biophys. Acta 1787, 1324–1333.

Higo, T., Hattori, M., Nakamura, T., Natsume, T., Michikawa, T., Mikoshiba, K., 2005. Subtype-specific and ER lumenal environment-dependent regulation of inositol 1,4,5-trisphosphate receptor type 1 by ERp44. Cell 120, 85–98.

Hooper, S.D., Bork, P., 2005. Medusa: a simple tool for interaction graph analysis. Bioinformatics 21, 4432–4433.

Hoozemans, J.J., van Haastert, E.S., Eikelenboom, P., de Vos, R.A., Rozemuller, J.M., Scheper, W., 2007. Activation of the unfolded protein response in Parkinson's disease. Biochem. Biophys. Res. Commun. 354, 707–711.

Hoozemans, J.J., van Haastert, E.S., Nijholt, D.A., Rozemuller, A.J., Eikelenboom, P., Scheper, W., 2009. The unfolded protein response is activated in pretangle neurons in Alzheimer's disease hippocampus. Am. J. Pathol. 174, 1241–1251.

Huang da, W., Sherman, B.T., Tan, Q., Kir, J., Liu, D., Bryant, D., Guo, Y., Stephens, R., Baseler, M.W., Lane, H.C., Lempicki, R.A., 2007. DAVID bioinformatics resources: expanded annotation database and novel algorithm to better extract biology from large gene lists. Nucleic Acids Res. 35, W169–W175.

Jensen, L.J., Kuhn, M., Stark, M., Chaffron, S., Creevey, C., Muller, J., Doerks, T., Julien, P., Roth, A., Simonovic, M., Bork, P., von Mering, C., 2008. STRING 8 – a global view on proteins and their functional interactions in 630 organism. Nucleic Acid Res. 37, D412–D416.

Li, Y., Camacho, P., 2004. Ca2+-dependent redox modulation of SERCA 2b by ERp57. J. Cell Biol. 164, 35–46.

Lytton, J., Westlin, M., Hanley, M.R., 1991. Thapsigargin inhibits the sarcoplasmic or endoplasmic reticulum Ca-ATPase family of calcium pumps. J. Biol. Chem. 266, 17067–17071.

Ma, Y., Hendershot, L.M., 2004. ER chaperone functions during normal and stress conditions. J. Chem. Neuroanat. 28, 51–65.

Matus, S., Glimcher, L.H., Hetz, C., 2011. Protein folding stress in neurodegenerative diseases: a glimpse into the ER. Curr. Opin. Cell Biol. 23, 239–252.

Michalak, M., Robert Parker, J.M., Opas, M., 2002. Ca2+ signaling and calcium binding chaperones of the endoplasmic reticulum. Cell Calcium 32, 269–278.

Michalak, M., Groenendyk, J., Szabo, E., Gold, L.I., Opas, M., 2009. Calreticulin, a multi-process calcium-buffering chaperone of the endoplasmic reticulum. Biochem. J. 417, 651–666.

Molloy, M.P., Brzezinski, E.E., Hang, J., McDowell, M.T., VanBogelen, R.A., 2003. Overcoming technical variation and biological variation in quantitative proteomics. Proteomics 3, 1912–1919.

Ni, M., Zhou, H., Wey, S., Baumeister, P., Lee, A.S., 2009. Regulation of PERK signaling and leukemic cell survival by a novel cytosolic isoform of the UPR regulator GRP78/BiP. PLoS ONE 4, e6868.

Ni, M., Zhang, Y., Lee, A.S., 2011. Beyond the endoplasmic reticulum: atypical GRP78 in cell viability, signalling and therapeutic targeting. Biochem. J. 434, 181–188.

Park, M., Kim, H., 2011. Thapsigargin-induced sequential expression of proteins related to autophagy and apoptosis in human breast cancer MCF-7 cells. Bull. Korean Chem. Soc. 31, 3469–3472.

Prell, T., Lautenschlager, J., Witte, O.W., Carri, M.T., Grosskreutz, J., 2012. The unfolded protein response in models of human mutant G93A amyotrophic lateral sclerosis. Eur. J. Neurosci. 35, 652–660.

Qian, Y., Harris, E.D., Zheng, Y., Tiffany-Castiglioni, E., 2000. Lead targets GRP78, a molecular chaperone, in C6 rat glioma cells. Toxicol. Appl. Pharmacol. 163, 260–266.

Rabilloud, T., Strub, J.M., Luche, S., van Dorsselaer, A., Lunardi, J., 2001. A comparison between sypro ruby and ruthenium II tris (bathophenanthroline disulfonate) as fluorescent stains for protein detection in gels. Proteomics 1, 699–704.

Rao, R.V., Peel, A., Logvinova, A., del Rio, G., Hermel, E., Yokota, T., Goldsmith, P.C., Ellerby, L.M., Ellerby, H.M., Bredesen, D.E., 2002. Coupling endoplasmic reticulum stress to the cell death program: role of the ER chaperone GRP78. FEBS Lett. 515, 122–128.

Rao, R.V., Poksay, K.S., Castro-Obregon, S., Schilling, B., Row, R.H., del Rio, G., Gibson, B.W., Ellerby, H.M., Bredesen, D.E., 2004. Molecular components of a cell death

pathway activated by endoplasmic reticulum stress. J. Biol. Chem. 279, 177–187.
Sagara, Y., Inesi, G., 1991. Inhibition of the sarcoplasmic reticulum Ca^{2+} transport ATPase by thapsigargin at subnanomolar concentrations. J. Biol. Chem. 266, 13503–13506.
Schneider, C.A., Rasband, W.S., Eliceiri, K.W., 2012. NIH image to ImageJ: 25 years of image analysis. Nat. Methods 9, 671–675.
Shevchenko, A., Wilm, M., Vorm, O., Mann, M., 1996. Mass spectrometric sequencing of proteins silver-stained polyacrylamide gels. Anal. Chem. 68, 850–858.
Simmen, T., Lynes, E.M., Gesson, K., Thomas, G., 2010. Oxidative protein folding in the endoplasmic reticulum: tight links to the mitochondria-associated membrane (MAM). Biochim. Biophys. Acta 1798, 1465–1473.
Stiess, M., Bradke, F., 2011. Neuronal polarization: the cytoskeleton leads the way. Dev. Neurobiol. 71, 430–444.
Stutzmann, G.E., Mattson, M.P., 2011. Endoplasmic reticulum Ca(2+) handling in excitable cells in health and disease. Pharmacol. Rev. 63, 700–727.
Szabadkai, G., Bianchi, K., Varnai, P., De Stefani, D., Wieckowski, M.R., Cavagna, D., Nagy, A.I., Balla, T., Rizzuto, R., 2006. Chaperone-mediated coupling of endoplasmic reticulum and mitochondrial Ca^{2+} channels. J. Cell. Biol. 175, 901–911.
Torres, M., Castillo, K., Armisen, R., Stutzin, A., Soto, C., Hetz, C., 2010. Prion protein misfolding affects calcium homeostasis and sensitizes cells to endoplasmic reticulum stress. PLoS ONE 5, e15658.
Vance, J.E., 1990. Phospholipid synthesis in a membrane fraction associated with mitochondria. J. Biol. Chem. 265, 7248–7256.
Wei, H., Wei, W., Bredesen, D.E., Perry, D.C., 1998. Bcl-2 protects against apoptosis in neuronal cell line caused by thapsigargin-induced depletion of intracellular calcium stores. J. Neurochem. 70, 2305–2314.
Xu, C., Bailly-Maitre, B., Reed, J.C., 2005. Endoplasmic reticulum stress: cell life and death decisions. J. Clin. Invest. 115, 2656–2664.
Yamashima, T., Kohda, Y., Tsuchiya, K., Ueno, T., Yamashita, J., Yoshioka, T., Kominami, E., 1998. Inhibition of ischaemic hippocampal neuronal death in primates with cathepsin B inhibitor CA-074: a novel strategy for neuroprotection based on 'calpain-cathepsin hypothesis'. Eur. J. Neurosci. 10, 1723–1733.
Yamashima, T., 2004. Ca^{2+}-dependent proteases in ischemic neuronal death: a conserved 'calpain-cathepsin cascade' from nematodes to primates. Cell Calcium 36, 285–293.
Zhao, L., Ackerman, S.L., 2006. Endoplasmic reticulum stress in health and disease. Curr. Opin. Cell Biol. 18, 444–452.

Journal of Alzheimer's Disease 36 (2013) 487–501
DOI 10.3233/JAD-120163
IOS Press

Docosahexaenoic Acid Reduces Amyloid-β Induced Toxicity in Cells of the Neurovascular Unit

Szilvia Veszelka[a], Andrea E. Tóth[a], Fruzsina R. Walter[a], Zsolt Datki[b], Emese Mózes[b], Lívia Fülöp[b], Zsolt Bozsó[b], Éva Hellinger[c], Monika Vastag[c], Barbara Orsolits[d], Zsuzsanna Környei[d], Botond Penke[b] and Mária A. Deli[a,*]
[a]*Institute of Biophysics, Biological Research Centre of the Hungarian Academy of Sciences, Szeged, Hungary*
[b]*Department of Medical Chemistry, University of Szeged, Szeged, Hungary*
[c]*Division of Pharmacology and Drug Safety Research, Gedeon Richter Plc., Budapest, Hungary*
[d]*Institute of Experimental Medicine of the Hungarian Academy of Sciences, Budapest, Hungary*

Handling Associate Editor: William Banks

Accepted 3 April 2013

Abstract. Alzheimer's disease (AD) is characterized by the accumulation of amyloid-β peptides (Aβ) as perivascular deposits and senile plaques in the brain. The intake of the polyunsaturated fatty acid docosahexaenoic acid (DHA) has been associated with decreased amyloid deposition and reduced risk in AD in several epidemiological trials; however the exact underlying molecular mechanism remains to be elucidated. The aim of the study was to test whether DHA can exert a direct protective effect on the elements of the neurovascular unit, such as neurons, glial cells, brain endothelial cells, and pericytes, treated with $A\beta_{42}$ (15 μM). A dose-dependent high cellular toxicity was found in viability assays in all cell types and on acute hippocampal slices after treatment with $A\beta_{42}$ small oligomers prepared *in situ* from an isopeptide precursor. The cell morphology also changed dramatically in all cell types. In brain endothelial cells, damaged barrier function and increased para- and transcellular permeability were observed after peptide treatment. The production of reactive oxygen species was elevated in pericytes and endothelial and glial cells. DHA (30 μM) significantly decreased the $A\beta_{42}$-induced toxic effects in all cell types measured by viability assays, and protected the barrier integrity and functions of brain endothelial cells. DHA also decreased the elevated rhodamine 123 accumulation in brain endothelial cells pre-treated with $A\beta_{42}$ indicating an effect on efflux pump activity. These results indicate for the first time that DHA can protect not only neurons but also the other elements of the neurovascular unit from the toxic effects of $A\beta_{42}$ and this effect may be beneficial in AD.

Keywords: Alzheimer's disease, amyloid-β, blood-brain barrier, brain endothelial cells, docosahexaenoic acid, glia, neuron, neurovascular unit, pericyte, P-glycoprotein

INTRODUCTION

Neurons and their associated glial cells interacting with endothelial cells and pericytes of brain microvessels are organized into well-structured neurovascular units. The proper function of this unit is responsible not only for the neuronal activity dependent oxygen and nutrient supply of the brain, but also for

*Correspondence to: Mária A. Deli, M.D., Ph.D., D.Sc., Institute of Biophysics, Biological Research Centre of the Hungarian Academy of Sciences, Temesvári krt. 62., H-6726 Szeged, Hungary. Tel.: +36 62 599602; Fax: +36 62 433133; E-mail: deli.maria@brc.mta.hu.

ISSN 1387-2877/13/$27.50

neuro-hemodynamic coupling, neuro-angiogenic coupling, and neuro-trophic coupling [1]. Neurovascular mechanisms play a crucial role in cognitive decline and neurodegeneration in Alzheimer's disease (AD) [2–6]. Cerebral amyloid angiopathy and senile plaques are two of the pathological hallmarks in brains of patients with AD. The major component of amyloid deposition is the amyloid-β peptide (Aβ), cleaved from amyloid-β protein precursor by secretases. The dysfunction of the cerebral circulation induces decreased clearance of Aβ across the blood-brain barrier (BBB) formed by brain microvascular endothelial cells and pericytes. In addition to production of the peptide, transport of Aβ across the BBB is essential in controlling Aβ levels in the brain [7, 8]. The dysfunction of the cerebrovascular system leads to disturbed homeostasis, neuronal dysfunction, and secondary neuronal loss [2, 4, 6]. Protection of the neurovascular unit from injury is among the proposed new strategies for the therapy of AD [1].

Epidemiological observations suggest that high unsaturated fatty acid intake has been associated with decreased risk of dementia [9–12]. In particular long-chain polyunsaturated ω-3 fatty acids (*n*-3 PUFAs) found in marine fish have become of major interest. Docosahexaenoic acid (DHA), the end product of n-3 PUFA synthesis, is essential for brain maturation and as an important membrane component it plays a primary role in neurotransmission. DHA is responsible for the neuroprotective action on developing cholinergic neurons against glutamate cytotoxicity [13]. A reduced level of DHA was found in AD patients [14] and in AD postmortem brains [15] compared with age-matched healthy controls. DHA reduces $A\beta_{42}$ peptide production in animal models of AD [16, 17] and chronic DHA treatment improves cognition in 3xTG-AD mice [18]. However clinical studies found no effect or only minor effects of DHA on the improvement of cognitive functions in the very early stage of the disease [19–22].

Based on these data, DHA can be potentially important in the prevention of AD, however there are no data on its effect on the cells of the neurovascular unit, except neurons [23–25], and its mechanism of action against $A\beta_{42}$ peptide toxicity. Therefore the aim of the present study was to test the effect of DHA not only on neurons, but also on other important elements of neurovascular unit, such as glial cells, brain endothelial cells, and pericytes. In addition, BBB functions and reactive oxygen species (ROS) production were also tested on a relevant *in vitro* BBB model made from primary rat brain endothelial cells, glial cells, and pericytes [26, 27].

MATERIALS AND METHODS

All reagents were purchased from Sigma-Aldrich, Hungary, unless otherwise indicated.

Synthesis of 'iso-$A\beta_{42}$' and characterization of oligomers

The synthesis of 'iso-$A\beta_{42}$' was discussed in details by Bozso et al. [28]. Briefly the peptide was synthesized using Boc-chemistry on a Boc-Ala-PAM resin. Acylation of the α-amino groups was done by activating threefold excess of N^{α} - Boc protected amino acids (or 2-Cl-Z-Ser(OtBu)-OH for position 26) with DCC/1-hydroxybenzotriazole in DCM/DMF (dichloromethane-dimethyl formamide, 1 : 1) and the peptide resin was reacted with this mixture for 2 h. If incomplete acylation was detected by the qualitative ninhydrin test, the coupling was repeated with DCC/1-hydroxy-7-azabenzotriazole activation. Boc and tBu groups were removed by treating the resin with 50% triflouroacetic acid/DCM mixture twice (5 + 25 min). Neutralization was performed with 5% N,N-diisopropylethylamine/DCM (2×1 min). Esterification of the hydroxyl group of Ser^{26} with Boc-Gly-OH was performed by treating the peptide-resin with Fmoc-Gly/DCC/N-methylimidazole (10-fold excess) in DCM/DMF (3 : 1) for 2×4 h. The peptide was cleaved from the resin with a mixture containing hydrogen fluoride (10 mL), anisol (0.2 mL), dimethyl sulfide (0.8 mL), and dithiothreitol (0.1 g) at 0°C for 45 min. The crude product was precipitated and washed with diethyl-ether, dissolved in 50% acetic acid/water, lyophilized, and purified by HPLC. At physiological conditions (37°C and pH 7.4), iso-$A\beta_{42}$ *in situ* forms oligomeric $A\beta_{42}$ via an O-N acyl-transfer reaction. The aggregates were visualized by transmission electron microscopy. Iso-$A\beta_{42}$ forms round shaped oligomers, which can be characterized with a bimodal size-distribution: the small aggregates have an average diameter of 5.3 ± 1.0 nm, while the large spherical aggregates have 7.9 ± 3.3 nm. The oligomers applied in 15 μM concentration aggregate slowly *in vitro* after 24 h of incubation. Protofibrillar assemblies having a length of 30–100 nm with an average diameter of 8.4 ± 2.1 nm are present together with spherical oligomers.

Cell culture

Primary neuronal cultures were prepared from Wistar rat forebrains at embryonic day 16 by mechanical

dissociation using fire-polished Pasteur pipettes as described previously [29]. The cell suspension was filtered through a nylon mesh with a pore diameter of 45 μm to obtain single cells. The cells were seeded onto poly-L-lysine coated 96-well plates or glass coverslips with a density of 2.5×10^5 cell/cm^2 in Eagle's Minimum Essential Medium (MEM) supplemented with 4 mM glutamine, 40 μg/ml gentamycin, and 5% fetal calf serum (FCS; PAA, Austria). The medium was changed to defined medium (MEM-F12 supplemented with insulin, transferrin, and sodium selenite) 24 h after plating. The cultures were maintained in humidified air atmosphere containing 5% CO_2, at 37°C. The obtained primary cultures has been extensively studied and characterized and the number of neurons was above 80–90% of total cell number [29].

Primary cultures of cerebral endothelial cells were prepared from 2-week-old rats as described earlier in detail [30–32]. Forebrains were collected in ice-cold sterile phosphate buffered saline (PBS); meninges were removed, gray matter was minced by scalpels to 1 mm^3 pieces and digested with 1 mg/ml collagenase CLS2 (Worthington, USA) in Dulbecco's modified Eagle medium (DMEM) for 1.5 h at 37°C. Microvessels were separated by centrifugation in 20% bovine serum albumin (BSA)-DMEM (1000×g, 20 min) from myelin containing elements, and further digested with 1 mg/ml collagenase-dispase (Roche) in DMEM for 1 h. Microvascular endothelial cell clusters were separated on a 33% continuous Percoll gradient (1000×g, 10 min), collected, and washed twice in DMEM before plating on collagen type IV and fibronectin coated dishes (Falcon, Becton Dickinson). Cultures were maintained in DMEM/F12 supplemented with 50 μg/ml gentamicin, 15% plasma-derived bovine serum (First Link, UK), 1 ng/ml basic fibroblast growth factor (Roche), insulin (5 μg/ml), transferrin (5 μg/ml), sodium selenite (5 ng/ml) (insulin-transferrin-sodium selenite media supplement), and 100 μg/ml heparin. In the first 3 days, culture medium contained puromycin (4 μg/ml) to selectively remove P-glycoprotein negative contaminating cells [33]. The endothelial cell cultures were immunopositive for von Willebrand factor and negative for the astroglia cell marker glial fibrillary acidic protein (GFAP) and α-smooth muscle actin (α-SMA) in accordance with earlier published results [33, 34]. When the cultures reached 80% confluency (fourth day *in vitro*), the purified endothelial cells were passaged to multiwell plates or Transwell filter inserts by a brief treatment with trypsin (0.05% wt/vol)-EDTA (0.02% wt/vol) solution, and used for experiments. To induce BBB characteristics, brain endothelial cells were treated with glia/pericyte-conditioned medium or co-cultured with rat cerebral glial cells and rat pericytes [26].

Primary cultures of glial cells were prepared from newborn Wistar rats [31, 32]. Meninges were removed, and cortical pieces were mechanically dissociated in DMEM containing 50 μg/ml gentamicin and 10% FBS and plated in poly-L-lysin coated 12-well dishes and kept for minimum 3 weeks before use. In confluent glia cultures, 90% of cells were immunopositive for GFAP, while the remaining 10% were immunopositive for CD11b, a marker of microglia. For co-culture, brain endothelial cells in cell culture inserts were placed into multiwells containing astroglia at the bottom of the wells with endothelial culture medium in both compartments.

Pure cultures of rat cerebral pericytes were obtained by a prolonged, 2-week culture of isolated rat brain microvessel fragments that contain pericytes beside endothelial cells. The same preparations yield primary brain endothelial cells except puromycin-treatment. Pericyte survival and proliferation were favored by selective culture conditions, using uncoated dishes, and DMEM supplemented with 10% FBS and antibiotics. Culture medium was changed every 3 days. As described in our previous papers [34, 35], cultured brain microvascular pericytes show typical morphology of large, flat multipolar cells with several branches in accordance with literature data [36] and look similar to the pericyte cultures described by Vandenhaute et al. [37]. Pericyte cultures are regularly checked and positive for α-SMA (97% positivity) and NG2 (94% positivity) and completely negative for GFAP and vWF immunostaining as shown by Nakagawa et al. [34]. Therefore we can exclude the glial and endothelial contamination of the pericyte cultures. Since the cultures are made from brain microvessel fractions where pericytes are more numerous than smooth muscle cells, we assume that the number of smooth muscle cells in our preparations is minimal.

To construct the three cell-type BBB model, Transwell cell culture inserts were placed into multiwell plates containing astroglia at the bottom of the wells, pericytes were seeded on the bottom side of the inserts, and finally endothelial cells were passaged to the upper side of the inserts coated with fibronectin and collagen type IV with endothelial culture medium in both compartments [26].

Preparation and treatment of acute hippocampal slices

A slightly modified version of the method reported by Datki et al. [38, 39] was used in our slice viability experiments. After anesthesia with chloral hydrate (0.4 g/kg), 10 ± 1 week-old male Wistar rats were decapitated and the whole heads (without scalp-leather) were put in ice cold distillated water for 1 min. The brains were quickly removed and immersed in H-ACSF/1 (preparation solution substituted with HEPES) with very low Ca^{2+} and with elevated Mg^{2+} concentration at 4ºC. The composition of this preparation solution (in mM) was the following: NaCl 122, KCl 3, $CaCl_2$ 0.3, $MgCl_2$ 3.7, $NaHCO_3$ 25, HEPES 5, D-glucose 10, pH = 7.4. Brain slices (thickness was 400 μm) were prepared from the hippocampus with a McIlwain tissue chopper at 4ºC. After the preparation of the slices in ice-cold H-ACSF/1 solution, we took photos of them (to measure the slice area). The slices (with an area of approximately 9 mm^2) were quickly transferred into the *ExViS* mini-chamber (maximum 5 slices in 1 ml) for conditioning (30 min) in the carboxygenated (95/5%: O_2/CO_2) preparation solution at room temperature (24ºC).

After resting (30 min) in the carboxygenated H-ACSF/1 solution at room temperature, the transduction of the brain slices from the mini-chamber into the plastic Petri dish was executed with cut-off pipettes (type 200 μl) and was left to rest in glucose- and carboxygenated-free (glucose-oxygen deprivation) H-ACSF/2 (4 ml/Petri dish) for 1 h. The composition of this H-ACSF/2 (in mM) was the following: NaCl 132, KCl 3, $CaCl_2$ 2, $MgCl_2$ 2, $NaHCO_3$ 25, HEPES 5, pH = 7.4. The Petri dish was continuously being stirred at 370 rpm (modified BIOSAN TS-100 thermo shaker). After resting being treated in glucose- and oxygen-free H-ACSF/2, the content (supernatant) of the Petri dish was changed to the H-ACSF/3 solution (3 ml/Petri dish). The composition of this preparation solution (in mM) was the following: NaCl 120, KCl 3, $CaCl_2$ 2, $MgCl_2$ 2, $NaHCO_3$ 25, HEPES 5, D-glucose 12, pH = 7.4 (with normal calcium, magnesium, and glucose levels). The slices were quickly transferred into the *ExViS* mini-chambers (maximum 5 slices in 1 ml) for treating with actual $A\beta_{42}$ peptide (50 μl stock solution was added into 950 μl H-ACSF/3 per chamber; 20 μM $A\beta_{42}$ in final concentration). Before each slice viability assay, the stock solution of $A\beta_{42}$ peptide (0.4 mM) was freshly prepared (and stored for maximum 10 min) in distilled water (pH = 5). The foaming was inhibited by a floating plastic ball (diameter: 5 mm) in mini tube chambers.

$A\beta_{42}$ treatment and cell toxicity assays in cell culture

Living cells convert the yellow dye 3-(4,5-dimethyltiazol-2-yl)-2,5-diphenyltetrazolium bromide (MTT, Sigma M5655) to purple, insoluble formazan crystals. For MTT reduction assay the neurons, rat brain endothelial cells, glial cells, or pericytes were cultured in 96-well plates. The 75 μM stock solution of $A\beta_{42}$ was freshly prepared in phosphate buffer and the further dilutions were in cell culture medium. DHA was diluted in culture medium from a 300 mM stock solution prepared in ethanol. Control conditions were similar to other treatment conditions except they did not contain peptide or DHA. The medium for the controls was also diluted with the vehicle (PBS) in the appropriate proportion. All stock solutions were prepared freshly and separately, and added to the cells consecutively. After treatments of $A\beta_{42}$ (24 h; 0.1–30 μM) or DHA (24 h; 1–300 μM in culture medium) endothelial cells were incubated with 0.5 mg/ml MTT solution for 3 h in CO_2 incubator. The amount of formazan crystals was dissolved in dimethyl-sulfoxide (DMSO) and determined by measuring absorbance at 595 nm with microplate reader (Fluostar Optima, BMG Labtechnologies, Germany).

Cell viability assay on acute hippocampal slices

After treating the slices with 20 μM $A\beta_{42}$ (or with 30 or 50 μM DHA) for 4 h, we changed the supernatant to H-ASCF/3 and we added 0.1 ml MTT (stock solution 5 mg/ml MTT dye in H-ACSF) to the wells in which they were left to rest for 15 min without carboxygenation (the H-ACSF/3 solution was saturated with carboxygen before using). To block the reduction of the MTT to formazan crystals, we changed the supernatant on the slices from H-ACSF/3 to pure DMSO and left the slices rest for 30 min in a 96-well plate (Costar 3595; 100 μl DMSO/slice/well). After dissolving the formazan, we transferred 70 μl DMSO from each slice (well) into another 96-well plate (Costar 3695). The optical density (OD) of the dissolved formazan was measured at 550 and 620 nm. To synchronize the data, we used the following formula: $[(OD_{550} - OD_{620})/\text{area of slice } (mm^2)] = 100\%$ in control ($A\beta_{42}$ untreated slices).

Evaluation of the barrier integrity

Transendothelial electrical resistance (TEER), representing the permeability of tight junctions for sodium ions, was measured by an EVOM resistance meter (World Precision Instruments Inc., USA) using STX-2 electrodes, and it was expressed relative to the surface area of endothelial monolayer ($\Omega \times cm^2$). TEER values of cell-free inserts (90–100 $\Omega \times cm^2$) were subtracted from the measured data. The TEER of rat primary brain endothelial monolayers in co-culture varied between 650 and 780 $\Omega \times cm^2$, with an average of 723 ± 41 $\Omega \times cm^2$ (mean $\pm$ S.D., $n = 12$).

The flux of sodium fluorescein and Evans blue-labeled albumin across endothelial monolayers was determined as previously described [31, 32]. Cell culture inserts, following treatment of $A\beta_{42}$ (24 h, 15 μM) and/or DHA (24 h, 30 μM) and measurement of TEER, were transferred to 12-well plates containing 1.5 ml Ringer–Hepes solution (118 mM NaCl, 4.8 mM KCl, 2.5 mM $CaCl_2$, 1.2 mM $MgSO_4$, 5.5 mM D-glucose, 20 mM Hepes, pH 7.4) in the basolateral compartments. In apical chambers, culture medium was replaced by 500 μl Ringer–Hepes containing 10 μg/ml sodium fluorescein (mw: 376 Da) and 165 μg/ml Evans blue bound to 0.1% BSA (mw: 67 kDa). The inserts were transferred at 20, 40, and 60 min to a new well containing Ringer–Hepes solution. The concentrations of the marker molecules in samples from the upper and lower compartments were determined. Evans blue (excitation: 584 nm, emission: 680 nm) and fluorescein (excitation: 485 nm, emission: 520 nm) concentrations were measured by a Fluostar Optima (BMG Labtechnologies, Germany) plate reader.

Transport was expressed as μl of donor (luminal) compartment volume from which the tracer is completely cleared. Transendothelial permeability coefficient (P_e) was calculated as previously described [32, 40]. Cleared volume was calculated from the concentration (C) of the tracer in the abluminal and luminal compartments and the volume (V) of the abluminal compartment (0.5 ml) by the following equation:

$$\text{Cleared volume } (\mu l) = \frac{C_{abluminal} \times V_{abluminal}}{C_{luminal}}$$

The average cleared volume was plotted versus time, and permeability × surface area product value for endothelial monolayer (PS_e) was calculated by the following formula:

$$\frac{1}{PS_{endothelial}} = \frac{1}{PS_{total}} - \frac{1}{PS_{insert}}$$

PS_e divided by the surface area (1 cm^2 for Transwell-12) generated the endothelial permeability coefficient (P_e; in 10^{-3} cm/min).

Functional assay for P-glycoprotein

Efflux pump activity was determined by the measurement of cellular accumulation of rhodamine 123 [41]. While rhodamine 123 is also a substrate of breast cancer resistance protein (BCRP or ABCG2), it is widely used as a P-glycoprotein (ABCB1) ligand [26, 32, 37, 41, 42]. In brief, endothelial monolayers pretreated with $A\beta_{42}$ (15 μM) and/or DHA (30 μM) for 24 h in 24-well plates were washed, and incubated with Ringer–Hepes buffer containing 10 μM rhodamine 123 for 1 h at 37°C. The solution was quickly removed; endothelial cells were washed three times with ice-cold PBS, and solubilized in 0.2 M NaOH. Rhodamine 123 content was determined by Fluostar Optima (BMG Labtechnologies, Germany) plate reader with excitation at 485 nm, emission at 520 nm. Verapamil (2 mM, 30 min preincubation) was used as a reference P-glycoprotein inhibitor.

Western blot

After amyloid and DHA treatment brain endothelial cells were washed in ice-cold PBS and scraped into 8 M urea/PBS containing 0.1% Triton-X, 1 μg/ml leupeptin, 10 ng/ml aprotinin, 100 μM phenylmethylsulphonyl fluoride (PMSF), 100 μM dithiothreitol, 200 μM sodium orthovanadate, and 1 mM sodium fluoride. Cells were lysed with three cycles of snap-freezing and thawing. The extracts were centrifuged at 12,000*g* for 20 min and protein concentration in the supernatant was determined using the method described by Lowry et al. [43]. For Western blotting, 25 μg protein samples were loaded on 7.5% Tris-glycine gel (PAGEr® Gold Precast Gel, Lonza, Rockland, ME, USA) and blotted onto polyvinylidene difluoride membrane (BioRad Laboratories, Hercules, CA, USA). Blots were probed overnight at 4°C with primary rabbit polyclonal anti-P-glycoprotein antibody (H-241, 1 : 200, Santa Cruz Biotechnology, Inc., Santa Cruz, CA, USA), or for loading control with primary rabbit anti-actin polyclonal antibody (1 : 200, Sigma-Aldrich, St. Louis, MO, USA) for 1 h at room temperature. Then, secondary antibody (goat anti-rabbit HRP-conjugated IgG antibody 1 : 3000, Bio-Rad) were added for 1 h at room temperature. Chemoluminescence method (SuperSignal West Pico Chemiluminescent Substrate,

Thermo scientific Rockford, IL, USA) was applied for detection of P-glycoprotein. For loading control, 3,3′-diaminobenzidine (Sigma-Aldrich) was used.

Detection of reactive oxygen species

To measure ROS, we used a fluorometric detection probe from Molecular Probes [32]. Chloromethyl-dichloro-dihydro-fluorescein diacetate (DCFDA) indicator penetrates the cells by diffusion and becomes deacetylated by intracellular esterases. Oxidation of CM-H_2DCFDA by ROS yields a fluorescent molecule. Confluent rat primary pericyte, glial, and brain endothelial cell layers cultured in 96-well plates were pretreated with $A\beta_{42}$ (15 μM) and/or DHA (30 μM) for 24 h, then washed, and incubated with Ringer–Hepes buffer containing 1 mM CM-H_2DCFDA for 1 h at 37°C. Hydrogen peroxide pretreatment (100 μM, 15 min) served as a positive control in the ROS assay. The plates were measured by Fluostar Optima fluorescent plate reader (BMG Labtechnologies, Germany) with excitation at 485 nm, emission at 520 nm.

Statistical analysis

All data presented are means ± S.E.M. The values were compared using the analysis of variance followed by Dunnett, Bonferroni or Newman-Keuls posthoc tests using GraphPad Prism 5.0 software (GraphPad Software Inc., San Diego, CA, USA). Changes were considered statistically significant at $p < 0.05$ or $p < 0.001$. All experiments were repeated at least three times, the number of parallel wells or inserts for each treatment and time point varied between 3 and 16.

RESULTS

The effect of $A\beta_{42}$ on the viability of the cells of the neurovascular unit

The direct effect of oligomeric $A\beta_{42}$ peptide on the viability of neurons, glial cells, brain endothelial cells, and pericytes was examined by MTT cytotoxicity assay. The yellow MTT dye was efficiently converted to purple formazan crystals by non-treated cells, but in the $A\beta_{42}$ treated groups a dose-dependent decrease in viability could be observed in all four cell types. The different cell types had different sensitivity for the peptide treatment (Fig. 1). The most sensitive cells were the neurons and the brain endothelial cells (Fig. 1A, C). Oligomeric $A\beta_{42}$ peptide-treatment in concentrations of 0.1 μM or higher for 24 h significantly decreased the viability of both cells. In contrast, only 5 μM or higher doses exerted significant effects in glial cells and pericytes (Fig. 1B, D).

The effect of DHA on the viability of the elements of the neurovascular unit

Before testing the potential protective effect of DHA against oligomeric $A\beta_{42}$ toxicity, its direct effect on cell viability was elucidated. Cells were incubated with DHA in the 1–300 μM concentration range for 24 h, than MTT assays were performed as shown in Fig. 2. In neurons (Fig. 2A), glial cells (Fig. 2B), and brain endothelial cells (Fig. 2C), the highest dose of DHA (300 μM) significantly decreased the MTT conversion. In pericytes, 10 μM DHA and higher doses significantly decreased the cellular viability and only the 1 μM concentration of DHA was found to be safe and non-toxic (Fig. 2D). In the most sensitive cell type, brain pericytes, these results were also supported by elevated lactate dehydrogenase release by 10 μM and higher concentrations of DHA (data not shown) indicating membrane perturbance.

The effect of DHA on $A\beta_{42}$-induced damages: toxicity tests

Based on the results of the toxicity assay (Fig. 1), the 15 μM concentration of oligomeric $A\beta_{42}$ was selected to be optimal to reproducibly induce damages to the cell cultures. The 30 μM dose of DHA was chosen to be tested as a protective agent against $A\beta_{42}$ toxicity in neurons and endothelial and glial cells. In the case of pericytes, the previously determined non-toxic 1 μM dose of DHA was selected (Fig. 3). DHA significantly decreased the $A\beta_{42}$-induced toxic effects in all cells of the neurovascular unit, neurons, glial cells, endothelial cells, and pericytes measured by MTT viability assays (Fig. 3). The DHA (30 μM) administration was most effective in brain endothelial cells (Fig. 3C). The protective effect of DHA was confirmed not only in cell cultures but also in experiments using acute hippocampal slices (Fig. 4). $A\beta_{42}$ treatment induced significant decrease in the viability of the hippocampal cells that was dose-dependently inhibited by DHA.

The effect of DHA on $A\beta_{42}$-induced damages: morphological changes

In the primary culture of neurons, the cells have small and rounded cell bodies connected with long

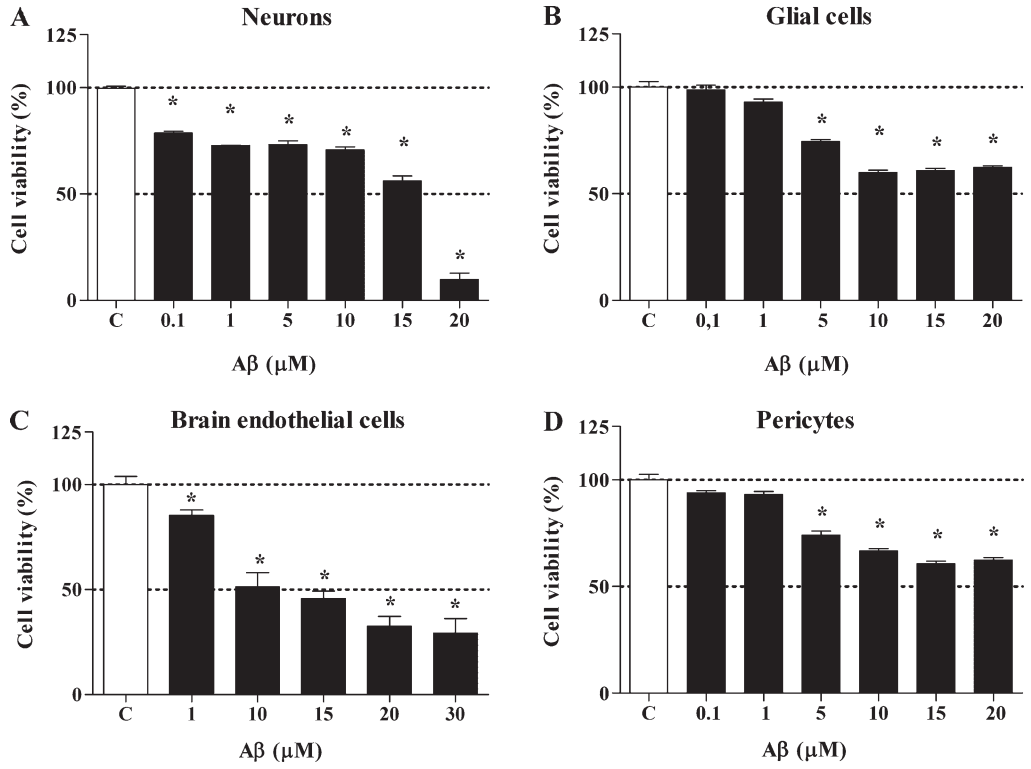

Fig. 1. Dose-dependent toxic effect of oligomeric amyloid-β 1-42 ($A\beta_{42}$) in neuronal (A), glial (B), brain endothelial (C), and pericyte (D) primary cell cultures measured by MTT assay. Values presented are means ± S.E.M., $n = 8$. Statistically significant differences ($p < 0.05$) between the controls and Aβ treated groups (*) are indicated.

neurites (Fig. 5 control). Oligomeric $A\beta_{42}$ peptide treatment (15 μM for 24 h) induced cell death in neuronal cultures; apoptotic cells and loss of cellular processes were observed. The co-administration of DHA (30 μM) with $A\beta_{42}$ attenuated the level of the damage in neurons; the network of the neurites was preserved (Fig. 5). In our culture conditions, glial cells showed a mature, differentiated phenotype with astroglia showing multiple, long and thin processes. After $A\beta_{42}$ treatment, glial cells underwent cellular hypertrophy, and fewer and thicker cell processes and increased number of apoptotic cells were observed. In the presence of DHA, more glial cell processes and less damaged cells could be seen. Brain endothelial cells formed confluent monolayers (Fig. 5) and the cellular morphology was typical for primary cultures as described earlier [32]. Treatment with $A\beta_{42}$ resulted in big intercellular gaps in the monolayers and floating apoptotic cells in the culture medium. At higher magnification, cytoplasmic vacuolization could be observed, as in our previous study earlier [44]. DHA inhibited these changes; the monolayer integrity was better preserved and resembled to the control ones. Brain microvascular pericytes in cell culture may form multiple cell layers. These cells are multipolar, large and flat with irregular projections. Even by phase contrast microscopy, the cytoskeletal fibers are visible (Fig. 5). After peptide treatment, the cytoplasmic fibers in pericytes were diminished and some rounded cells full with vacuoles could be observed. DHA (1 μM) was able to ameliorate the phenotypic changes in pericytes (Fig. 5).

Effect of DHA on $A\beta_{42}$-induced changes in barrier integrity of brain endothelial cells

Treatment of endothelial cell monolayers with oligomeric $A\beta_{42}$ (15 μM) reduced the TEER by 70% of the control after 24 h (data not shown). In $A\beta_{42}$ treated monolayers, the flux of the paracellular marker of fluorescein was 4.6 fold higher as compared to the control group (Fig. 6A). The P_e values for transcellular permeability marker albumin were lower with one order of magnitude than the values for fluorescein, in agreement with literature data [40] and our previous results [31, 32, 40]. The permeability for albumin was elevated by 5.9 fold in monolayers treated

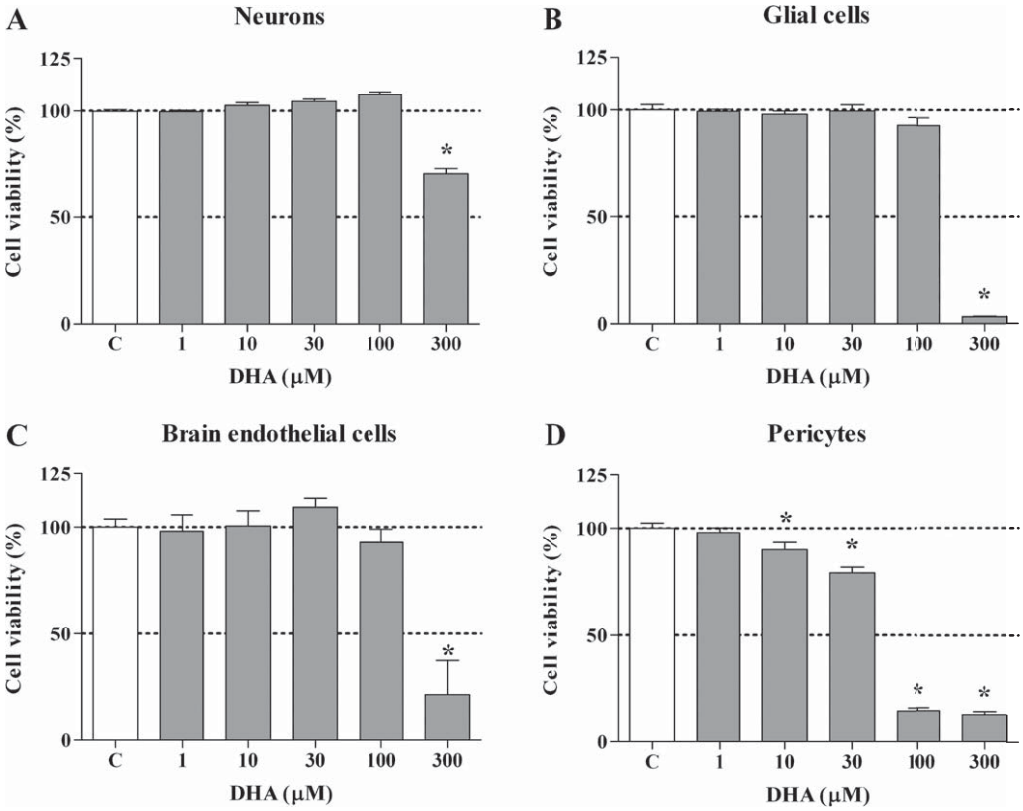

Fig. 2. Dose-dependent effect of docosahexaenoic acid (DHA) in neuronal (A), glial (B), brain endothelial (C), and pericyte (D) primary cell cultures measured by MTT assay. Values presented are means ± S.E.M., $n = 8$. Statistically significant differences ($p < 0.05$) between the controls and DHA treated groups (*) are indicated.

with $A\beta_{42}$ (Fig. 6B). Co-administration of DHA could significantly decrease the flux of permeability markers through endothelial monolayers (Fig. 6B). DHA alone had no effect on permeability of brain endothelial monolayers.

Effect of DHA on $A\beta_{42}$-induced changes in efflux pump activity and P-glycoprotein expression of brain endothelial cells

Brain endothelial cells expressed a functional P-glycoprotein efflux pump (Fig. 7B) similar to our previous studies [32, 34] and as demonstrated by the robust effect of verapamil, an inhibitor of P-glycoprotein used as a reference blocker in this rhodamine 123 uptake assay (Fig. 7A). Administration of oligomeric $A\beta_{42}$ (15 μM for 24 h) as a pre-treatment significantly decreased efflux pump activity of brain endothelial cells in the absence of the peptide as indicated by the high level of rhodamine 123 accumulation (Fig. 7A). The administration of DHA decreased the rhodamine 123 accumulation in brain endothelial cells pre-treated with $A\beta_{42}$ for 24 h (Fig. 7A). There was no significant difference in the protein level of P-glycoprotein in the treated groups as compared to the control group (Fig. 7B).

Effect of DHA on $A\beta_{42}$-induced reactive oxygen species production in brain endothelial cells

The ROS production in cultured pericytes, glial, and brain endothelial cells measured by DCFDA assay was significantly enhanced by oligomeric $A\beta_{42}$ treatment (15 μM, 24 h) compared to that in control cells (1.71 fold in glial cells, 1.4 fold in endothelial cells, 1.67 fold in pericytes compared to control group) (Fig. 8). DHA in 30 and 1 μM concentrations, which had no effect alone, effectively inhibited the Aβ -induced change in ROS production in brain endothelial and glial cells, and pericytes, respectively. Hydrogen peroxide treatment (100 μM, 15 min), a positive control in the ROS assay, elevated by 3.4 fold the amount of ROS measured in brain endothelial cells and 2.5 fold in glial cells and pericytes.

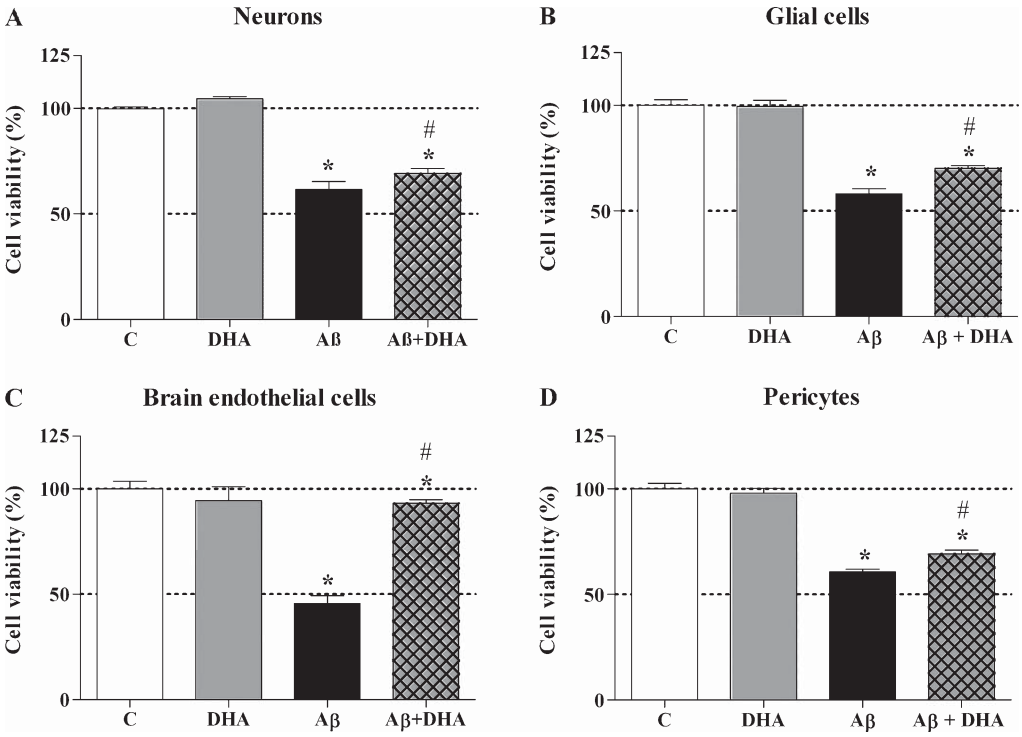

Fig. 3. The effect of docosahexaenoic acid (DHA, 1 μM on pericytes and 30 μM on the other three cell types) on oligomeric amyloid-β 1-42 ($A\beta_{42}$, 15 μM) induced toxicity in neurons (A), glial cells (B), brain endothelial (C), and pericyte primary cell cultures (D). Values presented are means ± S.E.M., $n = 8$. Statistically significant differences ($p < 0.05$) between the control and treated groups (*), $A\beta_{42}$ and $A\beta_{42}$ + DHA treated groups (#) are indicated.

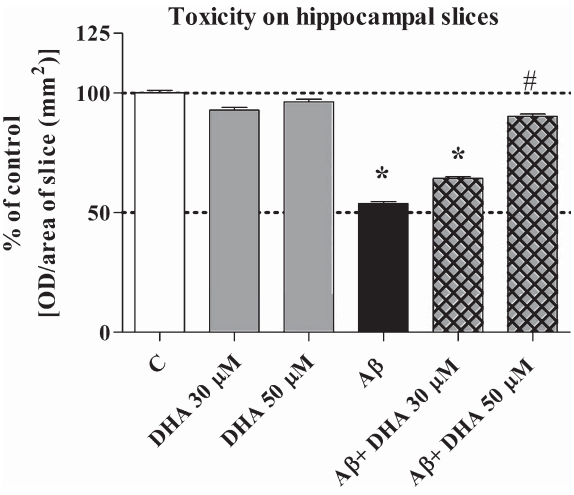

Fig. 4. The effect of docosahexaenoic acid (DHA) on oligomeric amyloid-β 1-42 ($A\beta_{42}$, 20 μM) induced toxicity on acute hippocampal slices measured by MTT assay. Values presented are means ± S.E.M., $n = 16$. Statistically significant differences ($p < 0.05$) between the controls and treated groups (*), $A\beta_{42}$ and $A\beta_{42}$ + DHA treated groups (#) are indicated.

DISCUSSION

The toxicity of $A\beta_{42}$ on the cells of the neurovascular unit

The direct toxic effect of different $A\beta_{42}$ peptides on cultured neurons and glial cells have been extensively investigated and established [39, 45, 46]. The present results confirm the toxicity of oligomeric $A\beta_{42}$ not only on cultured neurons but also on acute hippocampal slices. Brain endothelial cells are much less studied, despite their importance in the transport and clearance of $A\beta_{42}$ peptides and the pathological cerebrovascular changes in AD [2, 4, 7]. Studies on cultured brain endothelial cells demonstrate that $A\beta_{42}$ peptides are directly toxic to these cells [47, 44], disturb the barrier integrity, and increase the permeability of brain endothelial cell monolayers as presented in our previous study [44]. Cultured brain pericytes have been examined so far only by the group of Verbeek et al. [48, 49] and were found to be also sensitive to $A\beta_{42}$ toxicity. Our results are in agreement with these data.

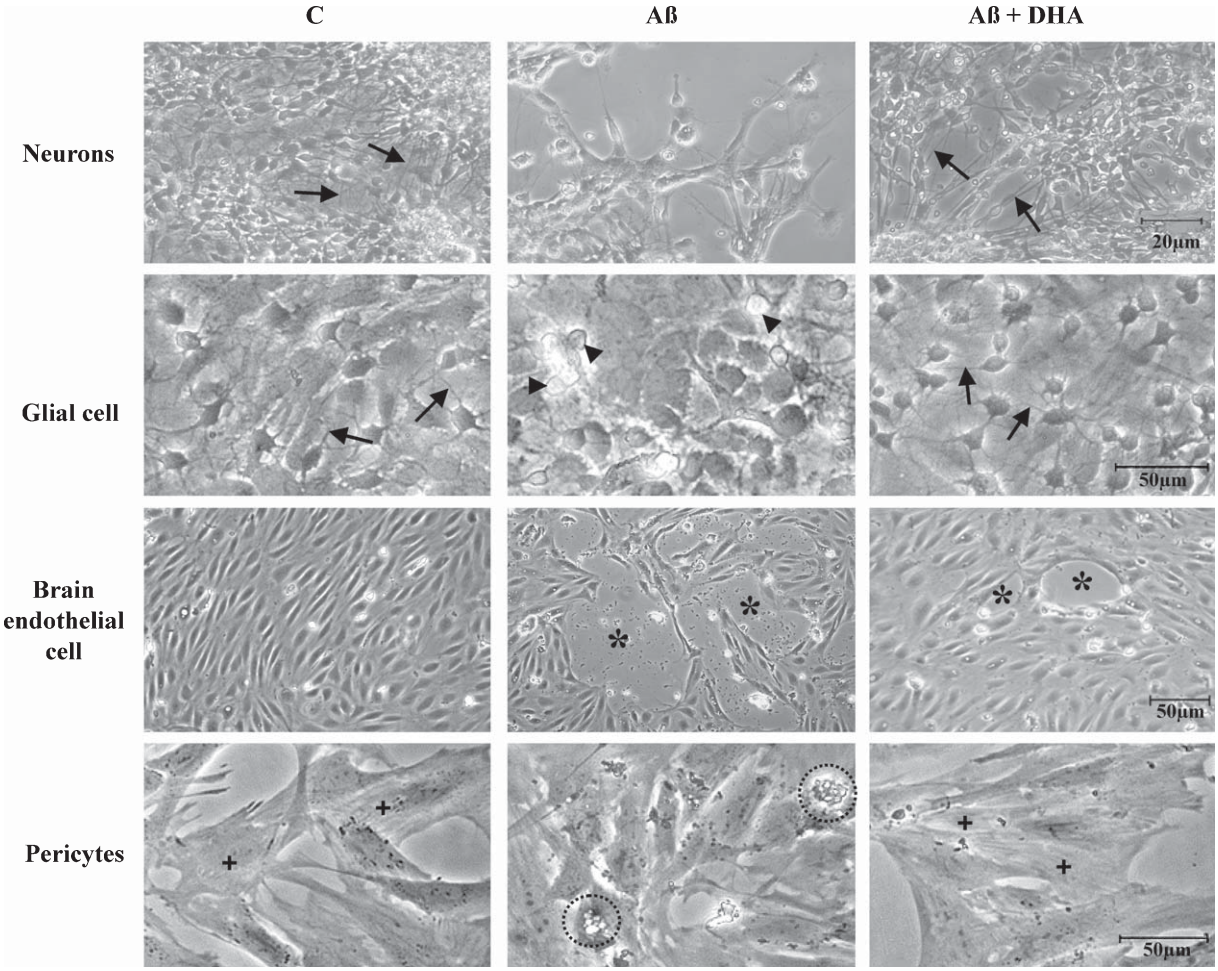

Fig. 5. The effect of docosahexaenoic acid (DHA, 1 μM on pericytes and 30 μM on the other three cell types) on oligomeric amyloid-β 1-42 ($A\beta_{42}$, 15 μM) induced toxicity on the morphology of neuronal, glial, brain endothelial, and pericyte primary cell cultures examined by phase contrast microscopy. Arrows show processes of neurons or glial cells, arrow heads point to apoptotic cells, asterisks show holes of in endothelial monolayers, cross signs show cytoplasmic fibers inside pericytes. The pericyte encircled by dotted line has cytoplasmic vacuolization.

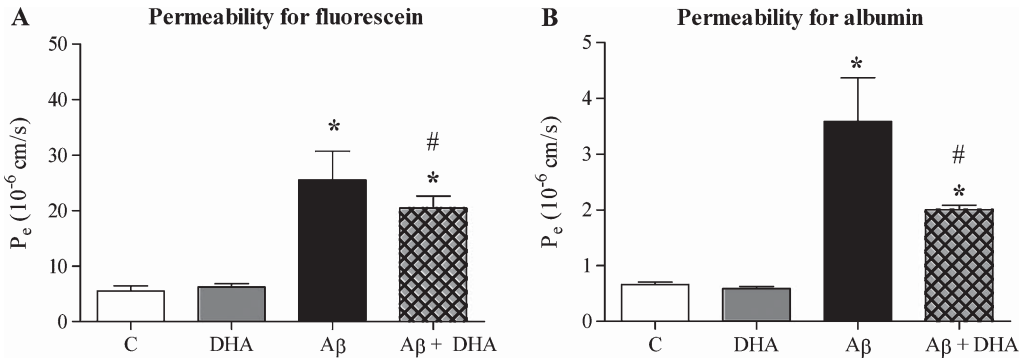

Fig. 6. Effect of docosahexaenoic acid (DHA, 30 μM) on oligomeric amyloid-β 1-42 ($A\beta_{42}$, 15 μM) induced changes in the permeability of primary brain endothelial cells for fluorescein (A) and Evans blue labeled albumin (B) Values presented are means ± S.E.M., $n = 6$. Statistically significant differences ($p < 0.05$) between the controls and treated groups (*), $A\beta_{42}$ and $A\beta_{42}$ + DHA treated groups (#) are indicated.

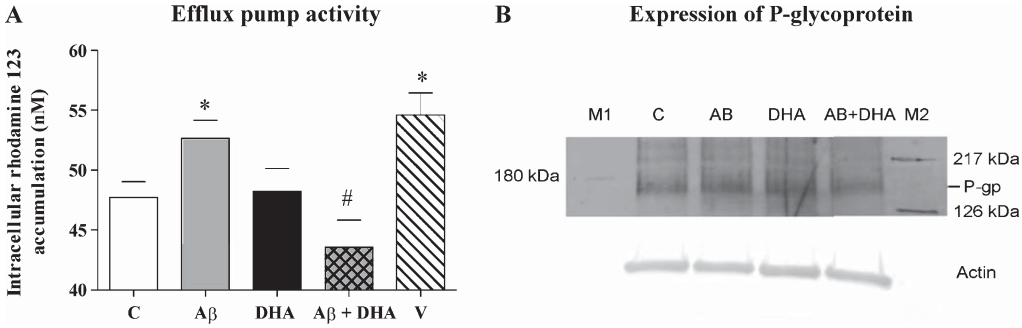

Fig. 7. Effect of docosahexaenoic acid (DHA, 30 μM) on oligomeric amyloid-β 1-42 ($A\beta_{42}$, 15 μM) induced changes in efflux pump activity of primary brain endothelial cells measured by rhodamine 123 accumulation (A). Changes of expression level of P-glycoprotein measured by Western blot analyses (B). Values presented are means ± S.E.M., $n = 5$. Statistically significant differences ($p < 0.05$) between the control and treated groups (*), $A\beta_{42}$ and $A\beta_{42}$ + DHA treated groups (#) are indicated.

It is important to note that the cellular toxicity of oligomeric $A\beta_{42}$ on the four types of cells was tested using the same assay conditions, therefore a comparison on their sensitivity can be made for the first time. The highest and similar level of toxicity was observed in the case of neurons and brain endothelial cells, while both glial cells and pericytes were more resistant to the damaging effect of oligomeric $A\beta_{42}$. This novel observation on cultured cells is in agreement with AD pathology, where the two hallmarks of the disease are the cerebrovascular damages and neuronal loss [50]. A possible explanation for the higher sensitivity of neurons and brain endothelial cells to oligomeric $A\beta_{42}$ as compared to glia and perictyes could be the higher expression level of receptors and transporters related to $A\beta_{42}$ efflux, uptake, or transport, but further comparative analysis is needed to prove this hypothesis.

Protection of the cells of the neurovascular unit against $A\beta_{42}$ by DHA

BBB dysfunction initiates and contributes to the disease process in AD [4]; therefore in addition to neurons, brain endothelial cells and other elements of the neurovascular unit are increasingly recognized as therapeutic targets in AD [1, 3]. There is little data on the protection of BBB and brain endothelial cells against the toxic effects of $A\beta_{42}$. Partial protection was described against $A\beta_{25–35}$ peptide induced cell damage by carnosine, an endogenous antiglycating dipeptide, homocarnosine and β-alanine on a rat brain endothelial cell line [51] and by simvastatin on a human brain endothelial cell line [47]. In a recent study on a human brain endothelial cell line, $A\beta_{42}$ cytotoxicity was reversed by administration of exogenous antioxidants, NADPH oxidase-2 inhibitors, and by blocking receptor for advanced glycation end products (RAGE) [52]. In our previous study, pentosan, a clinically used sulfated polysaccharide, protected rat brain endothelial cells against $A\beta_{42}$ toxicity [44].

The prospect of reducing the risk of AD by preventative strategies such as diet or lifestyle modification is highly favorable. Several epidemiological studies [9–12] and growing experimental data have shown that dietary DHA may improve neuronal development [53], restore and enhance cognitive functions [18, 54–56], and increase neuronal resistance to amyloid-induced oxidative stress [57–59]. Importantly, DHA readily crosses the BBB by diffusion [60, 61] and can easily reach glial cells and neurons.

Except for the highest tested dose, DHA was not toxic for neurons or glial and brain endothelial cells. Interestingly, pericytes showed an increased sensitivity to DHA treatment. The DHA content is high in retina, brain tissue, isolated brain microvessels, and cultured brain endothelial cells [62]. The high percentage of PUFAs in retinal microvessels was hypothesized to contribute to oxidation products and be involved in the pathogenic process of diabetic retinopathy [63]. Enrichment of cultured cells with DHA increases lipid peroxidation [64]. Differences in antioxidant enzyme activities, especially the higher level of superoxide dismutase and glutathione peroxidase were observed in retina endothelial cells as compared to retina pericytes, explaining their different behavior during the pathogenesis of diabetic retinopathy, early cell death of pericytes, and late endothelial cell proliferation [65]. No data on the ROS producing and antioxidant enzyme capacities of brain endothelial cells as compared to pericytes is available, but the high ROS-tolerance of brain endothelial cells was described recently [66]. We speculate that the lower level of ROS-scavenging capacity

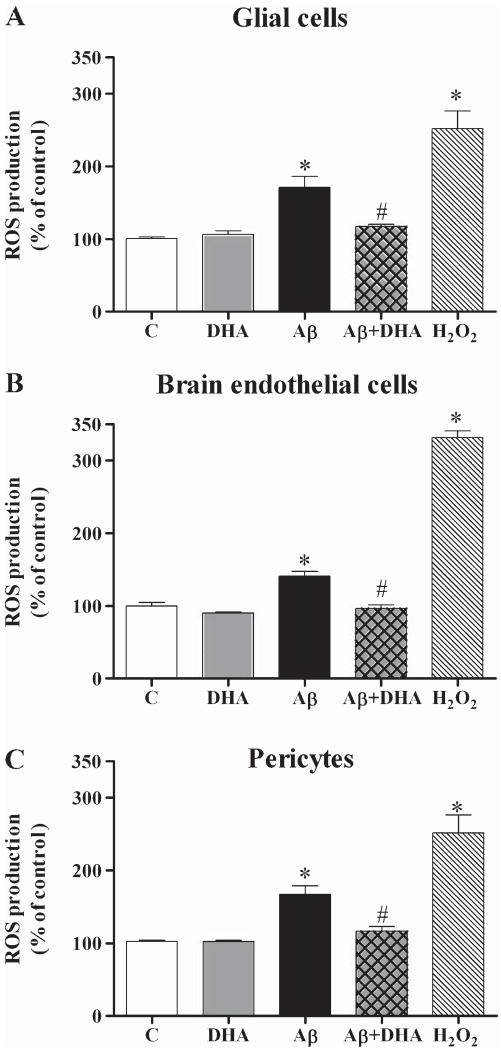

Fig. 8. Effect of docosahexaenoic acid (DHA, 30 μM) on oligomeric amyloid-β 1-42 ($A\beta_{42}$, 15 μM) induced changes in reactive oxygen species production in glial (A), brain endothelial cells (B), and pericyte (C) primary cell cultures measured by chloromethyl-dichloro-dihydro-fluorescein diacetate (DCFDA). Values presented are means ± S.E.M., $n = 8$. Statistically significant differences ($p < 0.05$) between the control and treated groups (*), $A\beta_{42}$ and $A\beta_{42}$ + DHA treated groups (#) are indicated.

of cultured brain pericytes, as compared to other neurovascular cells, might explain the observed sensitivity to DHA.

The beneficial effect of DHA was investigated in several model of AD but they were focused on neurons [17]. In neuroblastoma cells, DHA reduced amyloidogenic AβPP processing and $A\beta_{42}$ production [23]. In the present study DHA was not only protective against oligomeric $A\beta_{42}$ toxicity in primary neurons but also on acute hippocampal slices, a more complex, *ex vivo* model. Our main results indicate for the first time that DHA can protect not only neurons but also the other elements of the neurovascular unit (brain endothelial cells, glial cells, and pericytes) from the toxic effects of $A\beta_{42}$. DHA was effective in neuronal, endothelial, glial, and pericyte cell cultures in toxicity tests and improved the morphological changes in all four cell types after oligomeric $A\beta_{42}$ treatment, indicating a more extensive and diverse protective effect than previously supposed. The permeability of cerebral endothelial monolayers was increased by $A\beta_{42}$ similarly to our previous study [44], which was attenuated by DHA.

The mechanism of the DHA action is not fully understood. While there are no data on how DHA may affect RAGE, it was demonstrated recently in cultured brain endothelial cells that Aβ accumulation is lipid raft- and caveolae-dependent and involves RAGE and the caveolae-associated Ras signaling [67]. Disruption of lipid rafts by pretreatment with β-methyl-cyclodextrin protected against Aβ accumulation in this model. DHA is a well-known inducer of membrane fluidity [68] and by reducing cholesterol [23], it has a raft destabilizing effect and decreases the docking of Aβ [25], which may influence RAGE activity and contribute to the protective effect of DHA.

P-glycoprotein and BCRP are important efflux pumps at the BBB limiting the flux of drugs and xenobiotics to brain [69] and participating in $A\beta_{42}$ transport [70–72]. Beside changes in barrier function, $A\beta_{42}$ pretreatment inhibited the efflux activity of brain endothelial cells, in agreement with data from the literature [73, 74]. However, no change in P-glycoprotein expression level was observed. There could be several explanations for this observation: in addition to protein levels, several other factors influence the activity efflux pumps, like plasma membrane lipid composition, intracellular signaling pathways, and also intracellular ATP levels; and other pumps may also participate in rhodamine efflux.

The relevance of these results is emphasized by a recent clinical observation providing the first direct evidence that the P-glycoprotein transporter at the BBB is compromised in sporadic AD [75]. Since decreased P-glycoprotein function may be involved in the pathogenesis of AD [72, 75], our novel finding that DHA can prevent the decrease in P-glycoprotein activity induced by $A\beta_{42}$ treatment strengthens the therapeutic potential of DHA.

In AD, the accumulation of $A\beta_{42}$ increases the production of ROS resulting in increased lipid peroxidation in the brain [76]. Oxidative damage and

formation of oxidized lipids and proteins have been observed in the brains of patients with AD during postmortem analysis [77]. Lipid peroxide levels are significantly lower in DHA-administered rats indicating that dietary DHA contributes to the antioxidant defense, decreases oxidative stress, and protects against memory loss [12]. The levels of ROS in the cerebral cortex and hippocampus increase significantly after the infusion of $A\beta_{42}$ into the cerebral ventricle of rats, but then decrease significantly after the dietary administration of DHA [58]. In the present study, ROS production was elevated by oligomeric $A\beta_{42}$ in primary brain endothelial cells, in agreement with data obtained on a brain endothelial cell line [52]. Similarly to cytotoxicity and BBB dysfunction, this effect could be also inhibited by DHA. These observations suggest that DHA increases the antioxidant defense in the brain including the BBB and its mode of action may be related to direct scavenging of ROS or to the induction of antioxidant enzymes. Additional mechanisms cannot be excluded. Since the activation of the Wnt/β-catenin pathway increases BBB functions [78] and the effect of $A\beta_{42}$ on P-glycoprotein is mediated via Wnt/β-catenin signaling [73], it is tempting to speculate that DHA may also act through this pathway.

In conclusion, DHA may be a potent agent to prevent $A\beta_{42}$ induced damages on the elements of the neurovascular unit acting *via* multiple ways. Based on these new observations, DHA might exert a protective effect not only on neurons but also on the BBB and its functions, and this effect may be beneficial in AD.

ACKNOWLEDGMENTS

The research leading to these results has received funding from the European Community's 7th Framework Programme (FP/2007-2013) under grant agreement no. 211696 and TÁMOP-4.2.2.A-11/1/KONV-2012-0052 grant financed by the European Union and the European Regional Development Fund.

Authors' disclosures available online (http://www.j-alz.com/disclosures/view.php?id=1737).

REFERENCES

[1] Neuwelt EA, Bauer B, Fahlke C, Fricker G, Iadecola C, Janigro D, Leybaert L, Molnár Z, O'Donnell ME, Povlishock JT, Saunders NR, Sharp F, Stanimirovic D, Watts RJ, Drewes LR (2011) Engaging neuroscience to advance translational research in brain barrier biology. *Nat Rev Neurosci* **12**, 169-182.

[2] Zlokovic BV (2005) Neurovascular mechanisms of Alzheimer's neurodegeneration. *Trends Neurosci* **28**, 202-208.

[3] Deli MA (2005) The role of blood-brain barrier in neurodegenerative diseases. In *Molecular Bases of Neurodegeneration*, Di Liegro I, Savettieri G, eds. Research Signpost, Kerala, India, pp. 137-161.

[4] Zlokovic BV (2008) The blood-brain barrier in health and chronic neurodegenerative disorders. *Neuron* **57**, 178-201.

[5] Jaeger LB, Dohgu S, Hwang MC, Farr SA, Murphy MP, Fleegal-Demotta MA, Lynch JA, Robinson SM, Niehoff ML, Johnson SN, Kumar VB, Banks WA (2009) Testing the neurovascular hypothesis of Alzheimer's disease: LRP-1 antisense reduces blood-brain barrier clearance and increases brain levels of amyloid-β protein and impairs cognition. *J Alzheimers Dis* **17**, 553-570.

[6] Abbott NJ, Patabendige AA, Dolman DE, Yusof SR, Begley DJ (2010) Structure and function of the blood-brain barrier. *Neurobiol Dis* **37**, 13-25.

[7] Zlokovic BV, Yamada S, Holtzman D, Ghiso J, Frangione B (2000) Clearance of amyloid β-peptide from brain: Transport or metabolism. *Nat Med* **6**, 718-719.

[8] Banks WA, Niehoff ML, Drago D, Zatta P (2006) Aluminum complexing enhances amyloid beta protein penetration of blood-brain barrier. *Brain Res* **1116**, 215-221.

[9] Kalmijn S, Launer LJ, Ott A, Witteman JC, Hofman A, Breteler MM (1997) Dietary fat intake and the risk of incident dementia in the Rotterdam Study. *Ann Neurol* **42**, 776-782.

[10] Morris MC, Evans DA, Bienias JL, Tangney CC, Bennett DA, Wilson RS, Aggarwal N, Schneider J (2003) Consumption of fish and n-3 fatty acids and risk of incident Alzheimer disease. *Arch Neurol* **60**, 940-946.

[11] Lopez LB, Kritz-Silverstein D, Barrett Connor E (2011) High dietary and plasma levels of the omega-3 fatty acid docosahexaenoic acid are associated with decreased dementia risk: the Rancho Bernardo study. *J Nutr Health Aging* **15**, 25-31.

[12] Morley JE, Banks WA (2010) Lipids and cognition. *J Alzheimers Dis* **20**, 737-747.

[13] Hőgyes E, Nyakas C, Kiliaan A, Farkas T, Penke B, Luiten PG (2003) Neuroprotective effect of developmental docosahexaenoic acid supplement against excitotoxic brain damage in infant rats. *Neuroscience* **119**, 999-1012.

[14] Tully AM, Roche HM, Doyle R, Fallon C, Bruce I, Lawlor B, Coakley D, Gibney MJ (2003) Low serum cholesteryl esterdocosahexaenoic acid levels in Alzheimer's disease: A case-control study. *Br J Nutr* **89**, 483-489.

[15] Söderberg M, Edlund C, Kristensson K, Dallner G (1991) Fatty acid composition of brain phospholipids in aging and in Alzheimer's disease. *Lipids* **26**, 421-425.

[16] Lim GP, Calon F, Morihara T, Yang F, Teter B, Ubeda O, Salem NJr, Frautschy SA, Cole GM (2005) A diet enriched with the omega-3 fatty acid docosahexaenoic acid reduces amyloid burden in an aged Alzheimer mouse model. *J Neurosci* **25**, 3032-3040.

[17] Oksman M, Iivonen H, Hőgyes E, Amtul Z, Penke B, Leenders I, Broersen L, Lütjohann D, Hartmann T, Tanila H (2006) Impact of different saturated fatty acid, polyunsaturated fatty acid and cholesterol containing diets on beta-amyloid accumulation in APP/PS1 transgenic mice. *Neurobiol Dis* **23**, 563-572.

[18] Arsenault D, Julien C, Tremblay C, Calon F (2011) DHA improves cognition and prevents dysfunction of entorhinal cortex neurons in 3 x TG-AD mice. *PLoS ONE* **6**, e17397.

[19] Freund-Levi Y, Eriksdotter-Jönhagen M, Cederholm T, Basun H, Faxén-Irving G, Garlind A, Vedin I, Vessby B, Wahlund

LO, Palmblad J (2006) Omega-3 fatty acid treatment in 174 patients with mild to moderate Alzheimer disease: OmegAD study: A randomized double-blind trial. *Arch Neurol* **63**, 1402-1408.

[20] Kotani S, Sakaguchi E, Warashina S, Matsukawa N, Ishikura Y, Kiso Y, Sakakibara M, Yoshimoto T, Guo J, Yamashima T (2006) Dietary supplementation of arachidonic and docosahexaenoic acids improves cognitive dysfunction. *Neurosci Res* **56**, 159-164.

[21] Chiu CC, Su KP, Cheng TC, Liu HC, Chang CJ, Dewey ME, Stewart R, Huang SY (2008) The effects of omega-3 fatty acids monotherapy in Alzheimer's disease and mild cognitive impairment: A preliminary randomized double-blind placebo-controlled study. *Prog Neuropsychopharmacol Biol Psychiatry* **32**, 1538-1544.

[22] Quinn JF, Raman R, Thomas RG, Yurko-Mauro K, Nelson EB, Van Dyck C, Galvin JE, Emond J, Jack CRJr, Weiner M, Shinto L, Aisen PS (2010) Docosahexaenoic acid supplementation and cognitive decline in Alzheimer disease: A randomized trial. *JAMA* **304**, 1903-1911.

[23] Grimm MO, Kuchenbecker J, Grösgen S, Burg VK, Hundsdörfer B, Rothhaar TL, Friess P, de Wilde MC, Broersen LM, Penke B, Péter M, Vígh L, Grimm HS, Hartmann T (2011) Docosahexaenoic acid reduces amyloid β production via multiple pleiotropic mechanisms. *J Biol Chem* **286**, 14028-14039.

[24] Zhao Y, Calon F, Julien C, Winkler JW, Petasis NA, Lukiw WJ, Bazan NG (2011) Docosahexaenoic acid-derived neuroprotectin D1 induces neuronal survival via secretase- and PPARγ-mediated mechanisms in Alzheimer's disease models. *PLoS ONE* **6**, e15816.

[25] Hashimoto M, Katakura M, Hossain S, Rahman A, Shimada T, Shido O (2011) Docosahexaenoic acid withstands the Aβ(25-35)-induced neurotoxicity in SH-SY5Y cells. *J Nutr Biochem* **22**, 22-29.

[26] Nakagawa S, Deli MA, Kawaguchi H, Shimizudani T, Shimono T, Kittel Á, Tanaka M, Niwa M (2009) A new blood-brain barrier model using brain endothelial cells, pericytes and astrocytes. *Neurochem Int* **54**, 253-263.

[27] Tóth A, Veszelka S, Nakagawa S, Niwa M, Deli MA (2011) Patented *in vitro* blood-brain barrier models in CNS drug discovery. *Recent Pat CNS Drug Discov* **6**, 107-118.

[28] Bozso Z, Penke B, Simon D, Laczkó I, Juhász G, Szegedi V, Kasza A, Soós K, Hetényi A, Wéber E, Tóháti H, Csete M, Zarándi M, Fülöp L (2010) Controlled *in situ* preparation of Aβ(1-42) oligomers from the isopeptide "iso-Aβ(1-42)", physicochemical and biological characterization. *Peptides* **31**, 248-256.

[29] Környei Z, Tóth B, Tretter L, Madarász E (1998) Effects of retinoic acid on rat forebrain cells derived from embryonic and perinatal rats. *Neurochem Int* **33**, 541-549.

[30] Deli MA, Joó F, Krizbai I, Lengyel I, Nunzi GM, Wolff J-R (1993) Calcium/calmodulin stimulated protein kinase II is present in primary cultures of cerebral endothelial cells. *J Neurochem* **60**, 1960-1963.

[31] Kis B, Deli MA, Kobayashi H, Ábrahám CS, Yanagita T, Kaiya H, Isse T, Nishi R, Gotoh S, Kangawa K, Wada A, Greenwood J, Niwa M, Yamashita H, Ueta Y (2001) Adrenomedullin regulates blood-brain barrier functions *in vitro*. *Neuroreport* **12**, 4139-4142.

[32] Veszelka S, Pásztói M, Farkas AE, Krizbai I, Dung NTK, Niwa M, Ábrahám CS, Deli MA (2007) Pentosan polysulfate protects brain endothelial cells against bacterial lipopolysaccharide-induced damages. *Neurochem Int* **50**, 219-228.

[33] Perrière N, Demeuse P, Garcia E, Regina A, Debray M, Andreux JP, Couvreur P, Scherrmann JM, Temsamani J, Couraud P-O, Deli MA, Roux F (2005) Puromycin-based purification of rat brain capillary endothelial cell cultures. Effect on the expression of blood-brain barrier-specific properties. *J Neurochem* **93**, 279-289.

[34] Nakagawa S, Deli MA, Nakao S, Honda M, Hayashi K, Nakaoke R, Kataoka Y, Niwa M (2007) Pericytes from brain microvessels strengthen the barrier integrity in primary cultures of rat brain endothelial cells. *Cell Mol Neurobiol* **27**, 687-694.

[35] Ceruti S, Colombo L, Magni G, Viganò F, Boccazzi M, Deli MA, Sperlágh B, Abbracchio MP, Kittel Á (2011) Oxygen-glucose deprivation increases the enzymatic activity and the microvesicle-mediated release of ectonucleotidases in the cells composing the blood-brain barrier. *Neurochem Int* **59**, 259-271.

[36] Dore-Duffy P, Katychev A, Wang X, Van Buren E (2006) CNS microvascular pericytes exhibit multipotential stem cell activity. *J Cereb Blood Flow Metab* **26**, 613-624.

[37] Vandenhaute E, Dehouck L, Boucau MC, Sevin E, Uzbekov R, Tardivel M, Gosselet F, Fenart L, Cecchelli R, Dehouck MP (2011) Modelling the neurovascular unit and the blood-brain barrier with the unique function of pericytes. *Curr Neurovasc Res* **8**, 258-269.

[38] Datki Z, Hunya A, Penke B (2007) A novel and simple fluorescence method for the measurement of presynaptic vesicular zinc release in acute hippocampal slices with a fluorescence plate reader. *Brain Res Bull* **74**, 183-187.

[39] Datki Z, Juhász A, Gálfi M, Soós K, Papp R, Zádori D, Penke B (2003) Method for measuring neurotoxicity of aggregating polypeptides with the MTT assay on differentiated neuroblastoma cells. *Brain Res Bull* **62**, 223-229.

[40] Deli MA, Ábrahám CS, Kataoka Y, Niwa M (2005) Permeability studies on *in vitro* blood-brain barrier models: physiology, pathology, and pharmacology. *Cell Mol Neurobiol* **25**, 59-127.

[41] Fontaine M, Elmquist WF, Miller DW (1996) Use of rhodamine 123 to examine the functional activity of P-glycoprotein in primary cultured brain microvessels endothelial cell monolayers. *Life Sci* **59**, 1521-1531.

[42] Perrière N, Yousif S, Cazaubon S, Chaverot N, Bourasset F, Cisternino S, Declèves X, Hori S, Terasaki T, Deli M, Scherrmann JM, Temsamani J, Roux F, Couraud PO (2007) A functional *in vitro* model of rat blood-brain barrier for molecular analysis of efflux transporters. *Brain Res* **1150**, 1-13.

[43] Lowry OH, Rosebrough NJ, Farr AL, Randall RJ (1951) Protein measurement with the Folin phenol reagent. *J Biol Chem* **193**, 265-275.

[44] Deli MA, Veszelka S, Csiszár B, Tóth A, Kittel Á, Csete M, Sipos Á, Szalai A, Fülöp L, Penke B, Ábrahám CS, Niwa M (2010) Protection of the blood-brain barrier by pentosan against amyloid-β-induced toxicity. *J Alzheimers Dis* **22**, 777-794.

[45] Abramov AY, Canevari L, Duchen MR (2004) Calcium signals induced by amyloid beta peptide and their consequences in neurons and astrocytes in culture. *Biochim Biophys Acta* **1742**, 81-87.

[46] Verdier Y, Zarándi M, Penke B (2004) Amyloid beta-peptide interactions with neuronal and glial cell plasma membrane: Binding sites and implications for Alzheimer's disease. *J Pept Sci* **10**, 229-248.

[47] András IE, Rha G, Huang W, Eum S, Couraud P-O, Romero IA, Hennig B, Toborek M (2008) Simvastatin protects against amyloid β and HIV-1 Tat-induced promoter activities of

inflammatory genes in brain endothelial cells. *Mol Pharmacol* **73**, 1424-1433.

[48] Verbeek MM, de Waal RM, Schipper JJ, Van Nostrand WE (1997) Rapid degeneration of cultured human brain pericytes by amyloid beta protein. *J Neurochem* **68**, 1135-1141.

[49] Wilhelmus MM, Otte-Holler I, van Triel JJ, Veerhuis R, Maat-Schieman ML, Bu G, de Waal RM, Verbeek MM (2007) Lipoprotein receptor-related protein-1 mediates amyloid-β-mediated cell death of cerebrovascular cells. *Am J Pathol* **171**, 1989-1999.

[50] Jeynes B, Provias J (2008) Evidence for altered LRP/RAGE expression in Alzheimer lesion pathogenesis. *Curr Alzheimer Res* **5**, 432-437.

[51] Preston JE, Hipkiss AR, Himsworth DT, Romero IA, Abbott NJ (1998) Toxic effects of β-amyloid(25-35) on immortalized rat brain endothelial cell: Protection by carnosine, homocarnosine and β-alanine. *Neurosci Lett* **242**, 105-108.

[52] Carrano A, Hoozemans JJ, van der Vies SM, Rozemuller AJ, van Horssen J, de Vries HE (2011) Amyloid Beta induces oxidative stress-mediated blood-brain barrier changes in capillary amyloid angiopathy. *Antioxid Redox Signal* **15**, 1167-1178.

[53] Tixier-Vidal A, Picart R, Loudes C, Bauman AF (1986) Effects of polyunsaturated fatty acids and hormones on synaptogenesis in serum-free medium cultures of mouse fetal hypothalamic cells. *Neuroscience* **17**, 115-132.

[54] Greiner RS, Moriguchi T, Hutton A, Slotnick BM, Salem N Jr. (1999) Rats with low levels of brain docosahexaenoic acid show impaired performance in olfactory-based and spatial learning tasks. *Lipids* **34**, S239-S243.

[55] Gamoh S, Hashimoto M, Sugioka K, Hossain MS, Hata N, Misawa Y (1999) Chronic administration of docosahexaenoic acid improves reference memory-related learning ability in young rats. *Neuroscience* **93**, 237-241.

[56] Karr JE, Alexander JE, Winningham RG (2011) Omega-3 polyunsaturated fatty acids and cognition throughout the lifespan. *Nutr Neurosci* **14**, 216-225.

[57] Lauritzen I, Blondeau N, Heurteaux C, Widmann C, Romey G, Lazdunski M (2000) Polyunsaturated fatty acids are potent neuroprotectors. *EMBO J* **19**, 1784-1793.

[58] Hashimoto M, Tanabe Y, Fujii Y, Kikuta T, Shibata H, Shido O (2005) Chronic administration of docosahexaenoic acid ameliorates the impairment of spatial cognition learning ability in amyloid β-infused rats. *J Nutr* **135**, 549-555.

[59] Calon F, Lim GP, Yang F, Morihara T, Teter B, Ubeda O (2004) Docosahexaenoic acid protects from dendritic pathology in an Alzheimer's disease mouse model. *Neuron* **43**, 633-645.

[60] Lagarde M, Bernoud N, Brossard N, Lemaitre-Delaunay D, Thiès F, Croset M, Lecerf J (2001) Lysophosphatidylcholine as a preferred carrier form of docosahexaenoic acid to the brain. *J Mol Neurosci* **16**, 201-204.

[61] Ouellet M, Emond V, Chen CT, Julien C, Bourasset F, Oddo S, LaFerla F, Bazinet RP, Calon F (2009) Diffusion of docosahexaenoic and eicosapentaenoic acids through the blood-brain barrier: An *in situ* cerebral perfusion study. *Neurochem Int* **55**, 476-482.

[62] Bénistant C, Dehouck MP, Fruchart JC, Cecchelli R, Lagarde M (1995) Fatty acid composition of brain capillary endothelial cells: Effect of the coculture with astrocytes. *J Lipid Res* **36**, 2311-2319.

[63] Lecomte M, Paget C, Ruggiero D, Wiernsperger N, Lagarde M (1996) Docosahexaenoic acid is a major n-3 polyunsaturated fatty acid in bovine retinal microvessels. *J Neurochem* **66**, 2160-2167.

[64] Roig-Pérez S, Cortadellas N, Moretó M, Ferrer R (2010) Intracellular mechanisms involved in docosahexaenoic acid-induced increases in tight junction permeability in Caco-2 cell monolayers. *J Nutr* **140**, 1557-1563.

[65] Paget C, Lecomte M, Ruggiero D, Wiernsperger N, Lagarde M (1998) Modification of enzymatic antioxidants in retinal microvascular cells by glucose or advanced glycation end products. *Free Radic Biol Med* **25**, 121-129.

[66] Quimby S, Fern R (2011) Novel morphological features of developing white matter pericytes and rapid scavenging of reactive oxygen species in the neighbouring endothelia. *J Anat* **219**, 65-77.

[67] András IE, Eum SY, Toborek M (2012) Lipid rafts and functional caveolae regulate HIV-induced amyloid beta accumulation in brain endothelial cells. *Biochem Biophys Res Commun* **421**, 177-183.

[68] Yang X, Sheng W, Sun GY, Lee JC (2011) Effects of fatty acid unsaturation numbers on membrane fluidity and α-secretase-dependent amyloid precursor protein processing. *Neurochem Int* **58**, 321-329.

[69] Pardridge WM (2002) Drug and gene targeting to brain with molecular Trojan horses. *Nat Rev Drug Disc* **1**, 131-139.

[70] Tai LM, Loughlin AJ, Male DK, Romero IA (2009) P-glycoprotein and breast cancer resistance protein restrict apical-to-basolateral permeability of human brain endothelium to amyloid-beta. *J Cereb Blood Flow Metab* **29**, 1079-1083.

[71] Candela P, Gosselet F, Saint-Pol J, Sevin E, Boucau MC, Boulanger E, Cecchelli R, Fenart L (2010) Apical-to-basolateral transport of amyloid-β peptides through blood-brain barrier cells is mediated by the receptor for advanced glycation end-products and is restricted by P-glycoprotein. *J Alzheimers Dis* **22**, 849-859.

[72] Vogelgesang S, Jedlitschky G, Brenn A, Walker LC (2011) The role of the ATP-binding cassette transporter P-glycoprotein in the transport of β-amyloid across the loodbrain barrier. *Curr Pharm Des* **17**, 2778-2786.

[73] Kania KD, Wijesuriya HC, Hladky SB, Barrand MA (2011) Beta amyloid effects on expression of multidrug efflux transporters in brain endothelial cells. *Brain Res* **1418**, 1-11.

[74] Kuhnke D, Jedlitschky G, Grube M, Krohn M, Jucker M, Mosyagin I, Cascorbi I, Walker LC, Kroemer HK, Warzok RW, Vogelgesang S (2007) MDR1-P-Glycoprotein (ABCB1) Mediates Transport of Alzheimer's amyloid-beta peptides–implications for the mechanisms of Abeta clearance at the blood-brain barrier. *Brain Pathol* **17**, 347-353.

[75] van Assema DM, Lubberink M, Bauer M, van der Flier WM, Schuit RC, Windhorst AD, Comans EF, Hoetjes NJ, Tolboom N, Langer O, Müller M, Scheltens P, Lammertsma AA, van Berckel BN (2012) Blood-brain barrier P-glycoprotein function in Alzheimer's disease. *Brain* **135**, 181-189.

[76] Floyd RA, Hensley K (2002) Oxidative stress in brain aging. Implications for therapeutics of neurodegenerative diseases. *Neurobiol Aging* **23**, 795-807.

[77] Choi J, Levey AI, Weintraub ST, Rees HD, Gearing M, Chin LS, Li L (2004) Oxidative modifications and down-regulation of ubiquitin carboxyl-terminal hydrolase L1 associated with idiopathic Parkinson's and Alzheimer's diseases. *J Biol Chem* **279**, 13256-13264.

[78] Liebner S, Corada M, Bangsow T, Babbage J, Taddei A, Czupalla CJ, Reis M, Felici A, Wolburg H, Fruttiger M, Taketo MM, von Melchner H, Plate KH, Gerhardt H, Dejana E (2008) Wnt/beta-catenin signaling controls development of the blood-brain barrier. *J Cell Biol* **183**, 409-417.